A COMPUTATIONAL ANALYSIS FOR THE RISE, DISPERSION AND DEPOSITION OF BUOYANT PLUMES

by

XIAOMING ZHANG

B.S., Department of Mechanics
Zhejiang University, China
(1982)

M.S., Department of Earth, Atmospheric and Planetary Sciences
Massachusetts Institute of Technology
(1990)

Submitted to the Department of Mechanical Engineering
in Partial Fulfillment of the Requirements
for the Degree of

DOCTOR OF PHILOSOPHY

at the

MASSACHUSETTS INSTITUTE OF TECHNOLOGY

December, 1993
(February 1994)

Signature of Author _____
Department of Mechanical Engineering
October, 1993

Certified by _____
Ahmed F. Ghoniem
Professor, Mechanical Engineering
Thesis Supervisor

Accepted by _____
Ain A. Sonin
Chairman, Departmental Graduate Committee

A COMPUTATIONAL ANALYSIS FOR THE RISE, DISPERSION AND DEPOSITION OF BUOYANT PLUMES

by

XIAOMING ZHANG

Submitted to the Department of Mechanical Engineering
in Partial Fulfillment of the
Requirements for the Degree of Doctor of Philosophy
in Mechanical Engineering

ABSTRACT

Wind-blown, buoyancy-driven plumes are widely observed in nature, e.g., from forest fires, oil-well fires, uncontrolled explosions, tall industry chimneys, etc. To understand the phenomena involved in plume dispersion and to provide relevant information for assessing their environmental impact, a multi-dimensional computational model describing the rise, dispersion, fall and deposition of these plumes in stratified atmosphere is developed. Lagrangian numerical techniques, based on the extension of the vortex method to variable density flow, are used in solving the governing equations.

The computational model is applied to the study of the buoyant plume dynamics under three types of atmospheric stratifications: neutrally stratified, linearly stratified and sharply stratified. The important physical features involved, such as, the entrainment process, plume structure and buoyancy-generated turbulence, are investigated. Results show that, in most cases, the plume crosswind section exhibits a kidney-shaped pattern, as observed in laboratory and field experiments. This pattern persists for a long distance downstream the source and may bifurcate into separate and distinct lumps. This phenomenon is due to the formation of two counter-rotating streamwise vortices that develop as baroclinically generated vorticity rolls up on both sides of the plume cross section. The concomitant plume material distribution is not Gaussian, as conventionally modeled. The induced velocity field and the entrainment of the surrounding air are dominated by these vortices. Linear stratification and the presence of low level inversion substantially modifies the plume trajectory and may lead to the trapping of a large fraction of the plume material close to the ground. The computed plume trajectory, dispersion pattern and trapping fraction compare well with laboratory and field observations.

The model has also been applied to the dispersion of plumes with negative buoyancy. The study of a wind-blown descending heavy plume shows that the ground deposition pattern is also far from Gaussian. The computational model is finally extended to the prediction of the collapse and spread of an instantaneously released dense gas cloud, a problem encountered in the accidental release of heavy industrial hazardous materials. The numerical simulation reproduces the large frontal vortex ring and its spreading rate; reveals that the entrainment process occurs mainly at the cloud top through the engulfment of vortex rings. This is used to develop an analytical model for the description of major features of the dense cloud spreading.

Thesis Committee: Prof. James A. Fay
Prof. Ahmed F. Ghoniem (Chairman)
Dr. Steven R. Hanna
Prof. Gregory J. McRae
Prof. Kenneth A. Smith

To Peiying Gong and Yinghui Jiang

ACKNOWLEDGMENT

I would like to thank my thesis advisor Prof. Ahmed F. Ghoniem for his encouragement, many stimulating discussions, criticisms, and scholarly advice. I am grateful to him for his teaching on: how to choose the right research problem, how to convince people of new findings, and how to communicate effectively. He painstakingly read many drafts of this work and carefully cleared and corrected thousands of vague areas and grammar mistakes. Without his guidance and support, this thesis would not be possible.

I must also acknowledge the thesis committee members: Prof. James A. Fay, Dr. Steven R. Hanna, Prof. Gregory J. McRae and Prof. Kenneth A. Smith, for their interest, valuable questions, suggestions, and for accommodating my countless requests. I have learnt greatly from their profound expertise on various aspects of environmental sciences.

This work benefited from several lengthy discussions with Drs. Omar M. Knio and Marios Soteriou, and I wish to thank them for several enlightening conversations on the development and implementation of the transport element method, and many puzzling matters dealing with Cray and VAX. My colleagues at MIT, Pat Condon, Adrin Gharakhani, Van Luu, Costa Petrov, Chunhai Wang and Xiangdong He and many others have provided the friendly atmosphere which allowed me to endure the difficulties of graduate student life. Their immeasurable support is sincerely appreciated.

Special thanks go to my off-campus brotherhood, Joseph Chang, Nathaniel Lin and Daniel Lee. At last, I wish to express my deepest gratitude to my wife, Peiying Gong, for her patience, understanding, and love; and my parents and brother for their continuous encouragement.

This work has been jointly supported by the Mineral Management Services of the Department of the Interior, and the Building and Fire Research Laboratory of the National Institute of Standards and Technology. The computer support for this project is provided by the Illinois National Center for Supercomputer Application.

TABLE OF CONTENTS

A COMPUTATIONAL ANALYSIS FOR THE RISE, DISPERSION AND DEPOSITION OF BUOYANT PLUMES

OVERVIEW

The rise, dispersion, and the eventual settlement of large, strongly buoyant plumes generated from localized sources are responsible for distributing measurable amounts of hazardous material in the atmosphere and on the ground. The mechanisms governing the dispersion of these plumes in the near field of the source are fundamentally different from those encountered in the case of distributed sources. While atmospheric turbulence and meteorological conditions govern the primary dispersion mechanism in the latter case, which is widely studied, the former is controlled by buoyancy generated turbulence and is not well investigated. A collection of photographs and diagrams on the rise and dispersion of buoyant plumes are shown in the Appendix at the end of the thesis.

This thesis is primarily on the development of a computational model to the study of the buoyant plume motion when the effect of atmospheric turbulence is negligible. The first three chapters are on the rise and dispersion of wind-blown, buoyancy-driven light plumes under three types of atmospheric stratifications. They are, respectively: neutrally stratified atmosphere, where the air potential density (hereafter referred as density) is uniformly distributed; linearly stratified atmosphere, where the air density decreases linearly with altitude; and, sharply stratified atmosphere (inversion layer), where the air density experiences a sharp drop across a thin horizontal layer.

Beyond a point where equilibrium height is reached within a stably stratified atmosphere, the plume becomes negatively buoyant and starts to fall due to its heavy smoke loading. Chapter 4 is on the study of the trajectory of this wind-blown descending plume and the ground distribution pattern of its smoke material.

As another example of the application, Chapter 5 extends the computational model to the prediction of the spread and dispersion of instantaneously released dense gases. This subject is important in assessing the risk posed by the accidental release of

heavy industrial hazardous materials. Based on the numerical results, a simple analytical model is developed to capture the major features on the spreading front and the decaying concentration of the dense gas.

In each of these Chapters, the motivation of the work, numerical scheme, and computational results are given in detail. The fundamental mechanisms common to the dynamics of buoyant plumes, being either lighter-than-air or heavier-than-air, are delineated.

CHAPTER 1

A COMPUTATIONAL MODEL FOR THE RISE AND DISPERSION OF WIND-BLOWN, BUOYANCY-DRIVEN PLUMES
PART I. NEUTRALLY-STRATIFIED ATMOSPHERE

ABSTRACT

A multi-dimensional computational model for the rise and dispersion of a wind-blown, buoyancy-driven plume in a calm, neutrally stratified atmosphere is presented. Lagrangian numerical techniques, based on the extension of the vortex method to variable density flows, are used to solve the governing equations. The plume rise trajectory and the dispersion of its material in the crosswind plane are predicted. It is found that the computed trajectory agrees well with the two-thirds power law of a buoyancy-dominated plume, modified to include the effect of the initial plume size. The effect of small-scale atmospheric turbulence, modeled in terms of eddy viscosity, on the plume trajectory is found to be negligible. For all values of buoyancy Reynolds number, the plume cross-section exhibits a kidney-shaped pattern, as observed in laboratory and field experiments. This pattern is due to the formation of two counter-rotating vortices which develop as baroclinically generated vorticity rolls up on both sides of the plume cross-section. Results show that the plume rise can be described in terms of three distinct stages: a short acceleration stage, a long double-vortex stage, and a breakup stage. The induced velocity field and engulfment are dominated by the two large vortices. The effect of a flat terrain on the plume trajectory and dispersion is found to be very small. The equivalent radii of plumes with different initial cross-sectional aspect ratios increase at almost the same rate. A large aspect-ratio plume rises slower initially and then catches up with smaller aspect-ratio plumes in the breakup stage. The Boussinesq approximation is found to be valid if the ratio of the density perturbation to the reference density is less than 0.1.

NOMENCLATURE

A_R	$\equiv R_y/R_z$, aspect ratio of plume cross-section;
d	Characteristic dimension of plume density profile;
f_δ	Element core function;
g_r	Gravitational acceleration;
$\vec{g}(\vec{x},t)$	Density gradient;
h	Spatial discretization length in the numerical scheme;
H	Vertical thickness of plume cross-section;
H_T	H_T^*/R, dimensionless initial plume height;
l_b	Buoyancy length;
$\dot{m}_p$	$\equiv -\int \rho_p^*(y^*,z^*)\, U\, dA$, deficient mass flux of the plume;
L	Circumference of plume cross-section;
L_o	L at $t = 0$;
M	Number of discretization layers across plume-air interface;
N	Total number of computational elements;
p	Dimensionless perturbation pressure;
Pe_b	Buoyancy Peclet number;
R	Square root of plume cross-sectional area;
R_{eq}	Equivalent radius of plume cross-section;
R^*	Radius of plume cross-section;
R_y	Major (horizontal) scale of elliptical plume cross-section;
R_z	Minor (vertical) scale of elliptical plume cross-section;
Re_b	Buoyancy Reynolds number;
Re_s	Stack exit Reynolds number;
t	Same as the normalized x coordinate;
u, v, w	Perturbation velocity components in x, y, z direction, respectively;
U	Homogeneous wind speed;
V	$\equiv \sqrt{\varepsilon R\, g_r}$, buoyancy velocity;
$\vec{u}$	Velocity vector;
V	Velocity scale of buoyancy generated flow;
W	Plume horizontal width;
W_o	W at $t = 0$;
x	Horizontal wind direction;
$\vec{x}$	$= (y,z)$;

y Horizontal direction normal to the wind direction;

z Vertical direction;

α_e Turbulent eddy diffusivity;

β Entrainment coefficient;

Γ_i Circulation of a vortex element;

δ Core radius of a vortex/transport element;

δA_i Area associated with a computational element;

Δ_c Combination length;

Δ_i Insertion length;

ρ_p Dimensionless plume density;

$\delta\rho_p$ Density variation across a discretization layer;

Δt Time step;

$\Delta\chi i$ Distance between neighboring computational elements;

ε Plume mass flux ratio;

ν_e Turbulent eddy viscosity;

ρ_o^* Background air density;

ρ_p^* Deficient plume density;

ω Streamwise vorticity;

$\vec{\chi}_i$ Vortex/transport element trajectory.

Superscript

* Dimensional quantities

1.1. INTRODUCTION

Accurate prediction of buoyant plume rise and dispersion in a turbulent atmosphere is important in many practical applications. Buoyancy represents one of the primary mechanisms governing the motion of plumes generated from sources such as massive fires resulting from the burning of oil spills, uncontrolled oil wells, forest fires, and large-scale explosions (Evans et al., 1986 and 1989), and hot exhaust plumes emitted from tall industry stacks (Briggs, 1975, Weil, 1988a), among others. Besides buoyancy, the dispersion of these plumes, which determines their impact on the local, and possibly distant environment, is governed by the meteorological conditions, atmospheric turbulence, atmospheric stratification, ground terrain, etc. In this Chapter, we apply Lagrangian numerical techniques utilizing vortex and transport element methods to solve equations governing a plume rising in a crosswind in the case of a neutrally stratified atmosphere. Cases involving inversion layers, continuous atmospheric stratification, large-scale atmospheric turbulence, particulate matter and chemical reactions will be studied later.

Most plume studies, including analytical and numerical models, and laboratory and field experiments, can be divided into two categories. The first is concerned with the plume trajectory. Scaling laws for the trajectory of buoyancy-dominated plumes have been proposed (Briggs, 1975, Netterville, 1990). In deriving these laws: (1) the integral equations of volume, mass, and momentum conservation are applied; (2) an entrainment assumption, stating that ambient air influx velocity into the plume is proportional to the velocity difference between the plume and the wind, is used; and, (3) a self-similarity profile, Gaussian or top-hat distribution of momentum, buoyancy and pollutant concentration in the plume cross-sections, is introduced (see Appendix 1.A for detail and extension). The second category is concerned with the study of plume material dispersion (Venkatram 1986, Weil, 1988b), including the effects of the atmospheric boundary layer and atmospheric stratification (Deardorff, 1970, Nieuwstadt, 1992a,b).

Fundamentally, plume rise and dispersion are strongly interrelated (Nieuwstadt, 1992a,b), and fast dispersion often results from strong entrainment. Buoyancy not only contributes to plume rise, but also to dispersion. In general, for a buoyant material, one cannot independently calculate the plume rise and the dispersion.

Plume rise and dispersion studies have been used to: (1) improve our understanding of plume dynamics and the effect of atmospheric and emission conditions on the spread of pollutants; (2) provide data for atmospheric contamination in specific cases; and, (3) contribute, using accurate experimental data, to the development of working models. However, these models, although revealing, can hardly be extended to more complicated problems, such as: plume interaction with inversion layers; the effect of complex ground terrains; or cases when physical or chemical transformations of the plume material are important. Empirical constants built into these models, like the entrainment rate, are not universal (Gebhart et al, 1984), and a wide range is reported for their values (Fay et al, 1970, Hewett et al, 1971).

Large-eddy simulation of plumes in the convective boundary layer have recently been performed. In a large-eddy simulation, one computes the large-scale turbulent motion explicitly on a computationally manageable grid, while the effect of the small scales is represented with the aid of a "subgrid model." Since the incorporation of buoyancy effects into turbulence models has not been well established yet, as pointed out by Golay (1982), the description of the strong concentration gradient near the plume interface is not expected to be accurate. One major effect of plume buoyancy is to increase dispersion by self-generated turbulence. This effect is almost completely neglected in large eddy modeling. Furthermore, grid-based numerical methods, including finite-difference or finite-element approaches, involve numerical diffusion which reduces the effective Reynolds number of the simulations. Using a large-eddy model, Nieuwstadt (1992a,b) found that, for a modestly buoyant plume, the calculated concentration distributions were comparable with the experimental results. However, the calculated

plume rise did not follow the well-established two-thirds law, and the often observed formation of the two counter-rotating vortices in the plume cross-section was also not accurately resolved. Nieuwstadt suggested that these simulation results be considered with caution.

Numerical simulations of plume rise and dispersion without invoking entrainment hypotheses are still needed. A detailed understanding and accurate prediction of the buoyancy-driven turbulent entrainment process are undoubtedly useful in practice. This work is an attempt in this direction, considering only buoyant plume motion in a neutral atmosphere with small-scale atmospheric turbulence. The computational model is validated by comparing its results to available experimental data. Increasing the level of complexity, i.e., considering more interactions between the plume and its surroundings, will be dealt with in future publications.

This Chapter is organized as follows. The assumptions and formulation are discussed in Section 1.2. Section 1.3 is a brief summary of the vortex method and transport element method. Section 1.4 focuses on the study of the effects of buoyancy and small-scale atmospheric turbulence on the plume trajectory. Comparison with the two-thirds power law is presented. In Section 1.5, plume entrainment and dispersion characteristics are discussed. Field and laboratory observations are used in the comparison with the numerical results. The vorticity generation mechanism, traced back to buoyancy, is then delineated. The effects of the initial plume shape and height are investigated. In Section 1.6, the validity of the Boussinesq approximation in the buoyant plume study is investigated. Section 1.7 is a short conclusion.

1.2. FORMULATION

1.2.1. Scales

Before presenting the governing equations, we define several important scales in the buoyant plume problem. Let R denote the length scale of the plume cross-section, taken here as the square root of the initial plume cross-sectional area. The atmosphere is assumed to be neutrally stratified with constant density ρ_o^* and uniform horizontal wind velocity U. The initial plume density distribution is $\rho_o^* + \rho_p^*$ where $\rho_p^*(y^*, z^*)$ is the deficient plume density, which is negative for a high temperature, low density rising plume. The deficient plume mass flux is:

$$\dot{m}_p = -\int \rho_p^* U \, dA > 0 \tag{1.1}$$

A suitable buoyancy velocity scale is:

$$V = \sqrt{\varepsilon R g_r} \tag{1.2}$$

where

$$\varepsilon = \frac{\dot{m}_p}{\rho_o^* U R^2} << 1 \tag{1.3}$$

is the mass flux ratio, i.e., the ratio between the deficient plume mass flux and the air mass flux within the plume cross-section, and g_r is the gravitational acceleration. For a typical plume, $\left|\frac{\rho_p^*}{\rho_o^*}\right| \approx O(10^{-1})$, so that $\varepsilon \approx O(10^{-1})$. Thus, for $R = O(10m)$, a characteristic buoyancy velocity is $V = O(3\ m/s)$. This velocity scale is smaller than the usual ambient wind velocity $U \approx O(5 - 10\ m/s)$.

A buoyant Reynolds number can be defined as:

$$Re_b = \frac{VR}{\nu_e} \tag{1.4}$$

where ν_e is the small-scale turbulent eddy viscosity.[1]

---

[1] In this work, we loosely differentiate between large-scale turbulence and small-scale turbulence using the plume radius as a characteristic length scale. We only account for the effect of turbulent eddies whose size is much smaller than the plume radius. The effect of these eddies is to enhance turbulent diffusion. The effect of larger scales will be studied in future work.

1.2.2. Governing Equations

The goal of our study is to predict, using numerical simulations, the downwind trajectory and dispersion of the plume material, or the distribution of ρ_p^*. The problem is illustrated schematically in figure 1.1. The following assumptions are used to simplify the formulation without removing important physical processes:

(1) the plume motion is steady;

(2) the initial plume cross-section is elliptical ;

(3) the plume is advected with a uniform wind velocity U along x^*-axis; [2]

(4) the trajectory length scale is much larger than the size of the plume cross-section. This assumption eliminates the small scale irregularities of the plume in the wind direction (Weil, 1988a);

(5) wind stratification and density stratification effects are neglected;

(6) the effect of large scale atmospheric turbulence is neglected and the plume buoyancy dominates the motion; [3]

(7) the eddy viscosity ν_e and eddy diffusivity α_e, modeling the small scale turbulence, are assumed to have equal values; and

(8) the fluid is incompressible, as justified by Luti and Brzustowski (1977) and Briggs (1984).

These assumptions are used to simplify the physical model; an essential first step in the development and validation of the numerical scheme. In future work, these

---

[2] Note that the transfer of the horizontal momentum is essentially complete within a few, about 5, exit diameters from the emission source and the plume thereafter travels at a horizontal speed indistinguishable from the wind speed (Csanady, 1973).

[3] The effect of plume buoyancy relative to atmospheric turbulence can be assessed by a Richardson number

$$R_i \equiv \frac{g_r(\Delta\rho^*)R}{\rho_o^* w'^2}$$

where $\Delta\rho^*$ is the density difference across the plume surface, and w' is a characteristic atmospheric velocity in the vertical direction. For values of $R_i > 1$, corresponding to large plumes such as fire plumes, buoyancy is expected to be the dominant effect. For example, consider a fire plume with $R \sim 10$ m and $\Delta\rho^*/\rho_o^* \sim O(10^{-1})$ in a $w' \sim O(1$ m/s) atmospheric turbulence, $R_i \sim O(10)$.

assumptions will be relaxed and the computational model expanded to include, e.g., atmospheric density stratification and near-ground turbulence (Zhang and Ghoniem, 1993).

Denote the perturbation velocity, or the velocity induced due to buoyancy, by (u^*, v^*, w^*), the components in the horizontal wind direction, x^*, horizontal cross-wind direction, y^*, and the vertical z^*-direction, respectively. The governing equations are the three-dimensional, steady Navier-Stokes equations with $u^*/U << 1$. We define the dimensionless variables as follows:

$$
\begin{aligned}
&(y, z) = (y^*, z^*)/R \\
&(v, w) = (v^*, w^*)/V \\
&t = x = \frac{x^*/U}{R/V} = \frac{x^*}{U}\sqrt{\frac{\varepsilon g_r}{R}} \\
&\rho_p = \frac{\rho_p^*}{\varepsilon \rho_o^*} \\
&p = \frac{p^*}{\rho_o^* V^2} \\
&\rho = \frac{\rho_o^* + \rho_p^*}{\varepsilon \rho_o^*} = \frac{1}{\varepsilon}(1 + \varepsilon \rho_p)
\end{aligned}
\tag{1.5}
$$

The length scale in the x^*- direction is $U\sqrt{\frac{R}{\varepsilon g_r}}$, and for a reason which will become clear soon, the dimensionless x has been written as t. The normalized governing equations are:

$$\frac{\partial v}{\partial t} + v\frac{\partial v}{\partial y} + w\frac{\partial v}{\partial z} + \frac{1}{1+\varepsilon\rho_p}\frac{\partial p}{\partial y} = \frac{1}{Re_b}\nabla^2 v \tag{1.6}$$

$$\frac{\partial w}{\partial t} + v\frac{\partial w}{\partial y} + w\frac{\partial w}{\partial z} + \frac{1}{1+\varepsilon\rho_p}\frac{\partial p}{\partial z} + \frac{\rho_p}{1+\varepsilon\rho_p} = \frac{1}{Re_b}\nabla^2 w \tag{1.7}$$

$$\frac{\partial v}{\partial y} + \frac{\partial w}{\partial z} = 0 \tag{1.8}$$

$$\frac{\partial \rho_p}{\partial t} + v\frac{\partial \rho_p}{\partial y} + w\frac{\partial \rho_p}{\partial z} = \frac{1}{Pe_b}\nabla^2 \rho_p \tag{1.9}$$

where $Pe_b = \frac{V \cdot R}{\alpha_e}$ is the turbulent buoyancy Peclet number ($Pe_b = Re_b$ in this work) and $\nabla^2 = \frac{\partial^2}{\partial y^2} + \frac{\partial^2}{\partial z^2}$. The perturbation velocity in equations (1.6)-(1.9) stands for the instantaneous velocity averaged over the smallest numerically resolvable scale. The effects of eddies with even smaller scales are introduced in the form of a turbulent eddy viscosity and eddy diffusivity. As will be shown in the next Section, the numerical resolution is defined by the size of the vortex-element core. Within the element core, variables are distributed according to an assigned "core" function which, to simulate diffusion, evolves in time in a way that depends on Re_b. The solution constructed here, thus, can be considered as a large-eddy simulation of the plume motion in which the large scales are captured by solving the governing equations while the small scales are modeled phenomenologically.

Replacing x by t makes equations (1.6)-(1.9), governing the steady plume dispersion, the same as the Navier-Stokes equations of an unsteady, two-dimensional, incompressible flow in a gravitational field. The corresponding vorticity transport equation is obtained by cross differentiating these equations to eliminate p :

$$\frac{\partial \omega}{\partial t} + v\frac{\partial \omega}{\partial y} + w\frac{\partial \omega}{\partial z} + \frac{1}{(1+\varepsilon\rho_p)^2}\frac{\partial \rho_p}{\partial y} - \frac{\varepsilon}{(1+\varepsilon\rho_p)^2}\left[\frac{\partial \rho_p}{\partial y}\frac{\partial p}{\partial z} - \frac{\partial \rho_p}{\partial z}\frac{\partial p}{\partial y}\right] = \frac{1}{Re_b}\nabla^2\omega \qquad (1.10)$$

where $\omega = \frac{\partial w}{\partial y} - \frac{\partial v}{\partial z}$ is the dimensionless vorticity. Note that the Boussinesq approximation, which corresponds to setting $\varepsilon = 0$, has not been implemented. In Section 1.6, we discuss the range of ε in which this approximation is valid and the characteristics of the non-Boussinesq solution.

The final governing equations are (1.8), (1.9) and (1.10). The required pressure gradient in (1.10) can be obtained from the momentum equations (1.6) and (1.7):

$$\frac{\partial p}{\partial y} = -(1+\varepsilon\rho_p)\frac{Dv}{Dt} + \frac{(1+\varepsilon\rho_p)}{Re_b}\nabla^2 v \qquad (1.11)$$

$$\frac{\partial p}{\partial z} = - \rho_p - (1 + \varepsilon \rho_p) \frac{D w}{D t} + \frac{(1 + \varepsilon \rho_p)}{Re_b} \nabla^2 w$$

where $\frac{D}{Dt} \equiv \frac{\partial}{\partial t} + v \frac{\partial}{\partial y} + w \frac{\partial}{\partial z}$.

The initial conditions are defined in terms of the initial plume cross-section, which is taken here to be an ellipse symmetric about $y = 0$. The ellipse has a major axis R_y and a minor axis R_z, and its center is at a distance $H_T = H_T^* / R$ above the ground. This choice is motivated by the observation that as the plume rises, after the initial momentum-dominated stage, its originally circular cross-section is distorted into an ellipse. If we assume that the initial plume has uniform density, then from equations (1.1), (1.3) and (1.5), $\rho_p = - \int dA/R^2 = -1$. Using the above normalization, the parameters governing the problems are reduced to the aspect ratio, $A_R = R_y/R_z$, height, H_T, buoyancy Reynolds number, Re_b, and the mass flux ratio, ε. In the Boussinesq approximation, ε is absent from the governing equations so the number of dimensionless parameters is reduced to three.

1.3. NUMERICAL SCHEME

In the grid-free, Lagrangian, vortex method, the essential ingredient of the flowfield, the vorticity, is captured by the action of discrete, finite size, overlapping vortex elements whose size, strength and location are determined by approximately satisfying the governing equations. The vorticity field, ω, is discretized among vortex elements, with finite cores, which move along fluid particle trajectories, $\vec{\chi}_i(t)$ such that:

$$\omega(\vec{x},t)= \sum_{i=1}^{N} \Gamma_i(t) f_\delta(\vec{x} - \vec{\chi}_i(t)) \tag{1.12}$$

where $\Gamma_i = \omega_i \delta A_i$, ω_i and δA_i are the circulation, vorticity and the area associated with the *ith* element, respectively, N is the total number of vortex elements (Ghoniem et al., 1988b), $\vec{x}=(y,z)$ and t is time. The vorticity of an element is distributed according to a radially symmetric core function, f_δ, with a characteristic radius, δ, such that most of the vorticity is concentrated within $r < \delta$, where $r^2 = (y - y_i)^2 + (z - z_i)^2$. Initially, the vortex elements are distributed over the plume-air interface such that the distance between neighboring elements is h in the two principal directions. A Gaussian core, $f_\delta(r/\delta) = exp(-r^2/\delta^2)/(\pi \delta^2)$, leads to a second-order accurate scheme (Beale and Majda,1982a,b).

The equations describing the vortex algorithm are:

$$\frac{d\vec{\chi}_i}{dt} = \vec{u}(\vec{\chi}_i(t), t) \tag{1.13}$$

with initial positions $\vec{\chi}_i(0) = \vec{X}_i$, where the advection velocity is obtained from the desingularized Biot-Savart law:

$$\vec{u}(\vec{x},t) = -\sum_{i=1}^{N} \Gamma_i \frac{(z - z_i, -y + y_i)}{r^2} \kappa\left(\frac{r}{\delta}\right) \tag{1.14}$$

while $\kappa(r) = \frac{1}{2\pi}[1 - exp(-r^2)]$.

The change in the circulation of each element, which depends on the local density gradient, is calculated from the vorticity equation as will be shown shortly. As time progresses, the distance between neighboring elements increases in the direction of maximum strain rate. This leads to a deterioration of the discretization accuracy which

requires that $\delta > \Delta\chi$, $\Delta\chi$ being the distance between the centers of the elements. Thus, an algorithm is used such that when $\Delta\chi > \Delta_i$, where Δ_i is the maximum allowable distance between neighboring elements, an element is divided into two elements. The circulation of each of the two new elements is one-half of the circulation of the original element, while the vorticity is the same. The distance between neighboring elements may also decrease due to negative strains. This should be avoided since while it does not improve the spatial accuracy it leads to an unnecessary increase in the computational cost. Thus, when two nearby elements are too close so that $\Delta\chi < \Delta_c$, where Δ_c is the minimum allowable distance between neighboring elements, the two elements are combined into one whose circulation equals the sum of the original two elements (Ghoniem et al, 1988a,b).

The time marching algorithm for the integration of equation (1.13) uses Heun's second order predictor-corrector scheme (Dahlquist et al., 1974):

$$\vec{\chi}^{*} = \vec{\chi}^{t} + \vec{u}(\vec{\chi}^{t})\,\Delta t,$$
$$\vec{\chi}^{t+\Delta t} = \vec{\chi}^{t} + 0.5\,(\vec{u}(\vec{\chi}^{t}) + \vec{u}(\vec{\chi}^{*}))\,\Delta t \tag{1.15}$$

where Δt is the time step.

In updating the circulation of a vortex element, the density gradient is required. For this purpose, we use the transport element method (Krishnan and Ghoniem, 1992). This method is a natural extension of the Lagrangian vortex method in which scalar gradients, instead of scalar values, are used in the transport process. The adaptive grid-free form of the calculation allows one to simulate flow in an infinite domain while concentrating all the effort around zones of strong gradients.

To perform the computations, the gradient of the scalar, taken here as the density ρ_p, is discretized among a number of discrete elements such that;

$$\vec{g}(\vec{x},t) = \sum_{i=1}^{N} \vec{g}_i(t)\delta A_i f_\delta(\vec{x} - \vec{\chi}_i(t)), \tag{1.16}$$

where $\vec{g} = \nabla\rho_p$. Like vortex elements, transport elements are distributed where $|\vec{g}| > 0$ and are convected with the local velocity field. Density gradients are not conserved along a particle trajectory, but are modified according to the local straining and tilting of the material elements. The values of the density are obtained by direct summation over the field of transport elements,

$$\rho_p(\vec{x},t) = \sum_{i=1}^{N} \vec{g}_i(t) \frac{(y - y_i, z - z_i)}{r^2} \kappa\left(\frac{r}{\delta}\right) \tag{1.17}$$

where

$$\vec{g}_i(t) = \frac{\delta\rho_{pi} \left|\delta\vec{\chi}_i(t)\right|}{\delta A_i} \vec{n}_i(t) \tag{1.18}$$

In equation (1.18), $\delta\rho_{pi}$ is the density variation across a layer, $\vec{n}_i(t)$ is the unit vector in the direction of the density gradient, $\delta\vec{\chi}_i$ is the length of a element along a layer. With new elements introduced where excessive stretching is encountered, the scheme maintains high resolution well into the late stages of flow development after high concentration of vorticity and sharp density gradients have evolved. (For more detail, see Krishnan and Ghoniem, 1992, and Knio and Ghoniem, 1991 and 1992.)

In order to simulate the effect of diffusion in both of the vorticity and density transport equations, operator splitting is used. For variable vorticity, the diffusion equation is written for each element:

$$\frac{\partial\omega_i}{\partial t} = \frac{1}{Re_b} \nabla^2\omega_i \,. \tag{1.19}$$

Therefore, for a vortex element with a Gaussian distribution of vorticity, we have:

$$\frac{d\delta^2}{dt} = \frac{4}{Re_b} \tag{1.20}$$

whose solution is;

$$\delta^2 = \delta_o^2 + \frac{4t}{Re_b} \tag{1.21}$$

where δ_o is the initial core radius of the element. Thus, the effect of diffusion can be simulated by expanding the core radius as a function of time according to equation (1.21). This is done without changing the shape of the core function or the values of Γ_i and $\vec{g}_i$. If $Pe_b \neq Re_b$ ($\nu_e \neq \alpha_e$), different core sizes should be used for the vortex element and the transport element.

In the present study, the boundary conditions at the ground $z = 0$ are: the normal velocity and the material flux vanish. These are satisfied by including the effect of the images of the vortex and transport elements at $z < 0$. To avoid repeated calculations, we also impose images of vortex elements at $y < 0$, assuming that the plume cross-section maintains its initial symmetry across the original symmetry line, $y = 0$. Since the plume height is mostly well above the viscous boundary layer, the effect of this thin layer is neglected.

We discretize the zone of finite density gradient within the plume cross-section into M layers. The density along each layer is constant. The number of layers used depends on the distance across which the density changes from the value inside the plume to the value in the atmosphere. If this distance is very small, one layer is sufficient, otherwise more layers are necessary to maintain acceptable numerical resolution. The number of elements used to describe each layer increases as generated vorticity intensifies and the plume shape becomes increasingly convoluted.

Before we started the simulation of the cases of interest, we conducted a numerical study for the purpose of: (1) showing that the numerical solution converges as the resolution is refined; and (2) determining the optimal values of the numerical parameters which can be used to minimize the CPU time while maintaining the necessary accuracy (Ghoniem et al, 1991)[4]. The numerical parameters, which control the accuracy of the numerical method (see figure 1.2), are found to be optimal for the following

[4] Convergence and accuracy were defined in terms of global or integral parameters such as the plume trajectory and overall dimensions of its cross section.

values: the spatial resolution $h = 0.025$, the vortex element core radius, $\delta = 1.3\ h$, the number of layers, $M = 2$, the time step, $\Delta t = 0.025$, the insertion length, $\Delta_i = \delta$ and the combination length, $\Delta_c = \delta$. In the calculation, the Boussinesq approximation is used, except in Section 1.6. The density changes from that of plume to the air density linearly across the plume-air boundary. The length scale in the direction of the density gradient between the plume and the surrounding, normalized with respect to R, is $d = 0.1$.

1.4. THE TRAJECTORY OF A BUOYANT PLUME

1.4.1. Review of Studies on Plume Trajectory

The scaling length of buoyant motion in a crosswind, called the buoyancy length (Briggs, 1975), can be defined in terms of the notation adopted in this Chapter, as

$$l_b = \frac{1}{\pi}\left|\frac{\rho_p^*}{\rho_o^*}\right| \frac{g_r R^2}{U^2} \,. \tag{1.22}$$

For strongly buoyant plumes, the two-thirds law:

$$\frac{\tilde{z}^*}{l_b} = \left(\frac{3}{2\beta^2}\right)^{1/3} \left(\frac{x^*}{l_b}\right)^{2/3} \tag{1.23}$$

has been shown to approximate the trajectory, where $\tilde{z}^*$ is the plume center rise and x^* is the downwind distance from the source (Weil, 1988a, Briggs, 1975). The value of entrainment rate, β, is obtained by fitting the scaling law (1.23), to experimental data. It is found that β also depends on w_o/U, where w_o is the initial vertical exit velocity of the plume.

Laboratory and field experiments have been performed to find the value of β. The plume trajectory is determined by the height of the center of the cross-section, defined as the average, at each cross-wind section, of the highest and lowest points on the plume boundary, both identified from photographs (Fay et al, 1970). It should be noted that this height is not necessarily the centroid height of the cross-wind plume section if the latter is not vertically symmetric. Here we distinguish between these two as center height (local average) and centroid (mass mean) height. Laboratory experiments (Hewett, et al, 1971) showed that the dependence of the plume trajectory on the stack Reynolds number, $Re_s = \frac{2\, w_o\, r_o}{\nu}$, where r_o is the radius of the stack, is small, provided the plume is turbulent at the stack exit. The local atmospheric turbulence effect is found to be small and so it is neglected in the scaling law.

1.4.2. Extension of the Two-Thirds Law

The conventional two-thirds power law, equation (1.23), applies during the stage when buoyancy dominates the plume motion and the initial plume size is negligible (point source). In the case of a massive fire plume, the initial vertical momentum is negligible but the initial plume size is not. To account for the latter, we extended the two-thirds power law (See Appendix 1.A). The resulting expression for a strongly buoyant plume, written in a dimensionless form, is:

$$(\sqrt{\pi}\beta z + 1)^3 - 1 = \frac{3\sqrt{\pi}\,\beta}{2} x^2 \qquad (1.24)$$

1.4.3. Simulation Results

Three simulations, with same initial circular cross-section, $R_y = R_z = 0.5642\ R$, were performed for different buoyancy Reynolds numbers. In all cases, the initial plume height is $H_T=30$ and hence the ground effect is negligible. Figure 1.3 shows a comparison between the center trajectories of the three plumes and the extended two-thirds law, equation (1.24), for $\beta = 0.7$. Since more computational elements are required in calculating the higher Reynolds number flow, those cases were terminated earlier. It is seen that the rising plume trajectory is generally independent of the buoyancy Reynolds number (at least when buoyancy dominates). Thus, the effects of molecular diffusion and small scale turbulence on the trajectory are negligible. This is consistent with most experimental observations (Hewett et al., 1971). The computed trajectories are not smooth because of the fluctuations associated with the buoyancy generated turbulence. The trajectory agrees well with the extended two-thirds law when $\beta = 0.7$. The conventional (point source) two-thirds law, equation (1.23), with the suggested (Briggs, 1984) entrainment ratio of $\beta = 0.6$ is also shown.

The plume starts with $w_o = 0$. As it is accelerated, the generated vorticity at plume surface changes the shape of the cross-section and modifies the vertical velocity. Detailed study of the plume cross-sectional shape and entrainment characteristics are

delayed to the next section. Here, it suffices to mention the following. Part of the initial potential energy of the plume is transformed into kinetic energy which is distributed between the plume and the surrounding atmosphere. The rotational velocity induced by the plume sets up an entrainment field towards the plume center. The plume rising velocity is much smaller than that of a solid body of same density because the plume potential energy does not completely transform into plume kinetic energy as in the case of a solid body.

The effect of the initial plume height is determined by simulating the rise of two plumes whose initial cross-sections have the same circular shape but with $H_T = 1$ and 30. The first case is close to the situation of a ground fire, while the second is designed so that the ground does not affect the plume motion. Figure 1.4 shows that the two trajectories are very close. The plume trajectory is thus almost independent of the initial height, with the plume released closer to the ground staying slightly lower than the one released higher. We emphasize that this conclusion applies only when the atmosphere is calm, i.e., when atmospheric turbulence near the ground is weaker than the buoyancy effects. In future work, we plan to extend our modeling to include the effects of wind shear and atmospheric turbulence.

When the initial shape of the plume cross-section is that of an ellipse, the aspect ratio may have some effect on its trajectory. Figure 1.5 exhibits the three trajectories, A_R = 1, 2, 3. We can see that the larger A_R plume rises slowly at the beginning, then at around $x=15$, surpasses the lower A_R plume.

As will be shown in the next section, the plume cross-section, over most of its history, resembles an inverted kidney shape. Thus, its centroid (mean mass center) is not the same as its center. To confirm this conclusion using our numerical simulation, we plot the centroid and the center trajectories in figure 1.6. These plots show that the calculation of plume rise in terms of the center height may underestimate the maximum

concentration near the ground. Although the trajectory of the centroid is of more interest, it is difficult to measure in practice.

1.5. DISPERSION

1.5.1. Review of Plume Dispersion Studies

Plume dispersion is strongly related to its trajectory. In the literature, however, most studies calculate the pollutant distribution as if a non-buoyant plume was released from the maximum height it reaches. The most widely used model is that of Pasquill-Gifford-Turner which adopts the Gaussian plume equation and assumes that the lateral and vertical dispersion parameters are given by the Pasquill curves (Turner, 1970, Gifford, 1975, Seinfeld, 1986). As mentioned before, rise and dispersion, being manifestations of the same dynamics, are interrelated, (Nieuwstadt, 1992a).

It is often observed that the distribution of the plume material does not fit a Gaussian profile. Rather, the plume cross-section is kidney shaped (Briggs, 1975, Abdelwahed and Chu, 1978, etc.). In their laboratory experiment, Hewett et al (1975) showed that the cross-section was not completely circular, but kidney shaped, and Briggs (1975) proposed a distribution of various quantities within this kidney shaped cross-section. Moreover, under certain conditions, the plume could split into two separate plumes. Fanaki (1975) observed that bifurcated plumes, forming two lumps with an in-between region where the pollutant concentration is relatively low, traveled downwind forming two counter-rotating line vortices. It was also suggested that bifurcation may reduce the rise of the plume and lead to a horizontal scale larger than the vertical scale. An instrumented aircraft was used to measure the concentration profiles within a bifurcated plume (Janseen et al, 1990). These measurements confirmed the persistent nature of the two line vortices even after evidence of the plume was no longer present. Janseen et al. (1990) concluded that the Gaussian concentration profiles could not be used to represent the inhomogeneities in the concentration field.

The double-vortex structure has also been observed in experimental (Tsang, 1971), analytical (Csanady, 1965) and numerical (Lilly, 1964, and Meng and Thomson,

1978) studies on rising two-dimensional thermals. The significance of these observations in the study of plumes stems from the fact that the equations governing the dynamics of bent-over plumes, equations (1.6)-(1.9), are identical to those governing rising thermals. Thus, it is expected that the governing dynamics of both flow phenomena to be similar.

Investigations into the mechanism of the formation of this kidney-shaped cross-section and bifurcation have followed two lines. The first suggests that the interaction between the crosswind and a non-buoyant jet may be the cause of this distortion. McMahon et al. (1971) described the process of vortex shedding that occurred when a crossflow felt the presence of a non-buoyant jet as essentially a solid object. The effect of this vortex shedding, associated with the pressure drag on the plume, was to distort the shape of the plume and induce streamwise (with respect to the plume stream) vorticity into the flow. Crabb et al (1981) and Sherif and Pletcher (1989) performed several experiments and showed that a wake forms behind a non-buoyant jet due to the presence of crosswind. Near the exit of a stack, moderate wind develops shear stresses on the opposite sides of the plume thereby inducing vorticity with opposite signs at these points. The effectiveness of this mechanism depends on the initial momentum of the jet. On the other hand, Hewett et al, (1971), using 547 measurements within the plume cross-section, showed that a kidney shaped section formed even when the initial momentum was negligibly small. This suggest that the bifurcation phenomenon be independent of the plume initial momentum.

Another mechanism proposed to explain this distortion is buoyancy. The bent plume is more buoyant at its core where the density is the lowest and thereby rises faster at center. Turner (1959) assumed that the flow within the plume was similar to that generated by a vortex-pair with fixed circulation and showed that the bifurcation of the plume results from the lateral separation of the vortex pair. However, how the plume acquired this circulation was not explained in detail. Scorer (1958) concurred that the internal circulation, induced by buoyancy, caused the plume to bifurcate while Moore

(1966) indicated that for a non-turbulent flow, the plume remained continuous and bifurcation might persist for thousands of meters downwind. Khandekar and Murty (1975) claimed that the existence of an atmospheric elevated inversion layer was crucial to the separation of these vortices.

Having realized the kidney-shaped structure of the rising plume, Schwartz and Tulin (1972) developed a model based on the dynamics of a vortex-pair. The trajectory evaluated using this model also followed the two-thirds power law. Recently, the role of the concentration fluctuations in plume dispersion has come under investigation (Sykes, 1988). Since our numerical simulation can capture some of the small scale fluctuations, it can provide some insights into the mechanism of the distortion of plume cross-section.

1.5.2. Plume Cross-section and Vorticity Generation

Figure 1.7 depicts the evolution of the cross-section of a plume with $Re_b=10^3$, while the table shows the associated minimum dimensionless density which characterizes the maximum pollutant concentration at different locations. Due to the symmetry with respect to the plume center line, only half of the cross-section is shown. In this case, the ground effect is negligible since $H_T=30$. It is clear that, as indicated before, the center of the plume is higher than the centroid (mass mean height). The figure shows that a plume experiences three stages after its release:

(1) A very short acceleration stage, during which the deformation of the plume is very small, i.e, the plume rises like a solid body. The rising vertical velocity of the plume increases at an almost constant acceleration.

(2) A long double-vortex stage, during which vorticity generated on both sides of the plume forms two large-scale eddies tightly wound around the two horizontal ends of the plume. During this rollup stage, large entrainment of outside air into the plume core takes place on the lower side.

(3) A plume breakup stage, during which the plume is divided into two major lumps and several small blobs which diffuse much like passive pollutant. This stage can be also

called bifurcation stage. Clearly, the plume dispersion in this way is more efficient than the uniform plume dispersion as described by Gaussian models.

The mechanism of vorticity generation due to buoyancy, which is responsible for the evolution observed here, can be understood by examining the vorticity equation, equation (1.10). The vorticity generation term is proportional to the horizontal density gradient when, for simplicity, the Boussinesq approximation is invoked. For a plume of initially elliptical shape, the two large-scale, counter-rotating, streamwise vortices are formed due to the opposite horizontal density gradient, as shown in figure 1.8a, leading to a large-scale rollup which changes the plume shape significantly from that described by the traditional Gaussian type concentration distribution. The two eddies induce a velocity field which moves the plume upwards. After this large-scale rollup, the plume-air interface is stretched and distorted, secondary vortice, with the same or the opposite sign of vorticity, are generated and the plume motion becomes turbulent as shown in figure 1.8b. In all stages, turbulence within the plume is far from Gaussian, and the plume dynamics resemble that of a trailing vortex behind an aircraft rather than that of a homogeneous turbulence field.

While the plume trajectory appears to be insensitive to the Reynolds number, or small scale diffusion, the entrainment and mixing within the plume cross-section are related. Figure 1.9 shows the plume cross-sections at $x = 4.5$ for four different buoyancy Reynolds numbers. In all cases, the formation of the two large vortices on the sides of the plume contributes significantly to the redistribution of the plume material. The density field is smoother at lower Reynolds number. Figure 1.10 depicts the development of the plume cross-section at high Reynolds number, $Re_b = 10^5$. The patterns of the large-eddy formation and small eddy generation are shown. The small-scale perturbations developed at the top surface are rapidly growing along the vortex sheet, rolling into small eddies and propagating down towards the bottom side.

A detailed description of the acceleration stage, which is important in calculating the circulation of the two large eddies that govern the plume buoyant dynamics, has not been given in the literature (Turner, 1959). In this work, this total circulation is evaluated from the numerical results and is displayed in figure 1.11. The total circulation is obtained by summing over the circulation of all the vortex elements which lie on either side of the symmetry line, i.e., for one-half of the plume cross-section. As shown in the figure, right after the acceleration stage, the total circulation reaches a constant value and is sustained for a long time (at least upto the termination of our calculation, $x=17.5$), consistent with Turner's hypothesis. This is somewhat surprising since the plume cross-section continues to deform. To reconcile these two observations, we examine the two components of vorticity whose summation lead to the total circulation (see figure 1.8b). Figure 1.11 shows the positive circulation, obtained by summing over the elements whose circulation is positive; the negative circulation, obtained by summing over the elements whose circulation is negative. The total circulation can also be obtained by algebraically adding the positive and negative circulations. As expected from the schematic diagrams in figure 1.8, while the negative circulation grows steadily, secondary rollup forms positive circulation which, at the late stages, grows at the same rate as that of the negative circulation. Thus, beyond the early large-scale rollup stage, the total circulation on either side of the plume remains constant.

As mentioned before, Turner (1959) suggested a model in which the plume dynamics are represented by a pair of streamwise vortices of a given circulation which remains constant during the plume dispersion phase. Our results suggest that this model, although crude, may be a reasonable representation of some aspects of plume motion and that the total circulation of the large structure indeed converges towards a constant value. It is apparent that the saturation of the total circulation and the fact that the kidney-shaped coherent structure is fairly long-lived is what makes the entrainment assumption in

integral models approximately valid. It is interesting to note that in the normalized variables used here, the total circulation is of order unity.

Since the dynamics of the plume cross-section can be approximately modeled by two windwise line vortices, the weak effect of a flat ground terrain shown in figure 1.4 can be justified by considering the interaction between the vortices and their two images, as illustrated in figure 1.12. Since the induced velocity by a vortex decays away form its center as $1/|\vec{x} - \vec{x}_v|$, where $\vec{x}_v$ is the vortex center, and since in this case $|\vec{x} - \vec{x}_v|$ is proportional to twice the initial plume height, the ground effect weakens as H_T increases from one to 30. As shown in figure 1.12, the net velocity induced by the images on the plume has a horizontal component pointing towards the plume center. Thus, when the ground effect is measurable, it leads to a reduction in the horizontal spread. Let W, the maximum horizontal distance between any two computational elements, represents the width of the plume in the y -direction. Figure 1.13 shows $W(x)$ of two plumes, with and without the ground effect. In both cases, the width of the plume grows almost linearly with the downwind distance x. The presence of kinks is mainly due to the non-uniform rollup of the eddies. Without the ground effect, the plume expands slightly faster. Within the limitations of this model, the results suggest that the ground effect on the plume width is negligible. This is similar to the conclusion reached before regarding the ground effect on the plume trajectory. As mentioned before, wind shear effect may change these conclusions, especially close to the ground.

The effect of the aspect ratio of the plume cross-section on the plume trajectory, shown in Figure 1.5, can be explained by the rate of vorticity generation along the plume surface and its dependence on the plume shape. Since the rate of vorticity generation is proportional to $\frac{\partial \rho_p}{\partial y}$, for plumes of same cross section area, a large A_R -plume has smaller portion of interface where vorticity can be generated. Thus, in the early stages, the rise of a large A_R -plume is slower than that of a small A_R -plume. However, the faster

generation of vorticity also accelerates the entrainment process, thus limits the buoyancy strength hence eventually delaying its rise after $x=15$.

1.5.3. Entrainment and Entrainment Assumptions

There has been a growing realization that the transport properties of many turbulent shear flows are dominated by semi-deterministic large-scale vortex structures. Turner (1986) proposed using large-scale engulfment as a basis for the entrainment hypothesis. Viscous diffusion may only be important at the final digestion of external fluid into the turbulent flow and the evolution of the smaller-scale motions, but not in determining the overall rate of mixing.

Our numerical simulation confirms these observations. Figure 1.14a shows the induced velocity in the plume cross-section. For comparison, the unit velocity vector and the plume surface are also shown on the same plot. The material surrounding the plume is engulfed toward its center from below. Most of the entrainment into the plume core is induced by the two large eddies. The entrainment is thus neither homogeneous nor isotropic. Clearly, the nearby atmosphere is disturbed due to the presence of the plume, and the density distribution within the plume is distorted due to this large-scale entrainment. The strong wind and swirling motion often observed in the presence of a fire can be explained by the powerful entrainment currents established by the dynamic field of a rising plume as represented by the two large eddies. Figure 1.14b shows the plume motion in terms of the locations and velocity vectors of the computational elements used to discretize the outer surface of the plume cross-section.

The total inflow at any position x depends on the geometry and dynamics of the flow. From experimental measurements, the entrainment constant in equation (1.A7) is often taken as $\beta = 0.4$, which is different from $\beta = 0.6$ used in equation (1.23). This inconsistency in the integral model has been pointed out by numerous authors (Briggs, 1975). Since the plume is not of exact circular form, we define an equivalent radius R_{eq} so that

$$\pi R_{eq}^2 = \frac{\pi}{4} H \cdot W \tag{1.25}$$

where H is the maximum vertical extension of the plume cross-section, defined here as the distance between the highest and lowest computational elements, representing the plume vertical thickness. From our numerical solution, following the acceleration stage, R_{eq} is found to change almost linearly with x, almost independent of to the aspect ratio and the plume release height, as shown in figures 1.15a and b.

1.5.4. Plume Circumference

Another measure of entrainment is the circumference of the plume cross-section, defined by the summation of the distances between adjacent computational elements along the interface between the plume material and air. Since the plume surface is wrinkled due to local vorticity generation, the actual periphery is much longer than that calculated by simple circular or elliptical circumferences. During the acceleration stage, there is not much variation of this length as the plume rises undistorted, as shown in figure 1.16 for $x \leq 1.5$. The stretching of the circumference is distinctly faster during the small scale rollup, when several areas of the plume experience local stretching around concentrated vortices, than during the large-scale rollup. While the ground effect is negligible, the circumference increases faster for smaller A_R which is consistent with the fact that this plume experiences stronger vorticity generation.

Comparison between figures 1.15 and 1.16 shows that the equivalent radius is a better measure of entrainment since the length of the plume suffers from the evolution of several small eddies which do not contribute significantly to entrainment. We also note that the size and strength of the small scales is a function of the buoyancy Reynolds number, as shown in figure 1.9.

1.6. THE BOUSSINESQ APPROXIMATION

In practice, the Boussinesq approximation is a convenient simplification when small density variations are involved in fluid motion (Spiegel and Veronis, 1960). In many flows, including that of a plume, using the Boussinesq approximation renders the problem self-similar with respect to the density ratio and hence reduces the number of independent parameters. However, before using this approximation in extensive modeling, it is important to determine the limits within which the error introduced by the assumption is acceptable.

Invoking the Boussinesq approximation is equivalent to setting $\varepsilon = 0$ in the vorticity and momentum equations. We performed numerical experiments at $\varepsilon = \left|\frac{\rho_p^*}{\rho_o^*}\right| = 0,$ $0.01, 0.1$ and 0.5 for an initially circular plume at $H_T = 30$ with $Re_b=10^3$, to study the effect of the Boussinesq approximation on the solution for different density ratios.

Figures 1.17 and 1.18 show the plume trajectory and equivalent radius, respectively. The curves corresponding to cases with $\varepsilon = 0, 0.01$ and 0.1 are almost indistinguishable. This suggests that the Boussinesq approximation is valid when $\varepsilon \leq 0.1$, i.e., when, in the case of a plume with a circular cross-section, the density ratio $\left|\frac{\rho_p^*}{\rho_o^*}\right| \leq 0.1$. This restriction may be relaxed somewhat depending on the inaccuracies allowed in the calculation. For most fire and exhaust plumes, $\varepsilon \leq 0.1$ is usually satisfied.

The curve with $\varepsilon = 0.5$, i.e. $\left|\frac{\rho_p^*}{\rho_o^*}\right| = 0.5$, shows some departure, which increases at a longer time, from the Boussinesq approximation solution. It is evident that the Boussinesq approximation underestimates the plume rise and equivalent radius.

1.7. CONCLUSION

A Lagrangian model of buoyant plume rise and dispersion in a calm neutral atmosphere is developed in connection with vortex and transport element methods. The computed plume trajectory is compared with the experimentally based two-thirds power law. The transition from the early stages of buoyancy dominated plume to the later stages, when atmospheric turbulence begins to dominate the plume motion, is calculated. The main conclusions of this study are summarized in the following.

(1) The plume trajectory is insensitive to the small-scale atmospheric turbulence. The plume trajectory, for the case of $A_R=1$, follows closely the extended two-thirds power law.

(2) The plume experiences three stages which have distinctive characteristics; (i) a short acceleration stage, (ii) a long double vortex stage, and, (iii) a plume breakup stage.

(3) The plume cross-section is found to be kidney shaped. The process of double vortex formation and plume bifurcation can be explained by the baroclinic vorticity generation mechanism.

(4) The effect of a flat ground on the plume trajectory and dispersion is small.

(5) The aspect ratio of the plume cross-section is an important parameter. Large A_R plume rises slower initially and then catches up with small A_R plumes during the breakup stage.

(6) The entrainment field is dominated by large-scale engulfment which is neither isotropic nor homogeneous.

(7) The Boussinesq approximation is valid for $\varepsilon = \left|\frac{\rho_p^*}{\rho_o^*}\right| \leq 0.1$.

The long-term plan of our effort is to extend the modeling approach introduced in this work to include several important effects such as: (a) atmospheric density stratification; (b) wind shear; and, (c) atmospheric turbulence of scales comparable to and larger than the plume characteristic dimension. The parabolization of the equations in the

wind direction introduced here, which, in essence, restricts the vorticity to the streamwise component only and treats the flow within the plume cross-section as being two-dimensional, is expected to be sufficient in the study of (a). However, in order to investigate (b) and (c), the other vorticity components will have to be included in the formulation and the three-dimensional problem be treated in full.

REFERENCES

Abdelwahed M. A. T. and Chu V. H.(1978) Bifurcation of buoyant jets in cross flow. *Tech. Rep.* **78-1**, Dept. Civ. Eng., McGill Univ., 130pp.

Beale J. T. and Majda A.(1982a) Vortex method I: convergence in three dimensions, *Math. Comput.* **39**, 1-27.

Beale J. T. and Majda A.(1982b) Vortex method II: higher order accuracy in two and three dimensions, *Math. Comput.* **39**, 28-52.

Briggs G. A.(1975) Plume rise predictions. *Lectures on Air Pollution and Environmental Impact Analysis*, D. A. Haugen, Ed., Amer. Meteor. Soc., Boston, 59-111.

Briggs G. A.(1984) Plume rise and buoyancy effects. *Atmospheric Science and Power Production*, D. Randerson, Ed., U.S. Dept. of Energy DOE/TIC-27601, available from NTIS as DE84005177, 327-366.

Crabb D., Durao D.F.G. and Whitelaw J. H. (1981) A round jet normal to a crossflow. *Transactions of ASME*, **103**, 142-153.

Csanady G.T. (1965) The buoyant motion within a hot gas plume in a horizontal wind. *J. Fluid Mech.*, **22**, 225-239.

Csanady G.T. (1973) *Turbulent Diffusion in the Environment* , D. Reidel, Dordrecht.

Dahlquist G. and Björck A.(1974) *Numerical Methods*, Prentice Hall.

Deardorff J. W. (1970) Convective velocity and temperature scales for the unstable planetary boundary layer, *J. Atmos. Sci.*, **27**, 1211-1213.

Evans D., Baum H., McCaffrey B., Mulholland G., Harkleroad M. and Manders W. (1986) Combustion of Oil on Water, Report NBSIR 86-3420, National Bureau of Standards, Gaithersburg, MD 20899.

Evans D., Baum H., Mulholland G., Bryner N. and Forney G.(1989) Smoke Plumes From Crude Oil Burns, NISTIR Report, National Institute of Standard and Technology.

Fanaki F. H. (1975) Experimental observations of a bifurcation buoyant plume. *Boundary-Layer Meteorology*, **9**, 479-495.

Fay J. A., Escudier M. and Hoult D. P. (1970) A correlation of field observations of plume rise.*Journal of Air Pollution Control Association*, **20**, No.6, 391-397.

Gebhart B., Hilder D. S. and Kelleher M. (1984) The diffusion of turbulent buoyant jets. *Int. J. Heat Mass Transfer* 1-57.

Ghoniem A.F., Heidarinejad G. and Krishnan A. (1988a) On mixing, baroclinicity and the effect of strain in a chemically reacting shear layer. The AIAA 26th Aerospace Science Meeting, Reno, NV, January 11-15, AIAA-88-0729 and the 22nd Symposium

(International) on Combustion, Sydney, Australia, July 1992, The Combustion Institute, Pittsburgh, PA.

Ghoniem A.F., Heidarinejad G. and Krishnan A. (1988b) Numerical simulation of a thermally stratified shear layer using the vortex element method, *J. Comput. Phys.* **79**, pp. 135-166.

Ghoniem A.F., Zhang X., and Knio O.M. (1991) First Annual Report on Development of a Computational Model for Smoke Plume Dispersion and Deposition, NIST, National Institute of Standard and Technology, Gaithersburg, MD 20899.

Ghoniem A.F., Zhang X., Knio O.M., Baum H., and Rehm R.(1992) Dispersion and Deposition of Smoke Plumes Generated from Massive Fires, *J. Haz. Mat.* , **33**, pp. 275-293.

Gifford F. A. (1975) Atmospheric dispersion models for environmental pollution applications. *Lecture on air pollution and Environmental impact analyses*, D. A. Haugen, Ed., Amer. Meteor. Soc., Boston, 35-58.

Golay M. W.(1982) Numerical modeling of buoyant plumes in a turbulent, stratified atmosphere, *Atmos. Environ.*, **16**, 2373-2381.

Hewett T. A., Fay J. A. and Hoult D. P.(1971) Laboratory experiments of smokestack plumes in a stable atmosphere, *Atmos. Environ.* **5**, 767-789.

Janseen L. H. J. M., Nieuwstadt F. T. M. and Donze M. (1990) Time scales of physical and chemical processes in chemically reactive plumes, *Atmos. Environ.* **24A, 11**, 2861-2874.

Khandekar M. L. and Murty T. S. (1975) A note on bifurcation of buoyant bent-over chimney plumes, *Atmos. Environ.*, **9**, 759-762.

Knio O.M. and Ghoniem A.F. (1991) Three-dimensional vortex simulation of rollup and entrainment in a shear layer, *J. Comput. Phys.* **97**, No.1, 172-223.

Knio O.M. and Ghoniem A.F. (1992) The three-dimensional structure of periodic vorticity layers under non-symmetric conditions, *J. Fluid Mech.* (to appear).

Krishnan A. and Ghoniem A.F. (1992) Simulation of rollup and mixing in Rayleigh-Taylor flow using the transport element method, *J. of Comput. Phy.* 99, No.1, 1-27.

Lilly D.K. (1964) Numerical solution for the shape-preserving two dimensional thermal convection element, *J. Atmos. Sci.*, **21**, 83-98.

Luti F. M. and Brzustowski T. A. (1977) Flow due to a two-dimensional heat source with cross flow in the atmosphere, *Comb. Sci. and Tech.*, **16**, 71-87.

McMahon H. M., Hester D. D. and Palfery J. G.(1971) Vortex shedding from a turbulent jet in a cross wind, *J. Fluid Mech.*, **48**, 73-80.

Meng J. C. S. and Thomson J. A. L. (1978) Numerical studies of some nonlinear hydrodynamic problems by discrete vortex element methods, *J. Fluid Mech.* **84**, part.3, 433-453.

Moore D. J. (1966) Physical aspects of puff models, *Int. J. Air Water Pollu.* **10**, 411-417.

Netterville D. D. J. (1990) Plume rise, entrainment and dispersion in turbulent wind, *Atmos. Environ.* **24A**, No.5, 1061-1081.

Nieuwstadt F. T. M. (1992a) A large-eddy simulation of a line source in a convective atmospheric boundary layer - I. Dispersion characteristics, *Atmos. Environ.* **26A**, No.3, 485-495.

Nieuwstadt F. T. M.(1992b) A large-eddy simulation of a line source in a convective atmospheric boundary layer - II. Dynamics of a buoyant line source, *Atmos. Environ.* **26A**, No.3, 497-503.

Schwartz J. and Tulin M. P. (1972) Chimney plumes in neutral and stable surroundings. *Atmos. Environ.*, **6**, 19-35.

Scorer R. S. (1958) *Natural Aerodynamics*, pp. 143-217, Pergamon Press, New York.

Seinfeld J. H. (1986) *Atmospheric Chemistry and Physics of Air Pollution*, John Wiley & Sons, xxiii+738 p.

Sherif S. A. and Pletcher R. H. (1989) Measurements of the flow and turbulence characteristics of round jets in crossflow, *J. Fluid Engineering*, **111**, 165.

Spiegel E. A. and Veronis G. (1960). On the Boussinesq approximation for a compressible fluid, *J. Astrophy.* **131**, 442-447.

Sykes R. I. (1988) Concentration fluctuations in dispersing plumes, *Lectures on air pollution modeling* (eds. Venkatram A. and Wyngaad J. C.) Ame. Meteor. Soc., 325-356.

Tsang G. (1971) Laboratory study of line thermals, *Atmos. Environ.* **5**, 445-471.

Turner D. B. (1970) *Workbook of Atmospheric Dispersion Estimates*, U.S. Environmental Protection Agency, Office of Air Programs, Ref. No. AP-26, 84pp.

Turner J. S. (1959) A comparison between buoyant vortex rings and vortex pairs, *J. Fluid Mech.*, **7**, 419.

Turner J. S. (1986) Turbulent entrainment: the development of the entrainment assumption, and its application to geophysical flows, *J. Fluid Mech.*, **173**, 431-471.

Venkatram A. (1988) Dispersion in the stable boundary layer, *Lectures on air pollution modeling*, Editors, Venkatram A. and Wyngaard J. C., 229-265.

Weil J. C. (1988a) Plume rise, *Lectures on air pollution modeling*, Editors, Venkatram A. and Wyngaard J. C., 119-166.

Weil J. C. (1988b) Dispersion in the convective boundary layer, *Lectures on air pollution modeling*, Editors, Venkatram A. and Wyngaard J. C., 167-227, 1988.

Zhang X. and Ghoniem A. F. (1993) A computational model for the rise and dispersion of wind-blown, buoyancy-driven plumes, Part II, Linearly stratified atmosphere, (To be submitted to *Atmos. Environ.*)

APPENDIX 1.A EXTENDED TWO-THIRDS POWER LAW

The motion of a buoyant plume can be modeled by the following equations (Briggs, 1984):

$$U\frac{dR^{*2}}{dx^*} = 2\beta w^* R^* \tag{1.A1}$$

$$U\frac{d(R^{*2}w^*)}{dx^*} = R^{*2} g_r \frac{\Delta\rho^*}{\rho_o^*} \tag{1.A2}$$

$$U\frac{d}{dx^*}\left(R^{*2} g_r \frac{\Delta\rho^*}{\rho_o^*}\right) = 0 \tag{1.A3}$$

pertaining, respectively, to the conservation of mass (entrainment assumption), momentum and energy, where R^* is the radius of the plume cross-section, w^* is the vertical velocity of the plume, ρ_o^* is a reference density, taken as the ambient air density, $\Delta\rho^*$ is the density difference between the plume and surrounding at downwind location x^*, U is the mean wind speed, g_r is the gravitational acceleration and β is an entrainment constant. In the above equations it is assumed that U is uniform and that the plume density and vertical velocity have 'top hat' profiles (i.e. constant $\Delta\rho^*$ and w^* from 0 to R^*). Moreover,

$$w^* = U\frac{dz^*}{dx^*} \tag{1.A4}$$

$$R^*(x^*=0) = R_o^* \tag{1.A5}$$

$$z^*(x^*=0) = 0 \tag{1.A6}$$

where z^* is the mean plume rise, R_o^* is the radius of the initial plume size. Equations (1.A1) and (1.A4) show that

$$R^* = R_o^* + \beta z^* \tag{1.A7}$$

In a neutrally stratified atmosphere, equation (1.A3) shows that

$$R^{*2} g_r \frac{\Delta\rho^*}{\rho_o^*} = constant = \frac{F_b}{U} \tag{1.A8}$$

where $F_b = \left|\frac{\rho_p^*}{\rho_o^*}\right| R_o^{*2}\, Ug_r$ is the buoyancy flux. From equations (1.A2) and (1.A4), we find that

$$R^{*2}\frac{dz^*}{dx^*} = \frac{F_b}{U^3}x^* \tag{1.A9}$$

Combining equations (1.A5), (1.A7) and (1.A9), we obtain the following expression for the plume height

$$\left(\beta z^* + R_o^*\right)^3 - R_o^{*3} = \frac{3\beta F_b}{2U^3}x^{*2}. \tag{1.A10}$$

This is the extended two-thirds law. If $\beta z^* >> R_o^*$, the conventional two-thirds law for a point source plume is recovered. Using the procedure outlined in Section 1.2, we can write equation (1.A10) in dimensionless form: the x-direction length scale is $l_x = U\sqrt{\frac{R}{|\rho_p^*/\rho_o^*|\, g_r}}$ and the length scale in both y and z directions is $l_y = R$. The buoyancy length scale in equation (1.22) can be written in terms of the scales used in this study as

$$\pi l_b = \frac{l_y^3}{l_x^2} \tag{1.A11}$$

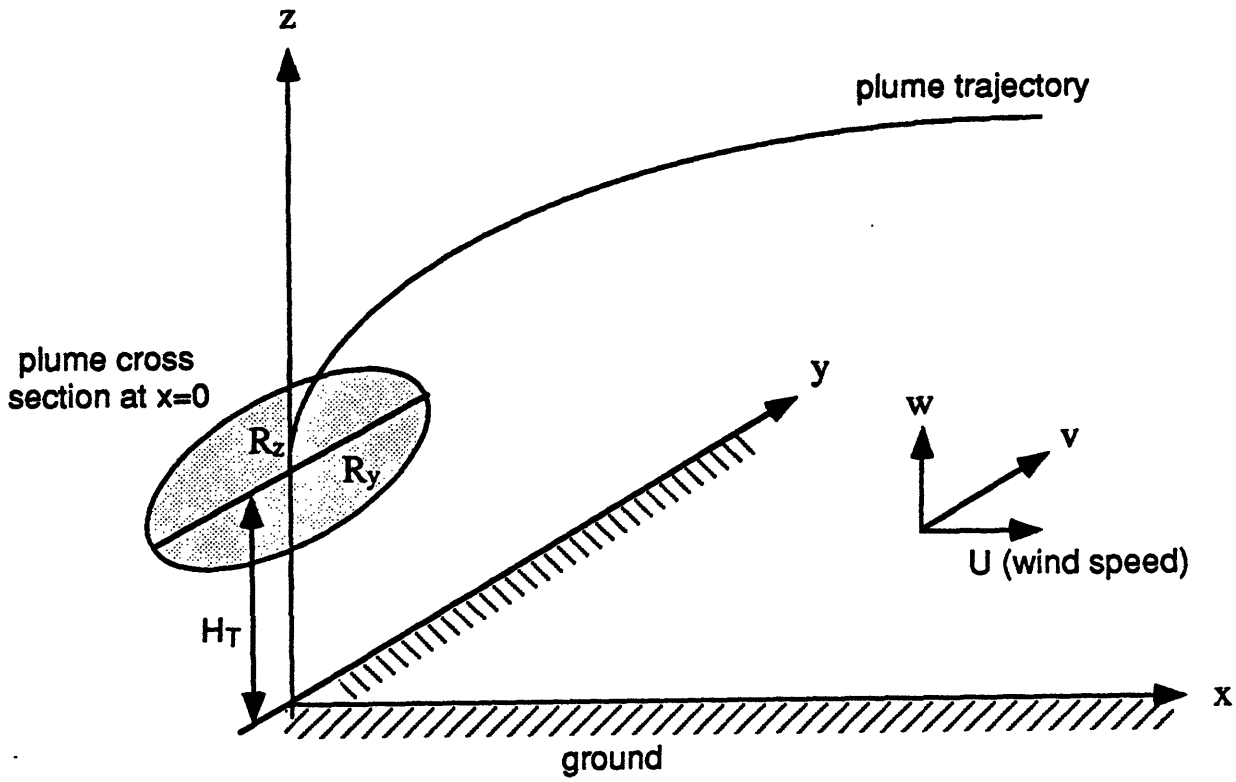

Figure 1.1. Schematic diagram showing the plume trajectory and coordinate system.

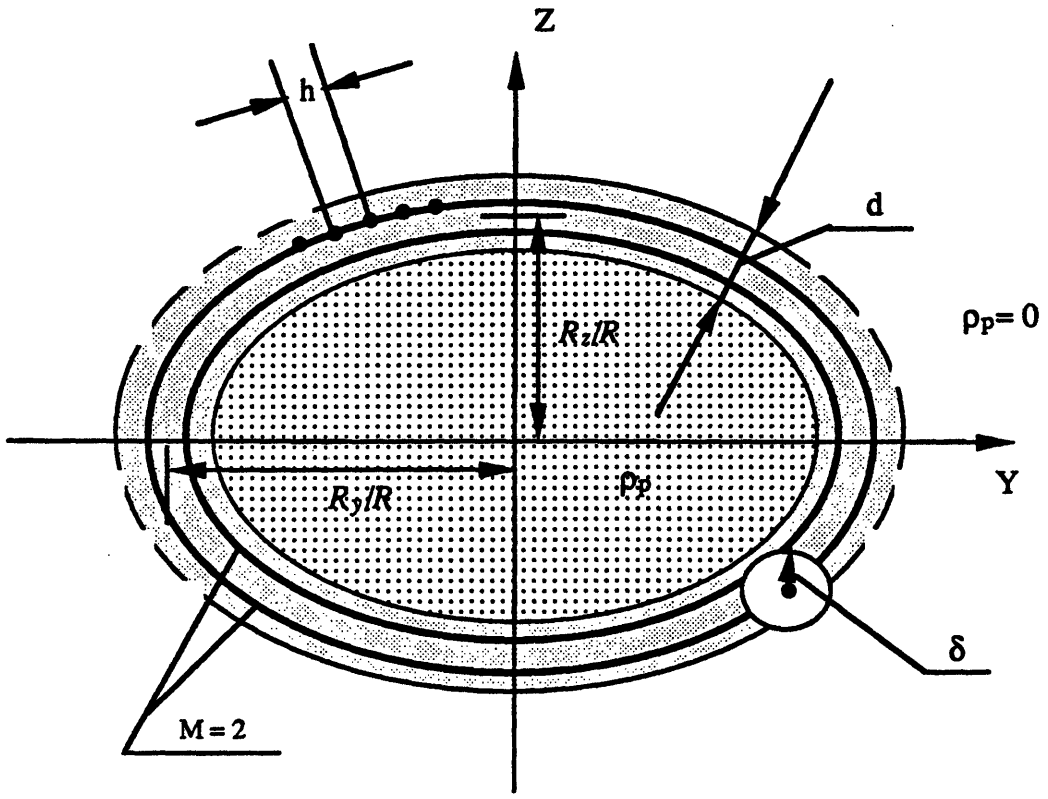

Figure 1.2. Schematic diagram showing the physical parameters used to define the geometry of the plume cross-section and the numerical parameters used to discretize the vorticity and density gradient fields. The two thin ellipses show two constant density lines representing the transitions between the plume core and the surrounding air. The two thick ellipses show the layers where the computational elements locate (dark dots) initially.

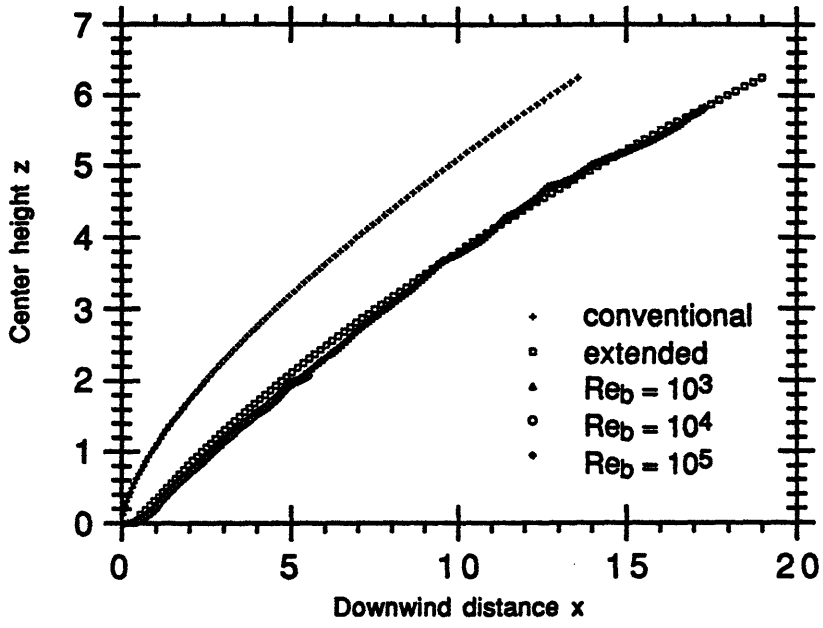

Figure 1.3. Trajectories of plume center for $A_R=1$, $H_T=30$, and different buoyant Reynolds numbers, obtained from the numerical simulations, the conventional two-thirds power law and the extended two-thirds power law.

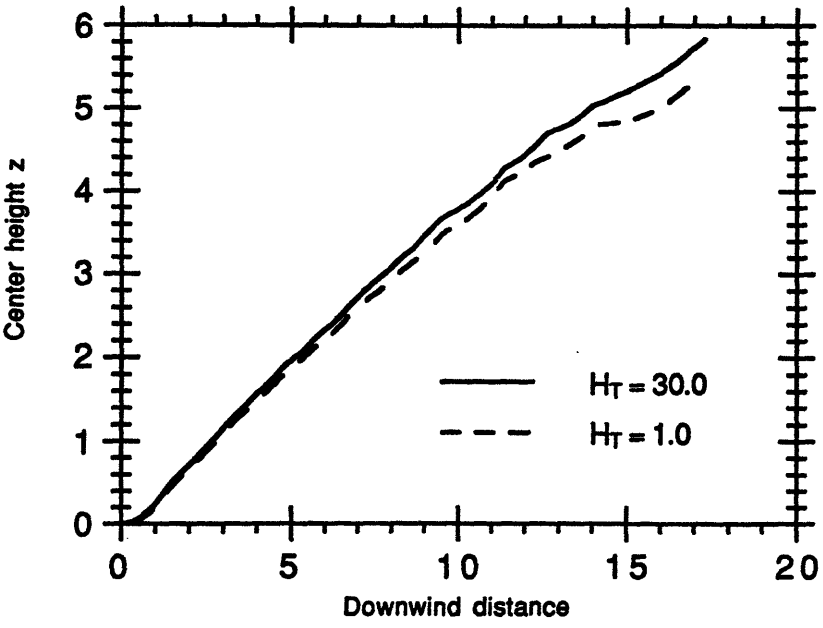

Figure 1.4. Trajectories of plume center for $A_R=1$, $Re_b=10^3$, with and without ground effect.

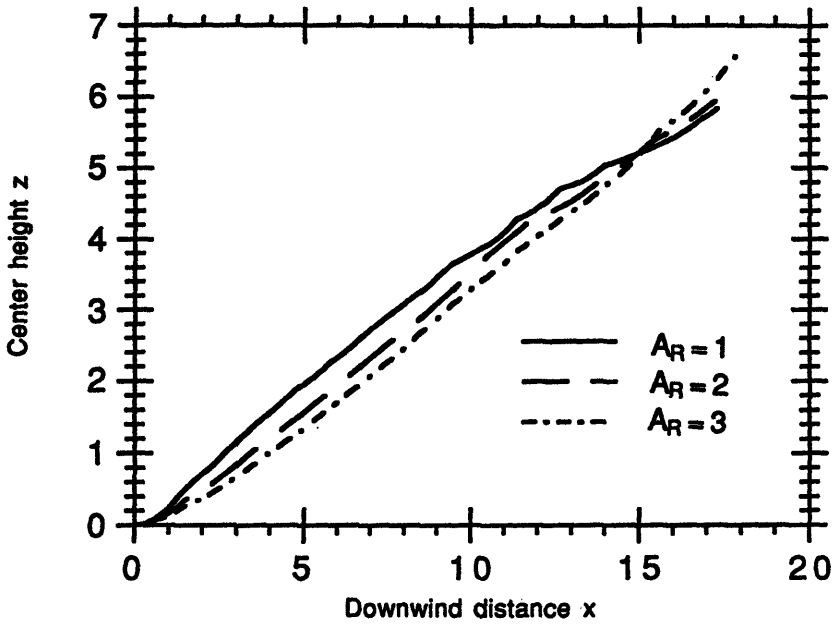

Figure 1.5. Trajectory of plume center for $H_T=30$, $Re_b=10^3$, for different aspect ratios.

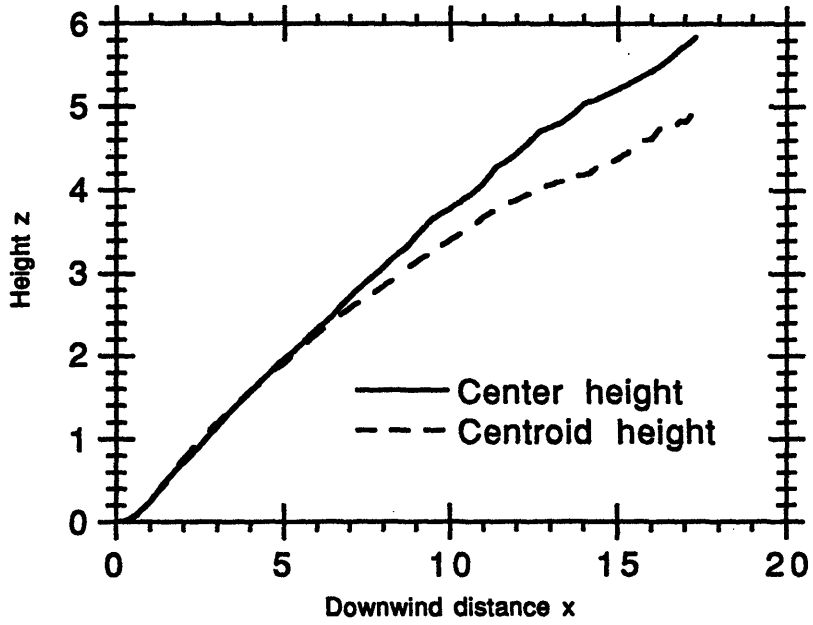

Figure 1.6. Trajectories of plume center and centroid for $A_R=1$, $H_T=30$ and $Re_b=10^3$.

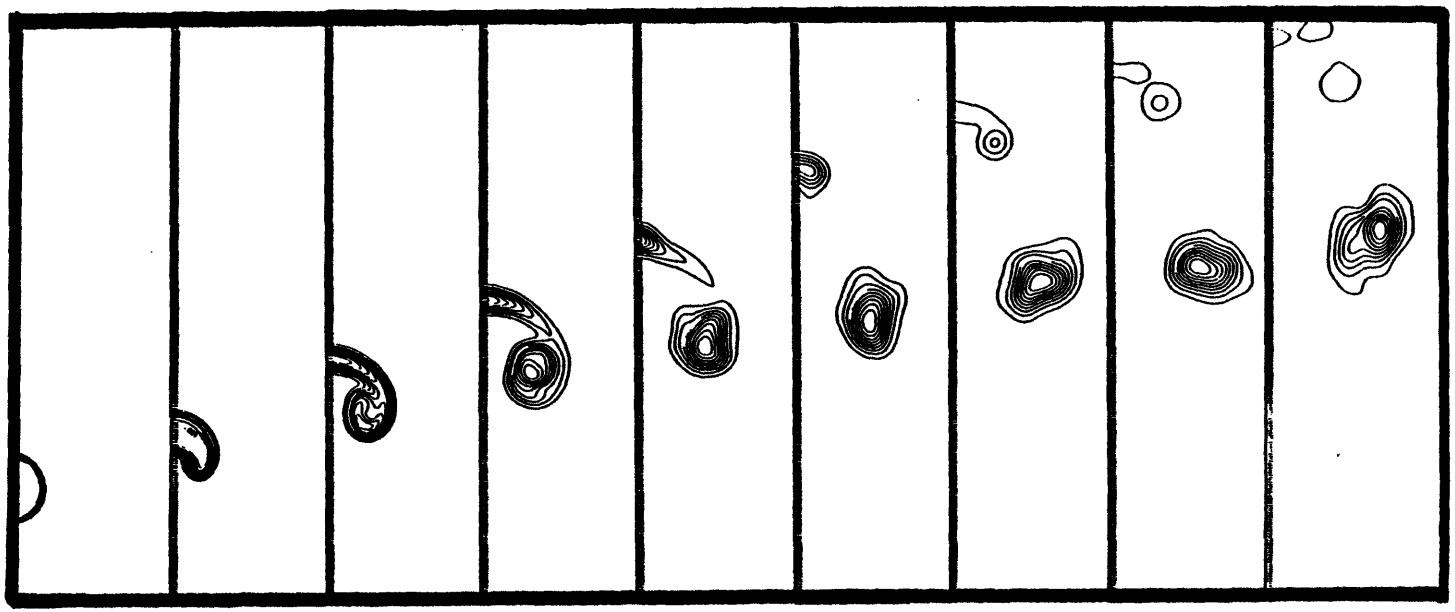

x	0	2	4	6	8	10	12	14	16
$\rho_{p,min}$	-1.00	-1.00	-0.81	-0.74	-0.70	-0.64	-0.63	-0.57	-0.50

Figure 1.7. The evolution of the cross-section of a plume with $A_R=1$, $H_T=30$, and $Re_b=10^3$ shown at different downwind locations x. The corresponding minimum dimensionless deficient plume density are listed in the table. All frames are from $z=28$ to $z=38$ and the horizontal scale is the same as z.

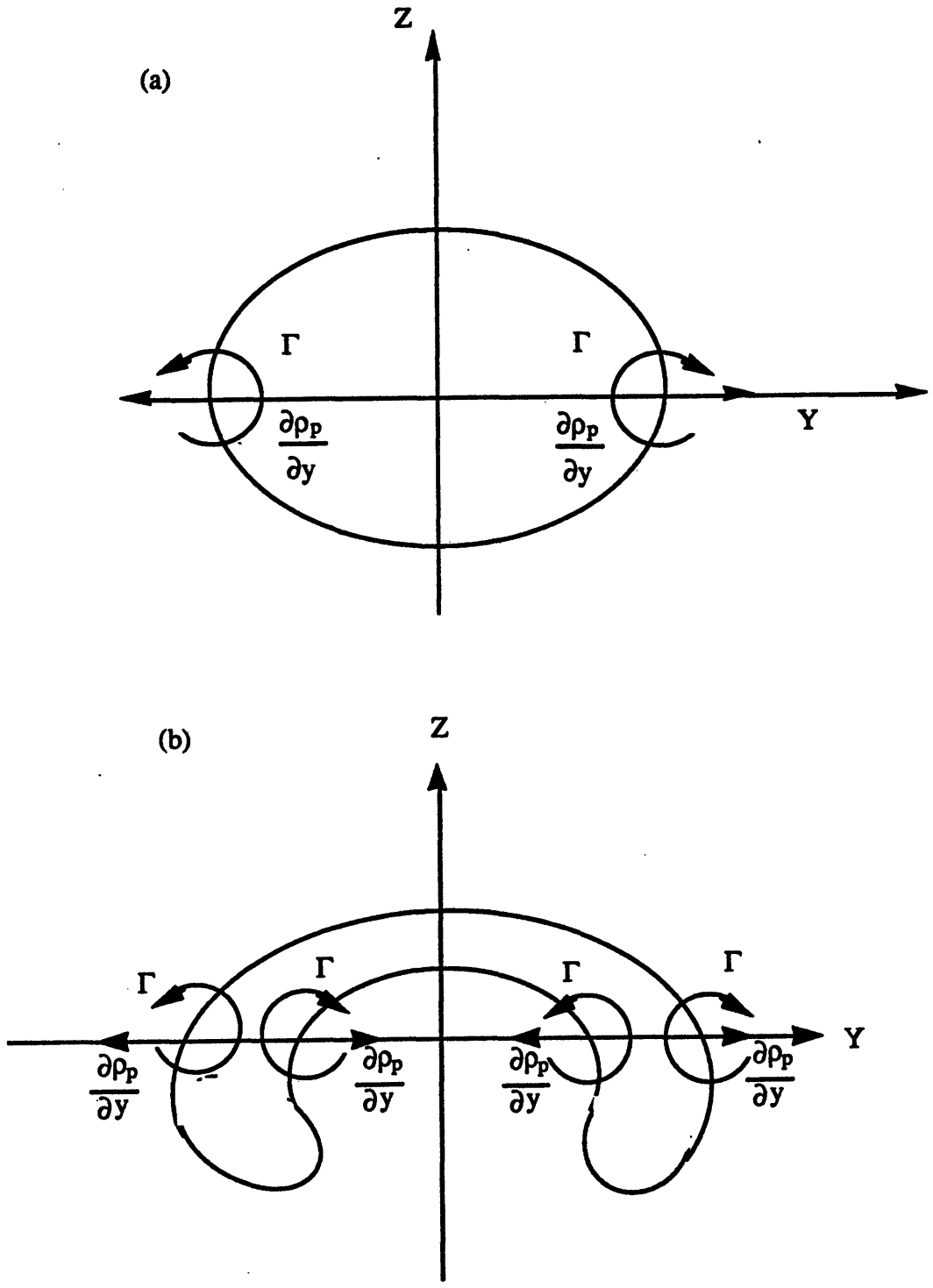

Figure 1.8. A schematic diagram showing the mechanism of (a) large eddy generation and (b) small eddy generation.

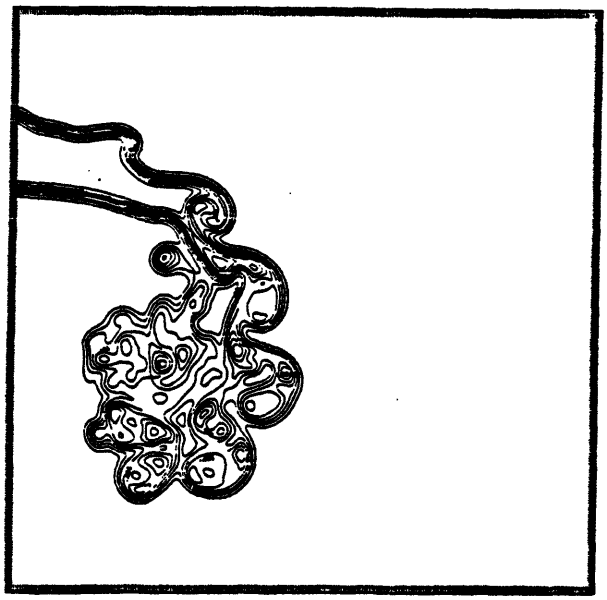

$Re_b = 10^5$

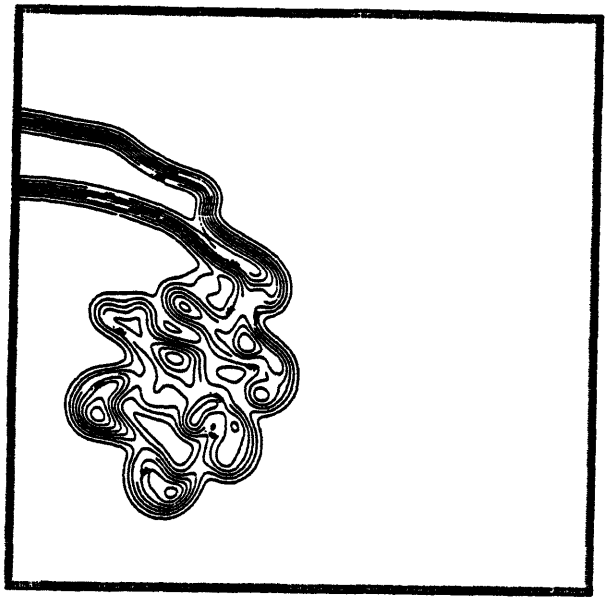

$Re_b = 10^4$

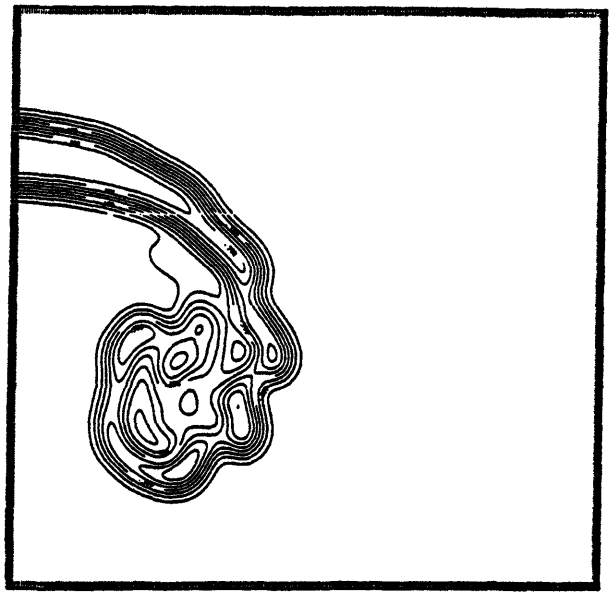

$Re_b = 5 \times 10^3$

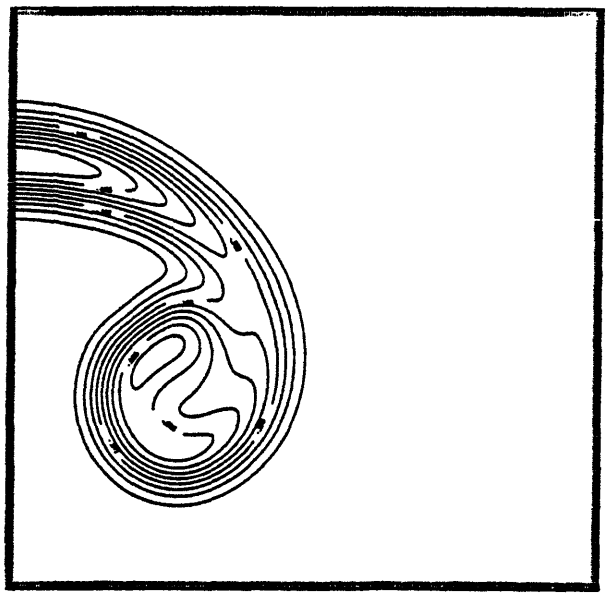

$Re_b = 10^3$

Figure 1.9. Plume cross-sections shown for different buoyant Reynolds numbers for $A_R=1$, $H_T=30$, at $x=4.5$. All frames are from $y=0$ to $y=2.5$ and $z=30.5$ to 33.5.

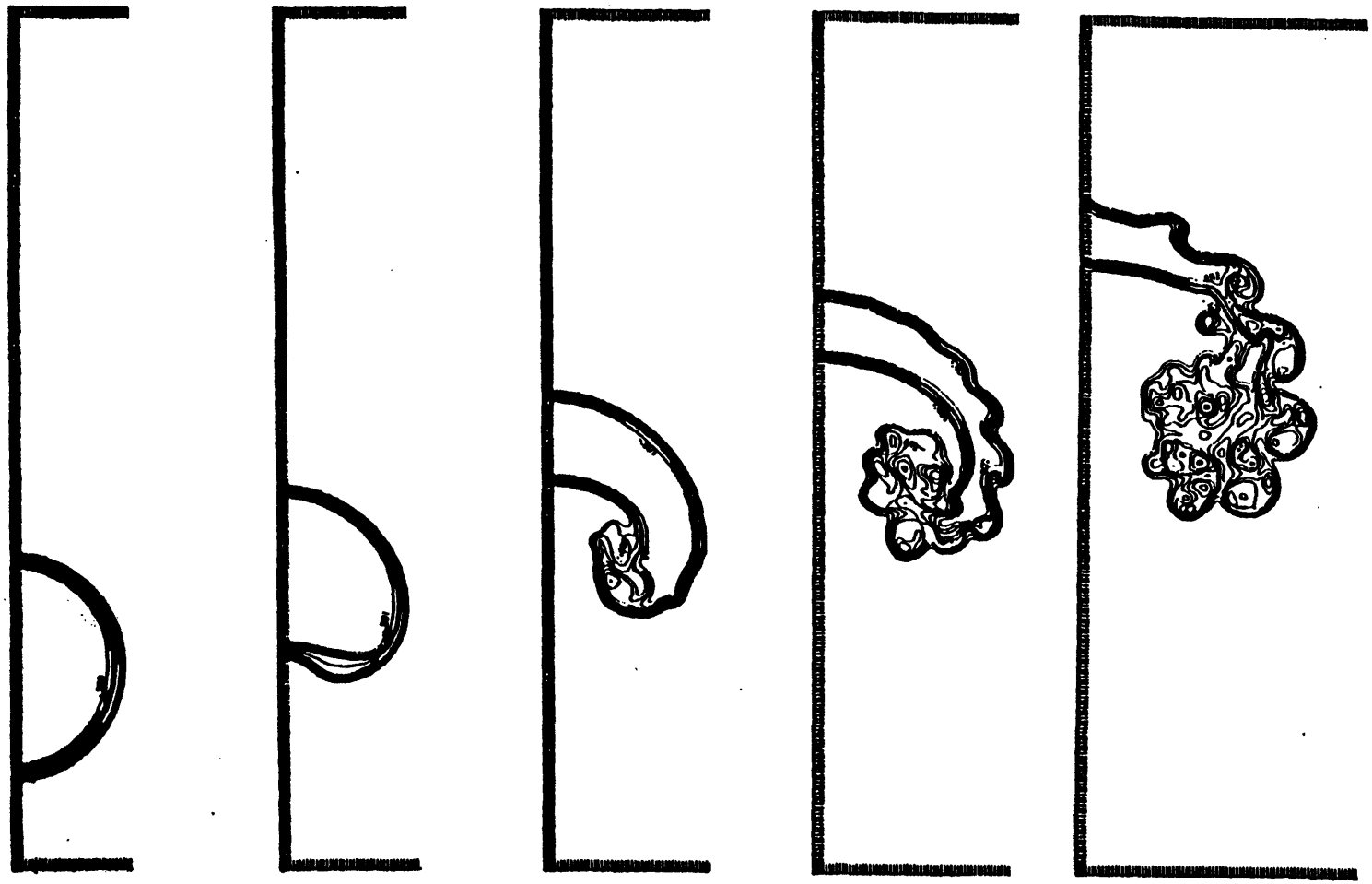

Figure 1.10. The evolution of the cross-section of a plume at different downwind locations for $A_R=1$, $H_T=30$, and $Re_b=10^5$. All frames are from $z=29.0$ to $z=33.5$ and $y=0.0$ to $y=4.5$.

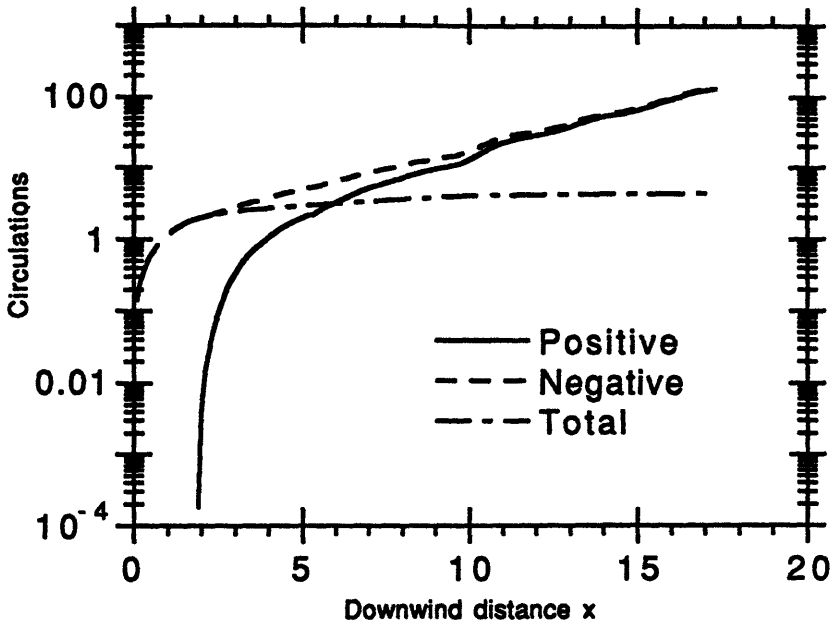

Figure 1.11. Absolute values of the positive circulation, negative circulation, and the sum of the two (total circulation), taken over the right half of the plume, $A_R=1$, $H_T=30$, and $Re_b=10^3$.

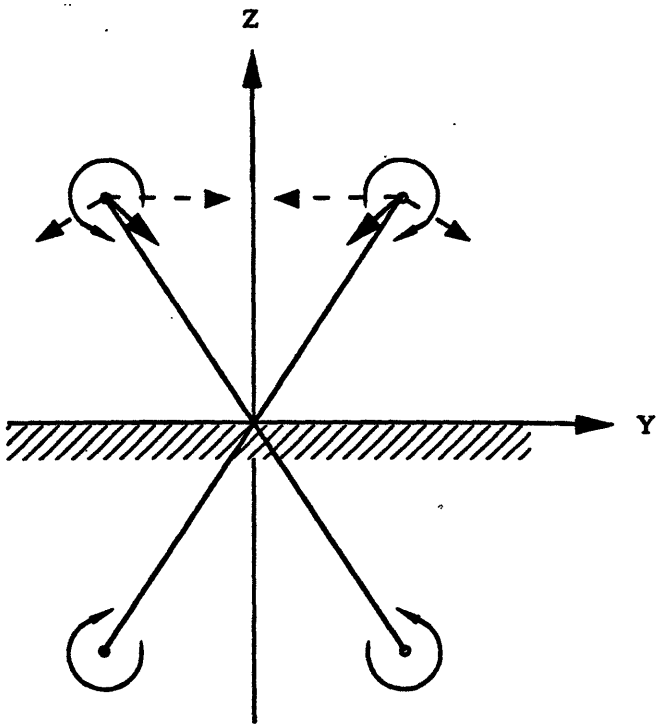

Figure 1.12. Schematic diagram showing the ground effect on the plume rise and dispersion. Dashed arrows are the velocity vectors induced by two images. The solid arrows acting on the vortices are the image-induced total velocity vectors.

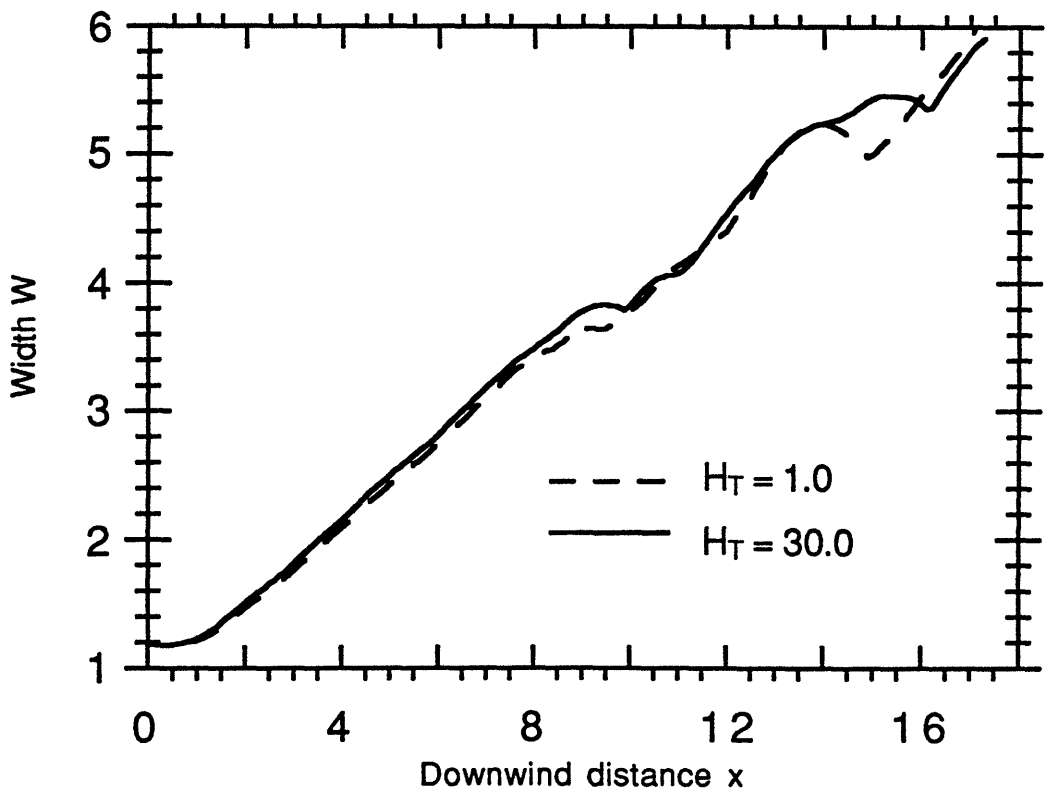

Figure 1.13. The plume width versus downwind distance x with and without ground effect. Both cases have $A_R=1$ and $Re_b=10^3$.

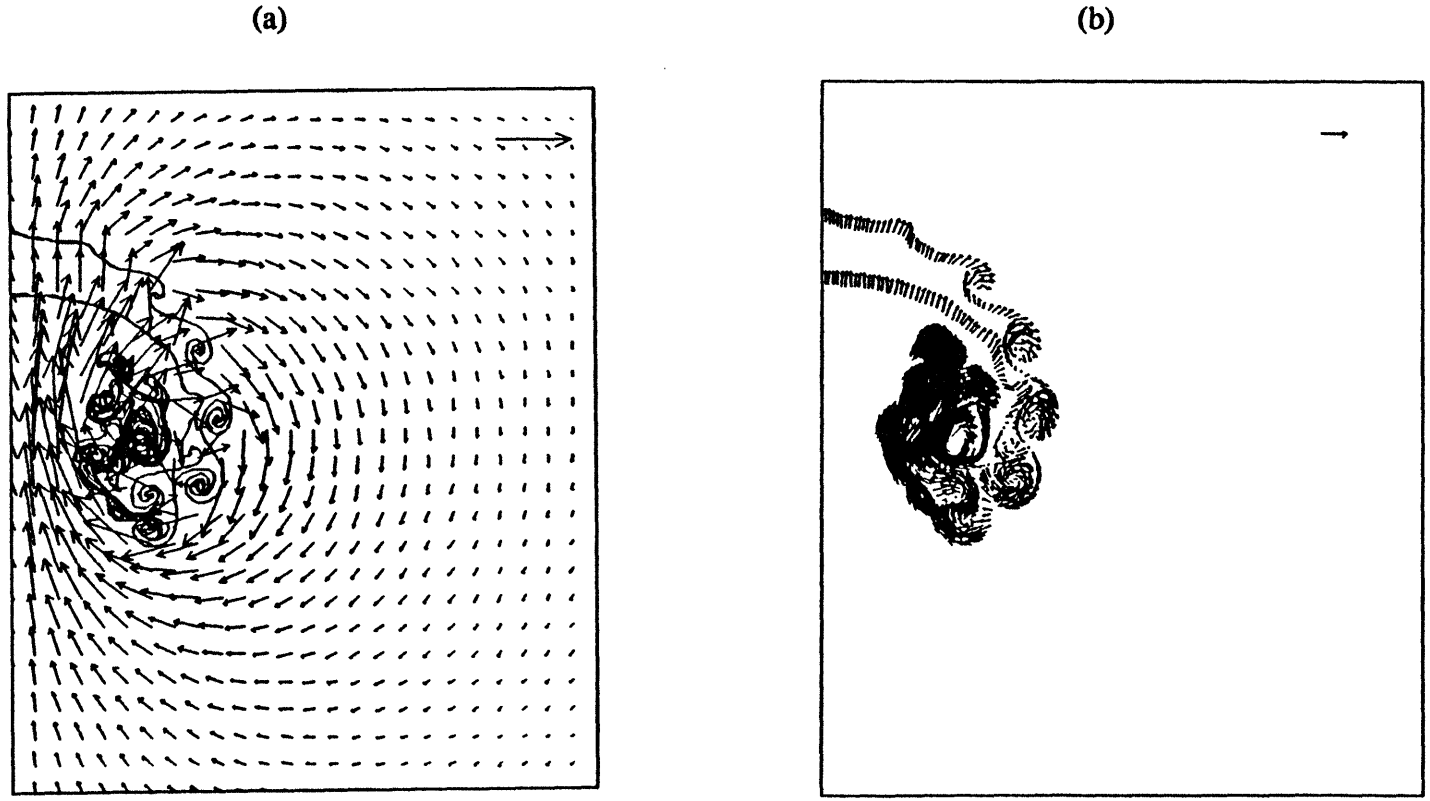

Figure 1.14. (a) The buoyancy induced velocity field and plume outer surface for $Re_b=10^5$, $A_R = 1$, and $H_T = 30$ at $x=4$, and (b) positions and velocities of the computational elements. Both frames are from $z=29.0$ to $z=33.0$ and $y=0.0$ to $y=3.0$.

(a)

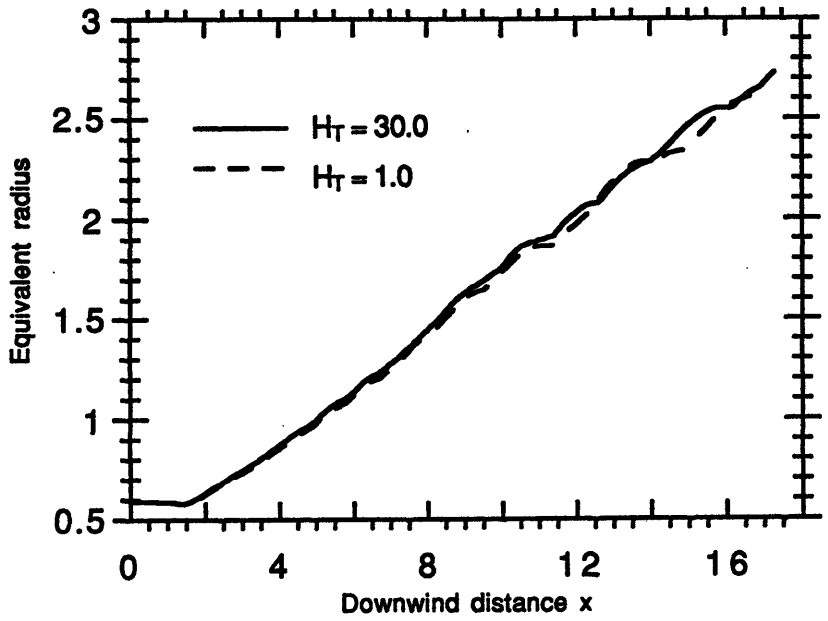

(b)

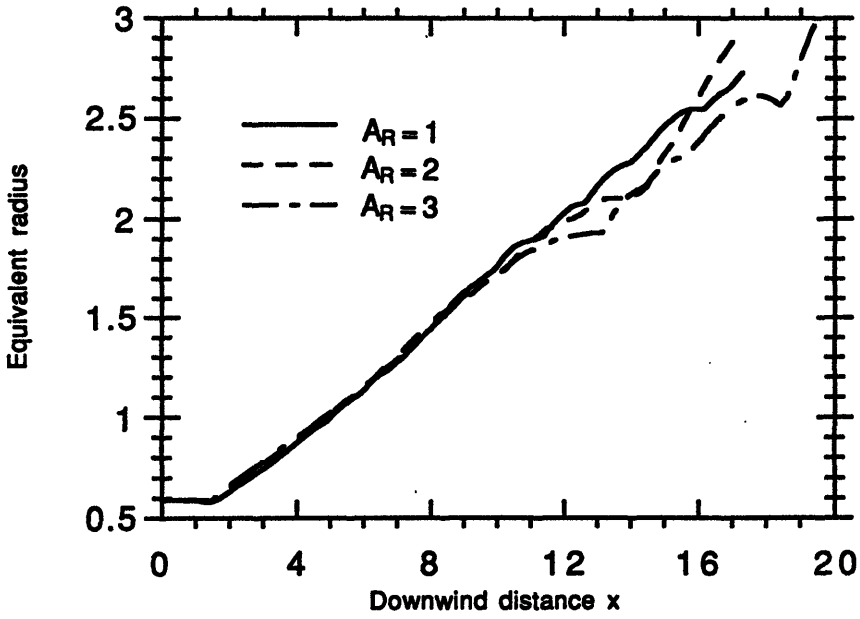

Figure 1.15. Equivalent radius of the plume cross-section versus the downwind distance x, for $A_R=1$, $Re_b=10^3$, (a) with and without ground effect, (b) for different aspect ratios.

(a)

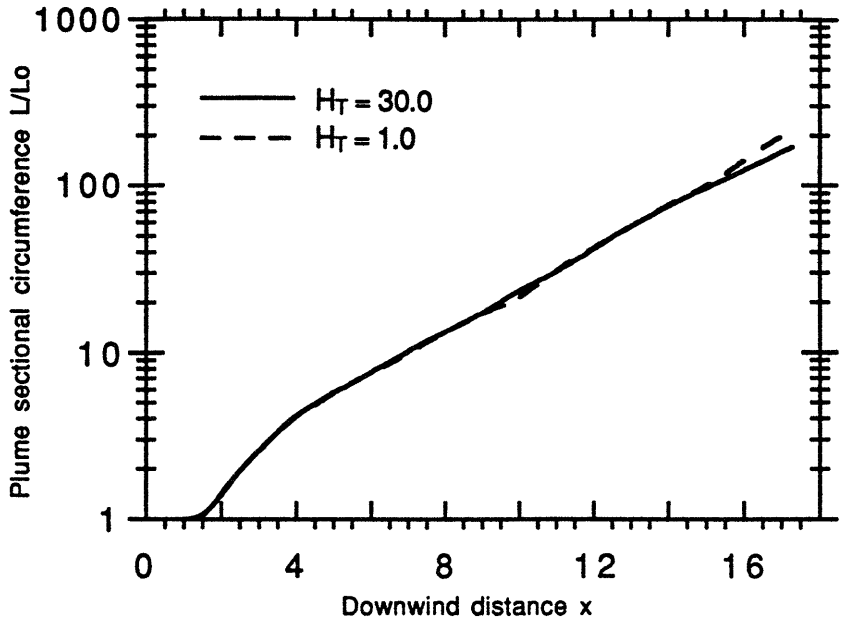

(b)

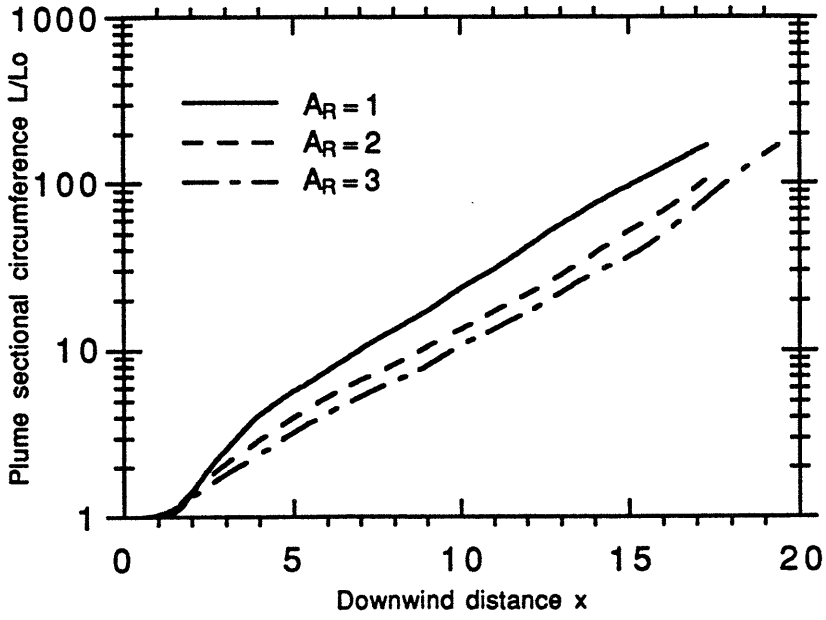

Figure 1.16. Circumference of the plume cross-section versus downwind distance x, $A_R=1, Re_b=10^3$, (a) with and without ground effect, (b) with different aspect ratios.

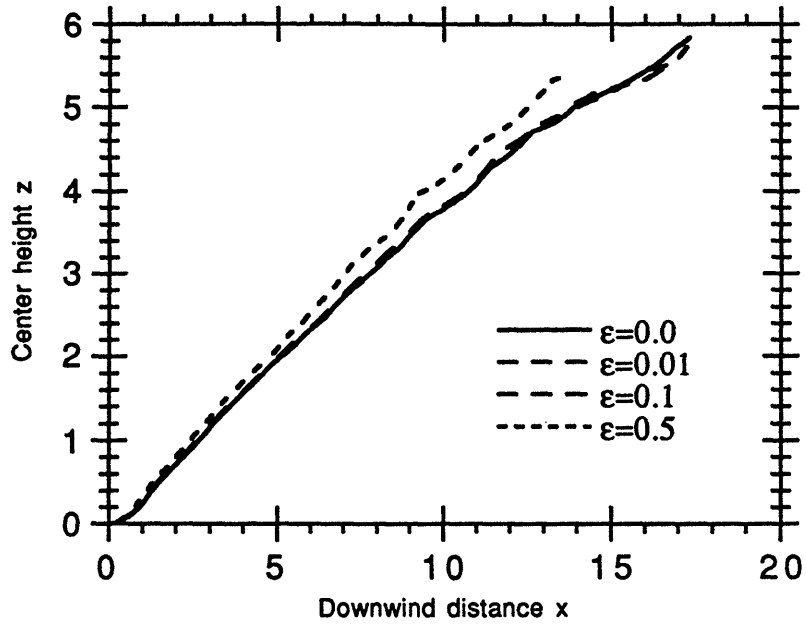

Figure 1.17. Center plume trajectory for $A_R=1$, $H_T=30$, and $Re_b=10^3$, with different deficient mass flux ratios.

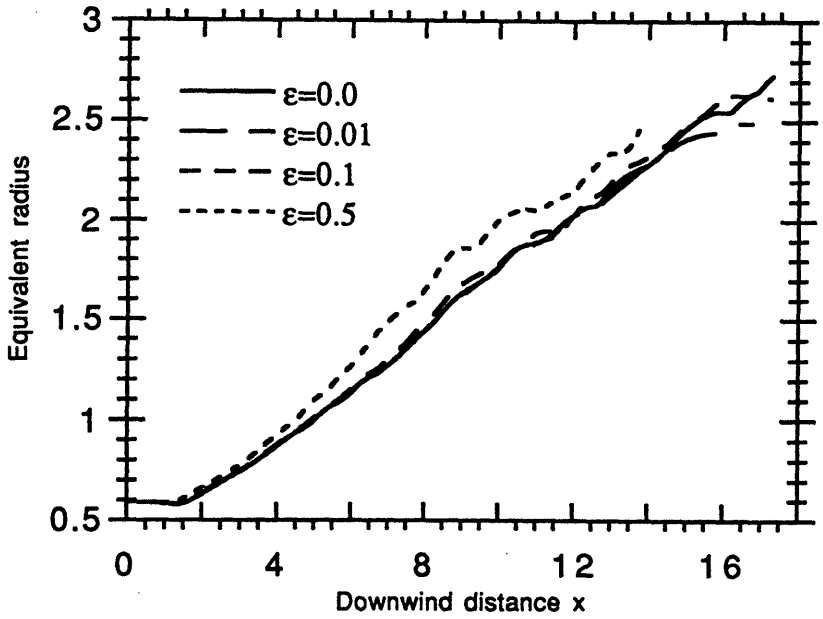

Figure 1.18. Equivalent radius of the plume cross-section, for $A_R=1$, $H_T=30$, $Re_b=10^3$, with different deficient mass flux ratios.

CHAPTER 2

A COMPUTATIONAL MODEL FOR THE RISE AND DISPERSION OF WIND-BLOWN, BUOYANCY-DRIVEN PLUMES PART II. LINEARLY STRATIFIED ATMOSPHERE

ABSTRACT

A multi-dimensional computational model of wind-blown, buoyancy-driven flows is applied to study the effect of atmospheric stratification on the rise and dispersion of plumes. The model utilizes Lagrangian transport elements, distributed in the plane of the plume cross section normal to the wind direction, to capture the evolution of the vorticity and density field, and another set of elements to model the dynamics in the atmosphere surrounding the plume. Solutions are obtained for a case in which atmospheric density changes linearly with height. Computational results show that, similar to the case of a neutrally stratified atmosphere, the plume acquires a kidney-shaped cross section which persists for a long distance downstream the source and may bifurcate into separate and distinct lumps. Baroclinic vorticity generated both along the plume boundary and in the surroundings are used to explain the origin of the distortion experienced by the plume and inhibiting effect of a stratified atmosphere, respectively. The vorticity within the plume cross section forms two large-scale coherent eddies which are responsible for the plume motion and the entrainment. Prior to reaching the equilibrium height, the computed plume trajectory is found to follow the two-thirds law, when extended to include the initial plume size, reasonably well. The entrainment and the added mass coefficients, *0.49* and *0.7*, respectively, are obtained from the numerical results over a wide range of the buoyancy ratio, defined as the ration between the plume buoyancy and the degree of background stratification. In the case of strong stratification, the plume trajectory shows weak, fast decaying oscillations around the equilibrium height. The origin and decay of these oscillations are explained using a simple analytical model.

NOMENCLATURE

B	Buoyancy Ratio;
g	Gravitational acceleration;
h	Spatial discretization length in the plume-air interface;
H	Vertical dimension of the computational domain;
h_s	Spatial discretization length in the stratified background;
H_T	Initial plume height above the ground;
k_v	Added mass coefficient;
N	Brunt-Väisäilä buoyant frequency;
N'	Modified buoyant frequency;
R	Radius of the circular plume cross section;
R_o	Initial Radius of the circular plume cross section;
R_{eq}	Equivalent radius of plume cross section;
R_y	Major (horizontal) axis of elliptical plume cross section;
R_z	Minor (vertical) axis of elliptical plume cross section;
Re_b	Buoyancy Reynolds number;
t	Same as the normalized x coordinate;
U	Homogeneous wind speed;
V	$\equiv \sqrt{\left\|\frac{\rho_p}{\rho_o}\right\| R\, g}$, plume buoyancy velocity;
w	Plume vertical velocity;
x	Horizontal wind direction;
y	Horizontal direction normal to the wind direction;
z	Vertical direction, plume rise;
β	Entrainment coefficient;
ρ_a	Air density;
ρ_o	Reference density;
ρ_p	Plume density apart from reference density;
ρ_s	Background air density apart from reference density;
ξ	Vertical displacement of plume from its equilibrium height;
Δt	Time step;
ε	$\equiv \left\|\frac{\rho_p}{\rho_o}\right\|$, plume mass flux ratio;

Superscript

*	Dimensional quantities.

2.1. INTRODUCTION

The dispersion of strongly buoyant plumes, similar to those generated from massive fires, cooling towers and tall industrial and power plant stacks, in a stable atmosphere is important in many practical applications. Stratification can limit the plume rise and distort its dispersion patterns in ways that worsen its impact on local air quality. Current models (Briggs, 1975) used to describe plume rise and dispersion in a stratified atmosphere, are based mostly on assumptions regarding entrainment and self-similarity and involve several adjustable constants (see Section 2.3 for a review). Application of computational methods is impeded by the difficulties encountered in the modeling of the buoyancy-generated turbulence, the large numerical diffusion associated with Eulerian discretization schemes, and the computational cost required when dealing with large domains.

A recently developed computational model, based on the Lagrangian interpretation of the dynamics of buoyancy-driven flows, attempts to overcome some of these difficulties (Zhang and Ghoniem, 1993, see Chapter 1). The numerical model utilizes the vortex element and transport element methods to solve the equations governing a wind-blown, buoyancy-driven plume derived directly from Navier-Stokes equations. This Chapter describes an extension of this model, originally intended for flows in a neutrally stratified atmosphere, to incorporate the effect of atmospheric density stratification on buoyant plume motion. We focus on the case in which the potential density[5] (referred to simply as density) of the air decreases linearly upwards. This form of stratification occurs frequently in elevated layers during the day and in the lowest 100 m or so at night (Briggs, 1975). In a following publication, the effect of an inversion layer will be described in detail.

---

[5] Potential density is defined as the density an air parcel would reach if it was brought adiabatically to a standard pressure, which for convenience is usually taken as the pressure at the ground. A neutrally stratified atmosphere is one in which the potential density is constant.

Atmospheric turbulence may be neglected if one is interested in buoyant plumes not too far away from the emission source, where the plume buoyancy dominates the motion. In general, and depending on how it is generated, there are two types of atmospheric turbulence. The first, characterized by $\sqrt{u'^2}$; where $u' = u - U$ is the fluctuating component of the instantaneous wind velocity, u, around its mean value, U, is due to wind shear instability. On the other hand, the plume buoyancy can be characterized by a buoyant velocity, $V = \sqrt{\left|\frac{\rho_p}{\rho_o}\right| R\, g}$, where ρ_o, ρ_p, R, and g are the reference density, the plume deficient density, the characteristic length of the plume cross section, and the gravitational acceleration, respectively (see Chapter 1). A criterion for neglecting this type of atmospheric turbulence may be given by

$$\frac{V}{u'} = \sqrt{\left|\frac{\rho_p}{\rho_o}\right| \frac{R\, g}{u'^2}} >> 1. \tag{2.1}$$

The second type of atmospheric turbulence is associated with the convective instability due to the uneven heating of air parcels in the atmosphere. A velocity scale representing the intensity of this turbulence over a horizontal distance equal to the plume size is given by $\sqrt{\left|\frac{\Delta\rho_a}{\rho_o}\right| R\, g}$, where $\Delta\rho_a$ is the scale of air density variation over a horizontal distance R. A corresponding criterion for neglecting this convective atmospheric turbulence is thus

$$\left|\frac{\rho_p}{\Delta\rho_a}\right| >> 1. \tag{2.2}$$

In this Chapter, we neglect atmospheric turbulence and focus on plume rise and dispersion due to buoyancy and buoyancy-generated turbulence in a stratified atmosphere (the effect of the former will be incorporated in future efforts). In Section 2.2, we describe the physical mechanism of baroclinic-vorticity generation in buoyant flows, and summarize how atmospheric stratification is implemented in our model. In Section 2.3, we review the integral models which have been developed to characterize the plume

trajectory, and refer to field observations on plume dispersion in a linearly stratified atmosphere. In Section 2.4, we present the computational results in the form of the plume trajectory and dispersion pattern, and compare our results with experimental data. An algebraic formula for the plume rise is obtained by modifying the classical two-thirds power law. The adjustable empirical constants in the formula: the entrainment coefficient, and the added mass coefficient are calibrated using the numerical results. The Chapter ends with a brief conclusion in Section 2.5, and a note on plume motion near its equilibrium height in the Appendix 2.A.

2.2. BACKGROUND

2.2.1. Vorticity Generation in a Disturbed Stratified Atmosphere

Dynamically, plume rise and dispersion in a weakly turbulent atmosphere is driven by the potential energy of the plume material. Kinematically, the plume motion is driven by the vorticity generated due to the density difference between the plume material and the surrounding air (see Chapter 1 for detail). The latter view has the advantage of allowing one to describe the turbulence generated within the plume cross section as well. To simplify the following discussion, we use the Boussinesq approximation which, in our previous work, has been shown to be accurate when the relative density perturbation is less than 0.1. With this approximation, baroclinic vorticity is generated only where a finite horizontal density gradient exists, i.e. along the distorted plume-air interface which at high Reynolds number, remains confined to a small subset of the entire domain. We also assume, as in Chapter 1, that the density distribution inside the initial plume cross section is uniform. The effects of density non-uniformity within the plume cross section, which is expected to be of secondary importance, will be investigated in the future.

In the presence of atmospheric density stratification, as the plume rises, the initially horizontal density isolines in the background are distorted. A density field with non-zero horizontal gradient component is thus established, and baroclinic vorticity is generated in the atmosphere. This is illustrated schematically in figure 2.1 for a crosswind section of a rising plume in a continuously stratified, stable atmosphere. As shown in the figure, vorticity generated in the background induces a net downward motion on the plume in the direction opposite to the flow induced by the vorticity generated due to the plume's own buoyancy. Eventually, the plume reaches a terminal, equilibrium, or level-off height where the effect of the background vorticity balances that of the vorticity around its surface. Occasionally, the plume may experience weak, fast decaying oscillations around this height (Briggs, 1975) due to a mechanism that will be discussed later. It should be noted, as will be shown later, that even after the plume

reaches its equilibrium height, vorticity generated both at the plume surface and in the surroundings still plays an important role in dispersing its material.

2.2.2. Model Formulation and Numerical Implementation

The partial differential equations governing the flow of a steady, three-dimensional, wind-blown, buoyancy-driven plume were presented in Chapter 1. Incorporating the atmospheric density stratification in the formulation does not change the governing equations, except for the fact that vorticity can now be generated in the background and its induced field must be incorporated in the solution.

In principle, in a continuously stratified atmosphere, we must discretize the entire space since non-zero horizontal density gradients could be established everywhere. However, the plume induced motion, and thus the distortion of the background, decays rapidly away from the plume center[6]. Moreover, the far field effect on the plume motion is generally negligible, see Section 2.4.1. Thus, to account for vorticity generated in the atmosphere noting that the air density isolines remain almost horizontal in the far field, we need only consider an area several plume characteristic length, R, around the plume center . Furthermore, in practice, the density gradient in the background is much smaller than that across the plume-air interface. Thus, we discretize the background density field into transport elements whose size is larger than the size of the elements used to discretize the plume-air interface. The discretization is schematically illustrated in figure 2.2. The choice of two different sizes of elements reduces the computational load while maintaining the numerical accuracy.

---

[6] Note that the distortion of the atmospheric density isolines, induced by the plume vorticity, is proportional to the velocity gradient, $\Delta u \approx \frac{\Gamma}{r^2}\Delta r$, where Γ is the circulation and r is the distance away from the vorticity center, i.e., the effect of vorticity induced distortion decays as the square of the distance away from the center of the vorticity.

2.3. REVIEW

Plume rise in a linearly stratified atmosphere has been analyzed in the literature. Denoting the reference density, taken here as the air density at the height of the plume source, by ρ_o, we write the density distribution as

$$\rho = \begin{cases} \rho_o + \rho_p(t,y,z) & \text{inside the plume} \\ \rho_o + \rho_s(t,y,z) & \text{outside the plume} \end{cases} \tag{2.3}$$

where ρ_p and ρ_s are the density perturbation of the plume and the air, respectively. The background stratification is characterized by the Brunt-Väisälä frequency, $N^2 = -\frac{g}{\rho_o}\frac{d\rho_s}{dz^*}$. As it rises, the plume entrains denser air until it reaches an equilibrium height where its average density is close to that of its surroundings. Meanwhile, the plume spreads out horizontally and vertically. The trajectory of a point source plume between the source and a point close to the level-off height has been described by the two-thirds power law (Briggs, 1969, 1975, Fay, 1973, Weil 1988). In a uniform wind with speed U, the trajectory of a buoyant plume generated from a finite size source can be obtained using the same procedure as in the derivation of conventional two-thirds power law after modifying the initial conditions to account for the finite initial plume size. The derivation follows Weil's (1988) and is similar to that described in Chapter 1 of this study. The resulting expression of the plume rise z^* is:

$$z^* = \frac{1}{\beta}\left\{\left[\frac{3\beta F_b}{(1+k_v)N'^2U}\left(1-\cos\frac{N'x^*}{U}\right)+R_o^{*3}\right]^{1/3} - R_o^*\right\} \text{ for } \frac{N'x^*}{U} \le \pi \tag{2.4}$$

where R_o^* is the radius of the initial plume cross section, k_v is the "added" or "virtual" mass coefficient which accounts for the momentum of the ambient fluid displaced by the plume as the latter rises and of the small scale motion inside the plume; $N' = N/(1+k_v)^{1/2}$ is a modified buoyancy frequency which takes k_v into account; β is

an entrainment coefficient used to describe the growth of the plume radius due to entrainment[7]; and $F_b = R_o^{*2}\, Ug \left|\frac{\rho_p}{\rho_o}\right|$ is the buoyancy flux.

The constants in equation (2.4) have been obtained using laboratory experiments and field observations of point-source plumes. However, as pointed out by Turner (1986), this two-thirds power "law" fails near the level-off region because the entrainment and similarity assumptions used in its development become invalid. Similar reasons, coupled with the difficulty in defining the plume center and the size of its cross section in different experiments (List 1982, Gebhart et al, 1984), have been used to describe the origin of the following unresolved problems:

(1) Good correlation between the two-thirds power law and different experiments are achieved by adjusting the entrainment coefficient for each case, i.e., the coefficients are not truly universal. From laboratory experiments, Slawson and Csanady (1967) found $\beta = 0.43$, while Hewett et al. (1971) got the best fit with $\beta = 0.71$. From field experiments, Hoult et al (1969) found that $0.3 < \beta < 1.0$, while Fay et al. (1970) obtained $0.5 < \beta < 2.0$.

(2) In models which assume that the plume cross section remains circular, the radius increases with the plume rise as

$$R^* = R_o^* + \beta z^*. \qquad (2.5)$$

Using data from the same experiment to fit the trajectory, equation (2.4), or the radius, equation (2.5), Briggs (1975) found $\beta = 0.6$ or 0.4, respectively. This inconsistency was also observed by other authors; Weil (1982) obtained $\beta = 0.6$ from the trajectory data while $\beta = 0.5$ from the radius data.

In the early development of the two-thirds power law, the added mass coefficient, k_v, was not included (Briggs, 1969, Fay et al, 1970). Later k_v was introduced (Briggs, 1975, Weil, 1988) to improve the accuracy of the trajectory law derived from the integral

---

[7] Weil (1988) used a modified entrainment rate related to the added mass coefficient in his derivation.

formulation. The added mass concept was originally developed for a solid body accelerating in a fluid (Yih, 1977) to account for the work done to increase the momentum of the ambient fluid. In the case of a circular cylinder moving in an inviscid flow, $k_v = 1$. The same value is usually suggested for plumes where the driving force is buoyancy. However, the actual value may deviate from unity since the plume is not a solid body and its cross section is not circular. If fact, the plume cross section, as shown in Chapter 1, is shaped in the form of an inverted kidney which evolves as the plume rises. Furthermore, not only a significant portion of surrounding air is induced into motion due to the presence of the plume, but also motion at scales smaller than the plume radius is developed within its cross section. In practice, k_v can be regarded as merely another empirical constant whose value should be adjusted to make the two-thirds power law fit the experimental trajectory better.

The shape of the plume cross section is an important feature of plume dispersion, especially for large-scale, strongly buoyant plumes. As the plume rises, two counter-rotating vortices, which divide the plume material into two lumps, are generated. Plume bifurcation is a frequently observed yet not well understood phenomenon. Some of the laboratory and field experiments describing this bifurcation have been reviewed in Chapter 1. Here we cite three more experiments, which have been documented carefully, in which bifurcation have been cited. The first is the fire plume experiment of Church et al (1980), conducted for the purpose of investigating the mechanism leading to the formation of large-scale vortices in fire plumes. These authors hypothesized that the generation of a double-vortex structure is due to the tilting and stretching of the vorticity originally associated with background wind shear, and the vorticity generated within the plume by the action of buoyancy and drag forces. The second is the Lidar measurements of cooling tower plumes (Hawley, 1985, Bennett et al, 1992). Sykes et al (1986) suggested that the interaction between the crosswind and the initial vertical momentum of the plume may be the cause for the bifurcation. The third experiment is the laboratory

water plume model of Alton et al (1993). Clearly, the mechanism leading to plume bifurcation requires further investigation (Zhang and Ghoniem, 1993).

2.4. NUMERICAL RESULTS

2.4.1. Entrainment, Added Mass and Plume Trajectory

The notations and normalization procedure used in this Chapter are the same as those employed in Chapter 1. To characterize the background in which the plume disperses, we define the buoyancy ratio as the ratio between the plume buoyancy to the degree of stratification,

$$B = \frac{V^2}{N^2 R^2} = \frac{\varepsilon g}{N^2 R} \tag{2.6}$$

where $\varepsilon = \left|\frac{\rho_p}{\rho_o}\right|$ is the plume deficient mass flux ratio and R is the plume length scale, taken as the square root of the initial plume cross sectional area. In terms of the buoyancy ratio, equation (2.4) becomes

$$z = \frac{1}{\beta\sqrt{\pi}}\left\{\left[3\sqrt{\pi}\,\beta B\left(1 - \cos\frac{x}{\sqrt{(1+k_v)B}}\right) + 1\right]^{1/3} - 1\right\}, \tag{2.7}$$

where the effects of plume buoyancy and background stratification have been grouped into a single dimensionless parameter[8], B. In terms of the variables defined above, the buoyancy ratio can be written as

$$B = \frac{\left|\frac{\rho_p}{\rho_o}\right| g}{-R\frac{g}{H}\frac{\rho_{st} - \rho_{sb}}{\rho_o}} = \frac{|\rho_p|/R}{(\rho_{sb} - \rho_{st})/H} \tag{2.8}$$

where ρ_{sb} and ρ_{st} are the air densities at the bottom and top boundaries of the computational domain, and H is the vertical dimension of this domain, as shown in figure 2.2. For typical low-level atmospheric stratification, $\left|\frac{\rho_{sb} - \rho_{st}}{\rho_o}\right| \approx 10^{-3}$ over a vertical

---

[8] The steady motion of a plume with initial circular cross section in a uniform wind, U, depends on four independent dimensional variables: R, g, ρ_p, and $\frac{\partial \rho_s}{\partial z^*}$. Only one dimensionless parameter can be formed from these four variables is, $B = \frac{\rho_p / R}{\partial \rho_s / \partial z^*}$.

range of $H = O(100m)$. If the plume size is of $R = O(10m)$, and with deficient density $\left|\frac{\rho_p}{\rho_o}\right| \approx 10^{-2}$, the corresponding buoyancy ratio is $B = 100$. For large plumes, the expected range of the buoyancy ratio is $10 < B < 1000$.

We ran the computational code for four values of the buoyancy ratio, $B = \infty$, 50, 25, and 12.5, ranging from neutral to strong stratification, with all other conditions: the initial plume size $(R_y, R_z) = (\frac{1}{\sqrt{\pi}}, \frac{1}{\sqrt{\pi}})$, the initial deficient plume density $\frac{\rho_p}{\varepsilon\rho_o} = -1.0$, the initial height $H_T/R = 23.0$, and the buoyancy Reynolds number $R_{eb} = 1000$, being the same. Symmetry across the plume centerline was enforced at all times. The discretization lengths for the computational elements is $h/R = 0.025$ for the plume-air interface, and $h_S/R = 0.5$ in the stratified atmosphere, as shown in figure 2.2. The marching step in the wind direction is $\Delta t = 0.025$[9]. The vertical extent of the domain is $15 \le z \le 40$, so that $H/R = 25$. The horizontal extent is $0 \le y \le 7.09$. The computational results were used, besides investigating the fundamental dynamics governing plume rise and dispersion, to determine the values of the entrainment coefficient and the added mass coefficient in the trajectory formula, equation (2.7). It should be noted that the values of these constants may vary with B. Similar to Chapter 1, we define the plume height at any downwind location as the algebraic mean of the maximum and minimum heights of the plume cross section.

The computed plume center height of each case was fitted to the trajectory formula by adjusting the arbitrary constants, β and k_v. The computed trajectories of the four cases, and the corresponding fitted curves are shown in figure 2.3. The best fit for all four cases were obtained using the following pair of constants: $\beta = 0.49$ and $k_v = 0.7$. It was found that while β had a stronger influence on the equilibrium height, k_v affected the downwind distance where the equilibrium height was reached. As mentioned earlier,

---

[9] In terms of the parameters used to check the convergence of the computations, such as the plume trajectory, numerical results with smaller values of h, h_S and Δt are indistinguishable from the results described in this paper.

equation (2.7) is expected to be valid only for the part of the trajectory prior to reaching the level-off height.

The top curve in figure 2.3 corresponds to the case of plume rising in a neutrally stratified atmosphere. In this case, the plume rises continuously and there is no equilibrium height. Equation (2.7) describes this curve using $N^2 = 0$, $\beta = 0.7$, and $k_v = 0$, as shown in Chapter 1. Therefore, the same trajectory can be represented by the two-thirds law using two different sets of constants; one with the a finite added mass coefficient and the other without[10].

The lowest curve in figure 2.3, where the plume reaches the equilibrium height early, corresponds to a case with strong stratification. Weak, fast decaying oscillations are observed in the level-off region. This is consistent with the experimental observations that the plume oscillations decay rapidly in the downwind direction (Briggs, 1975). Plume oscillations are generated as the buoyant plume overshoots its equilibrium height and disturbs the initially calm background. These oscillations, which possess a well-defined frequency, then travel through the atmosphere in the form of gravity waves due to the restoring action of the stratified background. A detailed discussion on the origin and the character of these oscillations is provided in the Appendix using a simple analytical model. The intermediate cases also follow the extended two-thirds law well until the plumes reach their corresponding equilibrium heights, where the analytical curves overestimate the heights. As expected, the trajectory formula (2.4) generally cannot predict the maximum plume rise.

Part of the kinetic energy associated with the plume motion, transformed from its initial potential energy through the vorticity, is radiated away in the crosswind section via

---

[10] Briggs (1969) proposed using β=0.4 in the formula for the plume radius, equation (2.5), and β=0.6 in the trajectory formula, equation (2.4). This means that, in the analytical model used to derive the two-thirds law, $R = R_0 + 0.6\,z$ is used to evaluate the plume momentum, while $R = R_0 + 0.4\,z$, is used to evaluate the plume size. Using larger values of R in calculating the momentum may account for part of the momentum of the background fluid which is set in motion by the plume. Thus, it is not surprising that the early version of the two-thirds law, which did not incorporate the concept of added mass, could still describe the plume trajectory well (Fay et al, 1970, Hewett et al, 1971).

the internal waves. Thus, a significant part of the surrounding air may be disturbed and a larger computational domain may be needed to capture the effect of these waves. To find out the effect of the finite domain size on the results, we repeated the calculation of the $B= 25$ case after doubling the horizontal extent of the computational domain to $y = 14.18$. No significant changes were observed in the result up to $x = 17.5$ where the calculations were terminated.

Now we compare the entrainment relation expressed by equation (2.5) with the simulation results. In dimensionless form, if we use the equivalent radius[11] to describe the size of the plume cross section, equation (2.5) can be written as

$$R_{eq} = 1/\sqrt{\pi} + \beta z \tag{2.9}$$

Figure 2.4 shows the computed equivalent radius as a function of the plume rise. Clearly, the growth of the plume cross section depends weakly on the buoyancy ratio before reaching the level-off height. Beyond $z=2$, and before the level-off distance, the computed equivalent radius grows almost linearly with height. Both equation (2.9) and its corresponding form for a point-source plume, $R_{eq} = \beta z$, are shown using $\beta = 0.49$ which was obtained from the trajectory. As shown in the figure, equation (2.9) overestimates the equivalent radius, although the slope is reasonably captured. Beyond $z=2$, the equivalent radius increases with height as if the plume had started from a virtual point source at $z=0$.

It is interesting to note how the buoyancy ratio affects the plume spread close to the level-off height. In the neutrally stratified case, $B = \infty$, the equivalent radius and the plume rise increase indefinitely. In the weakly stratified case, $B= 50$, the radius continues to expand after the plume reaches the level-off region. In the cases with stronger stratification, $B= 25$ and 12.5, the plume radius and rise are curtailed beyond the equilibrium height, as shown by the crowd of points near the level-off height.

---

[11] The equivalent radius is defined as the radius of the circle whose area the same as the actual plume cross-sectional area.

2.4.2. Other Integral Characteristics of the Plume

To investigate the effect of stratification on plume dispersion, we plot the evolution of the vertical and horizontal widths of the plume cross section, both as defined in Chapter 1. Figure 2.5 shows that beyond the level-off height, the vertical width of the plume cross section increases in the neutrally stratified case, oscillates around a nearly constant value in the weakly stratified atmosphere, and decreases in the strongly stratified atmosphere. Achieving an almost constant vertical width under conditions of intermediate stratification is consistent with experimental results (Briggs, 1975). The decrease of the vertical width under strong stratification is because while the top side of the cross section is capped, the bottom side continues to rise, as will be seen in more detail in the next section. On the other hand, as shown in figure 2.6, the plume horizontal width increases continuously, with the rate of expansion being approximately the same for all cases. Thus, atmospheric stratification affects the plume dispersion mainly by suppressing the vertical fluid motion.

As mentioned earlier, the effect of atmospheric stratification can be understood in terms of the vorticity generated in the background, as presented in figure 2.1. During the early stages, negative vorticity (on the right side of the centerline), which lifts the plume upwards, is generated at the interface between the plume and the surrounding. In the later stages, after the atmosphere has been disturbed, positive vorticity (on the same side), which tends to push the plume downwards, is generated in the stratified background. Using the results of the simulation, we can probe into this mechanism in more detail. Figures 2.7 and 2.8 show the total circulation, integrated over half of the computational domain, in the plume-air interface and in the background, respectively. Initially, and in all cases, the magnitude of the total circulation at the plume-air interface increases rapidly at a rate which is independent of B. However, The terminal value of the total circulation in the plume cross section is a function of B. The saturation of the total plume circulation is due to the reason described in Chpater 1: both negative and positive circulation grows

at the same rate following the large eddy roll-up stage. On the other hand, after the atmosphere has been disturbed, the positive background circulation increases continuously. The stronger the stratification, the faster the rate at which ambient circulation is generated. With strong stratification, the magnitude of the positive background circulation could be larger than that of the negative plume circulation. However, the induced motion by the former is not necessarily stronger because this positive background circulation is distributed over an area much larger than the plume cross section, as will be shown in the next section.

The deformation of the plume cross section can also be measured in terms of the growth of the boundary (interface) length between the plume and the surrounding atmosphere. The plume circumference, shown in figure 2.9, exhibits exponential growth following a short acceleration period with a high rate during the early large eddy roll-up stage and a lower rate during the small eddy roll-up stage. It is interesting to note that this circumference grows continuously beyond the point where the plume has reached a level-off height. This means that the buoyancy-generated turbulence still plays an important role in dispersing the plume material even at this later stage. The figure shows that the growth of the circumference is almost independent of the background stratification.

The plume equilibrium, or level-off, height, z_{eq}, is an important quantity. This height is commonly used in conventional models as the terminal rise of a buoyant plume in the presence of atmospheric stratification. At this height, the plume material is assumed to be distributed according to a Gaussian distribution. Figure 2.10 shows the plume terminal rise as a function of the buoyancy ratio (two additional cases, $B = 16.67$ and 33.3, were computed to establish this curve). In practice, it is customary to use equation (2.4) to calculate the maximum plume height and multiply the result by an empirical factor to obtain the final equilibrium height. This, however, may not always be appropriate due to the following reasons: (a) the plume trajectory formula, equation (2.4),

does not predict an accurate maximum plume height since the entrainment and similarity assumptions become invalid near this region; (b) the empirical multiplication factor is not a well defined quantity; and (c) the experimental results on point source buoyant plumes still involves fairly large uncertainties.

2.4.3. Concentration and Vorticity Distributions

Figure 2.11 shows the deficient density distribution across the plume cross section at successive downwind distances for the case of $B = 12.5$. The increment between the density isolines is the same in each cross section and decreases for larger downwind distance. The number of isolines in the background increases for larger x because, while the number of isolines are the same in each section, the range of density variation decreases. Initially the plume cross section is circular (only half of the section is shown) and the background stratification is horizontally uniform, so that the background density isolines are all horizontal. Due to buoyancy, a double-vortex structure, which induces the upwards motion and deforms the plume cross section into a kidney-shaped pattern, is generated. Concomitantly, the initially horizontal background density isolines are disturbed and positive background vorticity (on the same half of the plume) is generated.

Beyond $x=7$, each side of the cross section splits into two lumps with more material being associated with the lower lump. Both lumps continue to rise until the plume center reaches its equilibrium height at $x=12$. Thereafter, the top lump stays almost at a fixed height while the lower one continues to rise slowly thus decreasing the overall vertical width of the plume. This bifurcation phenomenon was also observed in the two-dimensional thermal experiment of Tsang (1971).

Figures 2.12 and 2.13 show contours of: (a) the plume deficient density, which is proportional to plume material concentration, $\frac{\rho_p}{\varepsilon\rho_o}$; (b) the vorticity; (c) the background deficient air density, $\frac{\rho_s}{\varepsilon\rho_o}$; and, (d) the velocity field in the cross-wind section at $x = 4$ and $x = 14$, respectively, all for the strongly stratified case with $B= 12.5$. Since we have used

separate transport elements for the plume perturbation density and air density, these two fields can be calculated and presented separately here.

At $x = 4$, the plume cross section exhibits the kidney shaped structure which was also observed in the neutrally stratified case (see Chapter 1). At this section, located only a short distance away from the source, negative vorticity is generated over a large portion of the plume-air interface, as demonstrated in figure 2.1. The cumulative action of this vorticity is to propel the plume upwards. Meanwhile, positive vorticity is generated in the surrounding, although its effect on the plume trajectory is not yet noticeable, see figure 2.3. The mechanism of positive vorticity generation in the surrounding atmosphere can be explained using figure 2.12c which exhibits the density isolines in the immediate vicinity of the plume. Heavy air from lower altitudes is entrained into the core, and is displaced by lighter air which flows downwards from higher altitudes along the plume sides. This imparts strong curvature on the background density isolines and leads to the generation of positive vorticity. The velocity field, shown in figure 2.12d, depicts a structure which can be attributed to a vortex dipole, coincident with the plume material concentration contours. At $x = 14$, and according to figure 2.3, the plume is at the level-off region. On each side of the centerline, the plume breaks up into two lumps with the lower one containing more of the original plume material. The break-up of a plume into several lumps has been observed by Richards (1963) and is considered to be one of the important mechanisms of turbulent plume dispersion.

The vorticity field in figure 2.13b shows two eddies: the lower eddy having strong negative circulation and the upper eddy having weak positive circulation (The sense of rotation of these eddies is confirmed by figure 2.13d). The positive background vorticity is distributed over a much larger area than that occupied by these two plume eddies. Since the plume is not rising at this stage, the net effect of these eddies on its trajectory must be balanced by the effect of the positive vorticity generated in the background. According to the conventional argument, the plume reaches the level-off height when its

average density, being that of the original plume material after getting diluted by the entrained air, is the same as the local atmospheric density. This "dynamic" argument, however, relies on quantities, such as the plume size, which are difficult to define. Our "kinematic" argument is based solely on the motion induced by the vorticity generated within the plume cross section and in the background.

The background density field in figure 2.13c illustrates the effect of the plume break-up on the motion of surrounding air. In the early stages, air, which is heavier than the plume material, is entrained vertically upwards into the core. At $x=14$, the entrained air is forced to move horizontally away from the centerline, indicating that the plume has stopped its vertical ascent and is spreading out horizontally. Meanwhile, some of the heavier air in the plume core is leaking downwards.

The velocity field, depicted in figure 2.13d, depicts the manifestation of the complex vorticity structure within and in the immediate vicinity of the plume. As mentioned earlier, the vorticity field is composed of a positive eddy on the upper side and a negative eddy on the lower side of the plume cross section. Near the center, $y=0$, the flow induced by this vorticity distribution acts to dislodge some of the air entrained earlier. It is important to add at this point that even after reaching the level-off height, the plume continues to disperse horizontally due to the action of the large scale vortices.

2.5. CONCLUSION

The computational plume model, which is based on the utilization of the transport element method to solve the equations governing a buoyant flow in a horizontal uniform wind, has been extended to include the effect of atmospheric density stratification. Results have been obtained for a wide range of the buoyancy ratio which characterizes the relative importance of the plume buoyancy to the change in the atmospheric density. The computed plume trajectory and dispersion patterns have been compared with experimental measurements whenever possible. The extended two-thirds power law is found to describe the plume trajectory reasonably well before the plume reaches its equilibrium height. The entrainment and the added mass coefficients are found to be $\beta = 0.49$ and $k_v = 0.7$, over a wide range of buoyancy ratio.

The computational results suggest that the plume cross section first changes from a circular into a kidney-shaped form, and then breaks up into several lumps at later stage. This behavior has been confirmed qualitatively by various field and laboratory observations. However, quantitative measurements of the plume material distribution, which can be used in direct comparison with the numerical results, are currently scarce. This problem may be overcome using the newly developed rapid-scanning Lidar technique which is capable of obtaining the instantaneous density distribution within the plume cross section (Bennett et al, 1992). Application of this technique may provide considerable field data to guide further model validation.

Many features of buoyant plume motion, e.g., the kidney-shaped cross section, the induced motion of the surrounding air and the inhibiting effect of atmospheric stratification, can be attributed to the buoyancy-generated vorticity. This turbulence, being neither homogeneous, nor isotropic or stationary, occurs often in fluid motion with finite density gradient. This vorticity exhibits itself in the form of a long-preserved, large-scale, coherent vortex structure, which governs the entrainment process. Since this

turbulence is frequently encountered in nature, its understanding and proper description is important both fundamentally and practically.

The agreement between the simulated results and the experimental observations shows the potential for applying the model to more complicated problems, such as, plume interaction with an inversion layer, heavy particle separation from buoyant plumes, and chemically reactive plume dispersion. Neglected from the current model are the initial momentum and/or shear in the plume section. Ways of modeling their effects are currently being investigated

REFERENCES

Alton B. W., Davidson, G. A. and Slawson, P. R. (1993) Comparison of measurements and integral model predictions of hot water plume behavior in a crossflow, *Atmos. Environ.* **27A**, 589-598.

Bennett M., Sutton, S. and Gardiner, D. R. (1992) An analysis of Lidar measurements of buoyant plume rise and dispersion at five power stations, *Atmos. Environ.* **26A**, 3249-3263.

Briggs G. A. (1969) *Plume rise.* USAEC Critical Review Series, TID-25075, NTIS, 81pp.

Briggs G. A.(1975) Plume rise predictions. *Lectures on Air Pollution and Environmental Impact Analysis*, D. A. Haugen, Ed., Amer. Meteor. Soc., Boston, 59-111.

Church C. R., Snow, J. T. and Dessens J. (1980) Intense Atmospheric vortices associated with a 1000 MW fire. *Bull. Am. Meteorol. Soc.*, **61**, 682-694.

Fay J. A., Escudier M. P. and Hoult D. P. (1970) A correlation of field observations of plume rise. *Journal of Air Pollution Control Association,* **20**, No.6, 391-397.

Fay J. A. (1973) Buoyant plumes and wakes, *Ann. Rev. of Fluid Mech.*, **5**, 151-160.

Gebhart B., Hilder D. S. and Kelleher M. (1984) The diffusion of turbulent buoyant jets. *Int. J. Heat Mass Transfer*, 1-57.

Hawley J. G. (1985) Plume model validation and development project: differential absorption Lidar measurements of SO_2 in moderately complex terrain. EA-3758, Research Project 1616-12, SRI international, 333 Ravenswood Avenue, Menlo Park, California 94025.

Hewett T. A., Fay J. A. and Hoult D. P.(1971) Laboratory experiments of smokestack plumes in a stable atmosphere, *Atmos. Environ.* **5**, 767-789.

Hoult D. P., Fay J. A. and Forney L. J. (1969) A theory of plume rise compared with field observations, *Journal of Air Pollution Control Association,* **19**, No.8, 585-590.

List E. J. (1982) Turbulent jets and plumes, *Ann. Rev. Fluid Mech.*, **14**, 189-212.

Richards J. M. (1963) The penetration of interface by cylindrical thermals, *Quart. J. Roy. Meteor. Soc.*, **89**, 254-264.

Slawson P. R. and Csanady G. T. (1967) On the mean path of buoyant, bent over chimney plumes, *J. Fluid Mech.* **28**, 311-322.

Sykes R. I., Lewellen, W. S. and Parker S. F. (1986) On the vorticity dynamics of a turbulent jet in a crossflow. *J. Fluid Mech.*, **168**, 393-413.

Tsang G. (1971) Laboratory study of line thermals. *Atmos. Environ.*, **5**, 445-471.

Turner J. S. (1986) Turbulent entrainment: the development of the entrainment assumption, and its application to geophysical flows, *J. Fluid Mech.*, **173**, 431-471.

Warren F. W. G. (1960) Wave resistance to vertical motion in a stratified fluid, *J. Fluid Mech.*, **7**, 209-229.

Weil J. C. (1988) Plume rise, *Lectures on air pollution modeling*, Editors, Venkatram A. and Wyngaard J. C., 119-166.

Yih C. S. (1977) *Fluid mechanics*, West River Press, 3530 West Huron River Drive, Ann Arbor, Michigan 48103, USA. xviii+pp.622.

Zhang X. and Ghoniem A. F. (1993) A computational model for the rise and dispersion of wind-blown, buoyancy driven plumes, Part I, Neutral stratified case. *Atmos. Environ.*, (in press).

APPENDIX 2.A. ON THE LEVEL-OFF REGION OF PLUME TRAJECTORY

In a stable atmosphere, the air density decreases with height. As a buoyant plume rises, it entrains ambient air and the plume volume-averaged density increases. When the plume reaches the maximum height, it loses its vertical momentum since most of its kinetic energy is transformed into gravitational potential energy. In the level-off region of a plume trajectory, a slight overshoot of the final height is often seen. However, more than one oscillation is infrequently observed (Briggs, 1975). The same strong damping of oscillations is exhibited by our numerical simulations. To explain this behavior, Warren (1960) studied the damping of oscillation of a rising axisymmetric thermal and suggested that the rapid damping of plume oscillation is due to "wave drag". In the following, we develop a simple model to explain this phenomenon.

We assume that the plume motion is steady; the ambient wind, U, is uniform and the atmosphere is linearly stratified. The plume is assumed to be a parcel with volume-averaged density and at the position of its mass center. We denote the coordinate in the wind direction by x^*, and the vertical distance above the equilibrium height by z^*. The vertical momentum equation, after incorporating the Boussinesq approximation, can be written as

$$U \frac{\partial w^*}{\partial x^*} = - \frac{\rho_p}{\rho_o} g \tag{2.A1}$$

where w^* is the plume vertical velocity. The rate of change of the average density inside the plume is approximated as

$$\frac{d}{dt}(\rho_a + \rho_p) = \frac{\dot{m}_e}{A} \tag{2.A2}$$

where ρ_a and ρ_p are the air density and plume deficient density, respectively; $\frac{\dot{m}_e}{A}$ is the influx of air per unit cross-sectional area into the plume due to entrainment. For a plume with larger deficient density, the entrainment is stronger, so that the influx of air into its core is higher. We parameterize this influx using an entrainment coefficient α:

$$\frac{\dot{m}_e}{A} = - \alpha \rho_p . \tag{2.A3}$$

Realizing $\frac{\rho_p}{\rho_a} << 1$ and that the air density is vertically stratified, we can simplify equation (2.A2) and rewrite it as

$$U \frac{\partial \rho_p}{\partial x^*} + w^* \frac{d \rho_a}{d z^*} = - \alpha \rho_p \tag{2.A4}$$

Eliminating ρ_p from (2.A1) and (2.A4), we obtain

$$U^2 \frac{\partial^2 w^*}{\partial x^{*2}} + \alpha U \frac{\partial w^*}{\partial x^*} + N^2 w^* = 0 \tag{2.A5}$$

where $N^2 = - \frac{g}{\rho_o} \frac{d \rho_s}{d z^*}$ is the square of the Brunt-Väisälä frequency which characterizes the stability of the atmosphere. Writing the vertical displacement of plume from the equilibrium height as $\xi^* = \int w^* \, dt^*$, then (2.A5) becomes

$$\frac{\partial^2 \xi^*}{\partial x^{*2}} + \frac{\alpha}{U} \frac{\partial \xi^*}{\partial x^*} + \frac{N^2}{U^2} \xi^* = 0. \tag{2.A6}$$

The solution of (2.A4) gives the trajectory of the plume:

$$\xi^* (x^*) = \xi_o^* \, exp \left(- \frac{\alpha}{2 U} x^* \right) cos \left(\frac{N}{U} \sqrt{1 - \frac{\alpha^2}{4 N^2}} \; x^* \right). \tag{2.A7}$$

where the origin of x^* is chosen at the location where ξ^* reaches its maximum value, ξ_o^*. Clearly, this maximum amplitude is related to the vertical momentum of the plume when it first crosses the equilibrium height.

Discussion:

(1) The oscillation amplitude decays exponentially as the plume proceeds in the wind direction. The decay length scale is

$$L_d = \frac{2 U}{\alpha} \tag{2.A8}$$

which is longer for large ambient wind speed U or small entrainment coefficient α. L_d depends on N since α is a function of stratification although it does not appear explicitly in (2.A8). For large N, or strong vertical stratification, the atmosphere is stable, and we

expect the plume entrainment to be weak, α to be small and L_d to be long. Therefore, the decay length scale is longer for stronger ambient stratification.

(2) The spatial wavelength is

$$L_w = \frac{U}{N\sqrt{1-\frac{\alpha^2}{4N^2}}} \tag{2.A9}$$

which is longer for faster ambient wind speed, shorter for stronger stratification and weaker entrainment.

(3) The number of plume oscillations depends on the ratio of $3L_d$, the distance over which 95% of the maximum amplitude decays, and $2\pi L_w$, the wavelength of the oscillation,

$$n = \frac{3L_d}{2\pi L_w} = \frac{3}{2\pi}\frac{2N}{\alpha}\sqrt{1-\frac{\alpha^2}{4N^2}}. \tag{2.A10}$$

For longer decay length or shorter wavelength, more oscillations are expected. There are two extremes. (a) $\alpha=0$, i.e., no entrainment is involved, the plume moves as a pure, non-dissipative internal wave. In this case, which corresponds to a passive plume in an internal wave field, we have an infinite number of oscillations. (b) $\alpha = 2N$, very large entrainment is involved and no oscillations occur. It is interesting to note that n is independent of the wind speed.

Generally, for $0 < \alpha/2N < 1$, the number of oscillations is finite and small if entrainment is large. The dependence of n on $\alpha/2N$ is shown on figure 2.A1.

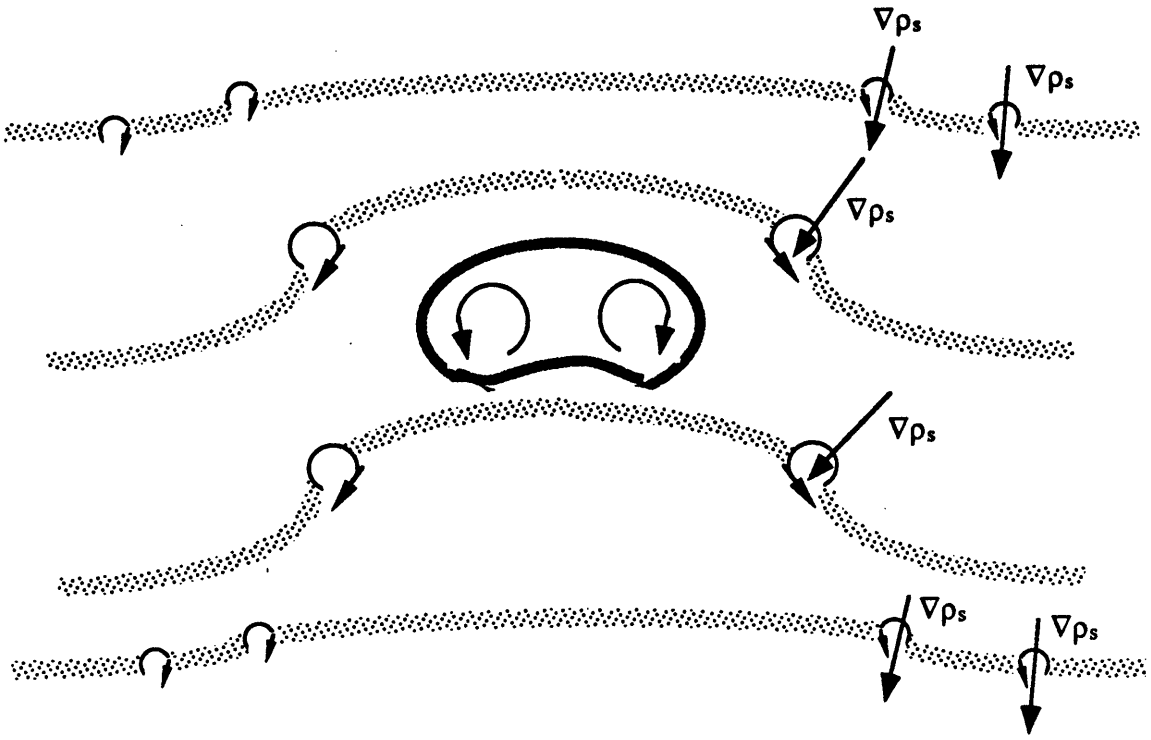

Figure 2.1. Schematic drawing showing the generation of vorticity along the plume interface and in the surrounding, when atmosphere stratification is finite.

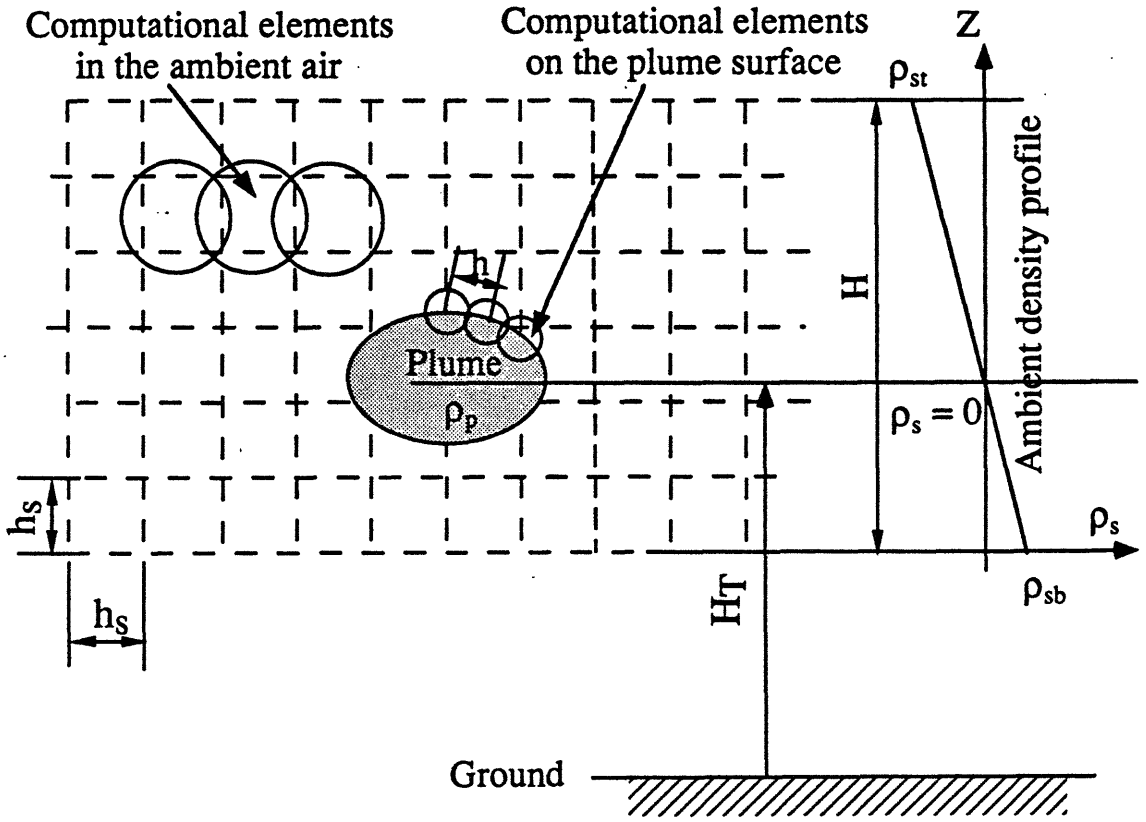

Figure 2.2. The computational domain in the cross-wind section at time $t = 0$, showing the discretization of the plume-air interface and the surrounding into transport elements. The air density profile is shown on the right-hand side.

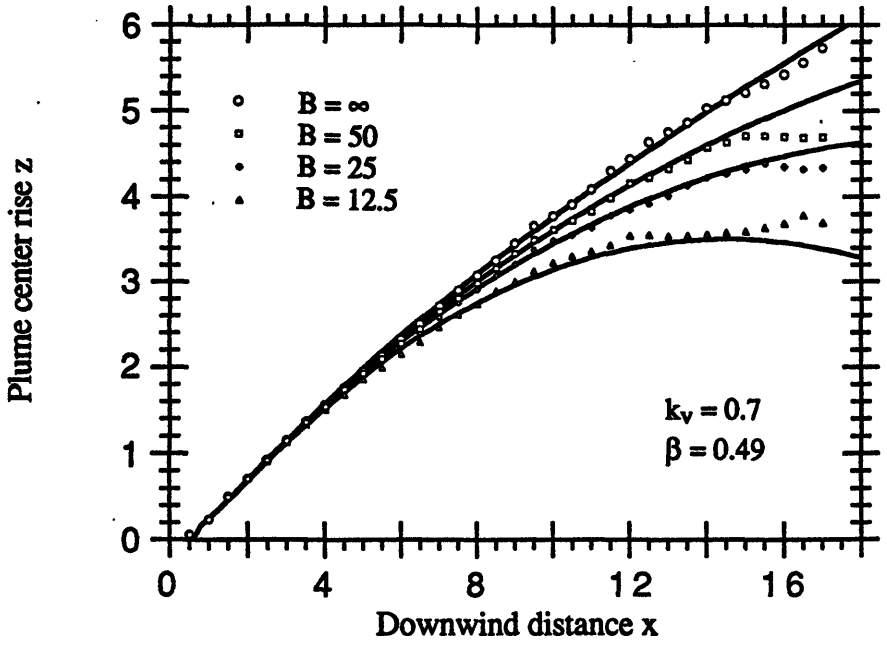

Figure 2.3. The trajectories of the plume center in a linearly stratified atmosphere. Open symbols depict the numerical simulation results for four different buoyancy ratios. The extended two-thirds law is shown by solid lines for the same cases.

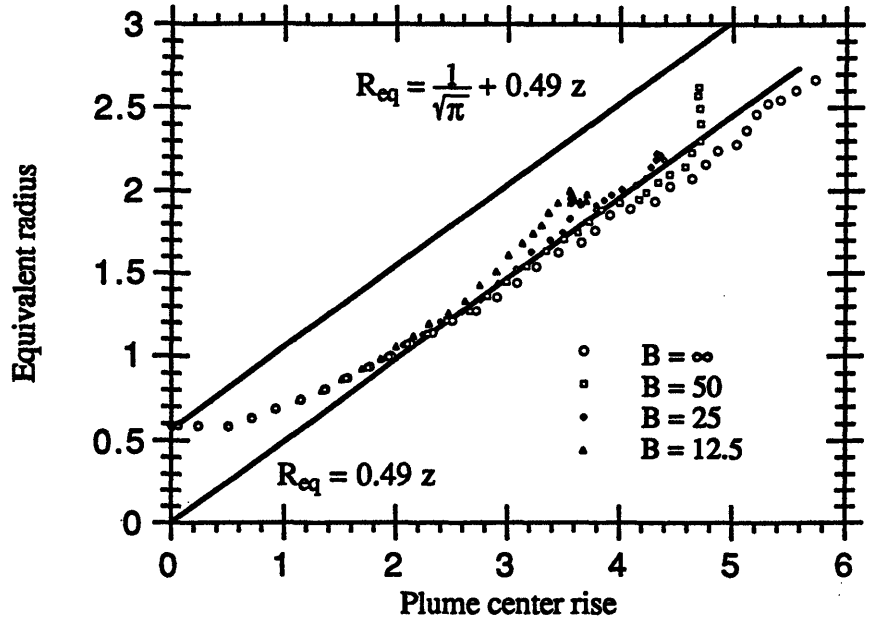

Figure 2.4. The equivalent radius of the plume cross section versus the plume rise for different buoyancy ratios. Numerical results are shown by open symbols while the integral relations are depicted by solid lines.

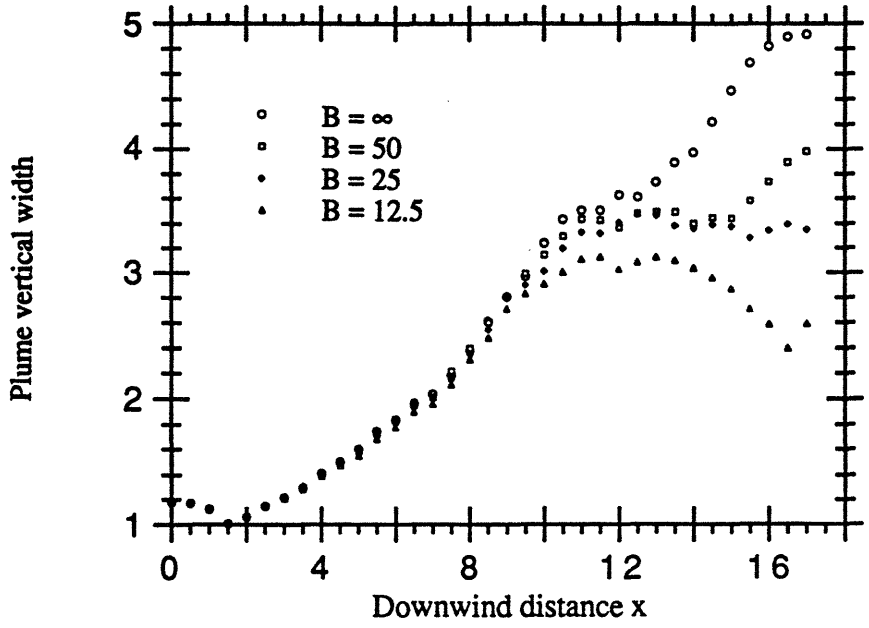

Figure 2.5. The change of the plume vertical width, defined in terms of the maximum vertical extension of the plume cross section, along the downwind distance.

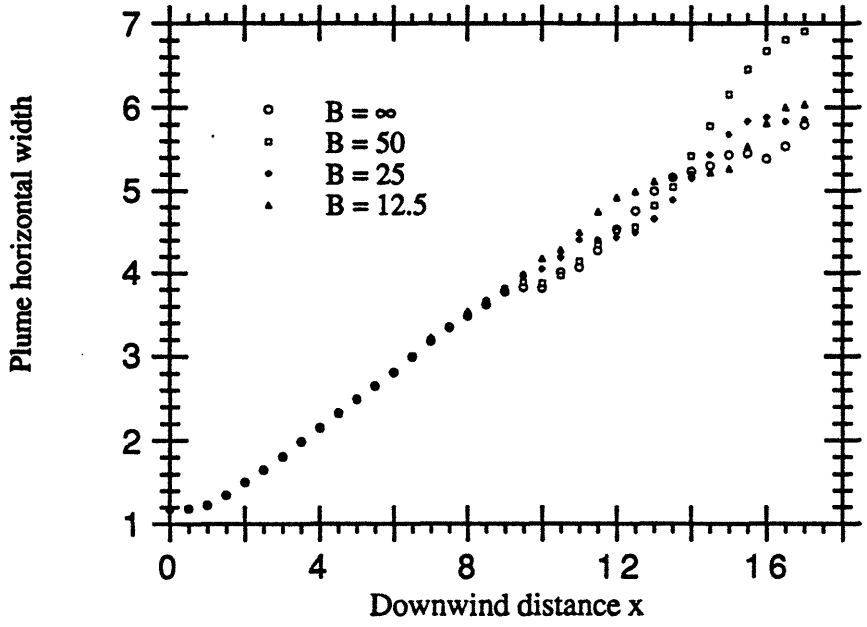

Figure 2.6. The variation of the plume horizontal width, described by the maximum crosswind horizontal extension, along the downwind distance.

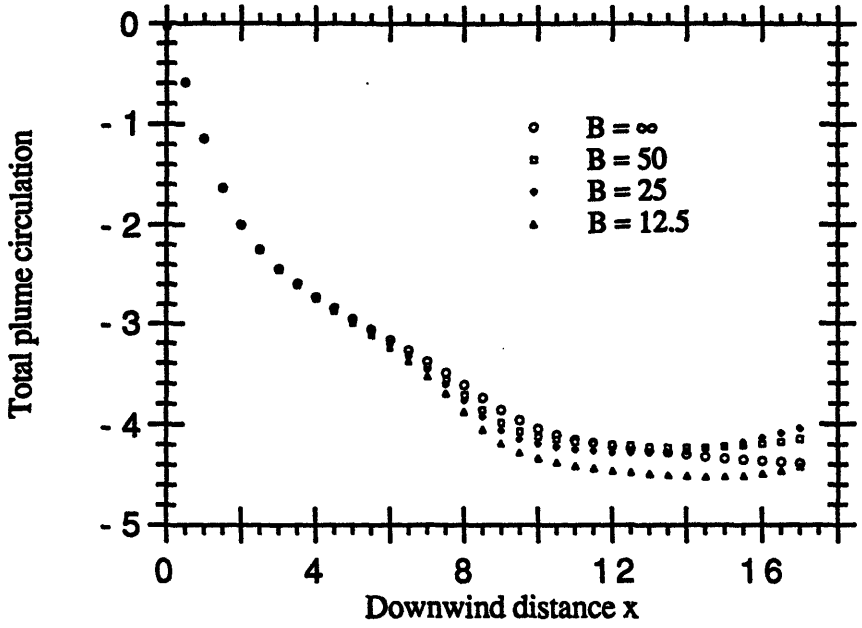

Figure 2.7. The total circulation generated at the plume-air interface on the right half of the plume cross section as a function of the downwind distance.

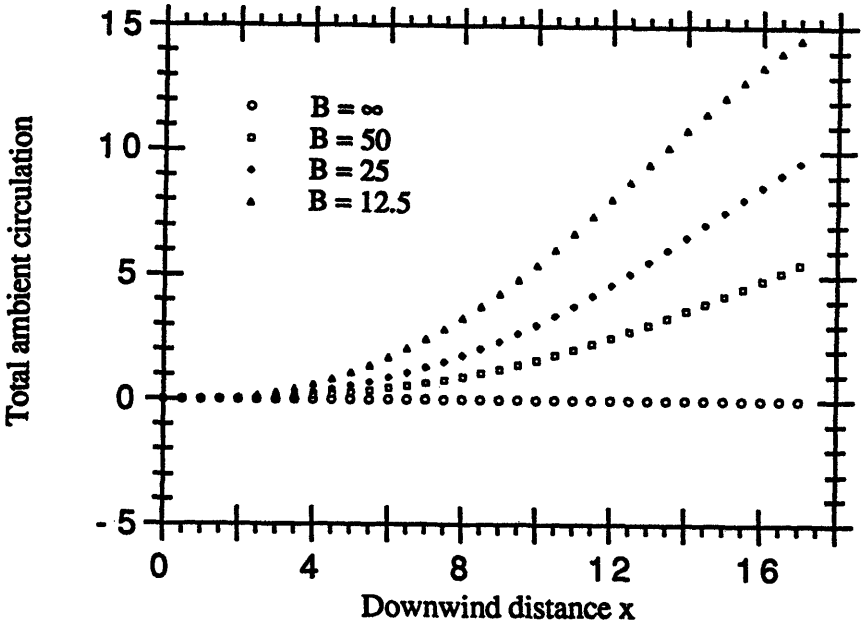

Figure 2.8. The total circulation generated in the background on the right half of the plume cross section as a function of the downwind distance.

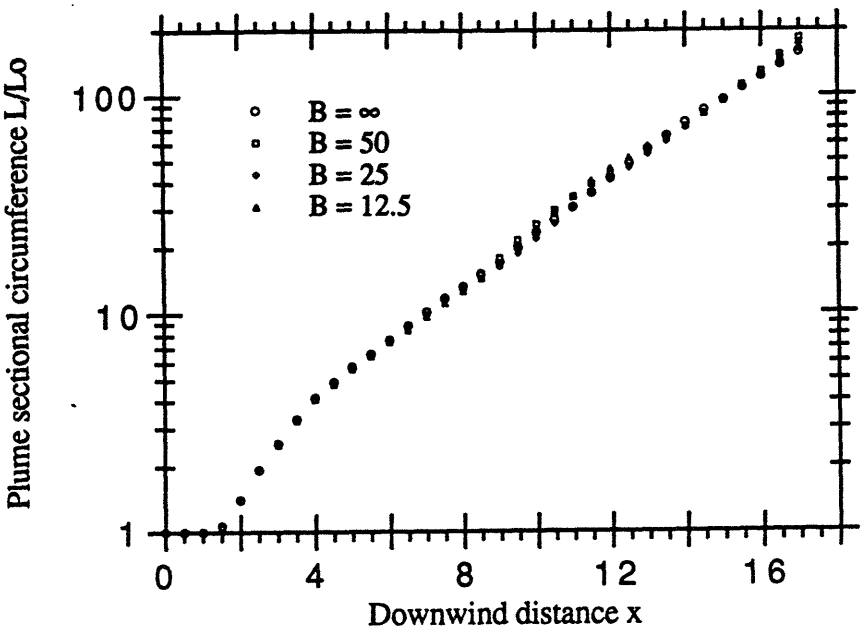

Figure 2.9. The length of the plume circumference along the downwind distance.

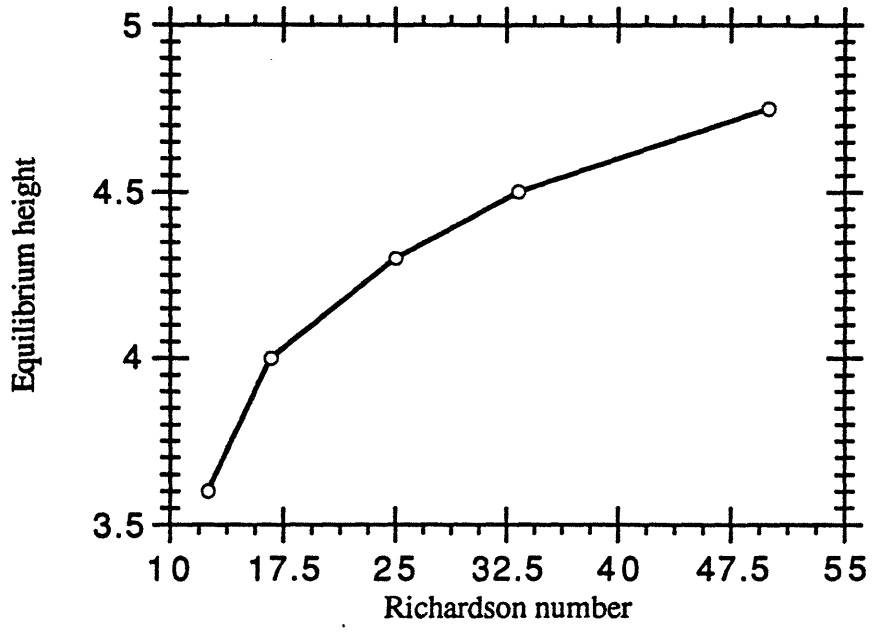

Figure 2.10. The terminal or equilibrium height of a buoyant plume rising in a linearly stratified atmosphere as a function of the buoyancy ratio.

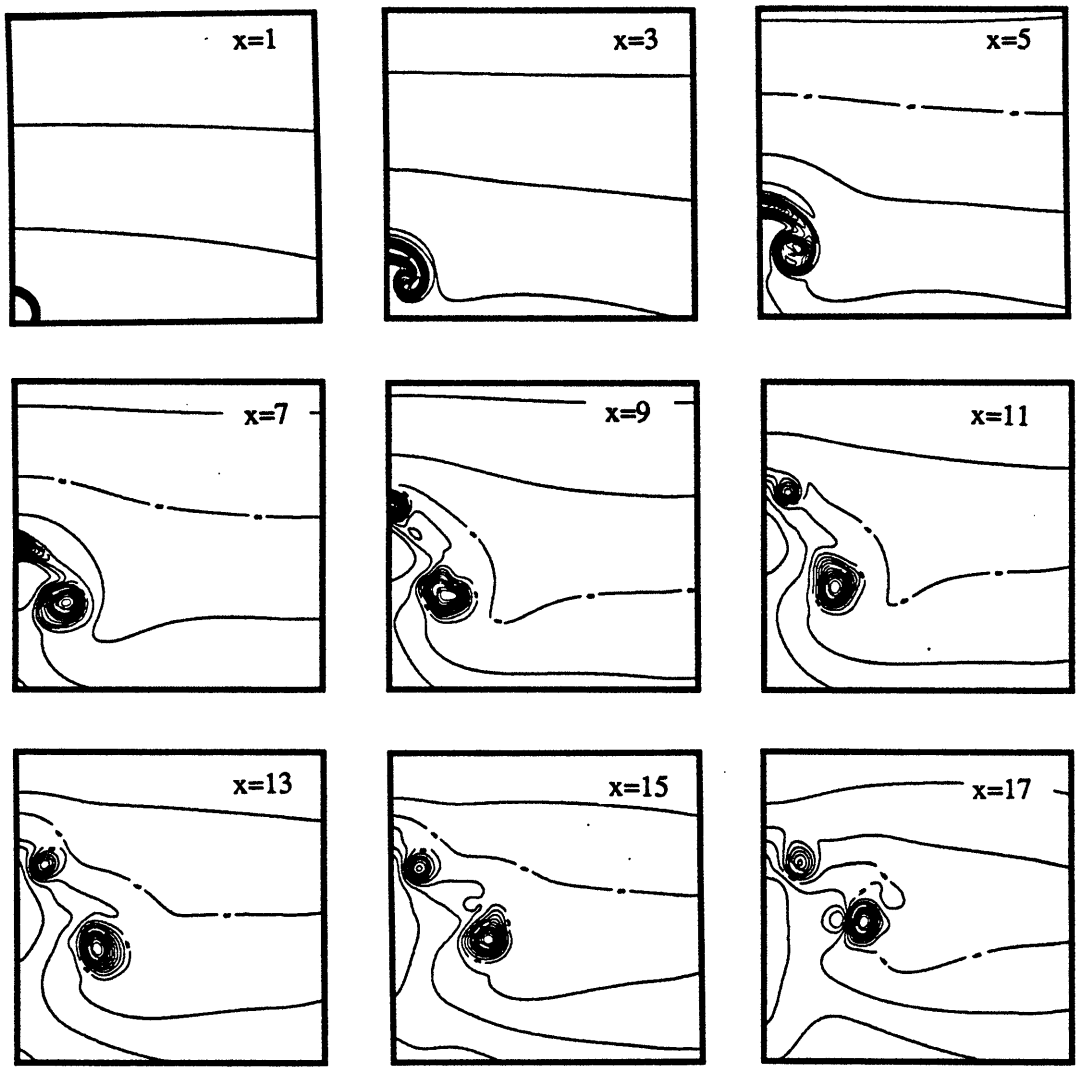

Figure 2.11. The evolution of the plume cross section, depicted in terms of the density contours, at different downwind locations for the case of $B=12.5$. All frames are from $y=0.0$ to $y=7.0$ and $z=23.0$ to $z=30.0$.

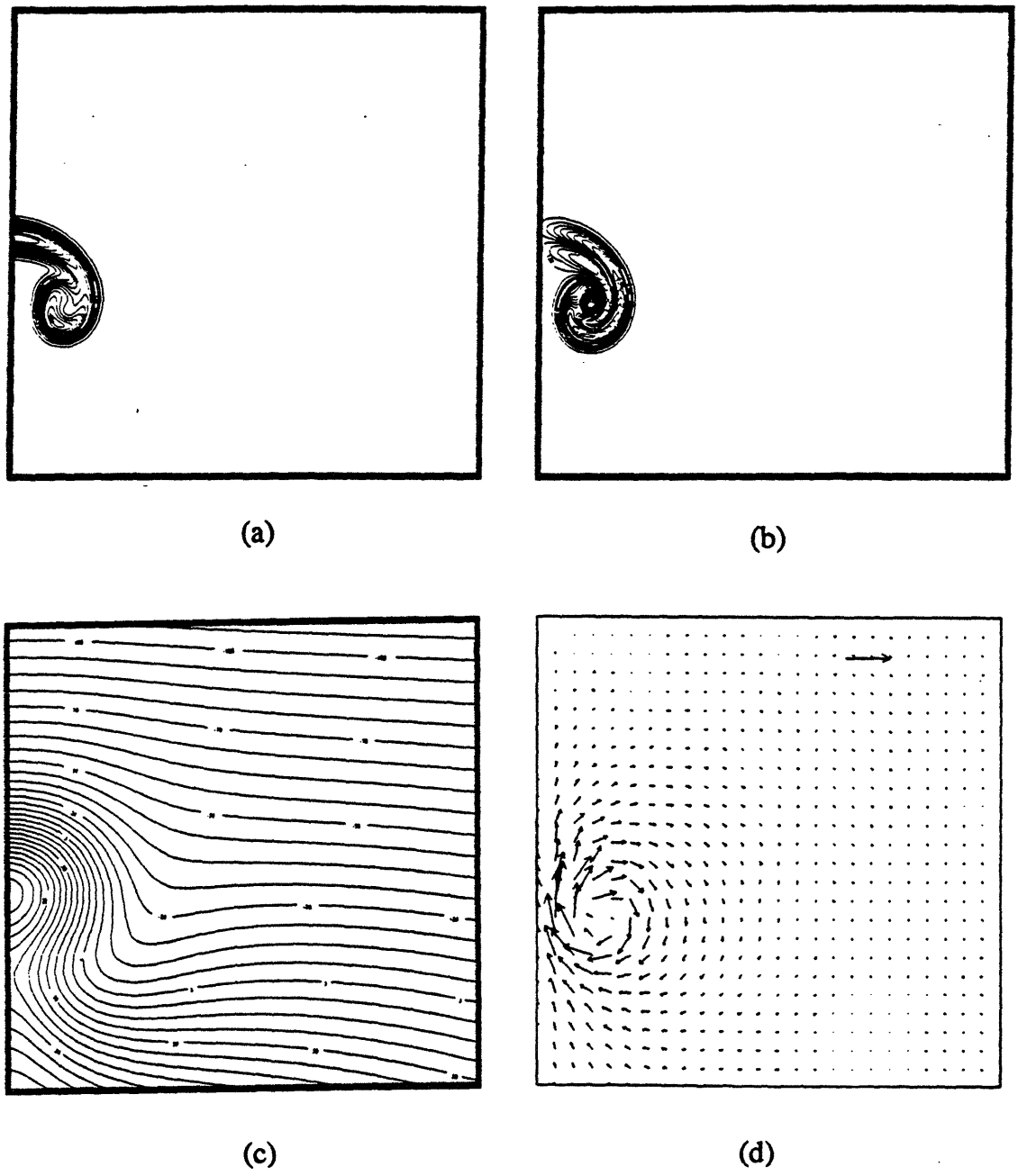

Figure 2.12. Contours of (a) the plume density, (b) vorticity, (c) the background density and (d) the velocity vectors in the plume cross section at $x = 4$ for a strongly stratified atmosphere, $B=12.5$. All frames are from $y=0.0$ to $y=6.0$ and $z=24$ to $z=30$.

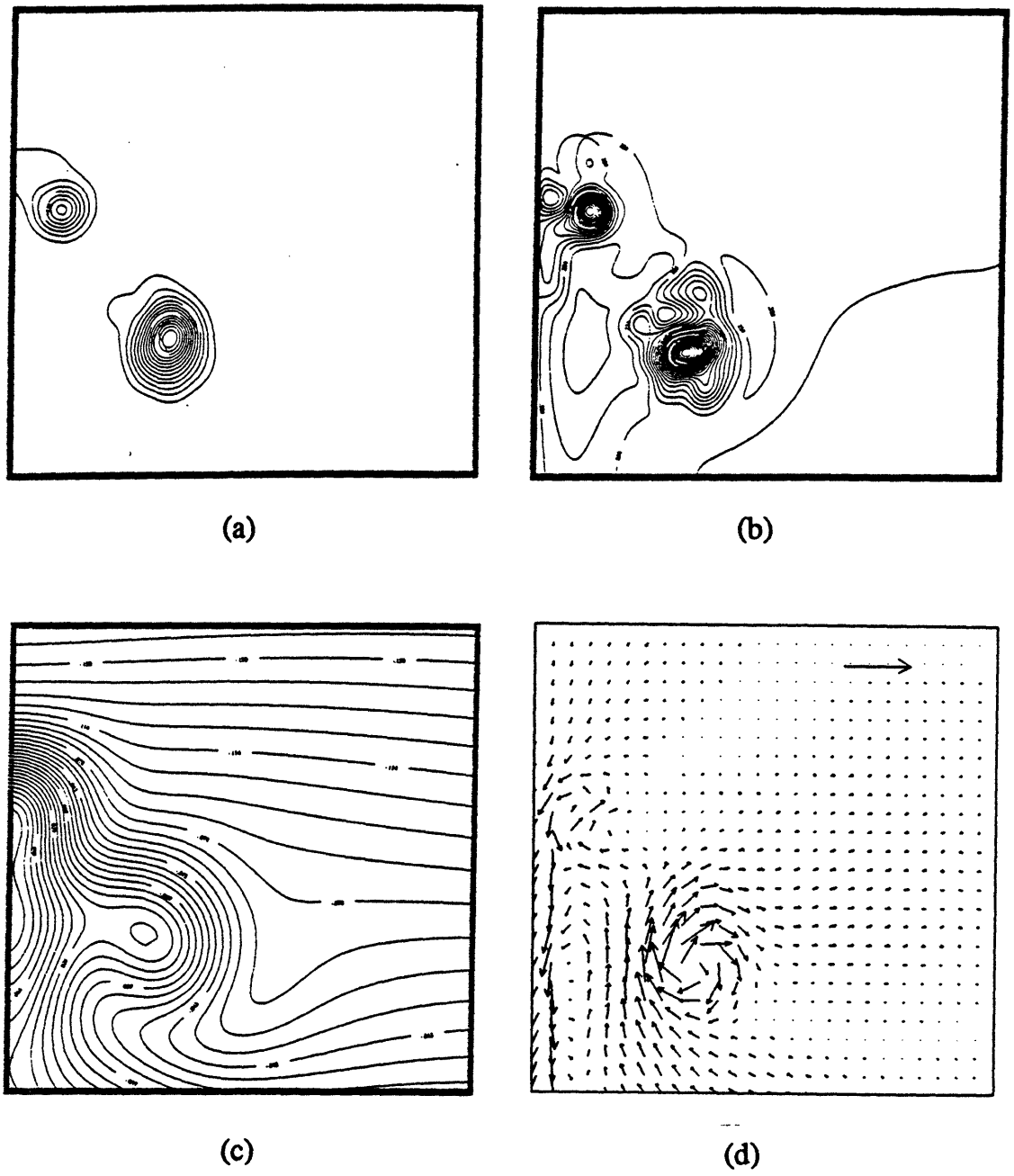

Figure 2.13. Contours of (a) the plume density, (b) vorticity, (c) the background density and (d) the velocity vectors in the plume cross section at $x = 14$ for a strongly stratified atmosphere, $B=12.5$. All frames are from $y=0.0$ to $y=6.0$ and $z=24$ to $z=30$.

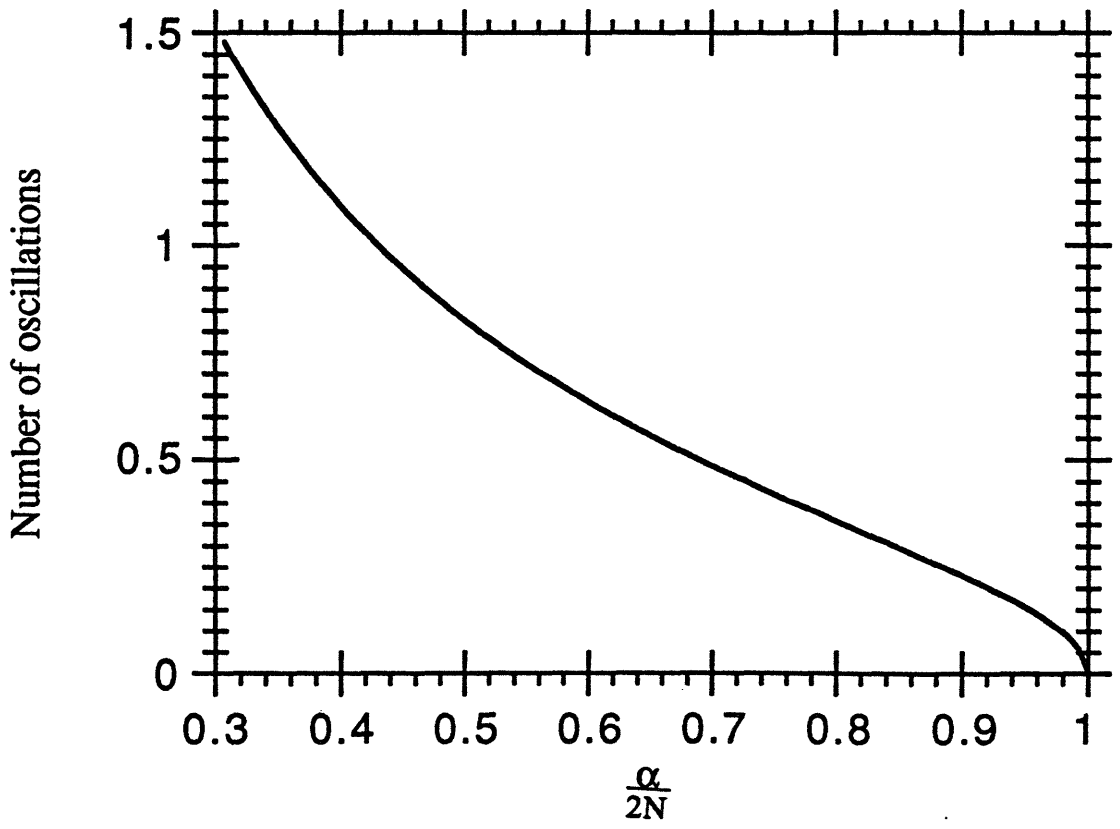

Figure 2.A1. Number of oscillations near the equilibrium height as a function of $\alpha/2N$.

CHAPTER 3

A COMPUTATIONAL MODEL FOR THE RISE AND DISPERSION OF WIND-BLOWN, BUOYANCY-DRIVEN PLUMES
PART III. PENETRATION OF ATMOSPHERIC INVERSION

ABSTRACT

The computational model of Zhang and Ghoniem (1993a,b) is applied to simulate the dispersion of a wind-blown, buoyancy-driven plume in a stratified atmosphere characterized by a sharp density drop across a thin horizontal inversion layer. Results show that the plume may completely penetrate, partially penetrate or get fully trapped below the inversion layer depending on the plume buoyancy, the height, strength, and thickness of the inversion layer. Plume penetration is favored by the lower height, weaker strength and larger thickness of the inversion layer. The presence of inversion accelerates the plume bifurcation into two diverging, downwind drifting material lumps, supported by the formation of two counter-rotating streamwise eddies, below the inversion. As a plume impinges on an inversion, internal gravity waves are generated along the layer absorbing some of the plume energy and reducing its penetration potential. Concomitant with the wave activities, re-entrainment plays an important role in determining the final equilibrium height and the generation of weak oscillations in the plume trajectory, ambient circulation and trapping fraction. The mechanism of baroclinic-vorticity generation is used to interpret various buoyancy-related phenomena in this problem. The plume trapping fraction, defined as the percentage of plume material held below the initial inversion height, is calculated under different conditions. Comparison with laboratory experiments shows that the predicted terminal trapping fraction agrees well with the measurements.

NOMENCLATURE

f	Plume trapping fraction;
g	Gravitational acceleration;
h_i	Vertical distance between initial plume center and inversion layer center;
H_T	Initial plume height above the ground;
P	Dimensionless plume buoyancy flux;
R	Square root of the initial plume cross sectional area;
Re_b	Buoyancy Reynolds number;
U	Homogeneous wind speed;
x	Horizontal wind direction;
y	Horizontal direction normal to the wind direction;
z	Vertical direction, plume rise;
β	Entrainment coefficient;
ρ_a	Air density;
ρ_o	Reference density, taken as the air density below the inversion layer;
ρ_p	Plume density with respect to the reference density;
ρ_s	Perturbation of air density with respect to the reference density;
Δh_i	Inversion thickness;
$\Delta \rho_i$	Inversion strength;
ε	$\equiv \left\lvert \frac{\rho_p}{\rho_o} \right\rvert$, plume mass flux ratio;

3.1. INTRODUCTION

An inversion layer refers to the situation where the atmosphere is nearly neutrally stratified except for a thin elevated layer across which the potential density (referred to as density hereafter) suddenly changes to a lower value. In the daytime, the top side of the convective mixing layer acts as an inversion layer whose height increases gradually with time. After sunset, close-to-the-ground inversion occurs as a result of the radiative heat loss from the earth's surface leading to the elevation of the interface between the cold and hot air to higher altitudes (Seinfeld, 1986).

The presence and properties of an inversion layer are critical to the dispersion of hot fumes. When a rising buoyant plume is able to penetrate an inversion layer, the stability of the layer prevents the plume from mixing downwards and the ground concentration of the fumes remains low. On the other hand, if the plume cannot penetrate the layer, upward dispersion is prevented, and the plume material is trapped beneath the inversion, leading to a high ground concentration of the fumes. It is customary to approximate an inversion by assuming that $d\rho_s/dz = 0$ everywhere except for a density drop at the height of the inversion, where z is the vertical coordinate pointing upwards, ρ_s is the deviation of air density from a reference density, ρ_o, taken as the air density below the inversion. The density drop across the inversion, $\Delta\rho_i$, at height, h_i, above the plume source, is a characteristic strength of the inversion. Most often, the thickness of the inversion layer is small compared to the plume size. A schematic diagram describing the notations is shown in figure 3.1.

Plume penetration models have been developed to evaluate the final trapping fraction; defined as the fraction of the plume material which remains below the initial height of the inversion layer. Some of these models are summarized in Table 3.1, where a dimensionless plume buoyancy flux, P, is used as a dependent variable. In terms of our notations, this dimensionless quantity can be defined as the ratio of the plume buoyancy

flux, $F_b = UgR_o^2|\rho_p/\rho_o|$, and the multiple of the uniform-wind speed, U, the dimensionless-inversion strength, $b_i = g|\Delta\rho_i/\rho_o|$, and the square of the inversion height, h_i:

$$P = \frac{F_b}{Ub_i h_i^2}, \tag{3.1}$$

where R_o is the initial radius of the plume crosswind section, ρ_p is the initial deficient density of the plume, and g is the gravitational acceleration. This quantity, similar to the buoyancy ratio defined in Zhang and Ghoniem (1993b), characterizes the relative importance of the plume rise potential and the impeding power of the stratification.

Richards (1963) was the first to perform a laboratory experiment to measure the penetration of inversion by a two-dimensional cylindrical thermal, recognizing the similarity between the latter and the cross section of a wind-blown, bent-over plume. He observed that the cross section of the thermal often changes from a circular into a kidney-shaped pattern and finally breaks up into a number of nearly unconnected lumps. Richards obtained an empirical formula for the terminal trapping fraction in terms of $\Delta\rho_i$, the cross-sectional area of the thermal at the inversion height, A_i, and the deficient mass per unit length in the axial direction, M_i. This formula, while instructive, is not easy to use in practice because the later two quantities are not known *a priori*.

Briggs (1975) noted that since the plume entrained some air below the inversion, it would remain more dense than the air above the inversion and must eventually settle back downwards, "sandwiching" itself somewhere within the inversion layer. He found that the plume penetration ability is very sensitive to the height of the inversion. Briggs developed a model based on buoyancy depletion of the plume as it crossed a zero thickness inversion layer, representing the plume cross section by a rectangular shape. The terminal trapping fraction was found to be a function of h_i/z_{eq}, where z_{eq} is the plume equilibrium height, calculated in terms of the dimensionless buoyancy flux as defined in equation (3.1) above.

Using results of a wind tunnel experiment, Manins (1979) proposed an analytical model based on a Gaussian distribution of the plume density. He showed that in a thin

inversion layer, the trapping fraction was approximately independent of the wind speed, and was only a function of the inversion elevation and the ratio of inversion strength to plume buoyancy. In his model, the initial overshoot of the plume beyond the inversion and its consequent re-entrainment downwards was included. The model results fit the laboratory measurements well. Similar to Richards' observation, the plume in Manin's experiment's broke up into a number of discrete lumps which grew and coalesced as they drifted downwind.

Weil (1988) extended the above models to include the effect of a finite-thickness inversion layer. He proposed two models. The first model assumed that the plume cross section is circular and introduced an entrainment coefficient $\beta \approx 0.4$. Recognizing that the plume cross section contains two concentrated cores of material rather than one single axisymmetric distribution, in his second model, Weil assumed that the plume cross section has a double Gaussian distribution. As listed in Table 3.1, models with zero and finite inversion thicknesses were developed. In these formulae, the parameter $a = 1.8$, is the separation between the two concentrated plume Gaussian cores, normalized by their radius.

The above models assume that the inversion layer was thin compared with the size of the plume cross section, $\Delta h_i/R \leq 1$. Models for thick inversion layers, $\Delta h_i/R \geq 1$, were also proposed. Briggs (1984) obtained a formula for the terminal trapping fraction after including the effect of a linearly stratified layer within the inversion, characterizing it by the Brunt-Väisälä frequency. In his model, the plume equilibrium height, z_{eq}, is calculated from a point-source buoyant plume rising in a linearly stratified atmosphere. Berkowicz et al. (1986) modified the calculation of z_{eq}, after considering the finite-size effect of the plume cross section.

Besides the models reviewed in Table 3.1, plume penetration of inversion layers was also studied in a number of other papers. Ero (1977) performed a theoretical analysis assuming Gaussian distribution of the plume velocity and temperature. He found that the

maximum plume rise was inversely proportional to the inversion strength. Robson (1983) solved the steady-state turbulent diffusion equation for a passive contaminant emitted from an elevated source, leaving out the buoyancy effect and parameterizing the inversion in terms of several turbulent eddy diffusion coefficients. Khandekar and Murty (1975) pointed out that plume bifurcation would be accelerated when the plume encountered an inversion layer. Willis and Deardorff (1987) studied the distribution of buoyant plume material as it rises in a convective planetary boundary layer capped by an inversion in a laboratory experiment. He found that the highest concentration was at the inversion height. However, the material distribution in the plume cross section was not reported, and the penetration process and the associated dynamics were not described. Dop (1992) formulated a Lagrangian buoyant plume dispersion model which included the effects of the turbulent characteristics and stratification. The model, however, contains a number of heuristic assumptions and involves several arbitrary constants which are hard to determine.

The rise and penetration of a buoyant plume through an inversion layer is strongly related to the plume dispersion pattern. In most available models, this pattern is assumed to be known irrespective of the interaction between the plume and the inversion, and the plume trajectory below the inversion is calculated as if the latter was not present. This, as will be shown in the next section, is inappropriate. In practice, many air quality models, such as CRSTER (Wilson, 1993) and UAM (Scheffe, 1993), use simple yet not fundamentally based penetration algorithms (Turner, 1985). All current models describe only the terminal plume trapping fraction, with no information regarding the partial penetration as a function of downwind distance. The problem of correctly modeling the plume partial penetration requires further investigation.

Since our computational plume model (Zhang & Ghoniem, 1993a,b) has shown considerable success in describing plume rise and dispersion in neutrally and linearly stratified atmosphere, we apply it here to simulate plume penetration through an elevated

inversion. In Section 3.2, we review the mechanism of baroclinic-vorticity generation; the basis for understanding buoyant flow phenomena and an essential component in the construction of our computational model. In Section 3.3, we use the computational results to examine the plume dispersion pattern under various inversion conditions, and compute the associated evolution of the trapping fraction as a function of downwind distance. Comparison with available laboratory measurements is performed. Section 3.4 is a short summary.

3.2. BAROCLINIC VORTICITY GENERATION AND NUMERICAL IMPLEMENTATION

As a buoyant plume rises, through the baroclinic-vorticity-generation mechanism, a double vortex structure is generated in the plume cross section (see Zhang and Ghoniem (1993a,b) same as Chapter 1 and Chapter 2, respectively). Simultaneously, the originally flat isolines of air density, which define the inversion layer, are distorted and pushed upwards by the action of this double vortex structure. The distortion of the inversion layer leads to the formation of a zone where the horizontal component of density gradient is non-zero. Thus, baroclinic vorticity, proportional to the density change across the inversion layer, is generated. The so-created background vorticity induces motion (or equivalently creates a drag) which slows down the upward plume motion, as shown schematically in figure 3.2. Simultaneously, this vorticity field modifies the entrainment process, as will be seen in more detail in Section 3.3. Kinematically, the plume penetration through the inversion layer is governed by the competing action of the vorticity field in the plume cross section and the inversion layer. Clearly, inversion affects the plume rise and dispersion even before the plume reaches the inversion height through the induced motion by the background vorticity field.

Since the background vorticity is generated only within the inversion layer, the implementation of this form of stratification in the numerical code is rather straightforward. We discretize both of the plume-air boundary and the inversion layer into a finite number of transport elements. The numerical calculation proceeds by updating the position and circulation of these elements at every time step. The velocity and density fields are obtained by summing over the fields of all transport elements through the desingularized Biot-Savart law.

The detailed description of the transport element method, treatment of boundary conditions, and the discretization parameters can be found in Chapters 1 and 2. In this Chapter, although it is not necessary, we use the Boussinesq approximation, which has

been shown to be accurate when the density perturbation relative to the reference density is less than 0.1. In all cases, the plume material is initially uniformly distributed within a circular cross section, perpendicular to the wind direction, with dimensionless radius $1/\sqrt{\pi}$. The buoyancy Reynolds number, characterizing the ratio between the buoyancy generated momentum and the small-scale turbulent diffusion is $Re_b = 250$. The initial plume height above the ground is $H_T/R = 10$ so that the ground effect is negligible. Dimensionless marching step and spatial discretization length are both 0.025. We used two computational layers to characterize the plume-air interface and two to six layers, depending on its thickness, to describe the inversion layer. The horizontal extent of the computational domain is ten folds the circumference of the initial plume cross section. These parameters are so chosen to achieve a reasonable compromise between numerical accuracy and computational efficiency. Reducing the discretization parameters or expanding the calculation domain did not have noticeable effect on the computational results.

3.3. COMPUTATIONAL RESULTS

The following three independent dimensionless parameters affect the interaction between the plume and inversion layer: (1) the distance between the initial plume height and the inversion height, h_i/R; (2) the density drop across the inversion layer, characterizing its strength, $|\Delta\rho_i/\varepsilon\rho_o| = \Delta\rho_i/\rho_p$, and (3) the inversion layer thickness, $\Delta h_i/R$. In this work, we use the same normalization procedure as adopted in Chapter 1. A typical inversion has strength $|\Delta\rho_i/\rho_o| \approx 2x\ 10^{-3}$, height $h_i = 50m$ and thickness $\Delta h_i = 1\sim 10m$. Considering a large buoyant plume with cross sectional length scale $R \sim 10m$ and deficient plume density $|\rho_p/\rho_o| \approx 10^{-2}$, these three parameters are $h_i/R = 5$, $\Delta\rho_i/\rho_p \sim 0.2$ and $\Delta h_i/R = 0.1 \sim 1.0$, respectively.

In this section, we first present the computational results in terms of the evolution of the plume cross section for three cases where full penetration, partial penetration and full trapping are observed. The flow structure for the case of partial penetration, in terms of the distributions of air density and plume density, and velocity field is also presented. Next, we show a parametric study on the effect of the parameters characterizing inversion on the plume trajectory and trapping fraction. Finally, we compare the computed terminal trapping fraction with experimental measurements.

3.3.1. Cross-wind Sections

Figure 3.3 shows the cross-wind plume sections at four consecutive downwind distances from their sources for three cases. The inversion layer is assumed to be thin, $\Delta h_i/R = 0.1$, with height and strength as follows: (a) $h_i/R = 5$, $\Delta\rho_i/\rho_p = 0.25$; (b) $h_i/R = 2$, $\Delta\rho_i/\rho_p = 0.25$; and (c) $h_i/R = 4$, $\Delta\rho_i/\rho_p = 0.1$. The contours represent the dimensionless density. One half of the crosswind section is shown since the plume is symmetric with respect to the centerline, $y = 0$. In all cases, the plumes, which start out with a circular cross section, acquire a kidney-shaped structure and bifurcate into two or more distinct material lumps, as observed in the simulations in neutrally and linearly

stratified atmosphere (Chapter 1 and Chapter 2), and in Richards' (1963) and Manins' (1979) laboratory experiments.

Case (a) corresponds to a plume initially far below a strong inversion layer. Following a brief rise in the neutrally stratified background and the gradual formation of two structures on its sides, the plume collides with the inversion layer and each structure slides away from the centerplane along the bottom of the layer. This resembles the case of a dense plume impinging on a flat ground (Ghoniem et al, 1993). The plume breaks up into two lumps, expands horizontally and is almost fully trapped below the inversion. The central part of the inversion layer is pushed upwards initially by the rising buoyant plume and then settles back downwards.

Case (b) corresponds to a plume impinging upon a strong inversion layer which is close to the plume emission source. The plume pushes up and partially mixes with the inversion. A significant part of the plume penetrates through, while a small fraction remains within the inversion layer. We consider this case as almost full penetration. On the other hand, case (c) corresponds to a plume encountering an inversion with moderate strength at a moderate height. In this case, the plume pushes the middle part of the inversion layer upwards from its original height while mixing with it. As described by Briggs (1975), most of the plume material is "sandwiched" inside the inversion layer. Therefore, the plume is considered as partially penetrated.

These results show that, at the inversion height, the plume expands horizontally below strong and high inversion, mixes with and disperses within an inversion with moderate strength and height, and penetrates through a low or weak inversion although some plume material still remains attached to the inversion. Thus, in most cases, the highest concentration occurs at the inversion height, confirming the laboratory observation of Willis and Deardorff (1987).

To analyze the flow pattern and the plume material distribution in more detail, we plot the perturbed air density contours, deficient plume density contours (representing the

material concentration) and the velocity field for case (c) in figure 3.4. The air density isolines show the initial upward lift of a portion of the inversion immediately above the plume. Along the inversion layer, and similar to what was observed in the case of a plume rising in a linearly stratified atmosphere (see Chapter 2), gravity waves are generated. Concomitantly, the plume breaks up into two lumps which separate horizontally along this layer. These two lumps are associated with two counter-rotating large structures as depicted in figure 3.4c.

The velocity distribution confirms the formation of a strong vortex dipole as the baroclinic vorticity builds up within the plume cross section. After the inversion layer is distorted, a positive eddy is generated on the depicted side of the cross section due to the mechanism described in Section 3.2. Since the driving force of the flow is buoyancy, the kinetic energy associated with the vortex dipole is converted from the initial potential energy of the plume. The interaction between the plume and the inversion layer leads to the gradual transformation of its kinetic energy into vorticity in the surrounding atmosphere. This can be seen by the drop in strength of the negative eddy within the plume cross section and the increase in strength of the eddy forming on the inversion layer in the last frame of figure 3.4c. Thus, the plume loses its energy to the inversion through the gravity waves.

In general, the inversion layer is distorted from its original flat-layer-like configuration. The complex structure of the inversion layer makes it difficult to assign a precise definition to plume penetration. A working definition of a plume trapping fraction, f, as the percentage of the plume material which remains below the center of the initial inversion height, is used here, see figure 3.5. In the following, we investigate the dependence of f and other integral quantities characterizing the plume dispersion on the governing parameters.

3.3.2. Effect of Initial Inversion Height

When h_i/R is large, the rising plume is expected to lose its penetration potential due to greater dilution of its buoyancy via entrainment before it reaches the inversion layer. As the plume interacts with the inversion, a turbulent flow is generated due to the action of the baroclinic vorticity within the plume and in the background[12]. The onset of a turbulent flow results in the growth of fluctuations in the plume trapping factor and other integral quantities. Figure 3.6 shows the evolution of the trapping fraction in the downwind direction for the case of $h_i/R = 3.5$, $\Delta\rho_i/\rho_p = 0.25$, and $\Delta h_i/R = 0.1$. Three thin lines represent results of runs with slightly different initial conditions, implemented by weakly perturbing the initial plume shape. The heavy line is obtained by averaging these three runs. It can be seen that the trapping fraction is independent of the weak perturbation prior to $x = 30$, when the plume is gradually penetrating through the initial inversion height. Beyond this point, the interaction of the plume and the inversion layer becomes more complex and the turbulent fluctuation increases due to the generation of small-scale vorticity at the plume surface and the inversion. In the following presentation of the computational results, we take, in each case, the average of at least three computational runs.

Figure 3.7 depicts the evolution of f in the downwind direction for plumes with $\Delta\rho_i/\rho_p = 0.25$ and $\Delta h_i/R = 0.1$, and six different initial inversion heights. As expected, the higher the inversion, the more difficult for the plume to penetrate through, and hence the larger the trapping fraction. For a plume which starts close to the inversion layer, $h_i/R = 2$, the trapping fraction quickly decreases to zero, signifying full penetration. A considerable fraction of the plume material for the cases with $h_i/R = 2.5$ and 3.0 first penetrates through the inversion and then bounces back. This phenomenon, recorded by Manins (1979) in his laboratory experiment, is due to re-entrainment. As shown in figure 3.3, beyond this stage, an oscillatory motion commences. Following the early overshoot,

---

[12] In plume studies, this buoyancy-generated turbulence is commonly neglected or confused with the atmospheric turbulence. Much efforts have been focused on the characterization of the later, while its effect becomes significant to the plume motion only after the former weakens.

the plume falls back due to the restoring action of the inversion, and internal gravity waves are generated. A similar phenomenon; the oscillatory motion near the equilibrium height in a linearly stratified atmosphere, was discussed and modeled analytically in Chapter 2. It is due to these oscillations that the plume takes longer to reach equilibrium. Part of the plume material mixes with the inversion and moves up and down as the gravity waves propagate away. (We note here that doubling the horizontal extent of the computational domain did not affect the result in any significant way. This assured us that our choice of the horizontal extent of the domain was long enough to take the effect of the wave into account accurately[13]). The case of $h_i/R = 3.5$ also shows partial penetration. The curves for $h_i/R = 4.0$ and 4.5 depict complete trapping by $x = 18$.

To characterize the dispersion pattern in more detail, we investigate the evolution of various integral quantities in the crosswind section. Since atmospheric stratification only occurs at the inversion, the background circulation is generated only within this layer. Figure 3.8 shows the total background circulation integrated over the right half of the inversion layer (as depicted in figure 3.3) versus downwind distance, for various inversion heights. The circulation is always positive, having the tendency to push the plume downwards. The circulation increases faster in the case of low inversion because the lower inversion is lifted upwards earlier. As can be seen from figure 3.4, part of the inversion layer which has been pushed upwards sinks back downwards, leading to the generation of negative baroclinic vorticity. This is the reason why the total ambient circulation in figure 3.8 settles to an oscillatory pattern, consistent with the discussion on the generation of internal gravity waves.

The vorticity generated at the plume surface is presented in figure 3.9 in terms of the total circulation integrated over half of the plume circumference. The magnitude of this circulation increases exponentially, saturating at a value which is almost the same for all cases except for case $h_i/R = 2.0$. The reason for this behavior was discussed in

[13] Internal waves in wind-tunnel plume experiments should be eliminated through some absorbing device. Otherwise, the reflected wave may rejoin the penetration area and affect the plume dispersion unnaturally.

Chapters 1 and 2. In the case of low inversion, the plume circulation is relatively large, apparently due to the strong influence of the inversion on the plume.

Figure 3.10 shows the plume horizontal width, defined as twice of the distance between the plume centerline and the center of mass of either sides of the plume[14]. Since most of the plume material is associated with two large lumps, this width characterizes the plume spread. In the case of low inversion, the plume width reaches a constant value which increases with the inversion height. The reason behind this is explained schematically in figure 3.2, where the effect of background circulation on the motion of the two large plume lumps is shown. For lower and weak inversion, the plume penetrates completely and stabilizes above the inversion. The positive background circulation induces a motion that limits the expansion of the plume width. For high inversion with strong strength, the plume remains below the inversion; and the background circulation tends to speed up the width expansion. Thus, the presence of an inversion layer favors the bifurcation of the plume below it, as pointed out by Khandekar and Murty (1975).

3.3.3. Effect of Inversion Strength

The effect of inversion strength is investigated by fixing the inversion height and thickness, $h_i/R = 4$ and $\Delta h_i/R = 0.1$, respectively, and varying the density drop across the layer. The trapping fraction history, figure 3.11, shows the expected consequences: the stronger the inversion strength, the more difficult for the plume to penetrate and the higher the trapping fraction. Under inversion with $\Delta\rho_i/\rho_p = 0.25$, the plume is almost fully blocked. For inversions with moderate strength, $\Delta\rho_i/\rho_p = 0.125$ and 0.100, the plume partially penetrates and exhibits the oscillatory behavior which has been described before. For weak inversions, $\Delta\rho_i/\rho_p < 0.075$, the plume can easily penetrate the layer.

The effect of inversion strength on the plume penetration can also be seen from the trajectory, defined as the rise of the plume center-of-mass above its original source, as

---

[14] Similar to Manins'(1979) experimental observations, the randomness of the turbulent plume motion results in some fluctuations in its measured width.

exhibited in figure 3.12. Since the five cases have the same inversion height, we expect that the stronger the inversion, the more effective the suppression of the vertical motion, and the smaller the plume rise. Under strong inversion, the plume stops rising as soon as it collides with the inversion. For inversion with moderate strength, the plume mixes with the inversion and oscillates in the downwind direction as the waves propagate along the inversion. Otherwise, the plume keeps rising.

3.3.4. Effect of Inversion Thickness

The last parameter of interest is the inversion-layer thickness across which the air density decreases linearly. We do not discuss the situation where $\Delta h_i/R >> 1$, since it has been covered in Chapter 2. Rather, we focus on situations of inversion thickness, $0 < \Delta h_i/R < 2$.

The plume trajectory for $\Delta h_i/R = 0.1, 0.7, 1.0$ and 2.0, with fixed strength and height, $\Delta\rho_i/\rho_p = 0.25$, $h_i/R = 4$, respectively, are displayed in figure 3.13. For a thick layer, the stratification is weak, the plume penetrates the inversion and continues to rise. For a thin-inversion layer, the plume is prevented from rising beyond the inversion height, apart from some minor oscillations. Figure 3.14 shows the evolution of the trapping fraction. In the cases of moderate thickness, the plumes are imbedded within the inversion and partial penetration occurs.

The above discussion indicates that the trapping fraction depends on the inversion thickness, especially beyond the distance where the plume reaches the bottom side of the inversion. This fact should be recognized in the development of future plume models. Although Weil (1988) extended the thin inversion model to include the effect of the finite inversion thickness, this effect has not been well studied in laboratory and field experiments.

3.3.5. Comparison with Experimental Measurements and Analytical Models

For a thin inversion layer, several models (Briggs, 1975, Manins, 1979) have suggested that the effect of the inversion height and strength on the terminal trapping fraction can be grouped into one parameter, the dimensionless plume buoyancy flux:

$$P = 1/\left(\pi\left|\frac{\Delta\rho_i}{\epsilon\rho_o}\right|\left(\frac{h_i}{R}\right)^2\right) = \frac{1}{\pi}\left|\frac{\rho_p}{\Delta\rho_i}\right|\left(\frac{R}{h_i}\right)^2, \qquad (3.2)$$

representing the ratio of plume buoyancy over inversion strength and the square of the inversion height.

In figure 3.15, we superimpose our results, presented in detail in Sections 3.2 and 3.3, over the experimental measurements by Richards (1963) and Manins (1979), and the prediction of the analytical models of Briggs (1975) and Manins (1979). The figure, except for our numerical results, is adapted from Weil (1988). The nine points representing the estimated terminal trapping fractions, ranging from $P = 0.051$ to 0.4, are well within the experimental results. The figure shows that Briggs' model (1975) underestimated the terminal trapping fraction, while that of Manins' bounds the data from above. The scattering of the laboratory results and the numerical results may be due to several reasons: (1) The later stages of plume motion is in the turbulent regime, and considerable fluctuation in the estimation of the terminal trapping fraction is unavoidable. (2) The results of laboratory experiments may be contaminated by the effects of the side walls of the wind tunnel. (3) As pointed by Briggs (1984) and Weil (1988), Manins' (1979) experimental technique and theory may have overestimated f because they relied on concentration measurement along the plume centerline only. In fact, according to our calculations and Richards' measurements (1963), the highest concentration of the plume material is associated with the bifurcated lumps, and not necessarily on the centerline. (4) The inversion thickness in Richards' experiment was not reported. (5) Few of our numerical results had not reached full equilibrium due to the oscillatory behavior in the later stages. (6) The effect of the finite initial plume size is neglected in the formulation

of P. (7) Our calculation and Richards' experiment have neglected the initial momentum of the plume.

3.4. DISCUSSION

The computational model of Zhang and Ghoniem (1993a,b) has been applied to the case of a wind-blown, buoyancy-driven plume rising in a sharply stratified atmosphere where the air density experiences a drop across a thin horizontal inversion layer. The model, based on the transport element method, has shown considerable success in predicting the plume trajectory and dispersion pattern in the cases of neutrally and linearly stratified atmosphere.

Our results show that the plume may completely penetrate, partially penetrate or get completely trapped below the inversion layer, depending on the buoyancy of the plume, the height, strength, and thickness of the inversion layer. It was found that the plume penetration is favored by lower height, weak strength and large thickness of the inversion layer. Comparison with existing laboratory experiments shows that the predicted terminal trapping fractions are consistent with the measurements. The baroclinic-vorticity-generation mechanism is found to be useful in explaining various buoyancy related phenomena encountered in this problem.

As the plume collides against an inversion, internal gravity waves are generated along the layer, radiating the energy of the plume and reducing its penetration power. Associated with the wave activity, re-entrainment is found to be important in determining the final equilibrium condition of the plume. Similar to the cases of neutrally and linearly stratified atmosphere, as the plume rises, a kidney-shaped pattern associated with the formation of two counter-rotating vortices, is established. Beyond the early stages, the plume bifurcates. The presence of the inversion leads to an earlier bifurcation below the inversion. The history of the plume trapping fraction, rise trajectory and the evolution of the background circulation exhibit oscillatory behavior. Our results show that accurate analytical models for the evolution of trapping fraction should take the effects of the inversion thickness, the generation of internal wave, and the bifurcation of the plume pattern into consideration.

REFERENCES

Berkowicz, R., Olesen, H. R., and Torp, U. (1986) The Danish Gaussian air pollution model (OML): Description, test and sensitivity analysis in view of regulatory applications. *Air Pollution Modeling and Its Application* V, C. De Wispelaere, F. A. Schiermeier, and N. V. Gillani, Eds., Plenum, New York, 453-481.

Briggs, G. A.(1975) Plume rise predictions. *Lectures on Air Pollution and Environmental Impact Analysis*, D. A. Haugen, Ed., Amer. Meteor. Soc., Boston, 59-111.

Briggs, G. A.(1984) Plume rise and buoyancy effects. *Atmospheric Science and Power Production*, D. Randerson, Ed., U.S. Dept. of Energy DOE/TIC-27601, available from NTIS as DE84005177, 327-366.

Dop, Han Van (1992) Buoyant plume rise in a Lagrangian framework, *Atmos. Environ.* **26A**. No.7, 1335-1346.

Ero, M. I. O. (1977) Buoyant plume rise in atmospheric inversions, *Int. J. Heat Mass Transfer*, **20**, 403-407.

Ghoniem, A. F., Zhang, X., Knio, O. M., Baum, H. R and Rehm, R. G (1993) Dispersion and deposition of smoke plumes generated from massive fires, *J. of Haz. Mat.*, **33**, 275-293.

Khandekar, M. L. and Murty, T. S. (1975) A note on bifurcation of buoyant bent-over chimney plumes, *Atmos. Environ.*, **9**, 759-762.

Manins, P. C. (1979) Partial penetration of an elevated inversion layer by chimney plumes. *Atmos. Environ.*, **13**, 733-741.

Richards, J. M. (1963) The penetration of interfaces by cylindrical thermals, *Quart. J. Roy. Meteor. Soc.*, **89**, 254-264.

Robson, R. E. (1983) On the theory of plume trapping by an elevated inversion, *Atmos. Environ.* **17**, No.10, 1923-1930.

Scheffe, R. D. (1993) A review of the development and application of the urban airshed model, *Atmos. Environ.* **27B**, No. 1, 23-39.

Seinfeld, J. H. (1986) *Atmospheric Chemistry and Physics of Air Pollution*, John Wiley & Sons, xxiii+738 p.

Turner, D. B. (1985) Proposed pragmatic methods for estimating plume rise and plume penetration through atmospheric layers, *Atmos. Environ.* **19**, No. 7, 1215-1218.

Weil, J. C. (1988) Plume rise, *Lectures on air pollution modeling*, Editors, Venkatram A. and Wyngaard J. C., 119-166.

Willis, G. E. and Deardorff J. W. (1987) Buoyant plume dispersion and inversion entrapment in and above a laboratory mixed layer, *Atmos. Environ.* **21**, No. 8, 1725-1735.

Wilson, R. B. (1993) Review of development and application of CRSTER and MPTER models, *Atmos. Environ.* **27B**, No. 1, 41-57.

Zhang, X. and Ghoniem, A. F. (1993a) A computational model for the rise and dispersion of wind-blown, buoyancy driven plumes, Part I, Neutrally stratified case. *Atmos. Environ.* (In press)

Zhang, X. and Ghoniem, A. F. (1993b) A computational model for the rise and dispersion of wind-blown, buoyancy driven plumes, Part II, Linearly stratified case. *Atmos. Environ.* (Submitted for publication.)

Models	Terminal Trapping Fraction	Parameter	Notes
Richards (1963)	$f = 1 - (0.93\,S + 1)\exp(-0.93\,S),\ 0 \le S \le 7.5$ $f = 1,\ S > 7.5$	$S = \frac{\Delta\rho_i A_i}{M_i}$	Experiment correlation
Briggs (1975)	$f = \begin{cases} 1, & z_{eq}/h_i < 2/3 \\ h_i/z_{eq} - 0.5, & 2/3 < z_{eq}/h_i < 2 \\ 0, & z_{eq}/h_i > 2 \end{cases}$	$z_{eq} = \frac{2}{3}(1 + 9\pi P)^{1/2}$	Zero thickness Buoyancy depletion
Manins (1979)	$f = \begin{cases} 1, & P < 0.08 \\ 0.08/P - (P - 0.08), & P > 0.08 \end{cases}$	$P = \frac{F_b}{U b_i h_i^2}$	Zero thickness Gaussian distribution
Weil (1988)	$f = 1 - \frac{1}{\pi}\left[\cos^{-1}\lambda - \lambda(1-\lambda)^{1/2}\right]$	$\lambda = \frac{h_i + \Delta h_i - z_{eq}}{\beta z_{eq}}$	Circular cross section Finite thickness
Weil (1988)	$f = \frac{1}{1 + a^2}\frac{\beta^2}{P}$	Double Gaussian Cores $\beta = 0.4$ $a = 1.8$	Zero thickness
	$f = \frac{1 + \delta^2}{1 + a^2}\frac{\beta^2}{P}$	$\delta = \frac{\Delta h_i}{h_i}$	Finite thickness
Briggs (1984)	Large thickness	$z_{eq} = 2.6\left[\frac{F_b}{U N_i^2}\right]^{1/3}$	$N_i^2 = -\frac{g}{\rho_o}\frac{d\rho_i}{dz}$
Berkowicz et al (1986)	$f = \begin{cases} 1, & z_{eq}/h_i < 2/3 \\ h_i/z_{eq} - 0.5, & 2/3 < z_{eq}/h_i < 2 \\ 0, & z_{eq}/h_i > 2 \end{cases}$	$\frac{z_{eq}}{h_i} = \left[2.6^3 P_s + \left(\frac{2}{3}\right)^3\right]^{1/3}$	$P_s = \frac{F_b}{U N_i^2 h_i^3}$

Table 3.1. Analytical models for the terminal trapping fraction as a function of the plume and inversion layer parameters.

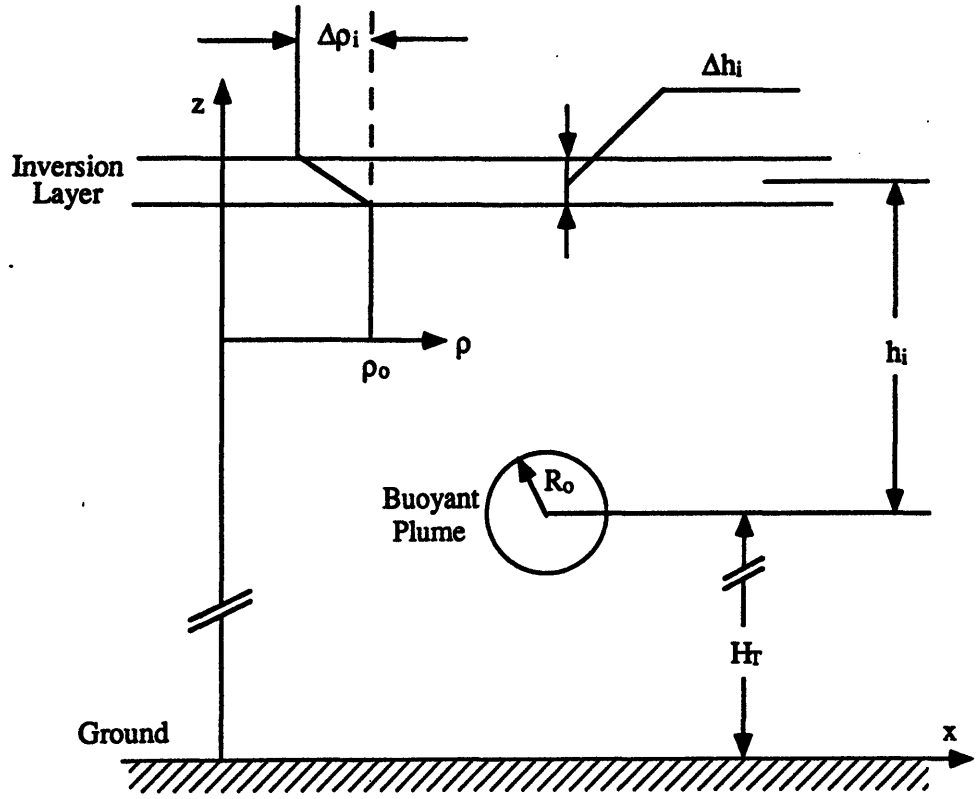

Figure 3.1. A schematic diagram showing the definitions of the parameters used to characterize the plume and the inversion layer.

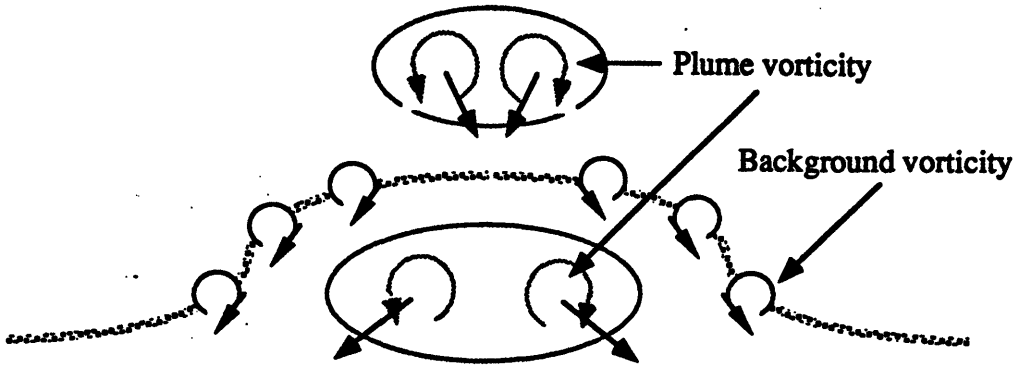

Figure 3.2. Schematic diagram showing the effect of a disturbed inversion layer on plume dispersion through the extra generated vorticity.

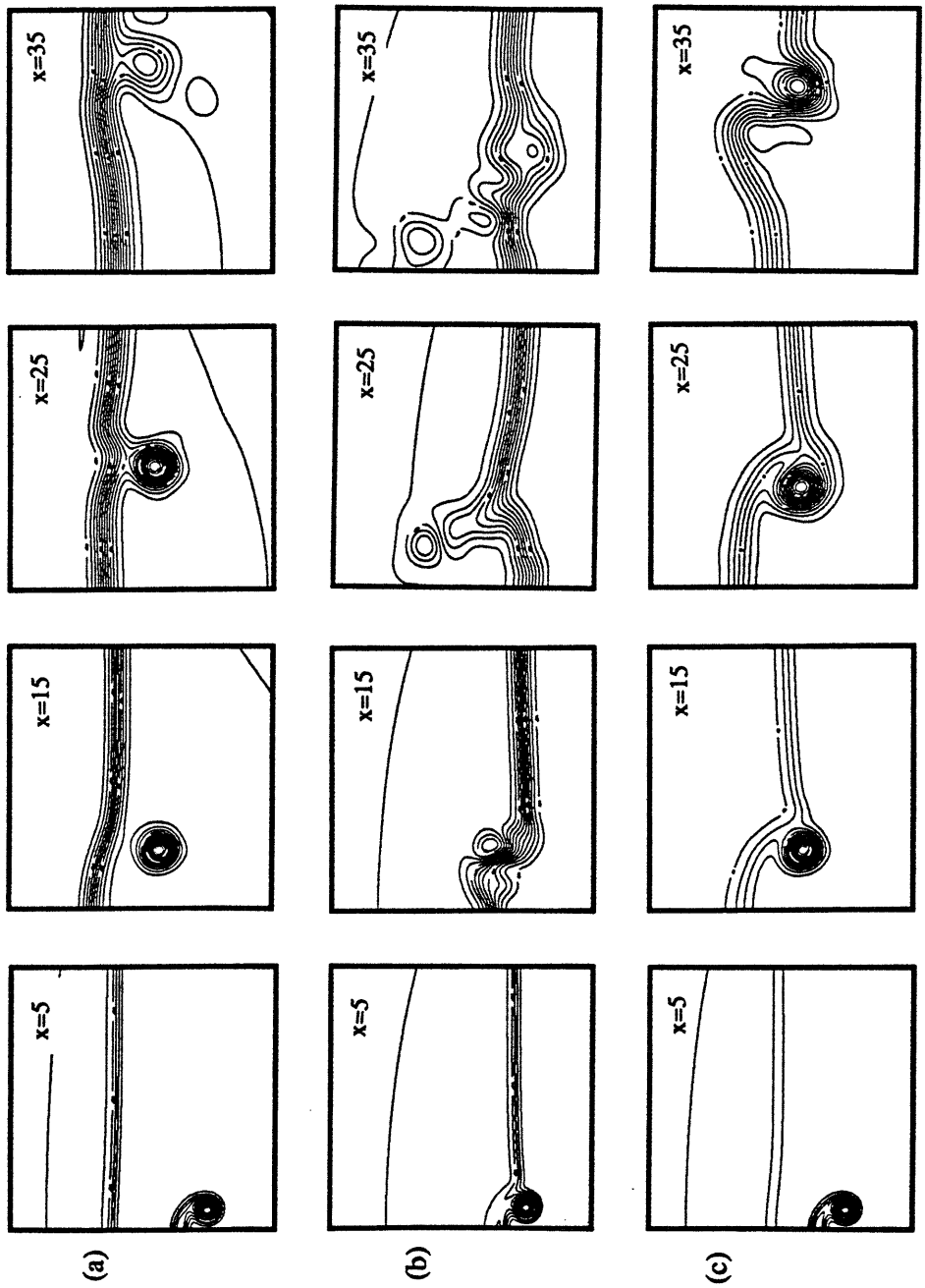

Figure 3.3. The density contours within the plume cross section at consecutive downwind distances for $\Delta h_i/R = 0.1$, with: (a) high, strong inversion, $h_i/R = 5$, $\Delta\rho_i/\rho_p = 0.25$, (b) low, strong inversion, $h_i/R = 2$, $\Delta\rho_i/\rho_p = 0.25$; and (c) moderate height and strength inversion, $h_i/R = 4$, $\Delta\rho_i/\rho_p = 0.1$. All frames are for $0.0 \le y \le 10.0$ and $9.0 \le z \le 19.0$.

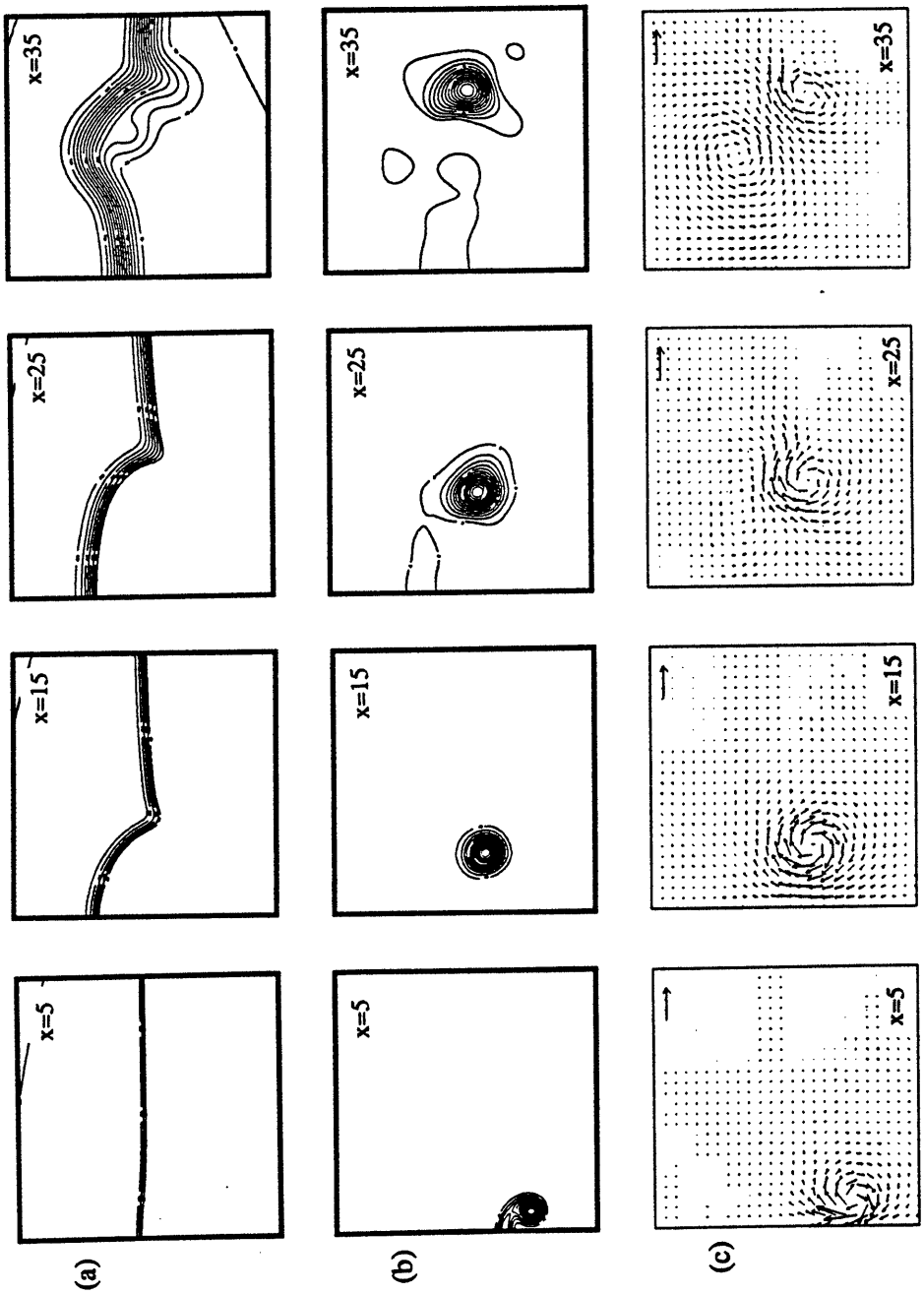

Figure 3.4. (a) The background air density contour, (b) the plume density contour, and (c) the velocity field in the crosswind sections for the case shown in figure 3.3(c). All frames are for $0.0 \leq y \leq 10.0$ and $9.0 \leq z \leq 19.0$.

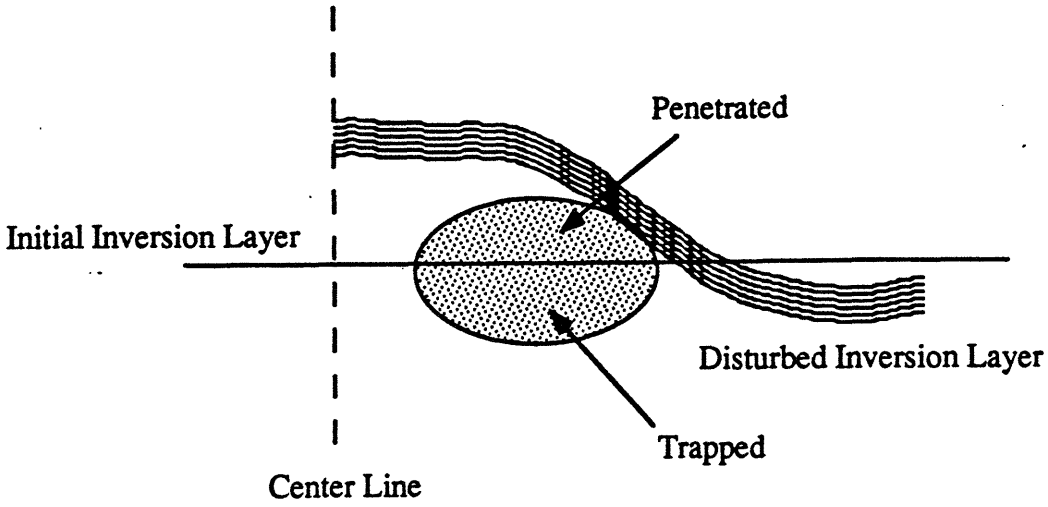

Figure 3.5. A schematic diagram showing the definition of the plume trapping fraction.

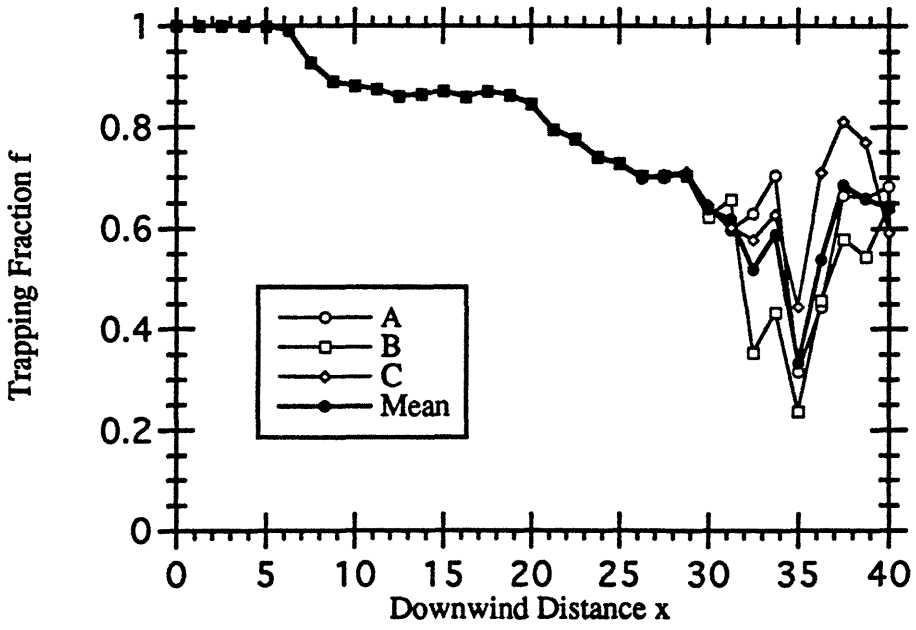

Figure 3.6. The evolution of the plume trapping fraction along the downwind direction. All three runs, depicted by thin lines, are for the same case, $h_i/R = 3.5$, $\Delta\rho_i/\rho_p = 0.25$, and $\Delta h_i/R = 0.1$, with slightly different initial conditions. The thick line shows the average of the three cases.

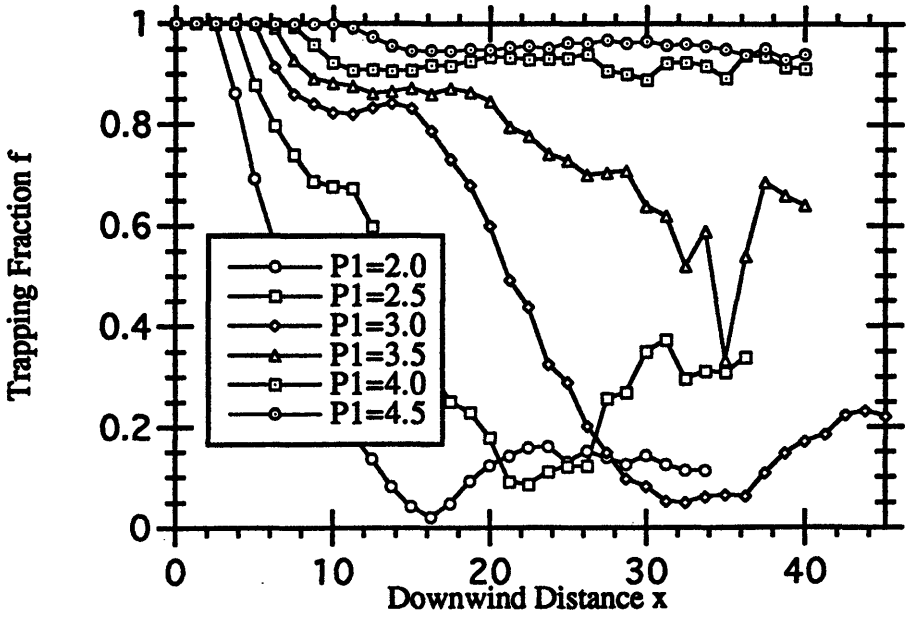

Figure 3.7. The evolution of the plume trapping fraction in the case of thin inversion with $\Delta\rho_i/\rho_p = 0.25$, $\Delta h_i/R = 0.1$, at six different heights, where $P1 = h_i/R$.

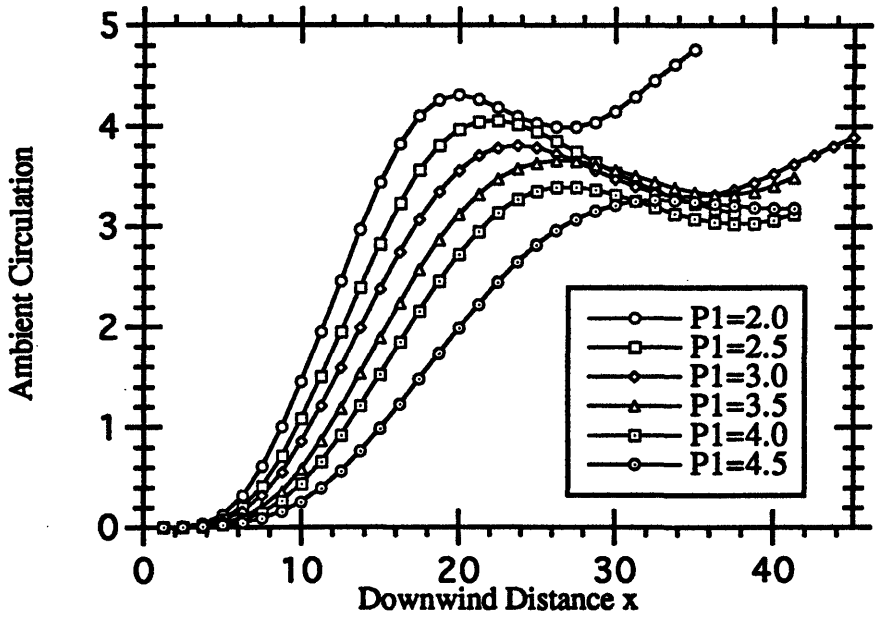

Figure 3.8. Total ambient circulation generated within one half of a thin inversion, with $\Delta\rho_i/\rho_p = 0.25$, $\Delta h_i/R = 0.1$, at six different heights, where $P1 = h_i/R$.

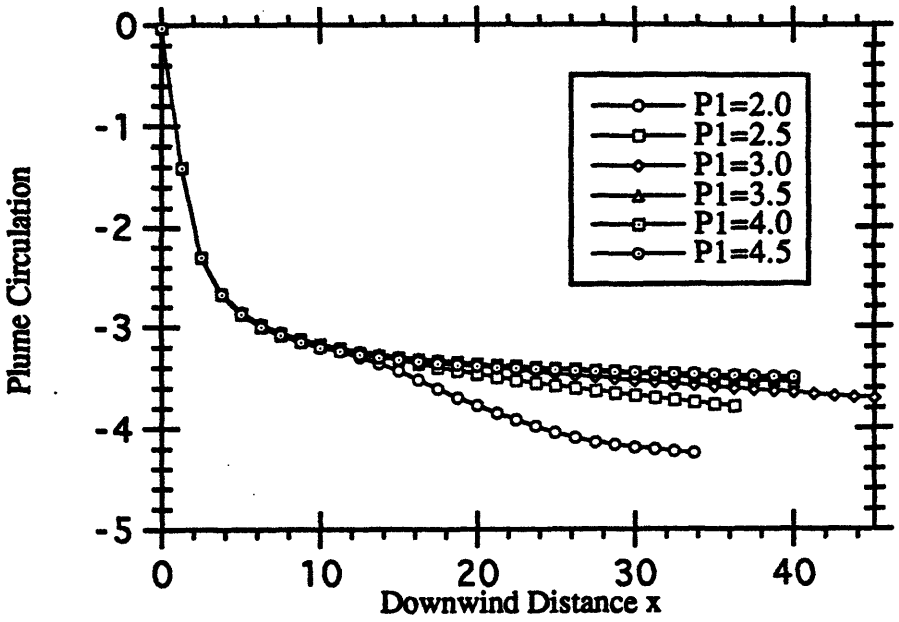

Figure 3.9. Total plume circulation generated within one half of the plume-air interface under thin inversion with $\Delta\rho_i/\rho_p = 0.25$, $\Delta h_i/R = 0.1$, at six different heights, where $P1 = h_i/R$.

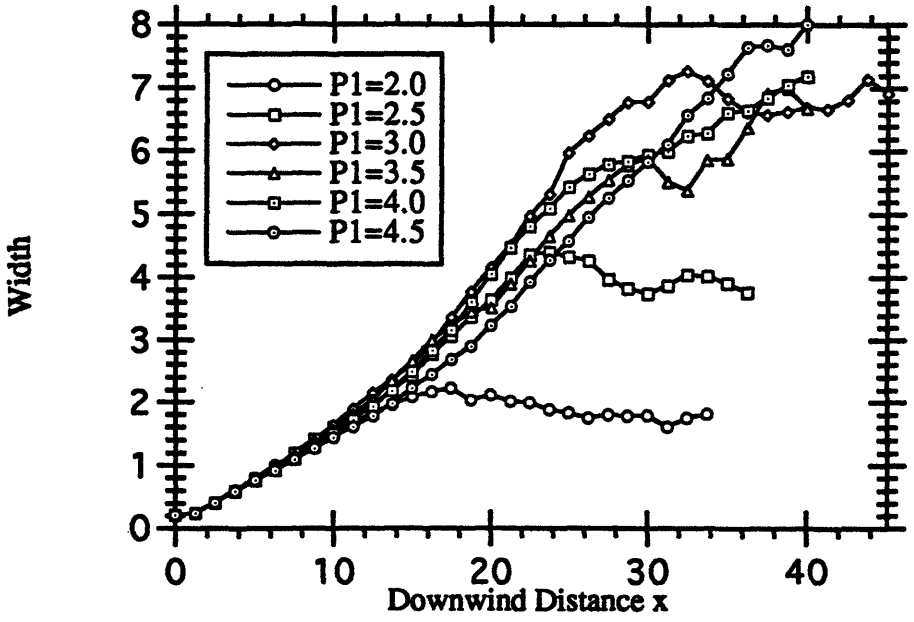

Figure 3.10. The growth of the plume width under inversion with $\Delta\rho_i/\rho_p = 0.25$, $\Delta h_i/R = 0.1$, at six different heights, where $P1 = h_i/R$.

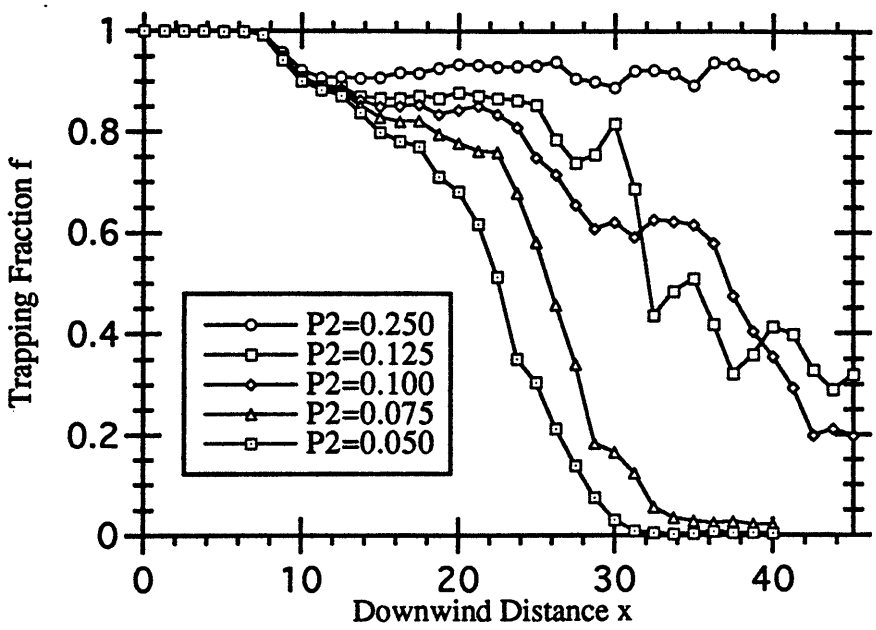

Figure 3.11. The evolution of the trapping fraction of a plume under thin inversion, with $h_i/R = 4$, $\Delta h_i/R = 0.1$, and five different strengths, $P2 = \Delta\rho_i/\rho_p$.

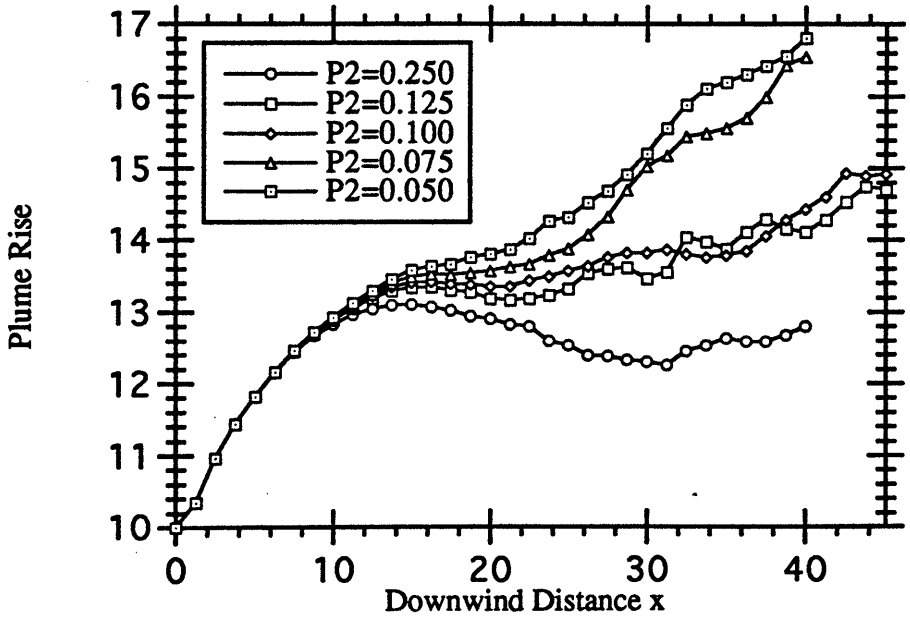

Figure 3.12. The plume trajectory under inversion, with $h_i/R = 4$, $\Delta h_i/R = 0.1$, and five different strengths, $P2 = \Delta\rho_i/\rho_p$.

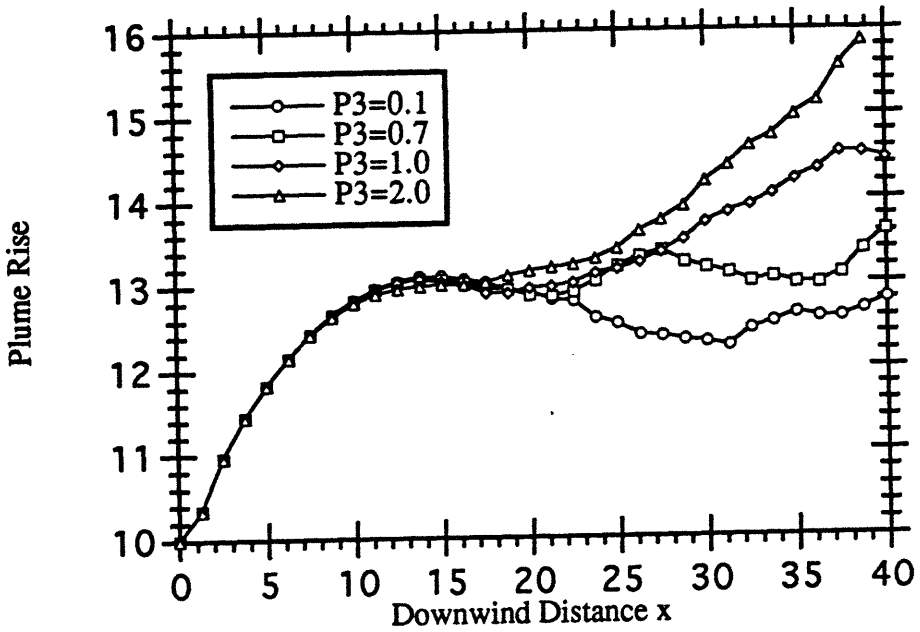

Figure 3.13. The plume trajectory under inversion with $\Delta\rho_i/\rho_p = 0.25$, $h_i/R = 4$, and four different thicknesses, $P3 = \Delta h_i/R$.

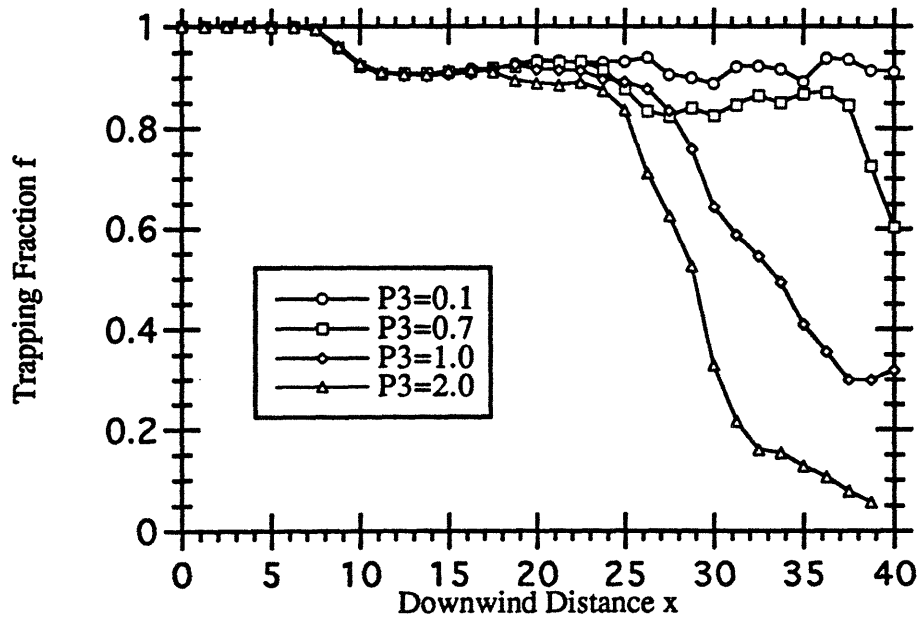

Figure 3.14. The evolution of the trapping fraction of the plume material under inversion layers with $\Delta\rho_i/\rho_p = 0.25$, $h_i/R = 4$, and four different thicknesses, $P3 = \Delta h_i/R$.

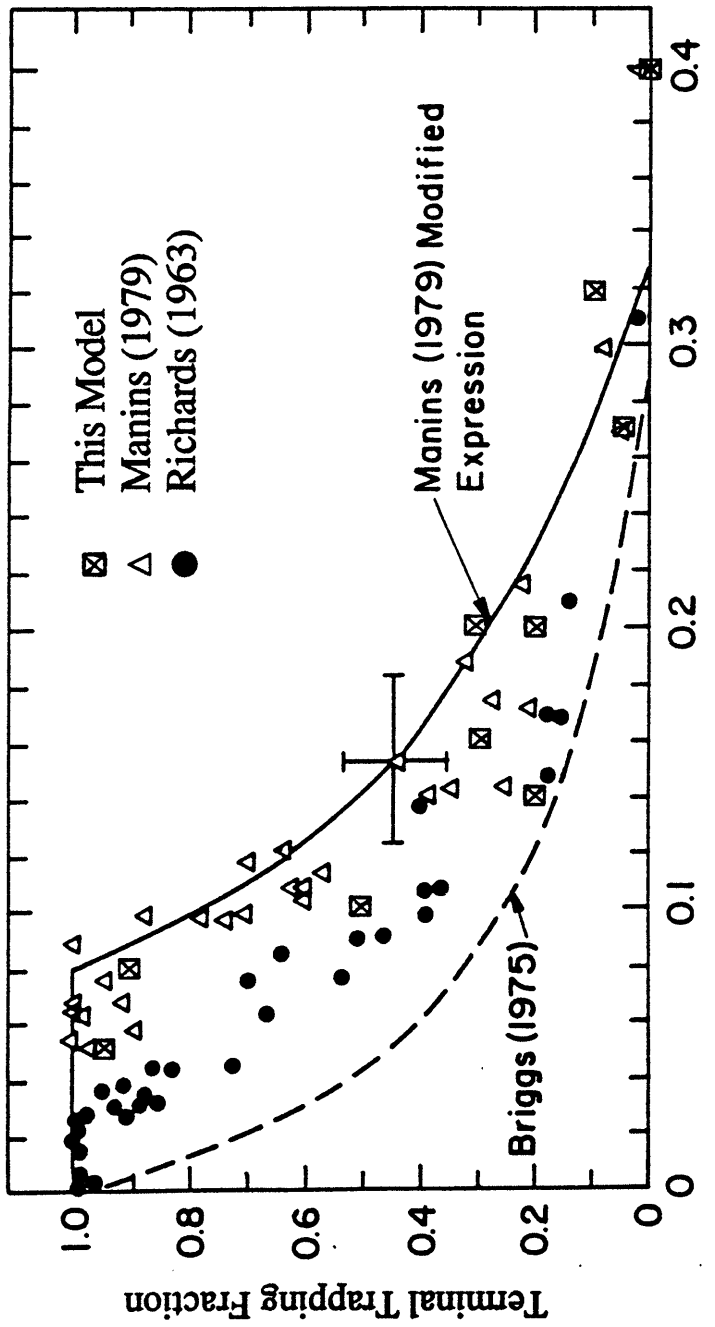

$$P = \frac{1}{\pi} \frac{\rho_p}{\Delta\rho_i} \left(\frac{R}{h_i}\right)^2$$

Figure 3.15. The terminal trapping fraction measured in laboratory experiments, predicted using our numerical model, and calculated from theoretical models. The figure, except for our numerical results, is adapted from Weil (1988).

CHAPTER 4

DISPERSION AND DEPOSITION OF SMOKE PLUMES GENERATED FROM MASSIVE FIRES

ABSTRACT

Massive fires resulting from the uncontrolled burning of crude oil from spills or industrial accidents produce large smoke-laden buoyant plumes which rise in the wind direction before they equilibrate within a stably stratified atmosphere. Beyond this point, the plume material cools by entrainment and the plume becomes negatively buoyant due to the heavy smoke loading. The trajectory of the descending plume, which determines the ground distribution of smoke, is the subject of this Chapter. A computational model for the simulation of large-scale smoke plumes resulting from such fires is developed and applied to investigate the effects of the plume initial properties on its trajectory and smoke deposition patterns. Attention is focused on the descent and dispersion of wind-driven plumes in a homogeneous atmosphere, and the smoke deposition on flat terrain. Results show that the plume dynamics in the cross-wind direction are dominated by two buoyantly generated, coherent, streamwise vortices which distort the plume cross section into a kidney-shaped structure. The strength of the two vortices and their separation increase as the plume falls. The plume width grows under the action of these vortices at a rate which increases as the plume settles on the ground, leading to a smoke footprint which does not resemble the prediction of Gaussian dispersion models. The effects of the injection altitude and the initial shape of the plume cross section on the transport and dispersion of the negatively buoyant smoke plume are investigated. Plumes falling from higher elevations disperse more in the vertical direction while those falling from lower elevations disperse further in the horizontal cross-wind direction. Plumes with circular cross-sections reach the ground faster and disperse horizontally further than plumes with elliptical cross-sections with the minor axes in the vertical direction. Vertical plume dispersion is weakly dependent on the shape of its initial cross-section.

NOMENCLATURE

AR: $= R_y/R_z$, plume aspect ratio;

g: gravitational acceleration;

HT: initial height of the plume center;

$\dot{m}_p$ $= \int \rho_p^*(y,z)\, U\, dA$, excess mass flux of the plume;

p: dimensional perturbation pressure;

R: square root of the plume cross sectional area;

R_y: major (horizontal) axis of the elliptical plume cross section;

R_z: minor (vertical) axis of the elliptical plume cross section;

u, v, w: perturbation velocity components in x, y, z direction, respectively;

U: uniform wind speed;

V: $= \sqrt{\varepsilon R_z g}$, velocity scale of the perturbation velocity;

x: horizontal wind direction;

y: horizontal direction normal to the wind;

z: vertical direction;

t nondimensional form of x^*;

δ: core radius of the vortex and transport element;

ε: $= \dfrac{\dot{m}_p}{\rho_o^* U R_z^2}$, plume mass flux ratio;

ρ^*: $= \rho_o^* + \rho_p^*$, total dimensional plume density;

ρ_o^*: uniform background air density;

ρ_p^*: excess particulate density due to the presence of the smoke;

ρ: nondimensional particulate density;

ω: vorticity in the wind direction.

Superscript

* dimensional quantity

4.1. INTRODUCTION

Wind-driven buoyant plumes are responsible for the long-range dispersion of smoke and chemicals emitted from massive fires resulting from oil spills, uncontrolled oil-well fires, and large-scale industrial accidents (Evans et al 1986, 1988, 1989, 1992). The environmental impact of the fire, which becomes a factor in whether the fire should be fought or left to burn, is determined by the plume trajectory. While the horizontal motion of the plume is governed by the prevailing wind, its vertical motion is determined by buoyancy and is a function of the initial density distribution within the plume cross-section and atmospheric stratification. Typically, the density of the plume is determined by the temperature and the smoke concentration of the fire plume. Both vary during the plume rise due to entrainment and mixing with the surrounding air. At a certain height, the plume becomes buoyantly stable (Hewett et al 1971, Fay 1973, and Rodi 1982) and as it cools further, it starts to fall due to the smoke concentration. Plumes generated by oil fires are of particular interest due to their high smoke loading (10-15 percent of the original fuel burned). This increases the environmental hazard and complicates the analysis, since the smoke cannot be treated as a passive convected scalar. The purpose of this work is to develop a computational model to simulate the buoyant plume dynamics.

Currently available plume models can be divided into two categories (Venkatram et al 1988, Askari et al 1990, Seinfeld 1986, Britter 1989): scale, or integral models; and numerical, or field models . In the former category, dimensional arguments and/or integral conservation expressions are used to derive relations among characteristic, global parameters, such as the maximum plume rise, as a function of the source and ambient conditions. These relationships contain constants, e.g. entrainment rates, which are determined using scaled experiments. In most cases, the plume concentration distribution is assumed to be Gaussian in the plane normal to the plume axis (Fay 1973, Seinfeld 1986). This simplification limits the applicability of integral models since, as shown below, the underlying assumptions may not hold in many relevant cases. On the other

hand, numerical models offer the possibility of more detailed and accurate predictions of the plume dynamics. Typically, these models rely on the numerical integration of the averaged conservation equations, supplemented with turbulence-closure schemes, to describe the field in detail. The application of these models has been limited by the uncertainty associated with the validity of turbulence models in buoyant flows, and the high computational expense associated with using fixed-grid integration schemes.

In this work, a comprehensive numerical model of smoke dispersion and deposition is developed as an effective alternative to both approaches. The model does not rely on experimentally-fitted constants or closure models, and is endowed with efficiency by relying on grid-free, Lagrangian numerical methods to integrate the equations of motion. In this formulation, Lagrangian elements are naturally convected and redistributed in regions of high strain, thereby adapting to severe and rapid changes in the plume structure (Ghoniem et al, 1988a,b, and 1992, Krishnan and Ghoniem 1992). Far-field and normal boundary conditions are easily applied by using the appropriate form of the Greens function used to represent the velocity induced by a given Lagrangian element. The capability of the model is illustrated by computing the dispersion of a wind-transported dense plume in a uniform atmosphere and its deposition on a flat terrain.

The quantity that is of direct environmental impact is the downwind "footprint" of the smoke plume as a function of fire strength, smoke loading, and wind pattern. This quantity is directly related to the trajectory of the descending plume, a problem which has so far received less attention than rising thermal plumes. Attention is therefore focused on negatively buoyant, descending smoke plumes and their interaction with a flat ground. Much, although not all, of the information required to assess the environmental damage of the smoke generated from large fires can be obtained from this analysis of the descending smoke plume. We consider cases in which the plume self-induced turbulence far exceed atmospheric turbulence and show that the former plays an important role in

determining the plume trajectory and the distribution of smoke within its cross section. We also show that this distribution differs greatly from the conventionally assumed Gaussian due to the formation of strong streamwise vorticity.

The Chapter is organized as follows. In Section 4.2, we describe the formulation of the model including the major assumptions used and the non-dimensionalization procedure. The numerical scheme is briefly summarized in Section 4.3. Detail of the latter can be found in the open literature. In Section 4.4, results pertaining to the shape of the plume, its trajectory and the smoke distribution are shown and analyzed. The effects of the initial height and shape of the plume are also discussed. Finally, conclusions are presented in Section 4.5.

4.2. FORMULATION OF THE PROBLEM

We consider the evolution of an isothermal smoke plume initially at the thermally stabilized height HT. The plume is characterized by the (excess) particulate mass flux $\dot{m}_p = \int \rho_p^* U \, dA$, the integration is over the plume cross-wind section, where ρ_p^* is the density of the particulate phase, with the total density $\rho^* = \rho_o^* + \rho_p^*$, and ρ_o^* is the ambient density. The initial plume cross section is taken to be an elliptical cross section of semi-major (horizontal) axis R_y and semi-minor (vertical) axis R_z. The major direction of motion is the horizontal x-direction, with a uniform ambient wind velocity U. The geometry is illustrated in figure 4.1. The specification of initial altitude and shape of the plume cross section is obtained from a plume rise analysis which will be described elsewhere.

The present analysis is based on the following assumptions:

(i) the large-scale plume motion of interest here can be regarded as steady;

(ii) molecular diffusion of mass and momentum are negligible compared with vorticity-induced entrainment;

(iii) the ambient-wind speed U is uniform and much larger than plume-induced velocity components (v,v,w) in the (x,y,z) coordinate directions;

(iv) the smoke particulate can be treated as a continuum fluid;

(v) the stratification and turbulence in the atmosphere can be neglected.

The first four assumptions are quite reasonable and widely adopted in most plume modeling. The last assumption is used as a first-order model for atmospheric conditions. It will be systematically relaxed in later work.

Given the above assumptions, the plume evolution can be described in a transverse (y^*,z^*) plane perpendicular to the ambient wind direction. We introduce dimensionless transverse coordinates, (y,z), and streamwise coordinate, t, as follows:

$$(y\ ,z\ ) = (y^*, z^*\ )/R_z \qquad (4.1)$$

$$t = \frac{x^*/U}{R_z/V} = \frac{x^*}{U}\sqrt{\frac{\varepsilon g}{R_z}}$$

where $V = \sqrt{\varepsilon R_z g}$, and $\varepsilon = \frac{\dot{m}_p}{\rho_o^* U R_z^2} << 1$, while g is the acceleration of gravity. The dependent variables are the transverse velocity components, (v^*, w^*), the perturbation pressure relative to its ambient hydrostatic value, p^*, and the particulate density ρ_p^*. They are made dimensionless as follows:

$$\begin{aligned}
(v, w) &= (v^*, w^*)/V \\
p &= \frac{U R_z}{\dot{m}_p g} p^* \\
\rho &= \frac{U R_z^2}{\dot{m}_p}\rho_p^* = \frac{\rho_p^*}{\varepsilon \rho_o^*}
\end{aligned} \tag{4.2}$$

The conservation of mass, particulates and momentum in the transverse plane then take the form:

$$\begin{aligned}
&\frac{\partial v}{\partial y} + \frac{\partial w}{\partial z} = 0 \\
&\frac{\partial \rho}{\partial t} + v\frac{\partial \rho}{\partial y} + w\frac{\partial \rho}{\partial z} = 0 \\
&(1+\varepsilon\rho)\left(\frac{\partial v}{\partial t} + v\frac{\partial v}{\partial y} + w\frac{\partial v}{\partial z}\right) + \frac{\partial p}{\partial y} = 0 \\
&(1+\varepsilon\rho)\left(\frac{\partial w}{\partial t} + v\frac{\partial w}{\partial y} + w\frac{\partial w}{\partial z}\right) + \rho + \frac{\partial p}{\partial z} = 0
\end{aligned} \tag{4.3}$$

The quantity ε is a measure of the particulate-to-ambient-air-density ratio, proportional to $\frac{\rho_p^*}{\rho_o^*}$, if ρ_p^* is uniformly distributed over the plume cross section. This ratio is quite small, typically O(0.01), making the Boussinesq approximation valid in most practical cases. Invoking this approximation, the problem then contains only two non-dimensional parameters, the plume initial stabilization height HT/R_z, and the initial plume aspect ratio R_y/R_z. Initially, the particulate density profile within the ellipse must be specified, together with the transverse components of the induced velocity field. In what follows, the initial smoke density is assumed constant, and the transverse velocity

components are zero. The velocity components must vanish as $(y,z) \to \infty$, and the normal component of the velocity $w = 0$ at the ground $z = 0$. For later use in connection with the vortex method, we note that equation (4.3) leads to the following evolution equations for the streamwise component of vorticity ω.

$$\frac{\partial \omega}{\partial t} + v\frac{\partial \omega}{\partial y} + w\frac{\partial \omega}{\partial z} + \frac{1}{(1+\varepsilon\rho)^2}\frac{\partial \rho}{\partial y} - \frac{\varepsilon}{(1+\varepsilon\rho)^2}\left[\frac{\partial \rho}{\partial y}\frac{\partial p}{\partial z} - \frac{\partial \rho}{\partial z}\frac{\partial p}{\partial y}\right] = 0 \qquad (4.4)$$

where the vorticity is defined as follows:

$$\omega = \frac{\partial w}{\partial y} - \frac{\partial v}{\partial z}$$

The non-Boussinesq terms in the equation are retained mainly for use in future work directed at the near-source plume-rise problem. They play no role in the present problem. Using the vorticity transport equation, the mathematical formulation of the problem is completed by invoking the pressure gradient from the momentum equations,

$$\frac{\partial p}{\partial y} = -(1 + \varepsilon\rho)\frac{dv}{dt},$$

and,

$$\frac{\partial p}{\partial z} = -\rho - (1 + \varepsilon\rho)\frac{dw}{dt} \qquad (4.5)$$

and satisfying the conservation of species and incompressibility condition, respectively:

$$\frac{d\rho}{dt} = 0$$

and

$$\frac{\partial v}{\partial y} + \frac{\partial w}{\partial z} = 0 \qquad (4.6)$$

4.3. NUMERICAL SCHEME

The vortex element method is used to integrate the vorticity transport equation (4.4). The method is based on the discretization of the support of vorticity into vortex elements, and the transport of these elements along particle trajectories. The vorticity of an element is radially distributed in a small neighborhood of its center according to Gaussian core function with a characteristic radius, δ. The velocity field is computed by discrete convolution over the fields of the vortex elements using the desingularized Biot-Savart law. Details of the method, as applied to the plume problem, are described in Krishnan and Ghoniem (1992) and Ghoniem et al (1992). Vorticity source terms appearing in equation (4.4) are evaluated using the transport element method. Similar to the vortex method, the latter relies on the discretization of the density gradient into a finite number of Lagrangian transport elements which move with the local velocity. The density gradient changes with the stretching and tilting of material lines, while the density is obtained by direct summation over the field of transport elements. Details of this method, which has also been applied in combustion problems (Ghoniem et al 1988b, 1990) are given in Krishnan and Ghoniem (1992).

Normal boundary conditions at the ground, $z = 0$, are satisfied by accounting for the image system of the vortex/transport elements. We discretize the zone of finite density gradient between the plume and the surrounding using two layers of elements. Both the vortex and transport element methods invoke a redistribution scheme which introduces new elements, as necessary, to maintain the spatial resolution of the computations. This results in an efficient and adaptive solution scheme which captures severe and rapid distortions of the flow map while concentrating the computational effort in zones of finite vorticity and density gradient. The accuracy of this scheme and of the associated plume predictions have been extensively investigated (Krishnan and Ghoniem, 1992, Ghoniem et al, 1992).

4.4. RESULTS

The global structure of descending plumes and of their vorticity field are discussed first for a plume with $HT/R_z = 5$, $AR = 3$ *and* $\rho = 0.016$. The results are illustrated by plotting, in figures 4.2 and 4.3, respectively, three-dimensional surfaces of constant smoke concentration and streamwise vorticity. Both figures were obtained by assembling the instantaneous, or local constant smoke density or vorticity contours into a three-dimensional plot, using the computational t-coordinate as a physical x-coordinate. Note that some inevitable numerical diffusion creeps into the plotting procedure, which employs interpolation formulae to find the functional values of smoke concentration and vorticity at the corner of a uniform mesh, that leads to the break-off of some of the plume material into separate blobs. These three-dimensional plots are meant to delineate what a laboratory experiment of a descending plume would show. The results indicate that the plume cross section is reshaped into a kidney shaped object and that close to the ground, the smoke distribution is far from the commonly assumed Gaussian.

From extensive computations, and as shown in figure 4.2 and 4.3, we find that the large-scale features of the dispersion and deposition of dense plumes can be described in terms of four distinct stages which separate the initial fall and the onset of smoke settlement on the ground. The dynamical processes which distinguish each of these stages are interpreted in terms of the correspondence between the plume structure and the vorticity field, as summarized below. The purpose of devising this way of describing the numerical results is to facilitate their use in formulating future integral models of plume motion. The plume descent starts with an initial acceleration stage, during which the deformation of the plume cross-section is very small and vorticity is generated along the plume-air interface. During the second stage, the streamwise vorticity on each side of the plume centerline intensifies and rolls into a large-scale eddy thus generating a counter-rotating vortex structure. The induced motion of this vortex pair deforms the plume's smoke distribution into a kidney-shaped cross-section. The structure of the plume at

large elevation is in qualitative agreement with the experimental measurements of Hewett et al. (1971) who observed a similar kidney-shaped cross-sections downwind the plume source.

With further intensification of the streamwise vorticity under the action of baroclinic torques, small-scale roll-up occurs. This third stage is characterized by the generation of streamwise vorticity of opposite signs on both sides of the symmetry plane, and by the increasing complexity of the smoke distribution. Vorticity generation and roll-up transforms some of the plume's potential energy into kinetic energy which is distributed between the plume and its surrounding. The rotational velocity field induced by the vorticity of the plume sets up an entrainment field towards its cross section. Most entrained fluid is engulfed by the large-scale eddy roll-up, while the secondary small eddies induce smaller entrainment currents. The continuous roll-up of the vorticity layer forming on the boundary of the plume cross section, which is responsible for maintaining the entrainment towards the plume center, is due to the familiar Kelvin-Helmholtz instability of vorticity layers.

As the smoke approaches the ground, a fourth, ground-settlement stage is observed. The dynamics of the flow in this stage is increasingly influenced by the proximity to the ground. The associated deceleration field leads to fast and tight widening of the plume structure and its cross-wind straining into two large blobs of smoke connected by a thin crescent. This mechanism is similar to the straining of thermals colliding with walls placed perpendicular to their direction of motion, observed and clearly recorded in laboratory experiments (Tsang 1971, Barker et al 1977). (Note that mathematically, the behavior of the plume cross section in the wind direction is exactly the same as that of a thermal in time). These experiments show the formation of similar large-scale features and their subsequent separation into two lumps of the thermal fluid as they collide with the wall. The further away from the wall/ground the release point of the thermal/plume is, the more concentrated its material becomes in the two large

structures. The early formation of the large-scale features is also depicted by the numerical results of Meng and Thomson (1978), who computed the motion of thermals.

One of the important implications of this side roll-up process is the resulting smoke deposition patterns. Clearly, the smoke distribution along the cross section close to the ground is not uniform and may not necessarily possess a maximum at the center $y=0$. This is contrary to classical plume dispersion models which assume that the smoke distribution is Gaussian both in y- and z-directions, and that the smoke ground imprint follows Gaussian function centered at the x -axis of the plume. We note that this departure from a Gaussian distribution is solely due to the plume self-generated vorticity, or turbulence which render the dynamics field surrounding the plume cross section highly non-uniform.

4.4.1. The Entrainment Field

Since most plume models rely on certain assumptions regarding the entrainment field and estimates of the entrainment velocity established by the plume, we examine here, using the numerical simulation results, the form and strength of this field. Besides the formulation of plume models, the entrainment field is used in other applications where the "fire-induced wind" may be important in determining the impact of the fire events on the local environment. Figure 4.4 shows a superposition of the plume cross sections and the velocity field in its surrounding for the case shown in figure 4.2. The velocity vectors in the plane of the plume cross section are displayed as short lines starting from a set of equally distributed mesh points. As indicated above, the roll-up of the vorticity generated along the boundary between the plume material and the surrounding establishes two strong coherent vortices at the far ends of the horizontally expanding plume cross section. The figure indicates that the field of the large eddy resembles that of a Rankine vortex in which the maximum velocity is reached close to but not at the center of the eddy. The maximum entrainment velocity, which as shown in the

figure is of the order of magnitude of V, occurs close to the center of the large eddy and stays around the same value for the majority of the plume's journey.

Two interesting observations can be made using these results: (i) The centers of the large eddies stay farther away from the ground than the rest of the plume cross section even as part of the plume material settles on the ground. This means that the turbulent field produced by the plume is not likely to be dissipated quickly as the plume approaches the ground and, at least for some time following the settlement, some circular wind motion will be felt close to the area of plume touch-down. The second observation is the waves developing on the lower side of the plume as it touches the ground. The evolution of these waves lead to the formation of small scale eddies which induce their own wind close to the ground, augmenting that induced by the primary large eddies.

4.4.2. Mechanism of Vorticity Generation

Detailed flow computations reveal that most of the vorticity generation occurs close to the interface between the plume and the air where density gradients are high. A short distance away from this interface, the density is uniform, vorticity is zero and the motion is essentially irrotational. A schematic interpretation of the generation and behavior of the streamwise vortices is shown in figure 4.5, where we have invoked the Boussinesq approximation. With $\varepsilon = 0$, the vorticity generation term in the transport equation is proportional to the horizontal density gradient. For a plume with an elliptical initial cross-section, vorticity of opposite signs form on the sides of the plume centerline due to the opposite horizontal density gradients, figure 4.5a, with its maximum absolute value at the far ends. This vorticity layer rolls up to form two large-scale counter-rotating streamwise vortices, so that two additional areas with opposite horizontal density gradients are established on both sides of the plume-air interface, figure 4.5b. Thus, at later stages, vorticity with opposite signs forms on either side of the symmetry plane. The evolution of the vorticity field indicates that a simplified overall plume model which describes the interaction of the plume with its surrounding and its settlement on the

ground can be constructed by assuming that the plume dynamics are driven by a kidney-shaped vortex with a time-dependent circulation and width. Values of circulation and distance between the two vortices will be given later.

Extensive numerical experiments have been conducted to investigate the dependence of the results on the initial conditions and plume configurations, the only two parameters left in the problem specification. The dynamics of falling plumes and details of the expected smoke-deposition process are further examined in the following sections. In particular, the effects of initial plume height and shape are discussed in detail. The dependence of the plume width on these two parameters is of special interest since it determines the area contaminated by the plume material. The strength of the plume induced vortex pair is also important since it governs the motion induced by the plume motion.

4.4.3. Effect of Initial Plume Height

Results depicting the plume cross-sections along its trajectory, shown in figure 4.6 for $HT/R_z = 3$ and 30, keeping all other parameters the same, suggest that plumes released from a height close to the ground produce a ground smoke distribution with higher concentration on the sides than at the center. We also find that higher initial elevations lead to more uniform ground smoke distribution. Moreover, the vertical dispersion is larger for plumes released from higher elevations, while the opposite is true for horizontal plume dispersion. These assertions are illustrated in figures. 4.7 and 4.8 which, respectively, show the trajectories of descending plumes with initial heights in the range $3R_z < HT < 30\ R_z$ and the corresponding horizontal dispersion, defined as the horizontal spread of the plume cross-section.

The plume descent occurs such that most of the horizontal dispersion develops at later stages, when the plume motion is strongly affected by the presence of the ground. When the plume falls from high altitude, its width exhibits an oscillatory behavior. This

is due to the intermittent roll-up of large eddies which entrain plume fluid towards their centers as they propagate in the cross-wind direction away from the symmetry plane.

The motion of these large eddies and the generation of smaller scale vortices generate entrainment currents which accompany the horizontal and vertical plume dispersion. The evolution of these currents is measured in terms of the total peripheral length of the interface separating the plume from ambient air at a given cross-section. During the initial acceleration stage, there is little entrainment as the plume suffers a mild deformation. The entrainment rate is higher following large-eddy roll-up which causes the engulfment of a large amount of ambient fluid, and increases further during the later stages when small-scale vortices, generated along the plume surface, induce local entrainment fluxes.

The plume deformation was also correlated with the large-scale features of the baroclinic generation of streamwise vorticity. The latter are determined by the total positive circulation, total negative circulation, and the sum of the two, all computed on one side of the symmetry plane ($y > 0$). While the positive circulation, which constitutes most of the vorticity in this region, grows steadily during the early stages, the negative vorticity increases only after large scale roll-up has occurred. Thus, during the first and second stages, the vorticity field can be modeled as a pair of counter-rotating vortices whose strength increases under the action of the gravitational field. However, at later stages, the single large eddy on each side of the plume should be replaced by a counter-rotating vortex pair, in order to model the generation of both signs of vorticity, and the associated small-scale roll-up and enhanced entrainment rates.

4.4.4. Effect of Initial Plume Shape

The effect of the initial plume shape on the descent and dispersion processes is now examined. We simulated the motion plumes with the same cross-sectional area but with different aspect ratios, $AR = 1, 3, 6$. In all cases, the initial height $HT = 5\ R$, R being the square root of the cross-sectional area. Figure 4.9 show a comparison between

the shape of the plume cross sections for AR = 1 and 6. Figures 4.10 and 4.11 show the heights and widths for all three cases, plotted against the downwind coordinate, t, which is defined as the normalized distance travelled from the initial source location.

Examination of these results indicates that different initial cross-sections produce different plume trajectories. This dependency is explained by noting that the rate of vorticity generation, which governs the strength and shape of the large-scale vortices, is strongly dependent on the curvature of the plume boundary. Plumes with small AR, i.e. rounded cross-sections, get more distorted, reach the ground earlier, and disperse horizontally faster than plumes with flatter cross-sections. However, in all cases, the plume tends to break-up into two parts symmetrical about $y = 0$. For $AR = 1$, this observation is confirmed by experimental results (Tsang 1971, Barker et al 1977). Moreover, the shape of the initial plume cross-section appears to have a weak effect on the rate of vertical dispersion.

4.4.5. Global Structure Parameters

Results presented here, which are supported by other results reported in the literature, show that the motion of the plume, when atmospheric turbulence is weak, is strongly governed by two large streamwise eddies which form due to the roll-up of the vorticity generated along the plume interface. This vortex pair is responsible for the conversion of some of the plume potential energy into kinetic energy, especially in the plane of its cross section. As we have seen, this kinetic energy is shared by the plume material and the surroundings, and is the source of the strong flow established by the plume motion and the associated entrainment. Thus, it is of interest to characterize this vortex pair by the smallest number of parameters and to study the dependence of these parameters on the initial plume conditions. These characteristic plume parameters could then be used in future plume studies.

A vortex pair can be described by the distance between the centers of the two vortices and the strength of each vortex. The first quantity is proportional to the plume

width shown in figure 4.8 and 4.11. Figure 4.12 shows the total circulation of each of the vorteices for the two cases shown in figure 4.6 and 4.9, i.e. for different initial plume height and cross section. As expected, vorticity generation, and thus enhancement of the eddies, is fastest during the early stages and is diminished quickly as the plume settles on the ground. The relationship between the acceleration of the plume cross section, its proximity to the ground and the circulation within its cross section is shown clearly in figure 4.12b where for a circular plume, which falls the fastest, the circulation rises at the highest slope. Later, and as the plume approaches the ground, the circulation of a circular plume reaches an asymptotic value earlier than any other plume.

4.5. CONCLUSIONS

A novel computational model for the simulation of buoyant plumes has been presented. The model was applied to study the plume dynamics, the dispersion and deposition of its material in a homogeneous atmosphere, and their dependence on the plume initial conditions. Results show that:

(1) Starting from a symmetrical elliptical distribution, the cross-section of descending smoke is deformed into a kidney-shaped structure due to the formation of a counter-rotating streamwise vortex pair. These vortices cause the large-scale engulfment of ambient air towards their centers. At later stages, small-scale vortices develop and enhance entrainment currents.

(2) As the plume approaches the ground, the large-scale eddies acquire a strong cross-wind convective motion away from the symmetry plane. This leads to horizontal dispersion of the smoke plume and results in the deformation of its cross-section into two large lumps separated by a thinning crescent. Accordingly, the ground smoke deposition is lower along the symmetry plane than at neighboring cross-wind locations.

(3) Plume trajectories and dispersion rates are strongly dependent on the initial plume height and shape. The corresponding variations are correlated with streamwise vorticity patterns, whose generation depends on the curvature of the plume interface and on the gravitational acceleration field.

(4) Plumes falling from a higher elevation disperse more in the vertical direction while those falling from a lower elevation disperse more in the horizontal direction.

(5) Plumes with a more rounded cross-section reach the ground faster and disperse horizontally further than plumes with a flatter cross section. The shape of the cross-section has a weak effect on the rate of vertical dispersion.

(6) The strong deformation of the plume cross section, which leads to a substantial departure of the plume material ground imprint from a Gaussian, is due to the buoyancy generated turbulence within the plume.

REFERENCES

Askari, A., Bullman, S. J., Fairweather, M. and Swaffield, F. (1990) *Combust. Sci. and Tech.* 73, 463.

Barker, S. J. and Crow, S. C.(1977) *J. Fluid Mech.* 82, 659.

Britter, R.E.(1989) *Ann. Rev. of Fluid Mech.* 21, 317.

Evans, D., Baum, H., McCaffrey, B., Mulholland, G., Harkleroad, M. and Manders, W. (1986) Combustion of Oil on Water, Report NBSIR 86-3420, NBS, Gaithersburg, MD.

Evans, D., Mulholland, G., Gross, D., Baum, H., and Saito, K.(1988) Environmental Effects of Oil Spill Combustion, Report NISTIR 88-3822, NIST, Gaithersburg, MD.

Evans, D., Mulholland, G., Gross, D. and Baum, H. (1989) Generation and Dispersal of Smoke from Oil Spill Combustion, Proceedings of the 1989 Oil Spill Conference, February 13-16, San Antonio, TX.

Evans, D., Baum, H., Mulholland, G., Bryner, N. and Forney, G.(1992) Smoke Plumes from Crude Oil Burns, NISTIR Report, NIST, Gaithersburg, MD.

Fay, J. A.(1973) *Ann. Rev. of Fluid Mech.*, 5, 151.

Ghoniem, A.F., Heidarinejad, G. and Krishnan, A.(1988a) *J. Comput. Phys* 79, 135

Ghoniem, A.F. and Krishnan, A.(1988b) Twenty-Second Symposium (International) on Combustion, p. 665,The Combustion Institute.

Ghoniem, A.F., Knio, O.M. and Krishnan, A.(1990) Twenty-Third Symposium (International) on Combustion, p. 699, The Combustion Institute.

Ghoniem, A.F., Zhang, X. and Knio, O.M.(1992) First Annual Report on Development of a Computational Model for Smoke Plume Dispersion and Deposition, NIST, National Institute of Standard and Technology, Gaithersburg, MD 20899.

Hewett, T. A., Fay, J. A. and Hoult, D. P.(1971) *Atmos. Environ.* 5, 767.

Krishnan, A. and Ghoniem, A.F.(1992) *J. Comput. Phys*, 99, No.1.

Meng, J. C. S. and Thomson J. A. L.(1978), *J. Fluid Mech.* 84, 433.

Puttock, J. S. (1988) Ed. *Stably Stratified Flow and Dense Gas Dispersion*, Clarendon Press, Oxford.

Rodi, W. (1982) Ed.*Turbulent Buoyant Jets and Plumes*, Pergamon Press, Oxford.

Seinfeld, J.(1986) *Atmospheric Chemistry and Physics of Air Pollution*, John Wiley & Sons.

Tsang, G.(1971) *Atmos. Environ.* 5, 445.

Venkatram, A. and Wyngaard, J.C. (1988) Eds. *Lectures on Air Pollution Modeling*, American Meteorological Society, Boston.

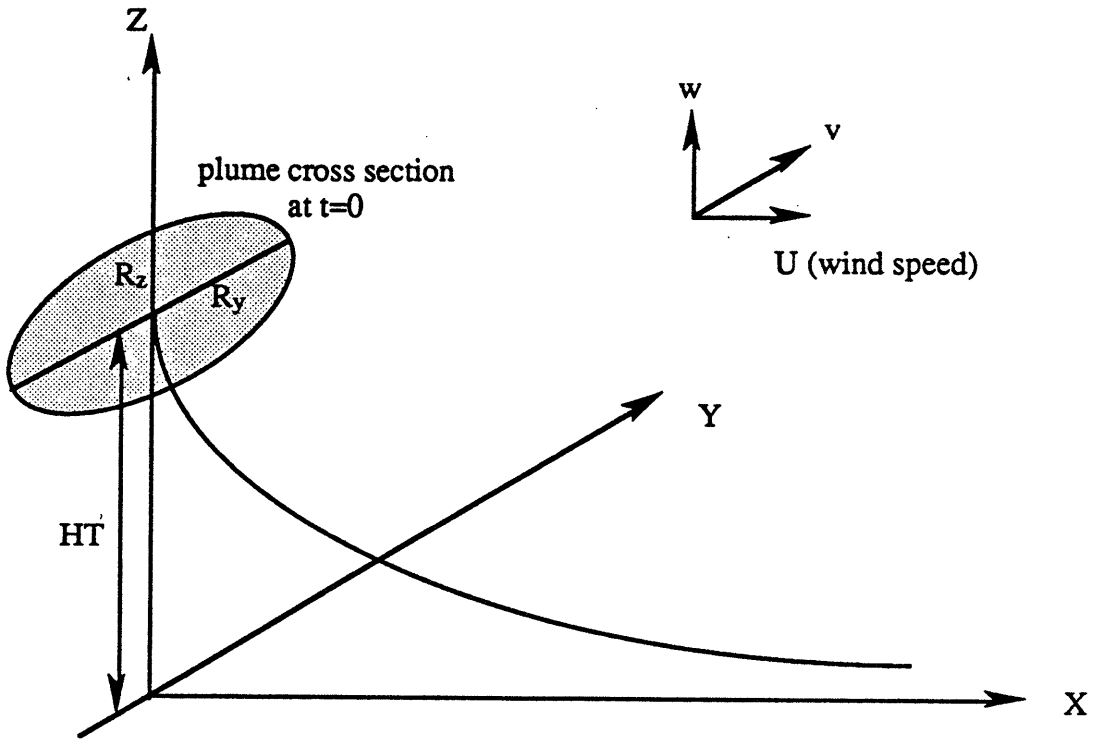

Figure 4.1. A schematic representation of the of the initial conditions plume height, its trajectory in the ind direction, the coordinate system and the velocity components.

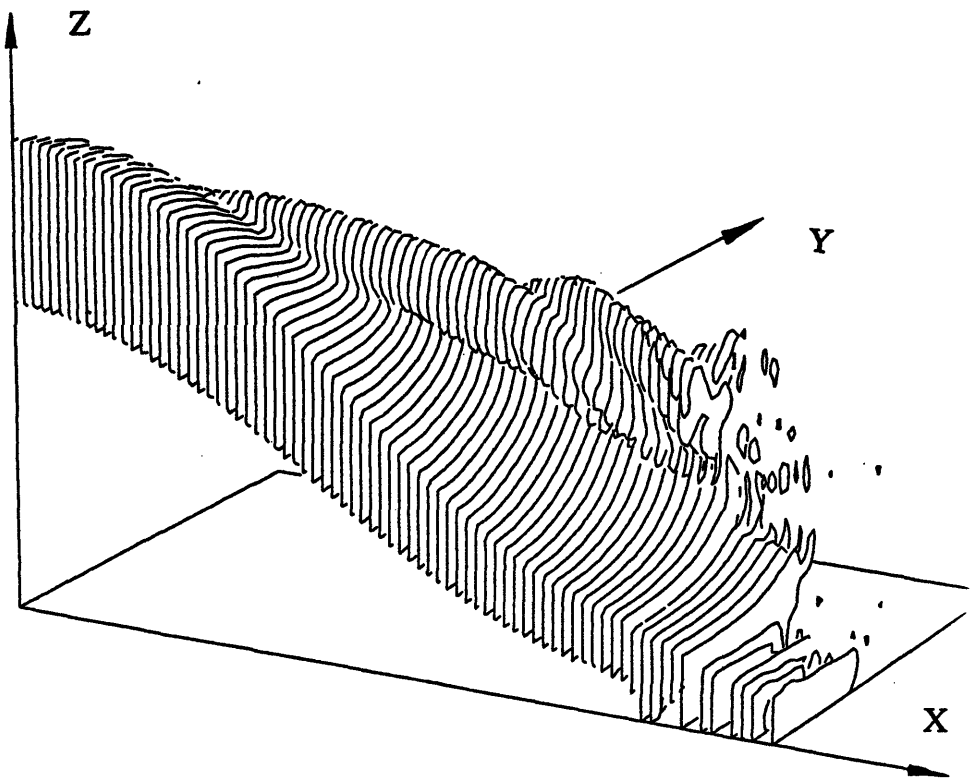

Figure 4.2. A three-dimensional perspective plot depicting a surface of constant smoke concentration, $\rho = 0.03$, generated for a case with $HT = 5\ R_z$, $R_y = 3\ R_z$, and $\rho = 0.106$. Due to symmetry with respect to the x-z plane, contours lying in the $y < 0$ region have not been reproduced. The location of the observer is th esame as that in figure 4.1.

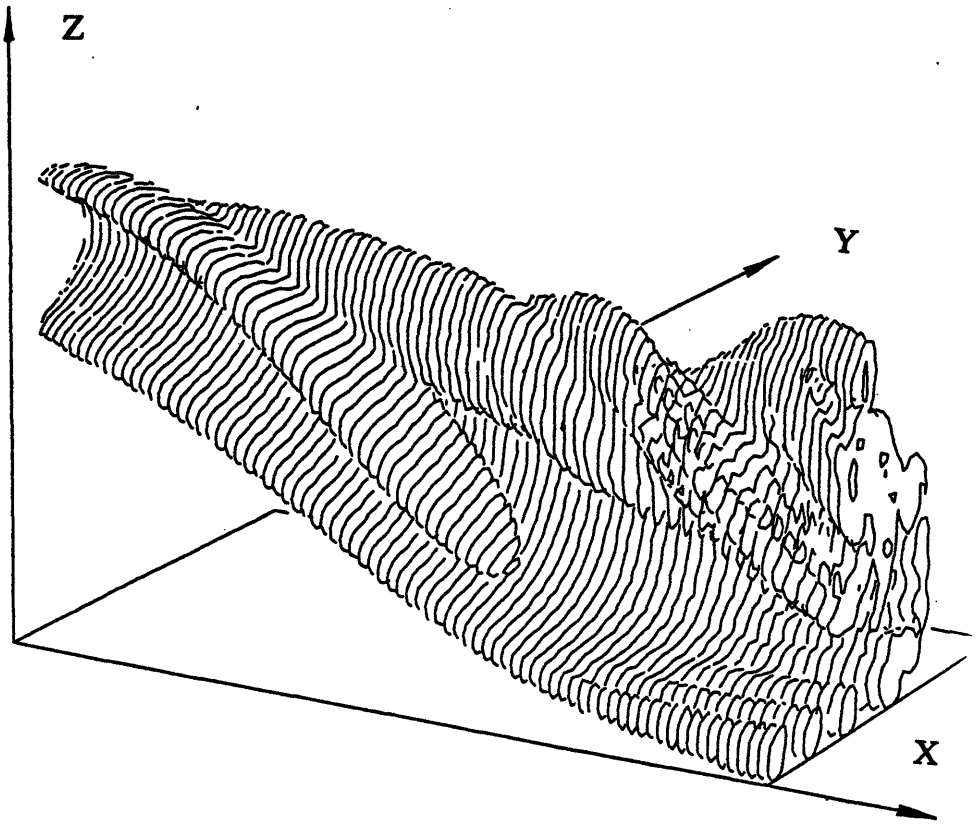

Figure 4.3. A three-dimensional perspective plot of streamwise vorticity, $\omega = 0.2$, for the same plume shown in figure 4.2.

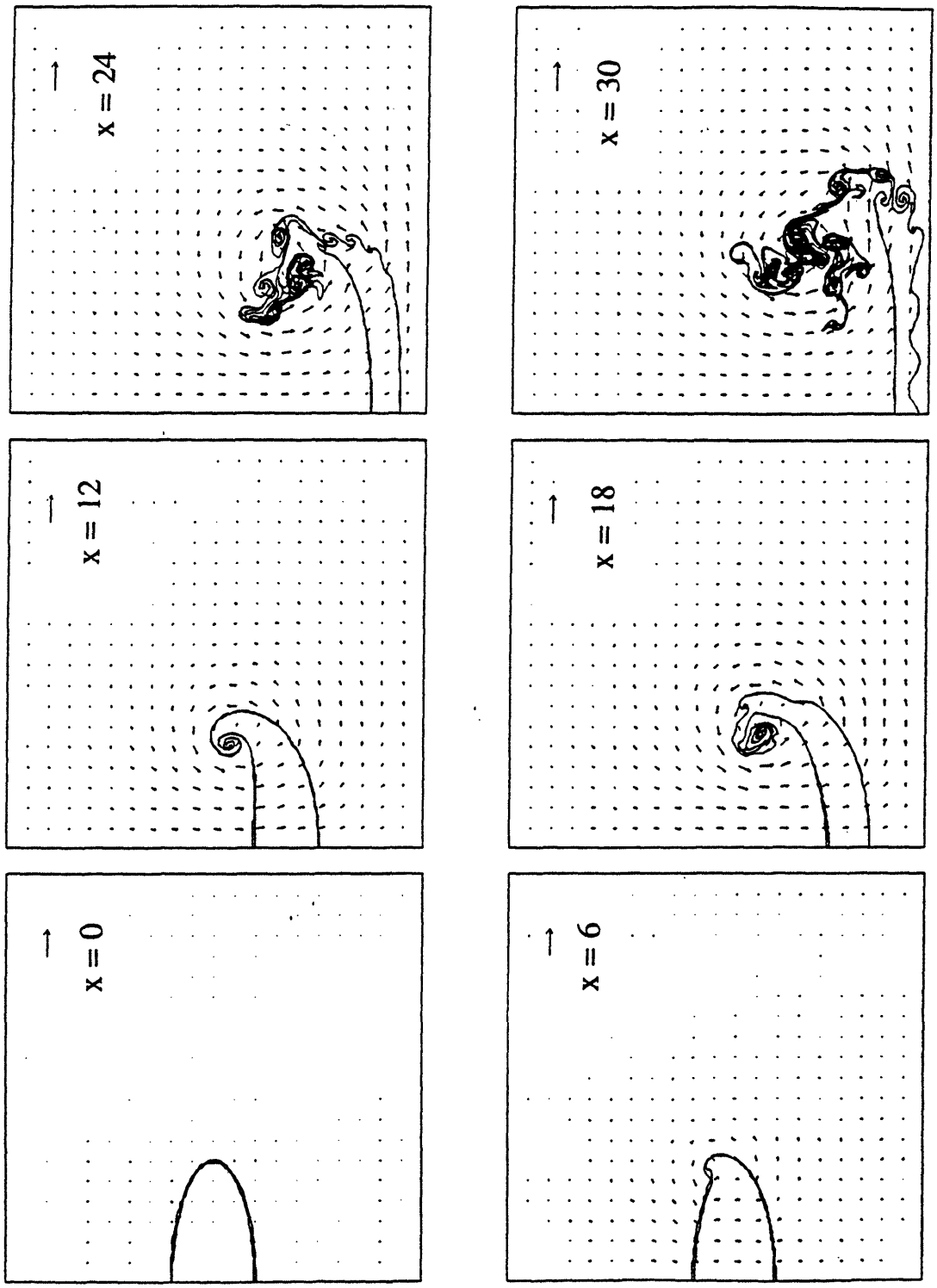

Figure 4.4. A superposition of the boundary between the plume and the surrounding, and the velocity induced by the plume motion. The characteristic velocity of the gravity induced flow is shown by the horizontal arrow on the top right-hand corner. The velocity field is shown by a vector whose length is proportional to the velocity, starting from the point where the velocity is computed.

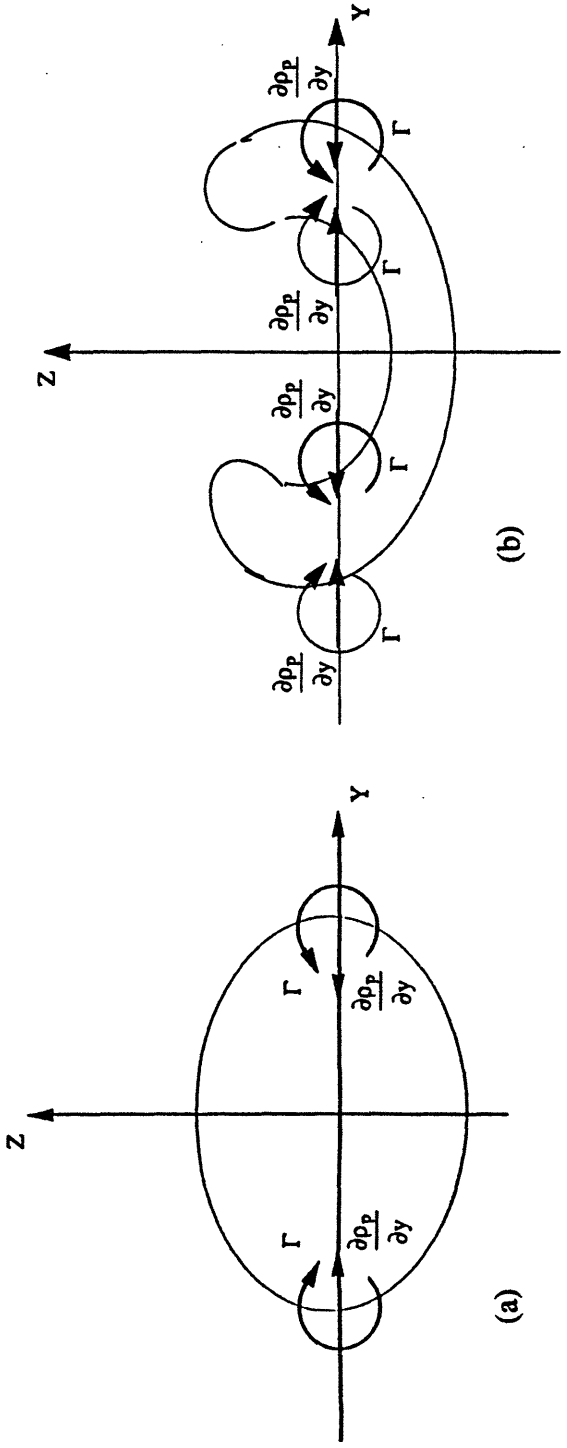

Figure 4.5. Schematic illustrations showing (a) the mechanism of baroclinic vorticity generation, and (b) the roll-up of the streamwise vortices and the resulting deformation of the plume cross-section.

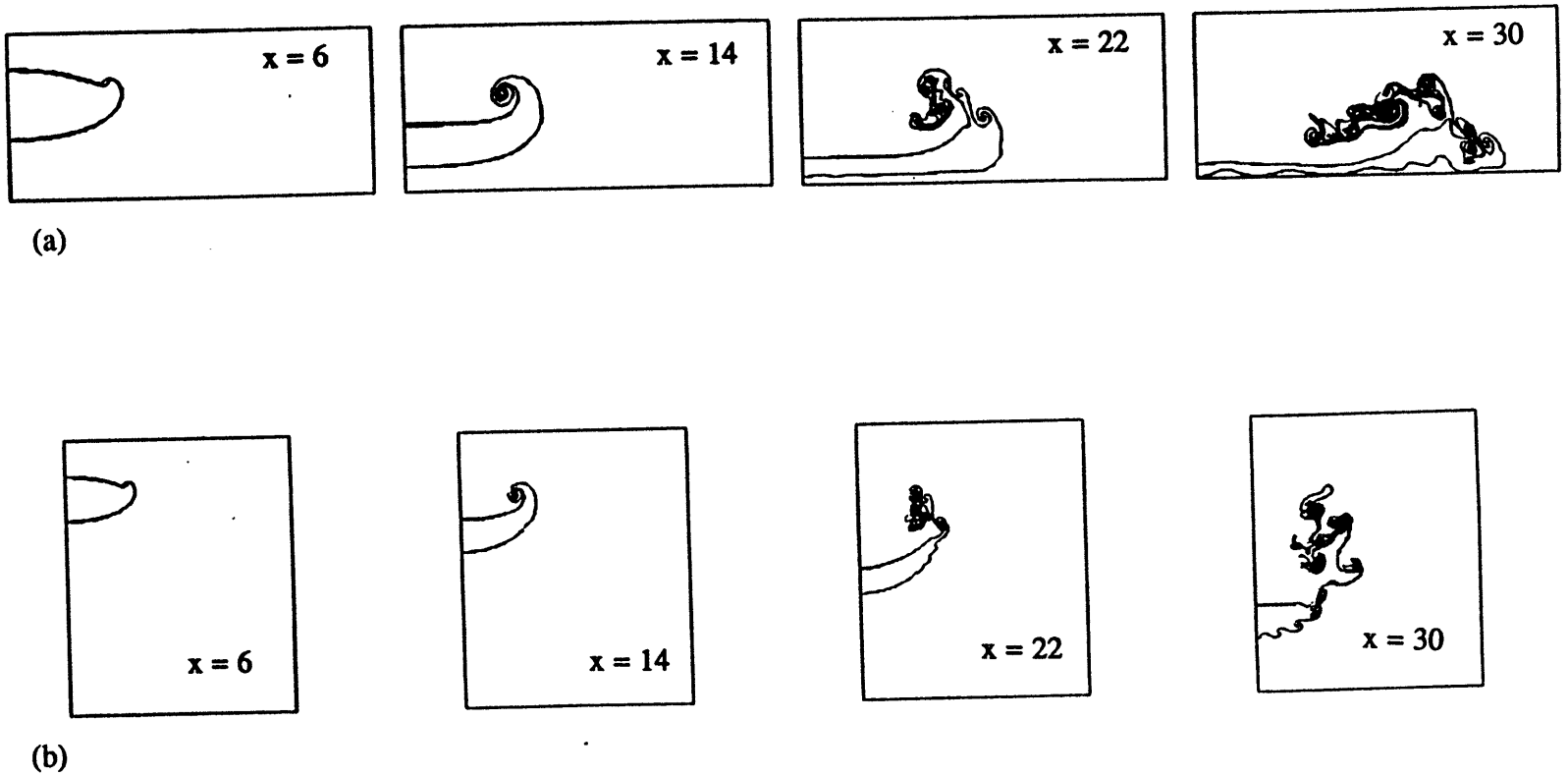

Figure 4.6. The plume cross section at different downwind stations for the case with: (a) $HT/R_z = 3$, and (b) $HT/R_z = 30$. Both cases start with same cross section and same smoke distribution.

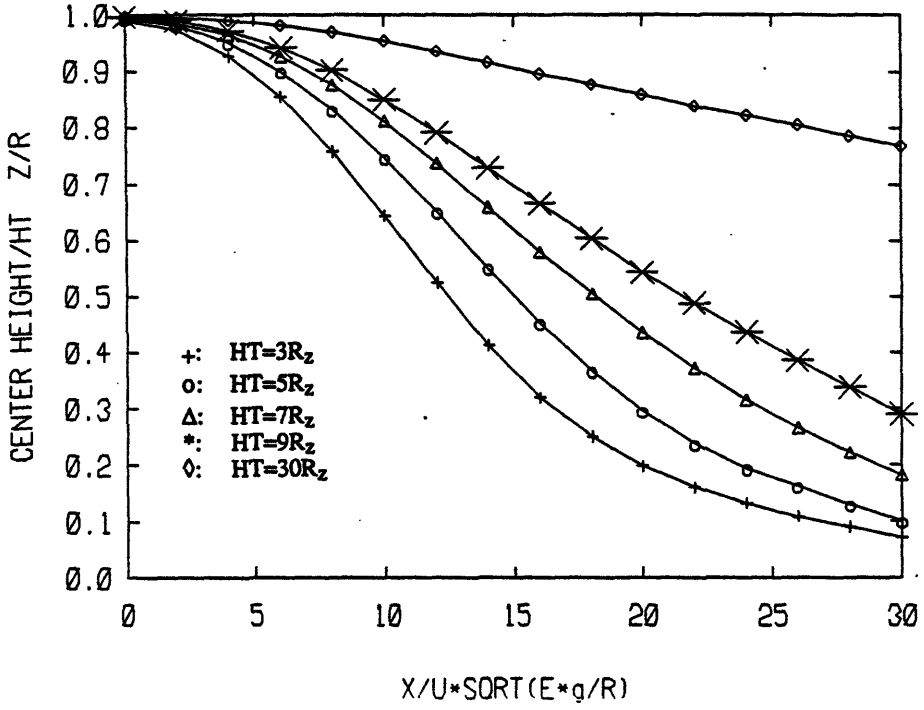

Figure 4.7. Streamwise evolution of the height of smoke plumes with $R_y = 3\ R_z$, and $\rho = 0.106$. Curves are generated for initial heights $HT = 3\ R_z$ (+), $5\ R_z$ (o), $7\ R_z$ (Δ), $9\ R_z$ (*), and $30\ R_z$ (◊).

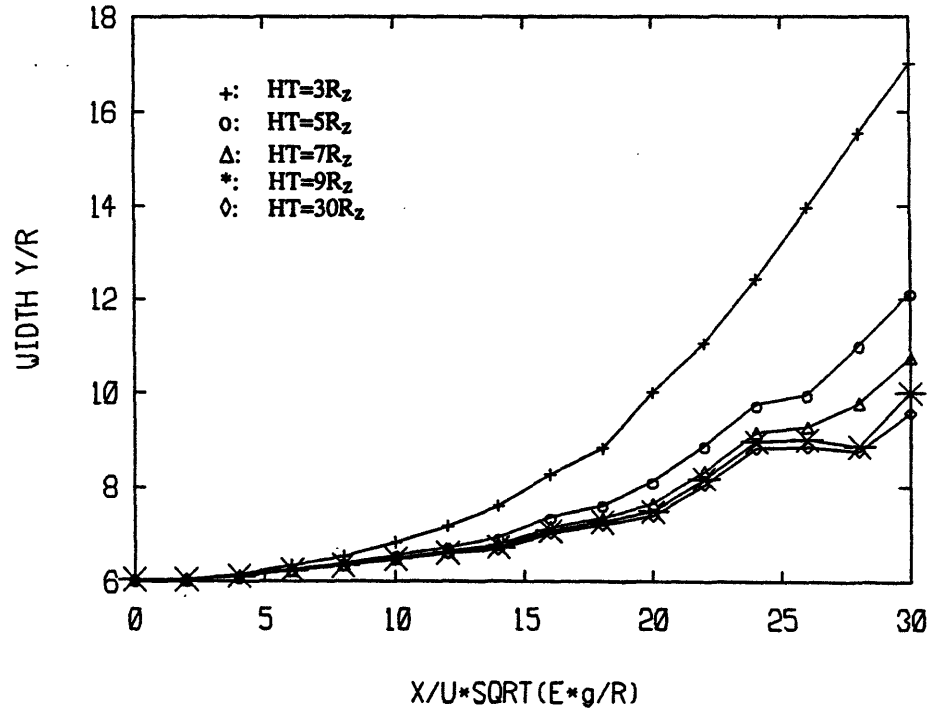

Figure 4.8. Streamwise evolution of the width of the smoke plume in figure 4.7. For meaning of symbols, refer to the caption of figure 4.7.

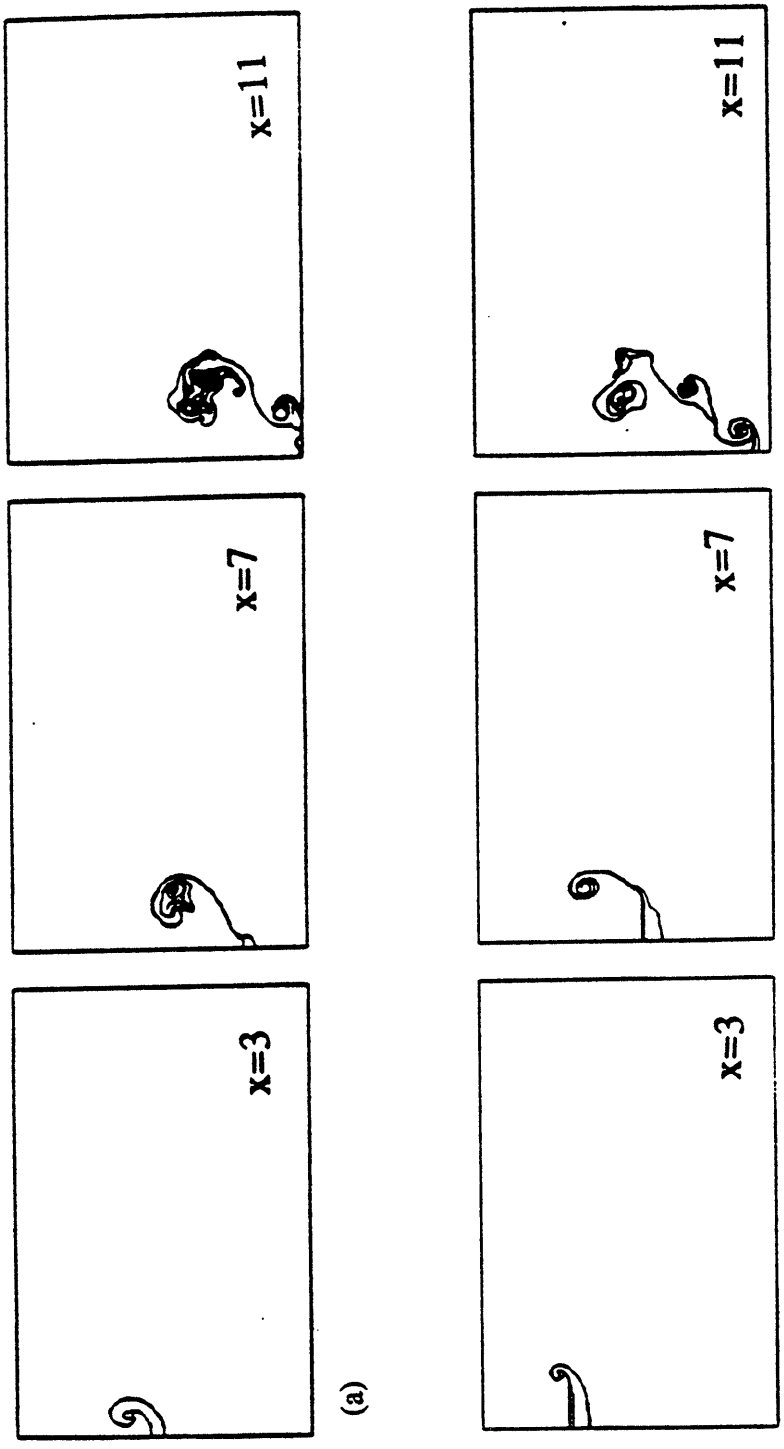

Figure 4.9. the plume cross section at different downwind station for plumes with: (a) *AR* = *1* and (b) *AR* = *6*. Both cases have the same initial height and smoke density distribution within the plume cross section.

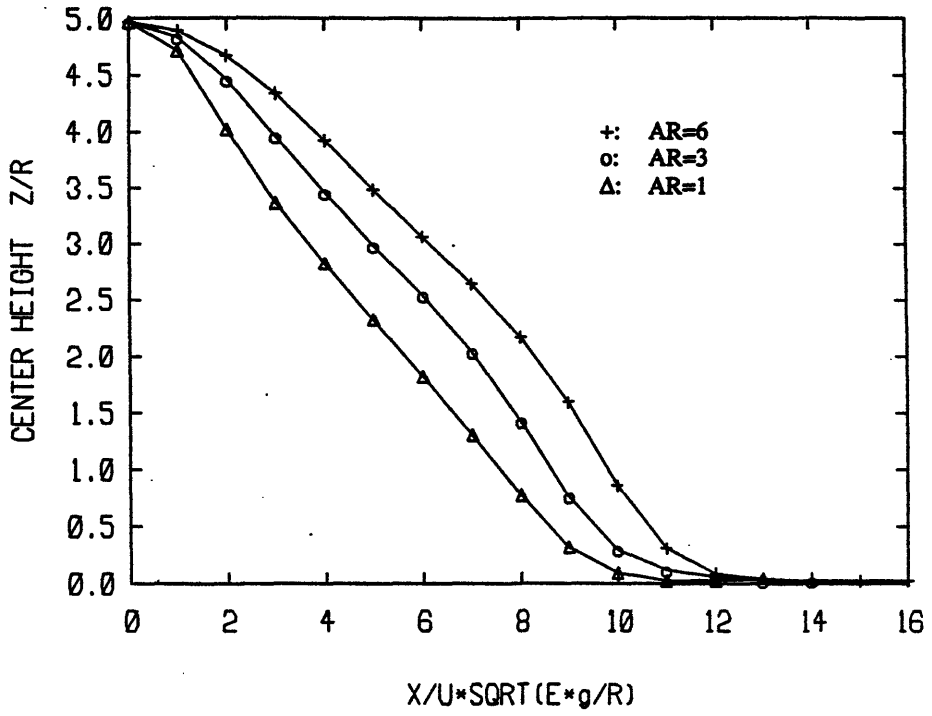

Figure 4.10. The streamwise evolution of the height of smoke plumes with $\rho = 1$, $HT = 5$ R and same initial cross-sectional area. Curves are generated for aspect ratios of initial plume sections of $AR = 6$ (+), 3 (o), and 1 (Δ).

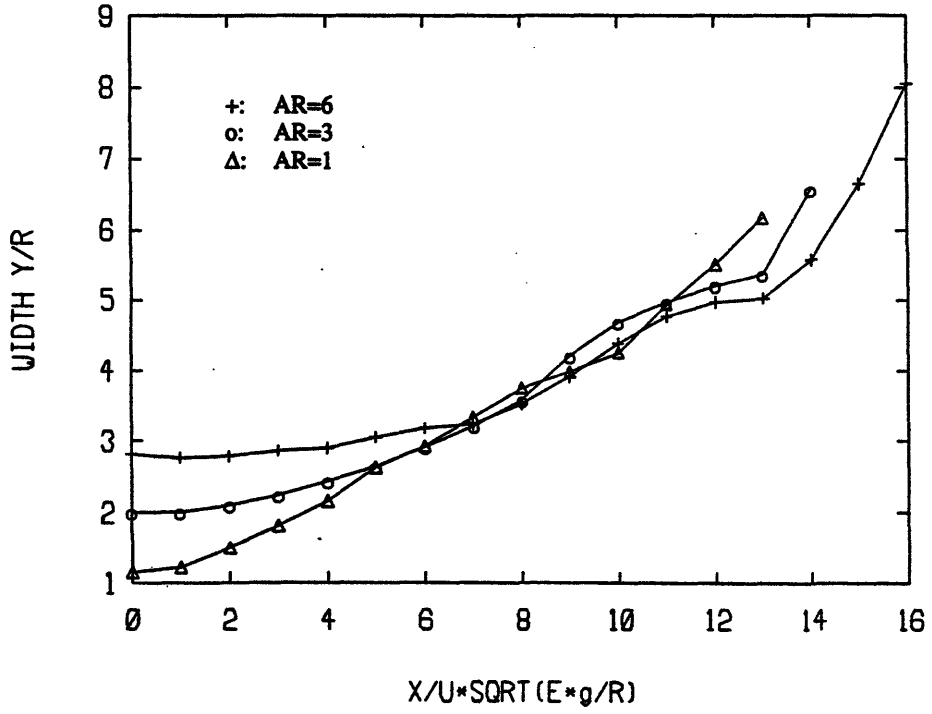

Figure 4.11. Streamwise evolution of the width of the plumes in figure 4.10. For meaning of symbols, refer to the caption of figure 4.10.

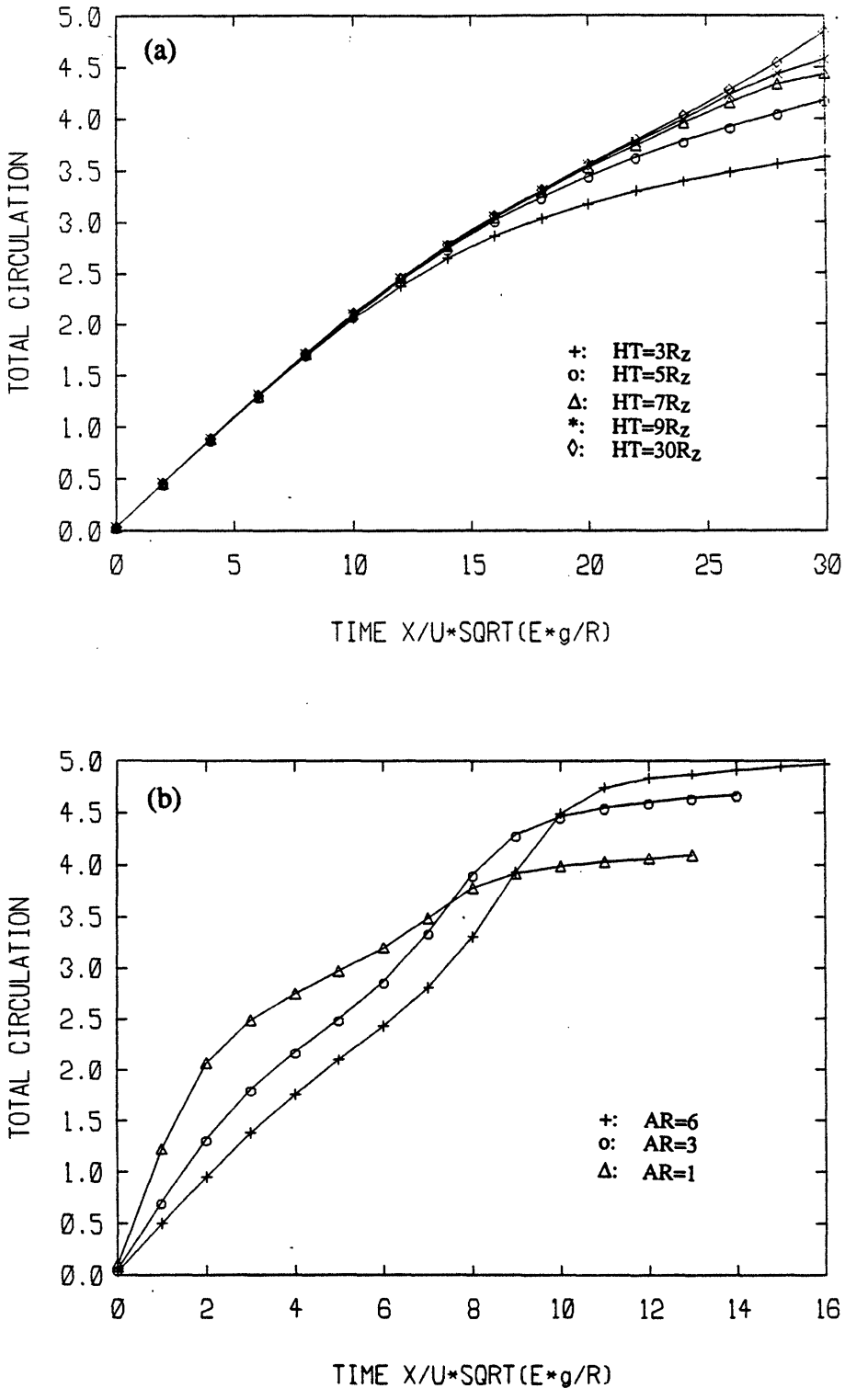

Figure 4.12. Variation of the total circulation of each large coherent vortex in the plume cross section with downwind distance. Shown is the circulation of the right-hand side of the plume for (a) the cases shown in figure 4.6, and (b) the cases shown in figure 4.9.

CHAPTER 5

THE SPREAD AND DISPERSION OF AN AXISYMMETRIC DENSE CLOUD

ABSTRACT

A computational model based on the Lagrangian transport element method is used to simulate an axisymmetric dense cloud motion. The methodology, free of the Boussinesq approximation and turbulent closure modeling, models the spreading and dispersion of a heavy gas cloud after its sudden release when the flow motion is driven by the cloud buoyancy and the atmospheric turbulence is negligible. Simulations of the collapse of an initially upstanding cylindrical dense cloud show that multiple large scale concentric vortex rings are generated at the cloud surface. Most of the cloud material is associated with the spreading front, where the largest and strongest vortex ring is located. The generation of these vortex rings is explained using the baroclinic vorticity generation mechanism. The entrainment of surrounding air into the dense cloud is shown to occur mainly at the cloud top through the large-scale engulfment by the vortex rings. This fact is employed to formulate an entrainment hypothesis which is used in our analytical modeling. The results on the cloud dispersion pattern and the spreading of horizontal cloud compare well with experimental observations.

A simple analytical model to describe the cloud motion is also developed. This model utilizes the law of mechanical energy conservation and parameterizes the kinetic energy and dissipated energy in terms of quantities characterizing the mean motion. The entrainment into the cloud is assumed to be proportional to the spreading area of the top cloud surface. The model gives a simple relation for the time dependence of the cloud radial extent. The decay of the maximum concentration is found to be inversely proportional to the square of the frontal radius. The model is validated through intensive comparison with laboratory and field measurements for various initial volume, density ratios and geometrical aspect ratios.

NOMENCLATURE

C_a: Cloud averaged concentration;

C_m: Maximum cloud concentration;

C_o: Initial cloud concentration;

D: Diameter of the cylindrical dense cloud (initially, D_o);

g: Gravitational acceleration;

H: Height of the cylindrical dense cloud (initially, H_o);

r: Radial direction;

R: Frontal spreading radius (initially, R_o);

t: dimensional time;

t^*: $\equiv t\sqrt{g/V_o^{1/3}}$, dimensionless time used in numerical computation;

t': $\equiv t\sqrt{\frac{\rho_o-\rho_a}{\rho_a}\frac{g}{V_o^{1/3}}}$, dimensionless time used in physical experiments and in theory;

t'': $\equiv t\sqrt{\frac{\rho_o-\rho_a}{\rho_o+\rho_a}\frac{g}{V_o^{1/3}}}$, dimensionless time suggested by Yih (1965) and Fay (1982);

u, w: Velocity components in r, z direction, respectively;

V: Volume of the dense cloud (initially, V_o);

x^*: Dimensionless radial extent of the dense cloud increased after its horizontal spreading;

z: Vertical direction;

δ_i: Radius of the cross section of computational ring element;

Γ_i: Circulation of a vortex ring element;

ρ_a: Density of air surrounding the dense cloud, reference density;

ρ_i: Radius of computational ring element;

ρ_o: Initial density of the dense cloud.

5.1. INTRODUCTION

Public concern over the risk posed by the accidental release of hazardous materials has grown over the past decade (McQuaid 1985, Puttock 1988a, Britter 1989). The sudden release of hazardous industrial materials produce a cloud which is denser than the air. Most current interest centers on combustible hydrocarbon fuels, e.g., liquefied methane (LNG), ethane and propane or butane (LPG); and toxic gases, ammonia, chlorine, sulfur dioxide and hydrogen sulfide, etc. (Fay, 1980). Due to the extreme volatility of these liquefied gases, a very large vapor cloud forms in a short period of time if the liquid is suddenly released. Thus, the vapor release is often modeled as an ideal instantaneous formation of the full volume of cloud. The information on the dispersion of these dense gases that is interest to a hazard analyst is mainly the distribution of concentration as a function of location and time.

The case of the collapse and spread of an isothermal dense cloud over a smooth surface in calm air is of special interest. The initial state is a quiescent upstanding cylindrical cloud with volume V_o, radius R_o and height H_o. Its density ρ_o is uniform and greater than the air density ρ_a. The cloud temperature is the same as the ambient temperature. Understanding the dispersion of this case, which has been the focus of many studies (Britter 1989), is very instructive.

Large scale field experiments, like the Thorney Island experiment (1982-83) (McQuaid 1985), and laboratory experiments (Havens and Spicer 1985) have been performed to explain the dispersion of a dense cloud cylinder. Figure 5.1.1 shows the Thorney Island experiment, where (a) is taken at the moment right before the dense cloud collapse; and (b) is a top view of the cloud shortly after its collapse. Figure 5.1.2 shows a laboratory experiment, in which 135 liters of Freon-12/air mixtures was released, at different view angles and times. The measured results were frequently utilized to guide the development of models and/or to validate them.

It is frequently observed from these experiments that, after a sudden release of heavy gas on the ground, its dispersion can be approximately divided into two stages. The first stage, when the cloud collapses and a toroidal vortex ring is generated at the spreading front, is the acceleration and fast spreading stage. During this stage, most of the cloud material is contained within the vortex ring, see figure 5.1.1b and 5.1.2a,b. When the ambient wind is weak, this vortex ring is quite stable and the flow structure stays fairly coherent (Rottman and Hunt 1985). Sometimes, multiple concentric rings or waves, which continue to expand nearly axisymmetrically, are observed (Spicer and Havens 1985), see figure 5.1.2c. The dominant driving force for this first stage is the negative buoyancy of the dense cloud. In the second stage, the cloud acts more like a passive tracer and its dispersion is controlled by the ambient wind and atmospheric turbulence. Clearly, a simple Gaussian model can not describe the vortex ring formation and the gravity spreading during the first stage, and a through understanding of the controlling dynamics is not available at the moment.

Since the major difficulty rests upon the study of the first stage, on which the dispersion of the later stage depends, several analytical and numerical models have been developed. A detailed review can be found in Puttock (1988a) and Britter (1989). The main interest of the studies is in the rate of frontal spreading and the formation of the vortex ring. Analytical models, mostly of integral type, are usually based on fundamental physical principles, an entrainment assumption, and turbulent modeling. (Fay 1980, Byggstoyl and Saetran 1983, Carn 1987, van Ulden 1988, Matthias 1992, etc.) The validity of the entrainment assumption is crucial to the performance of the model. Hanna and Drivas (1987) studied several correlations for the cloud top entrainment when the horizontal area of the cloud is increased. Puttock (1988b) studied the effect of the frontal edge entrainment velocity. Most often, these models contain too many free constants, such as entrainment rates and effective time delay, which are not easy to determine. The calculation of the maximum concentration still involves large uncertainty. Furthermore,

most analytical models use the Boussinesq approximation, which is invalid in practice since most gases of interest in the accidents are much heavier than air.

Numerical models provide more detailed and accurate predictions of the cloud dynamics (England et al 1978, Chan et al 1987, Havens et al 1987, Jacobson et al 1987, Ermak et al 1988). However, large numerical diffusion and the limited validity of the turbulence-closure formulation (Eidsvik 1980) for buoyant flows restrict the application of these models. Although the formation of the frontal vortex ring is recognized to be important, its description is still unsatisfactory (Rottman and Hunt 1985).

In this work, we first develop a numerical model to simulate an axisymmetric dense cloud dispersion during the first stage using the transport element method. Performed without invoking turbulence models, the numerical calculation is intended to improve our understanding of the entrainment process, the effect of large density ratio between the dense gas and air, and the effect of the cloud aspect ratio (the ratio between the diameter and the height of the initially cylindrical dense cloud). Based on the numerical result that the entrainment is mostly associated with the multiple ring formation at the cloud top, a simple analytical model is developed. The model is constructed in terms of mechanical energy balance and involves fewer arbitrary constant. The Boussinesq approximation is not invoked in the numerical and the analytical models.

This Chapter is organized as follows. In Section 5.2, we present the formulation of the physical model and delineate the mechanism of baroclinic vorticity generation which is responsible for the vortex ring formation. In Section 5.3, we describe the numerical scheme in detail. In Section 5.4, we present the numerical results in terms of cloud shape, spreading and entrainment analysis. Parametric studies on the effects of density ratio and aspect ratio are performed. In Section 5.5, a theoretical model is developed and the results are compared with laboratory and field experiments. Finally, the main results of the work are summarized in Section 5.6.

5.2. PHYSICAL MODEL AND MECHANISM OF VORTEX RING FORMATION

In our numerical simulation, only the first stage of the dense cloud dispersion is considered and the following approximations are applied:

(1) the buoyancy of the dense cloud dominates the flow, and atmospheric turbulence is negligible[15];

(2) the dense cloud is released on a flat terrain and the motion is axisymmetric;

(3) the ground friction and heat transfer are negligible since the viscous and thermal boundary layer thicknesses are much smaller than the cloud height;

(4) the thermodynamic effects, including heat capacity, air moisture, and condensation, are neglected.

Based on these assumptions, the governing equations describing the collapse and dispersion of a dense cloud are:

$$\frac{1}{r}\frac{\partial}{\partial r}(ru)+\frac{\partial w}{\partial z}=0 \tag{5.2.1a}$$

$$\frac{\partial u}{\partial t}+u\frac{\partial u}{\partial r}+w\frac{\partial u}{\partial z}=-\frac{1}{\rho}\frac{\partial p}{\partial r} \tag{5.2.1b}$$

$$\frac{\partial w}{\partial t}+u\frac{\partial w}{\partial r}+w\frac{\partial w}{\partial z}=-\frac{1}{\rho}\frac{\partial p}{\partial z}-\frac{\rho_p g}{\rho} \tag{5.2.1c}$$

$$\frac{\partial \rho}{\partial t}+u\frac{\partial \rho}{\partial r}+w\frac{\partial \rho}{\partial z}=0 \tag{5.2.1d}$$

where, r and z are radial and vertical coordinates pointing outwards and upwards; u and w are the velocity components in these directions; t is the time counted from cloud release; p is the pressure; and $\rho_p = \rho - \rho_a$ is the density perturbation. For nondiffusive flow, a suitable boundary condition at the ground is

$$w = 0 \text{ and } \frac{\partial \rho}{\partial z}=0, \qquad \text{at } z = 0. \tag{5.2.1e}$$

---

[15] A criterion for this approximation may be expressed in terms of Richardson number, the ratio of the relative importance of the gravitational slumping flow to atmospheric turbulence, $Ri=\frac{(\rho-\rho_a)g}{\rho_a}\frac{V^{1/3}}{u^{*2}}$, where ρ, V, u^* are the cloud density, cloud volume, and the friction velocity of the ambient flow, respectively.

The initial condition for the instantaneously released dense cloud is

$$u = w = 0,$$

$$\rho = \begin{cases} \rho_o, & r \le R_o \text{ and } z \le H_o \\ \rho_a, & \text{anywhere else} \end{cases} \qquad \text{at } t = 0. \tag{5.2.1f}$$

We use the following dimensionless variables to normalize the above equations,

$$(r^*, z^*) = (r/V_o^{1/3}, z/V_o^{1/3}) \tag{5.2.2a}$$

$$(u^*, w^*) = (u/\sqrt{g\, V_o^{1/3}}, w/\sqrt{g\, V_o^{1/3}}) \tag{5.2.2b}$$

$$t^* = t\sqrt{\frac{g}{V_o^{1/3}}} \tag{5.2.2c}$$

$$p^* = \frac{p}{\rho_a g V_o^{1/3}} \tag{5.2.2d}$$

$$\rho_p^* = \frac{\rho_o - \rho_a}{\rho_a} = \frac{\rho_p}{\rho_a}, \tag{5.2.2e}$$

where $V_o = \pi H_o R_o^2$ is the initial volume of the dense cloud. The normalized governing equations (after omitting *) become

$$\frac{1}{r}\frac{\partial}{\partial r}(r u) + \frac{\partial w}{\partial z} = 0 \tag{5.2.3a}$$

$$\frac{\partial u}{\partial t} + u\frac{\partial u}{\partial r} + w\frac{\partial u}{\partial z} = -\frac{1}{1+\rho_p}\frac{\partial p}{\partial r} \tag{5.2.3b}$$

$$\frac{\partial w}{\partial t} + u\frac{\partial w}{\partial r} + w\frac{\partial w}{\partial z} = -\frac{1}{1+\rho_p}\frac{\partial p}{\partial z} - \frac{\rho_p}{1+\rho_p} \tag{5.2.3c}$$

$$\frac{\partial \rho_p}{\partial t} + u\frac{\partial \rho_p}{\partial r} + w\frac{\partial \rho_p}{\partial z} = 0. \tag{5.2.3d}$$

Defining a dimensionless vorticity, taken positive in the anticlockwise direction if viewing downwards, $\omega = \frac{\partial u}{\partial z} - \frac{\partial w}{\partial r}$, and cross differentiating the momentum equations (5.2.3b,c), we get the vorticity transport equation

$$\frac{D\omega}{Dt} = \frac{u\omega}{r} - \frac{1}{(1+\rho_p)^2}\left(\frac{\partial \rho_p \partial p}{\partial r\, \partial z} - \frac{\partial \rho_p \partial p}{\partial z\, \partial r}\right) + \frac{1}{(1+\rho_p)^2}\frac{\partial \rho_p}{\partial r} \tag{5.2.4}$$

where $D/Dt = \partial/\partial t + u\,\partial/\partial x + w\,\partial/\partial z$ is the substantial derivative. In deriving (5.2.4), the Boussinesq approximation has not been applied. In conservative form, equation (5.2.4) is

$$\frac{D(\omega/r)}{Dt} = \frac{G}{r} \tag{5.2.5}$$

where G, on the right hand side of the equation, is the baroclinic vorticity generation term:

$$G = \frac{-1}{(1+\rho_p)^2}\left(\frac{\partial \rho_p \partial p}{\partial r\, \partial z} - \frac{\partial \rho_p \partial p}{\partial z\, \partial r}\right) + \frac{1}{(1+\rho_p)^2}\frac{\partial \rho_p}{\partial r} \tag{5.2.6}$$

The components of the pressure gradient in (5.2.6) are obtained from equations (5.2.3b,c) as

$$\frac{\partial p}{\partial r} = -(1+\rho_p)\frac{Du}{Dt} \tag{5.2.7}$$

$$\frac{\partial p}{\partial z} = -(1+\rho_p)\frac{Dw}{Dt} - \rho_p \tag{5.2.8}$$

These equations are to be solved by the axisymmetric transport element method, which will be described in detail in the next section.

From the vorticity equation (5.2.5), we know that the vorticity component in the circumferential direction is generated due to the fact that the surfaces of constant pressure and constant density do not coincide, i.e., non-zero baroclinicity expressed by equation (5.2.6). The major contribution to G initially is from the horizontal density gradient. At the moment of release of the dense cloud, the horizontal density gradient is very large. The term G is significant over the entire side wall of the cylindrical cylinder. This so-generated vorticity field induces a motion which pulls the cloud downwards and outwards, see figure 5.2.1. As the cloud front spreads, the circulation associated with the front ring gradually increases and rings of smaller sizes are also generated behind it. An entrainment process, which accompanies the rollup of the thin vorticity layer between the cloud and the surrounding, is controlled by the strength of the vortex rings.

5.3. NUMERICAL SCHEMES

5.3.1. The Axisymmetric Vortex Method

The application of the vortex method to the solution of axisymmetric flow is based on the discretization of the vorticity field into a number of thin vortex ring[16] elements of finite volume and the transport of these elements along their corresponding trajectories. The method has been developed and used in the calculation of bluff-body flow dynamics (Ghoniem et al, 1991). In this method, the vortex ring element is chosen to be of the Rankine type, that is, the vorticity inside the ring's cross section is uniform ω_i and outside zero. We denote $\Gamma_i = \omega_i \, \delta A_i$ as the circulation around the ith vortex-ring with center location at $\chi_i = (\rho_i, \zeta_i)$ in any meridional plane, where δA_i is the cross sectional area of this vortex ring element, $\delta A_i = \pi \, \delta_i^2$, and δ_i be the finite core radius, see figure 5.3.1 for notation. The discretization can be written as

$$\omega(\mathbf{x}, t) = \sum_{i=1}^{N} \frac{\Gamma_i}{\delta A_i} H\left(\frac{|\mathbf{x} - \chi_i|}{\delta_i}\right) \tag{5.3.1}$$

where H(.) is the Heaviside function, which is one if the argument is greater or equal to 1 and zero if otherwise. Since the continuity equation for an incompressible flow ensures the volume conservation of any ring element, $\delta A_i \rho_i = constant$, we can obtain the following circulation equation for each vortex ring element from equation (5.2.5),

$$\frac{d\,\Gamma_i}{d\,t} = \delta A_i G, \tag{5.3.2}$$

where G is the vorticity generation term. If $G = 0$, equation (5.3.2) is the well known Kelvin theorem which states that the circulation of a closed vortex ring does not change as the ring moves in a non-diffusive, uniform density field, although the cross sectional area of the ring, δA_i, varies as the radius of element ring increases or decreases. If $G \neq 0$, the circulation of each element ring changes due to the generation of baroclinic vorticity. The change can be calculated based on an accurate evaluation of G which will be described in the subsection for the transport element method. The vortical velocity

---

[16] The vortex ring is thin if the radius of its cross section is much smaller than the radius of the ring.

components at point $x = (r, z)$ induced by a single vortex ring element located at χ_i, when $|\mathbf{x} - \chi_i| \geq \delta_i$, is calculated from (Lamb 1945)

$$u_i(\mathbf{x}, t) = \frac{-\Gamma_i}{2\pi r} \frac{(z-\zeta_i)(s_{1i}+s_{2i})}{s_{1i}\, s_{2i}} \{ K(\lambda_i) - \frac{E(\lambda_i)}{2} [\frac{s_{2i}}{s_{1i}} + \frac{s_{1i}}{s_{2i}}] \} \tag{5.3.3a}$$

$$w_i(\mathbf{x}, t) = \frac{\Gamma_i}{2\pi r} \{ [\frac{r-\rho_i}{s_{1i}} + \frac{r+\rho_i}{s_{2i}}] [K(\lambda_i) - E(\lambda_i)] + \frac{s_{2i}-s_{1i}}{2} E(\lambda_i) [\frac{r+\rho_i}{s_{2i}^2} - \frac{r-\rho_i}{s_{1i}^2}] \} \tag{5.3.3b}$$

where

$$s_{2i/1i} = \sqrt{(z-\zeta_i)^2 + (r +/- \rho_i)^2} \tag{5.3.4a}$$

$$\lambda_i = \frac{s_{2i}-s_{1i}}{s_{2i}+s_{1i}} \qquad 0 \leq \lambda_i \leq 1 \tag{5.3.4b}$$

$$K(\lambda) = \int_0^1 \left[(1-t^2)\left(1-\lambda^2 t^2\right)\right]^{-1/2} dt \tag{5.3.4c}$$

$$E(\lambda) = \int_0^1 (1-t^2)^{-1/2} \left(1-\lambda^2 t^2\right)^{1/2} dt. \tag{5.3.4d}$$

A thin vortex ring travels in an unbounded, incompressible, frictionless flow with all properties invariant with a self-induced velocity given by (Saffman 1970):

$$u_{si} = 0 \qquad \text{and} \qquad w_{si} = \frac{\Gamma_i}{4\pi\rho_i} [\, ln\frac{8\rho_i}{\delta_i} - 0.558\,]. \tag{5.3.5}$$

The induced velocity within the core, $|\mathbf{x} - \chi_i| < \delta_i$, is approximated by linear interpolation between (u_{si}, w_{si}) at the center of the core to a velocity calculated using equations (5.3.3) and (5.3.4) at its outer edge, at point $\mathbf{x} = \chi_i + \delta_i \mathbf{e}$, where $\mathbf{e}$ is the unit vector in the direction of $\mathbf{x} - \chi_i$.

This algorithm only holds for thin vortex rings, $\delta_i/\rho_i << 1$. In the situation when the vortex ring is not thin, the element's circular cross section can not be maintained and the expressions (5.3.3)-(5.3.5) do not approximate the velocity accurately. The treatment of "fat" vortex rings can be facilitated using Hill's spherical vortex which is discussed in the next subsection. Thus, the vortical velocity induced by N thin vortex ring elements is obtained from

$$u_\omega(\mathbf{x},t) = \sum_{i=1}^{N} u_i(\mathbf{x},t) \qquad \text{and} \qquad w_\omega(\mathbf{x},t) = \sum_{i=1}^{N} w_i(\mathbf{x},t). \tag{5.3.6}$$

5.3.2. Hill's Spherical Vortex

The induced velocity of fat vortex ring elements, which are generally located very close to the axis $r=0$, is approximated using Hill's spherical vortex. Before presenting the calculation scheme, we first review the properties of Hill's spherical vortex (Lamb 1945). For a stationary spherical vortex, centered at $(r=0, z=0)$, the flow field is divided into two regions. Outside the vortex, $R^2 = r^2 + z^2 > a^2$, where a is the radius of the vortex and R is the radial distance to the center, the streamfunction is given by

$$\varphi_o = \frac{1}{2} U (R^2 - z^2) \left(1 - \frac{a^3}{R^3}\right), \tag{5.3.7}$$

the same as a potential flow, with velocity U at infinity, over a sphere. Within the vortex, $R < a$, the flow is described by

$$\varphi_i = \frac{1}{2} A (R^2 - z^2)(a^2 - R^2), \tag{5.3.8}$$

where A is a constant, which can be determined by a condition of continuous radial velocity at $R=a$, $\partial\varphi_i/\partial R = \partial\varphi_o/\partial R$, as $A = -3U/2a^2$. The vorticity field inside the vortex is thus

$$\omega_i = -5 A r = \frac{15 U r}{2 a^2}, \tag{5.3.9}$$

and the associated circulation surround a Hill's vortex ring in any meridional plane is

$$\Gamma = \int_0^{\pi} d\theta \int_0^{a} \omega_i r \, dr = \frac{5\pi}{2} U a \tag{5.3.10}$$

From equation (5.3.7), the induced velocity by a Hill's vortex is given by

$$u = \frac{1}{r}\frac{\partial \varphi_o}{\partial z} = \frac{3}{2} U r z \frac{a^3}{(r^2 + z^2)^{5/2}} \tag{5.3.11a}$$

$$w = -\frac{1}{r}\frac{\partial \varphi_o}{\partial r} = -U\left[1 - \frac{a^3}{(r^2 + z^2)^{3/2}}\right] - \frac{3}{2}\frac{U a^3 r^2}{(r^2 + z^2)^{5/2}} \tag{5.3.11b}$$

This velocity field is induced by a non-moving Hill's vortex. The far field flow is moving at a velocity U downwards (in the negative z direction) which is related to the circulation of the vortex through (5.3.10). Equivalently, a Hill's spherical vortex moves in a stationary field at a self-induced velocity U upwards, and sets up the following vertical velocity field outside its boundary

$$w = \frac{U a^3}{(r^2 + z^2)^{3/2}} - \frac{3}{2}\frac{U a^3 r^2}{(r^2 + z^2)^{5/2}}. \tag{5.3.12}$$

In summary, the Hill's spherical vortex has: radius a; circulation described by (5.3.10); self-induced upwards velocity U; and induced velocity (5.3.11a) and (5.3.12).

Norbury (1973) pointed out that the classical thin vortex ring as described above and the Hill's spherical vortex are two extremes of a family of vortex rings based on a single parameter $\alpha = \delta_{eff}/\rho$, where δ_{eff} is the radius of the cross section as if it were circular and with the same area, and ρ is the major radius of the ring. When $\alpha \to \sqrt{2}$, the vortex ring approaches a Hill's spherical vortex, and $\alpha \to 0$ to a thin vortex ring with circular cross section. Norbury's computation indicates that for $\alpha \leq 0.2$ the shape of the cross section of the vortex ring is indistinguishable from that of a circular. Knio and Ghoniem (1990), through numerical calculation, found that equation (5.3.5) worked well for $\delta_i/\rho_i \leq 0.2$. Therefore, vortex ring with $\delta_i/\rho_i \leq 0.2$ can be considered as thin, and the induced vortical velocity field can be calculated by equations (5.3.3)-(5.3.5).

To have a practical treatment of the flow region near the axis, the collective effect of all fat vortex rings, with $\delta_i/\rho_i > 0.2$, is approximately accounted for by a Hill's spherical vortex with radius $a=5\delta$, where δ is the largest of δ_i. The circulation of the Hill's vortex is the algebraic sum of the circulation of all the rings inside the vortex. Since δ is of the same order of magnitude as the spatial resolution of the discretization, and since the flow near the axis does not involve much vorticity, $\omega = 0$, $\partial\rho/\partial r = 0$ and $u = 0$ on the axis, this approximation is expected to be reasonable. The induced vertical velocity w of Hill's vortex at $r=0$, by ring elements outside its boundary seems to be singular in equations (5.3.3) and (5.3.4). However, the singularity is removable. After some calculation using the L'Hospital's rule, this induced vertical velocity can be calculated from

$$w(r=0) = \sum \frac{\Gamma_i \rho_i^2}{2 s_\delta^3} \tag{5.3.13}$$

where the summation is over all elements with $\delta_i/\rho_i > 0.2$.

5.3.3. Transport Element Method

To calculate the vorticity generation term G on the right hand side of the vorticity equation, as given by (5.2.6), we use the axisymmetric form of the transport element method. In this method, instead of directly discretizing the density field, we discretize the density gradient field $\mathbf{g} = \nabla\rho_p$ into a finite number of Lagrangian transport elements,

$$\mathbf{g}(\mathbf{x}, t) = \sum_{i=1}^{N} \mathbf{g}_i H\left(\frac{|\mathbf{x} - \chi_i|}{\delta_i}\right) \tag{5.3.14}$$

where $\mathbf{g}_i$ is the density gradient of the flow field at the location of the ith element, as shown in figure 5.3.2. The time variation of the density gradient of each element can be obtained by a simple and accurate formula as follows. Assign layers which coincide with the density contours in any meridional plane with increment $\delta\rho_p$. When the fluid motion is incompressible and nondiffusive, the density of a fluid particle does not change as it moves[17]. Thus, the density increment $\delta\rho_p$ across any two layers does not change with time. The density gradient according to the definition is

$$\mathbf{g}_i(t) = (\nabla\rho_p)_i(t) = \frac{\delta\rho_p}{(\delta n(t))_i}\,\mathbf{n}_i(t) \tag{5.3.15}$$

where $n_i(t)$ is the unit vector normal to the density contour at the location where the ith element is located, $(\delta n(t))_i$ is the normal distance between the two adjacent density layers. We discretize the field into elements each with cross sectional area δA_i initially in the meridional plane. This cross section is stretched due to the fluid motion. This can be characterized by the length $(\delta l(t))_i$ along the density contour and $(\delta n(t))_i$ as defined above. Since the density of a fluid particle does not change as the flow evolves, mass conservation gives

$$(\delta n(t))_i\,(\delta l(t))_i\,\rho_i(t) = \delta A_i(0)\,\rho_i(0) \tag{5.3.16}$$

where $\rho_i(t)$ and $\rho_i(0)$ are the radii of the ring element at time t and $t=0$, respectively. Upon substitution of the above into equation (5.3.15), we have

---

[17] However, the turbulent mixing, generated by cloud buoyancy, alters the measured density in practical experiments. This is because the measurement is taken as an average over certain temporal and spatial scales when and where both dense gas and air are sampled.

$$\mathbf{g}_i(t) = \frac{\delta\rho_p \left(\delta\forall(t)\right)_i}{\delta A_i(0)} \frac{\rho_i(t)}{\rho_i(0)} \mathbf{n}_i(t) \tag{5.3.17}$$

Since the quantities on the right hand side of equation (5.3.17) can be obtained easily in our Lagrangian calculation, the transport element method, described by (5.3.17), is both accurate and efficient. This method has been used in two and three dimensional calculations of shear and gravity driven flows (Krishnan and Ghoniem 1992, Knio and Ghoniem 1991). We expect it to be equally useful in the axisymmetric case considered here.

5.3.4. Boundary Conditions

The condition of no normal flow, $w = 0$, at ground, $z = 0$, is satisfied by superimposing a counter-rotating vortex ring image for each vortex ring element. The image of the vortex ring element at $\chi_i = (\rho_i, \zeta_i)$ with circulation Γ_i is at $\chi_{ie} = (\rho_i, -\zeta_i)$ with circulation $-\Gamma_i$. The satisfaction of the zero normal density gradient at the ground $z = 0$ is done in a similar way.

To achieve accurate numerical results, we used the following numerical parameters: spatial discretization, $h=0.05$, time marching step, $\Delta t=0.01$, number of layers used to describe the large density gradient between the cloud and air, $L=4$. These parameters are chosen so that numerical results with smaller values of h, Δt and L are indistinguishable from the results described in this Chapter.

5.4. NUMERICAL RESULTS

The driving energy for the collapse and spread of a dense cloud is its initial potential energy. It is expected that with a large density ratio, ρ_o/ρ_a, or a small aspect ratio, D_o/H_o, i.e., with large initial potential energy, the collapse and spread of the cloud become faster. In this section, we study the instantaneous behavior of the dense cloud collapse, paying special attention to the entrainment of surrounding air and the effects of these two parameters on this process.

We performed numerical computations for five cases, whose parameters are provided in Table 5.1, where cases 1, 2 and 3 have the same density ratio but different aspect ratio, and case 1, 4 and 5 have the same aspect ratio but different density ratio. Figure 5.4.1 shows the dispersion pattern of a dense cloud with same initial volume and: (a) small aspect ratio and small density ratio, $D_o/H_o=1$, $\rho_o/\rho_a = 1.5$; (b) large aspect ratio and small density ratio, $D_o/H_o=3$, $\rho_o/\rho_a = 1.5$; and (c) small aspect ratio and large density ratio, $D_o/H_o=1$, $\rho_o/\rho_a = 4$.

The evolution of these three cases generally shows the similar overall pattern: as the cloud height decreases: the horizontal extent increases quickly, a large and intense vortex ring is generated at the frontal edge of the spreading cloud, and several smaller rings are generated behind the frontal ring.

The decrease of cloud height and the increase of the frontal radius show the conversion of initial potential energy into kinetic energy. Comparing (a) with (b), it is seen that for same cloud-to-air density ratio and same amount of cloud material released, the tall cloud, being of small radius initially, spreads faster. This is because the initial potential energy associated with case (a) is larger. Similarly, having the same aspect ratio and initial cloud volume as case (a), the cloud in case (c) which has a larger density ratio and therefore higher the potential energy, collapses and spreads faster. With smaller initial potential energy, case (b) retains considerable portion of the cloud material behind the evolving rings.

The mechanism for the generation of the large-scale frontal vortex ring and several smaller rings has been explained using the baroclinic vorticity generation mechanism in Section 5.2. These rings play a very important role in the dispersion of cloud material. As shown in figure 5.4.1, the frontal ring, being at the location of largest radius from the center and with largest thickness vertically, contains most of the cloud material, in accordance with the observations of both field and laboratory experiments. The generation of smaller rings behind the front was also a prevailing phenomenon in the laboratory experiment of Spicer and Havens (1885), where it is described as multi-rings and wave activity. The entrainment of surrounding air into the cloud is observed to be mostly through engulfment at the top side of the cloud. As the cloud spreads and covers more horizontal area, the intensity and the size of the rings are also increased. This reveals an entrainment relation: the volume of entrained air is proportional to the top surface of the spreading cloud. We will use this relation in the development of a simple analytical model to capture the major features of the dense cloud spreading in the next section.

Figure 5.4.2 shows case 5 at time $t^* = 7.7$ in terms of: (a) an enlarged frame of the rollup and convolution of the cloud-air interface; and (b) the position of the computational elements and their instantaneous velocity vectors. It is seen that the cloud material concentration is not uniform inside the rings, and thus considerable fluctuations maybe encountered in the experimental measurements of the concentration. This is because the mixing originates from buoyancy generated turbulence instead of diffusion of molecular type. Figure 5.4.2b shows that most of the computational elements are within the complex flow region, the rings; and fewer elsewhere, confirming the adaptivity of the numerical method. The instantaneous velocity vectors also show that the size of the horizontal velocity increases with radius, the front spreading speed being the largest.

The generation of baroclinic vorticity can also be measured quantitatively in terms of circulation associated with these vortex rings, which represents their strength. Figure

5.4.3 shows the total circulation integrated over a meridional plane for all five cases. The cloud with large initial potential energy generates the largest circulation, pulling the cloud downwards and outwards. Large initial potential energy is associated with larger initial density difference between the cloud and air, or a large area of side wall of the initial cylinder, to which baroclinic vorticity is proportional. It is also seen that in all five cases, the rate of increase of circulation slows down eventually. This is because of a reason similar to the one described in a buoyant plume rising in the atmosphere: vorticity with opposite sense also develops after certain time (Ghoniem et al 1993).

Figure 5.4.4 shows the dimensionless cloud radial extent, $x^* = (R^2 - R_o^2)/V_o^{2/3}$, versus time. This quantity is of primary interest in practice because a large portion of cloud material is within the frontal head. In the calculation of the area covered by the cloud, the frontal radius is defined by the computational ring element with the largest radius. The relation is presented in terms of dimensionless time,

$$t' \equiv t\sqrt{\frac{\rho_o-\rho_a}{\rho_a}\frac{g}{V_o^{1/3}}}, \qquad (5.4.1)$$

conventionally used in the laboratory and field experiments. The figure shows that three cases with the same density ratio but different aspect ratio almost overlap. While the three curves with same aspect ratio but different density ratio diverge considerably. However, it can also be seen that all these five curves asymptote to a linear relation after a rather short initial adjustment process, beyond $t^*=3$. This linear relation, of almost the same slope for all five cases, confirms the well observed relation which will be described in more detail in the next section. Thus, the initial collapse only produces a shift at the beginning of the linear behavior. At the later stages, the difference among the five cases becomes negligible compared to the large magnitude of the extended area. This suggests that the aspect ratio effect and the density ratio effect can be approximately grouped into the normalized variables x^* and t^*.

Fay (1982) has pointed out that the reduced gravity $g' = g(\rho_o-\rho_a)/\rho_a$ in equation (5.4.1) is not appropriate in describing the motion of very heavy gas, because this

modified gravitational acceleration could exceed the original one, g, for high (but not unusual) density ratios. A more physical choice of the scale should be $g''= g(\rho_o-\rho_a)/(\rho_o+\rho_a)$, which is the same one used by Yih (1965) in his compilation of experimental data on the frontal spread of gravity current[18]. Figure 5.4.5 shows the dimensionless cloud radial extent versus dimensionless time, $t'' \equiv t\sqrt{\frac{\rho_o-\rho_a}{\rho_o+\rho_a}\frac{g}{V_o^{1/3}}}$. We see that these five curves are getting much closer initially. However, considerable departure is still observed and the curves approach different slopes beyond $t''=1.5$. This suggests that neither normalization procedures can collapse all the curves into one over the entire period. Yih's scale, although considerably better during the early stage of collapse, will not be used further in this work because (1) the different asymptotic slopes make it difficult to compile data for the spreading at later time; (2) most experimental measurements are presented in terms of normalized time, t'.

The cloud height is an important parameter in the dispersion pattern. Figure 5.4.6 shows the evolution of the cloud height, defined as the height of the top computational element, for all five cases. It is seen that the height initially decreases rapidly and then approaches an asymptotic value. For the three cases with different initial height but same density ratio, the asymptotic height is almost the same, apart from a small fluctuation due to the turbulent nature of the flow. The asymptotic heights of the other two cases are only slightly higher. This agrees well with experimental measurements and confirms the assumption of several theoretical models developed in the past that the cloud height approaches a constant value after the fast collapse. It should also be pointed out that the highest thickness of the dense cloud after the initial collapse, as shown in the figure, is mostly associated with the frontal ring. Therefore, the slumping frontal vortex ring has a fairly long-lived coherent structure and its vertical size is described by this asymptotic height.

---

[18] Yih's experiment considered the gravitational intrusion of a heavy fluid into a lighter one within a channel with density ratio very close to one.

Figure 5.4.7 shows a comparison between numerical result, the laboratory measurements and the theory developed in the next section in terms of dimensionless cloud radial extent versus time. Since cases 1, 2 and 3 almost overlap, see figure 5.4.4, we draw only case 1, 4 and 5. The numerical computations are terminated before $t'=5$, considering that the assumption of neglecting friction near the ground becomes gradually invalid. The numerical result compares well with the experimental measurements within the small range of collapse and initial spread of the dense cloud. Since the simulation neglects the ground friction which would slow down the spreading, the radial extent of the simulated clouds increases faster than that of the physical experiments beyond $t'=4$.

Although the numerical simulation cannot be carried out to a later stage, it does reproduce the general features of the initial cloud collapsing quantitatively. The physics revealed from the computation, especially on the entrainment process, supported the development of a simple analytical model on the dense cloud spreading, as described in the following.

5.5. THEORY

5.5.1. Model Development

A schematic diagram for the notations used to describe a cylindrical dense cloud spreading under the influence of gravity after its sudden release is shown in figure 5.5.1. As in most analytical models, we use the similarity assumption: the dense cloud maintains a cylindrical shape with a time-dependent uniform density distribution as it disperses. From the results of the numerical simulations described in Section 5.4, and observations in both laboratory and field experiments, we notice that the turbulent mixing occurs mostly at the top side of the cloud as a result of engulfment of lighter air into the fields of a set of eddy rings. Based on these observations, we propose the following entrainment hypotheses: the volume of air entrained into the cloud is proportional to the extended surface of the top side of the cloud. Thus, at time t, measured from the moment of release, the volume of the dense cloud can be written as:

$$\pi R^2 H = \pi R_o^2 H_o \left[1 + \alpha^2 (R^2 - R_o^2)\right] \qquad (5.5.1)$$

where α, which has the unit of the inverse of length, characterizes the efficiency of entrainment. This parameter is expected to be dependent on the initial geometry of the gas and the density ratio between the gas and the air.

Due to mixing with surrounding air, the density of the cloud decreases according to the following mass conservation equation:

$$\rho V = \rho_o V_o + \rho_a V_o \ \alpha^2 (R^2 - R_o^2) \qquad (5.5.2)$$

where ρ_a, ρ_o and ρ are the air density, cloud density initially and at time t, respectively.

We notice that the cloud spread is driven by negative buoyancy. The source of energy needed for the dispersion of dense cloud in calm air is its initial potential energy. As the cloud spreads, part of the initial potential energy is transformed into the kinetic energy associated with the motion of the diluted cloud and part is dissipated due to ground friction. This statement can be written as:

$$PE_o = PE_t + KE_t + DE_t \qquad (5.5.3)$$

where the potential energy initially and time t are, respectively:

$$PE_o = \frac{1}{2}(\rho_o - \rho_a)\, g\, \pi R_o^2 H_o^2 \quad \text{and} \quad PE_t = \frac{1}{2}(\rho - \rho_a)\, g\, \pi R^2 H^2. \tag{5.5.4}$$

Since more energy is expected to be dissipated if more kinetic energy is attained by the cloud, the kinetic energy and the dissipated energy can be grouped together and written as

$$KE_t + DE_t = \frac{\rho}{2}(1 + k_v) \int_0^H \int_0^R (u^2 + w^2)\, 2\, \pi r\, dr\, dz \tag{5.5.5}$$

where u and w are the fluid velocity inside the cloud; u is assumed to be uniform vertically and w is uniform horizontally. The dimensionless empirical constant k_v is used here as an added mass coefficient accounting for the difference of mixing rate between volume and energy, to be determined by comparing the theory with experimental measurements. Equation (5.5.5) includes the kinetic energy of the dense gas and the air, contained in all scales equal to or smaller than the cloud size, and also the energy dissipated. This approach, which is based on the energy budget instead of the momentum equation, does not invoke the Boussinesq approximation and maintains the cloud density ρ as time dependent. The velocities u and w can be approximated in terms of the spreading frontal velocity dR/dt as:

$$u = \frac{r}{R}\frac{dR}{dt} \qquad \text{and} \qquad w = -2\,\frac{z}{R}\frac{dR}{dt}. \tag{5.5.6}$$

For most clouds, beyond the moment of collapse, $D/H >> 1$. Denoting the reduced gravity by $g' = \dfrac{\rho_o - \rho_a}{\rho_a} g$ and substituting for $H_o = V_o/\pi R_o^2$ and $H = V/\pi R^2$, the energy equation can be finally written as

$$1 - \frac{R_o^2}{R^2}\left[1 + \alpha^2(R^2 - R_o^2)\right] = \frac{1 + k_v}{2\, g' H_o}\left[\frac{\rho_o}{\rho_a} + \alpha^2(R^2 - R_o^2)\right]\left(\frac{dR}{dt}\right)^2. \tag{5.5.7}$$

This equation governs the evolution of the cloud frontal radius, given the initial condition $R = R_o$, at $t = 0$. Before solving equation (5.5.7), we normalize it using the same procedure as used in the compilation of experimental data;

$$x^* = \frac{R^2 - R_o^2}{V_o^{2/3}} \qquad t' = \frac{t}{\sqrt{V_o^{1/3}/g'}}. \tag{5.5.8}$$

Equation (5.5.7) becomes:

$$\frac{dx^*}{dt'} = \beta^* \frac{\sqrt{x^*}}{\sqrt{x^* + \alpha^*}} \tag{5.5.9}$$

and the initial condition is $x^* = 0$ at $t' = 0$, where $\alpha^* = \frac{\rho_o}{\rho_a} \frac{1}{\alpha^2} \frac{1}{V_o^{2/3}}$ and $\beta^* = \frac{2}{\alpha R_o} \sqrt{\frac{2\,(1 - \alpha^2 R_o^2)}{\pi\,(1 + k_v)}}$ are two dimensionless parameters related to entrainment and added mass coefficients. An analytical solution can be obtained for equation (5.5.9) :

$$\sqrt{x^*\,(x^* + \alpha^*)} + \alpha^* \ln \frac{\sqrt{x^*} + \sqrt{x^* + \alpha^*}}{\sqrt{\alpha^*}} = \beta^*\, t'. \qquad (5.5.10)$$

Both field and laboratory experiments have suggested the following correlation for frontal radius (Puttock, 1988) for large t',

$$R^{*2} = R_o^{*2} + \frac{2\,C_E}{\sqrt{\pi}}\, t' + constant \qquad (5.5.11)$$

where $R^* = R / V_o^{1/3}$, $R_o^* = R_o / V_o^{1/3}$. The parameter in (5.5.11), $C_E = 1.15 \pm 0.05$, is obtained from analysis of a number of published experiments (van Ulden, 1984)[19]. An asymptotic approximation to (5.5.10) for $x^* >> \alpha^*$ is

$$x^* \approx \beta^*\, t' \qquad (5.5.12)$$

apart from a slow time varying term. Therefore, one of the two empirical constants can be obtained by comparing the slope of (5.5.11) and (5.5.12),

$$\beta^* = \frac{2\,C_E}{\sqrt{\pi}} = 1.3. \qquad (5.5.13)$$

This value is quite universal since the error bound for C_E is very small. Next, we determine the constant α^* by fitting (5.5.10) with experimental measurements.

5.5.2. Extent Area of the Spreading Cloud

Havens and Spicer (1985) reported a series of laboratory experimental results on the instantaneous release of dense gas mixtures (Freon-12/air). The initial dense clouds are in the form of upstanding cylinder with initial volumes ranging from 0.034 m^3 to 0.135 m^3, density ratios 2.2 to 4.2, and aspect ratio 0.4 to 1.58. We first fit our model solution (5.5.10) with these measurements to obtain the empirical constant, α^*, and then use the model to predict, and compare with the large scale Thorney Island experiments.

---

[19] The proposed effective time delay in several box models is somehow related with this constant, but the detailed connection is unclear.

Figure 5.5.2 shows the comparison of theoretical prediction, equation (5.5.10), and the laboratory measurements under various initial conditions. In figure 5.5.2a, the initial density ratio is 4.18, aspect ratio is 1.0, and the initial volumes are 530, 135, 34.2, and 54.1 liters. The measurement data are read from the hardcopy of figure 1 in Havens et al. (1987). A satisfactory fit is obtained using $\alpha^*=1.7$. This suggests that the initial volume effect can be absorbed into the normalization in (5.5.8).

Figure 5.5.2b shows the comparison of the analytical result, using the same value of α^*, with the release of dense clouds with initial density ratio 2.16, aspect ratio 1.0, and different volumes: 34.2, 54.1, and 135 liters. The good fit indicates that the analytical result with same value of α^* is also representative for different initial density ratios. Further comparison of the same analytical curve and experiments with $\rho_o/\rho_a = 4.19$, $V_o=54.1$ liters, and different aspect ratios is shown in figure 5.5.2c. Again good fit is achieved. Thus, equation (5.5.10) can be used to predict the spreading of dense clouds with various initial volumes, density ratios and aspect ratios.

Now, we compare the model prediction with the large-scale Thorney Island experiment (McQuaid 1985), Trial 34, in figure 5.5.3. In this trial, the dense cloud is released under relatively calm wind condition with initial volume 2110 m^3, aspect ratio 1.0 and density ratio 1.83. The experimental data, as shown, are calculated by $x^* = R^{*2} - R^{*2}_o$ where the value of R^* is read from the hardcopy of figure 7 in Havens et al. (1987) and R^*_o is calculated from $R^{*2}_o = R^2_o/V^{2/3}_o = (R_o/\pi H_o)^{2/3} = 0.294$. The predicted trend is very good. However, the measured extent of the cloud area is somewhat larger than predicted. Part of the reason is that the cloud spreading is also influenced by the ambient wind, its mean speed at 10m height above the ground is 1.1m/s. The predicted radial extent of the cloud assumes no advection of the centroid. It is expected that the allowance for advection of the cloud centroid by the wind would improve the agreement.

Based on the two dimensionless empirical constants, $\alpha^*=1.7$ and $\beta^*=1.3$, their dimensional counterparts can be determined from the following:

$$\alpha^2 = \frac{\rho_o}{\rho_a}\frac{1}{\alpha^*}\frac{1}{V_o^{2/3}} \quad \text{and} \quad 1 + k_v = \frac{8\,(1 - \alpha^2 R_o^2)}{\pi \beta^{*2} \alpha^2 R_o^2} \tag{5.5.14}$$

5.5.3. Maximum Concentration

The entrainment relation (5.5.1) suggests that the cloud volume averaged concentration, C_a, is

$$\frac{C_a}{C_o} = \frac{V_o}{V} = \frac{1}{1 + \alpha^2 (R^2 - R_o^2)} = \frac{1}{1 + \frac{\rho_o}{\rho_a}\frac{x^*}{\alpha^*}} \tag{5.5.15}$$

where V_o and V are the volume of the cloud initially and at time t; C_o is the concentration of the dense gas initially. When this volume averaged concentration is compared with the locally observed concentration, the spatial variation should be accounted for since the concentration is higher close to the ground and at the front vortex ring. Furthermore, it should be noticed that the usual calculation of the volume of the dense cloud counts only the part where the concentration is higher than 2.5% or 1%, thus excluding a significant portion of gas with concentration lower than these values. Thus, the actual mean concentration is considerably less than the calculation indicates. Probably because of these difficulties, the data of mean concentration is seldomly reported.

However, the maximum concentration, while is of most interest in practice, can be easily measured. We assume the maximum concentration is proportional to the volume averaged concentration and can be calculated in terms of dimensionless variables by the following expression:

$$\frac{C_m}{C_o} = P\, R^{*-2}, \tag{5.5.16}$$

when $x^* >> \alpha^*$, where the parameter P is a proportionality factor, to be determined.

Figure 5.5.4 shows the decay of maximum concentration as a function of the cloud frontal radius R^* using equation (5.5.16) and laboratory experiments with: (a) $D_o/H_o=1.0$, $\rho_o/\rho_a = 4.19$ and different initial cloud volumes; (b) $D_o/H_o=1.0$, and

different density ratios; (c) $\rho_o/\rho_a = 4.19, V_o=54.1$ liters, and different aspect ratios. All the data in these three graphs are taken from Havens and Spicer (1985), while the model results are shown as solid lines. It is seen that most data points, in a log-log plot, can be characterized well by a line with slope -2 in the range $2<R^*<10$ for cases with different initial volumes, density ratios and aspect ratios[20]. The fit gives the following formula for the approximate calculation of the maximum concentration:

$$\frac{C_m}{C_o} = \begin{cases} 4/R^{*2}, & 2<R^*<10 \\ 1, & \text{otherwise} \end{cases} \qquad (5.5.17)$$

where R^* can be obtained from equation (5.5.10).

This formula is used to predict the results of Trial 7 of the Thorney Island experiment (Spicer and Havens 1985), as shown in figure 5.5.5. The agreement is satisfactory although considerable scattering of measurements is observed.

---

[20] The decay of concentration beyond $R^*=10$ is dominated by atmospheric turbulence and has been studied by Fay et al. (1983).

5.6. CONCLUSION

The collapse of a dense cloud after its sudden release is first studied numerically. The numerical model, based on the assumption that the cloud buoyancy dominates the flow and on the application of the transport element methods, simulates well the early dispersion process including the formation and evolution of a frontal vortex ring and the rings behind it. The numerical results show that these vortex rings are responsible for the dense cloud spreading and dispersion. The entrainment of air into the dense cloud occurs mainly on the top side through the engulfment of air by the vortex rings developed along the cloud surface. The dynamics is explained through the mechanism of baroclinic vorticity generation.

The physics, revealed by the numerical results, laboratory and field observations, suggest the entrainment hypothesis that the amount of entrainment is proportional to the extended surface area of the cloud. Based on this hypothesis, a simple analytical model is developed to better characterize the major features of the cloud dispersion. Two empirical constants built into the model are determined from the comparison with physical experiments with value $\alpha^*=1.7$, $\beta^*=1.3$. Analytical solutions for the extended cloud area, equation (5.5.10), and the maximum concentrations, equation (5.5.17), well fit the measurements of dense gas releases with various initial cloud volumes, density ratios and aspect ratios. These results provided accurate quantitative information for the development of later stage models describing the cloud dispersion when the atmospheric turbulence dominates.

It should be pointed out that the results of this work can also be applied to the spreading of hot fire gases under ceilings. The effects neglected in this work, such as, atmospheric turbulence, heat transfer, and ground terrain, will be investigated in further work.

REFERENCES

Britter R. E. (1989) Atmospheric dispersion of dense gases, *Ann. Rev. Fluid Mech.*, **21**, 317-344.

Byggstoyl S. and Saetran L. R. (1983) An integral model for gravity spreading of heavy gas clouds, *Atmos. Environ.*, **8**, 1615-1620.

Carn K. K. (1987) Estimates of the mean concentration and variance for the Thorney Island phase I dense gas dispersion experiments, *J. Haz. Mat.*, **16**, 75-101.

Chan S. T., Ermak D. L. and Morris L. K. (1987) FEM3 model simulation of selected Thorney Island Phase I trials, *J of Haz. Mat*, **16**, 267-292.

Eidsvik K. J. (1980) A model for heavy gas dispersion in the atmosphere, *Atmos. Environ.*, **14**, 769-777.

England W. G., Teuscher L. H., Hauser L. E., Freeman B. E. (1978) Atmospheric dispersion of liquefied natural gas vapor clouds using SIGMET, a three-dimensional time-dependent hydrodynamic computer model. *Proceedings of the 1978 Heat Transfer and Fluid Mechanics Institute* (ed. by C.T. Crowe and W. L. Grosshandler), 4-20, Stanford Univ. Press., Stanford, CA.

Ermak D. L. and Chan S. T. (1988) Recent development on the FEM 3 and SLAB atmospheric dispersion models, Puttock J. S. ed., *Stably stratified flow and dense gas dispersion*, Oxford: Clarendon, 264-284.

Fay J. A. (1980) Gravitational spread and dilution of heavy vapor clouds, *Second international symposium on stratified flows*. The Norwegian Institute of Technology, Trondheim, Norway.

Fay J. A. (1982) Some unsolved problems of LNG vapor dispersion. MIT-GRI, *LNG Safety and Research Workshop*. Gas Research Institute, Chicago.

Fay J. A. and Ranck D. A. (1983) Comparison of experiments on dense gas cloud dispersion, *Atmos. Environ.*, **17**, 239-248.

Ghoniem A. F. and Martins, L.-F, (1991) Effect of velocity ratio on bluffbody dynamics; steady and transitional regimes, AIAA-91-0580, AIAA, 370 L'Enfant Promenade, S.W., Washington, D.C. 20024.

Ghoniem A. F., Zhang X., Knio O. M., Baum H., and Rehm R., (1993) Dispersion and deposition of smoke plumes generated in massive fires, *J. of Haz. Mat.* **33**, 275-293.

Hanna S. R. and Drivas P. J. (1987) Vapor cloud dispersion models. *Rep. Cent. Chem. Process Saf.*, AIChE, New York.

Havens J. A., Schreurs P. J. and Spicer T. O. (1987) Analysis and Simulation of Thorney Island Trial 34, *Journal of Hazardous Materials*, **16**, 139-148.

Havens J. A. and Spicer T.O. (1985) Development of an atmospheric dispersion model for heavier-than-air gas mixtures, Volume II: Laboratory calm air heavy gas dispersion experiments, No. CG-D-23-85.

Jacobsen O. and Magnussen B. F. (1987) 3-D Numerical simulation of heavy gas dispersion, *Journal of Hazardous Materials*, **16**, 215-230.

Johnson D. R. (1985) Thorney Island Trials: systems development and operational procedures, McQuaid J. ed., *Heavy gas dispersion trials at Thorney Island*, Elsevier, 35-64.

Knio O. M. and Ghoniem A. F. (1990) Numerical study of a three-dimensional vortex method, *J. Comput. Phys.*, **86**, 75-106.

Knio O. M. and Ghoniem A. F. (1991) Three-dimensional vortex simulation of rollup and entrainment in a shear layer, *J. Comput. Phys.*, **97**, 172-223.

Krishnan A. and Ghoniem A. F. (1992) Simulation of rollup and mixing in Rayleigh-Taylor flow using the transport element method, *J. Comput. Phys.*, **99**, 1-27.

Lamb H. (1945) *Hydrodynamics*, 6th Edition, Dover Publications, New York.

Matthias C. S. (1992) Dispersion of a dense cylindrical cloud in a turbulent atmosphere, *J. Haz. Mat.* **30**, 117-150.

McQuaid J. (1985) ed., *Heavy Gas Dispersion Trials at Thorney Island*, Elsevier, xii+435p.

Norbury J. (1973) A family of steady vortex rings, *J. Fluid Mech.*, 57, 417-431.

Puttock J. S. (1988a) ed., *Stably Stratified Flow and Dense Gas Dispersion*, Clarendon Press, Oxford, xiv+430p.

Puttock J. S. (1988) A model for gravity-dominated dispersion of dense-gas clouds, Puttock J. S. ed., *Stably stratified flow and dense gas dispersion*, Oxford: Clarendon, 233-260.

Rottman J. W. and Hunt J. C. R. (1985) The initial and gravity-spreading phases of heavy gas dispersion: comparison of models with phase I data, McQuaid J. ed., *Heavy Gas Dispersion Trials at Thorney Island*, Elsevier, 261-279.

Saffman P. G. (1970) The velocity of viscous vortex rings, *Studies in Appl. Math.*, **49**, 371-380.

Spicer T. O. and Havens J. A. (1985) Modeling the Phase I Thorney Island Experiments, McQuaid J. ed., *Heavy Gas Dispersion Trials at Thorney Island*, Elsevier, 237-260.

van Ulden A. P. (1984) A new bulk model for dense gas dispersion: two-dimensional spread in still air. Eds. Ooms G. and Tennekes H., Atmospheric dispersion of heavy gases and small particles, Spring-Verlag, 419-440.

van Ulden A. P. (1988) The spreading and mixing of a dense cloud in still air, Puttock J.S. ed., *Stably stratified flow and dense gas dispersion*, Oxford: Clarendon, 141-168.

Yih C-S. (1965) *Dynamics of Nonhomogeneous Fluids*, Macmillan.

Table 5.1. Parameters used in the numerical experiments

Case	D_o/H_o	ρ_o/ρ_a	$R_o=D_o/2$	H_o
1	1	1.5	$1/\sqrt{2\pi}$	$\sqrt{2/\pi}$
2	2	1.5	$\sqrt[3]{2}/\sqrt{2\pi}$	$\sqrt[3]{2}/\sqrt{2\pi}$
3	3	1.5	$\sqrt[3]{3}/\sqrt{2\pi}$	$2\sqrt[3]{3}/3\sqrt{2\pi}$
4	1	4	$1/\sqrt{2\pi}$	$\sqrt{2/\pi}$
5	1	3	$1/\sqrt{2\pi}$	$\sqrt{2/\pi}$

(a)

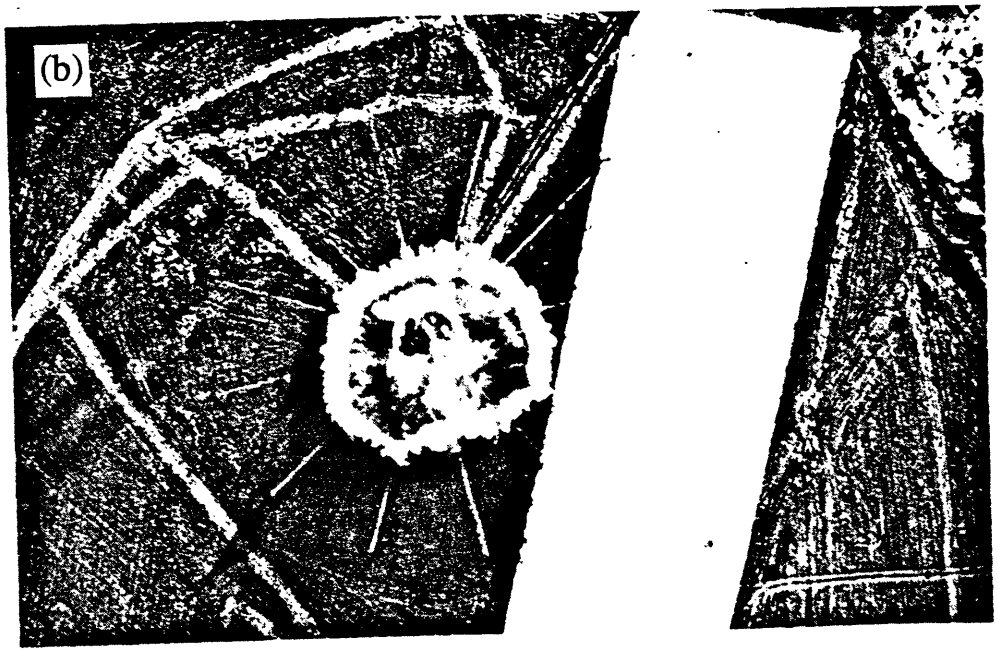

Figure 5.1.1. The Thorney Island experiment: instantaneous dense gas release (a) viewed at ground level, (b) viewed from overhead, taken from Johnson (1985).

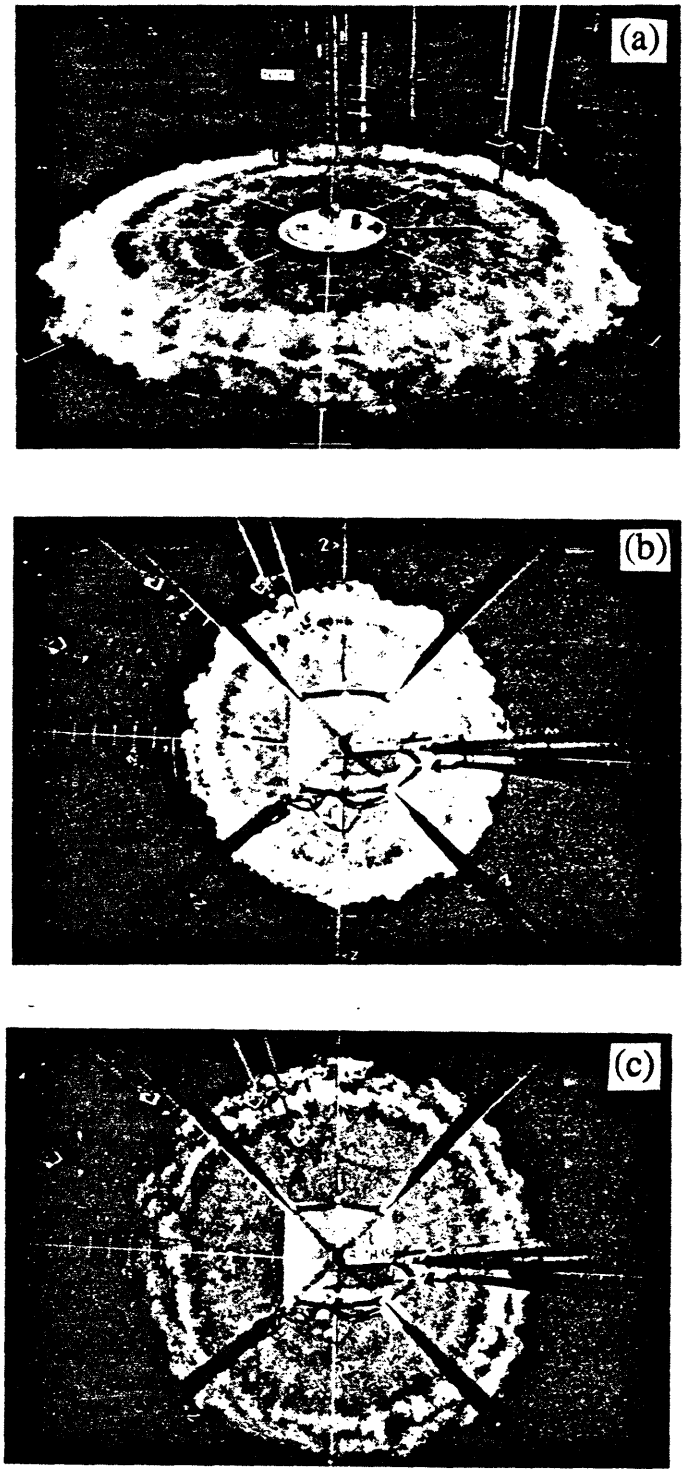

Figure 5.1.2. A case of laboratory experiment observed at different view angles and times after the instantaneous release of 135 liter Freon-12/air mixtures: (a) $t=1.2$s; (b) $t=1.2$s; (c) $t=1.7$s, taken from Spicer and Havens (1985).

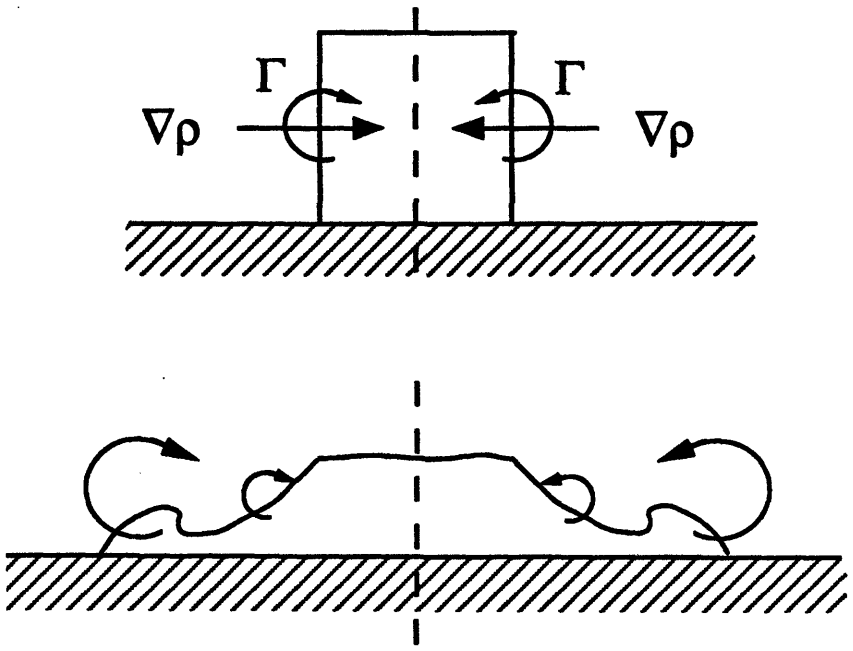

Figure 5.2.1. A schematic diagram showing the mechanism of baroclinic vorticity generation.

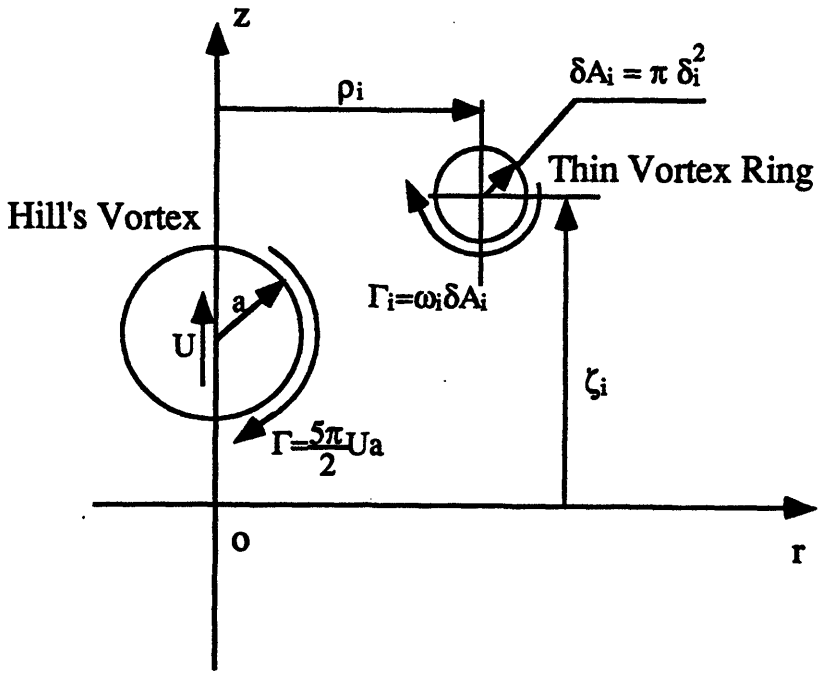

Figure 5.3.1. A schematic diagram describing the notations for the vortex ring element and Hill's spherical vortex.

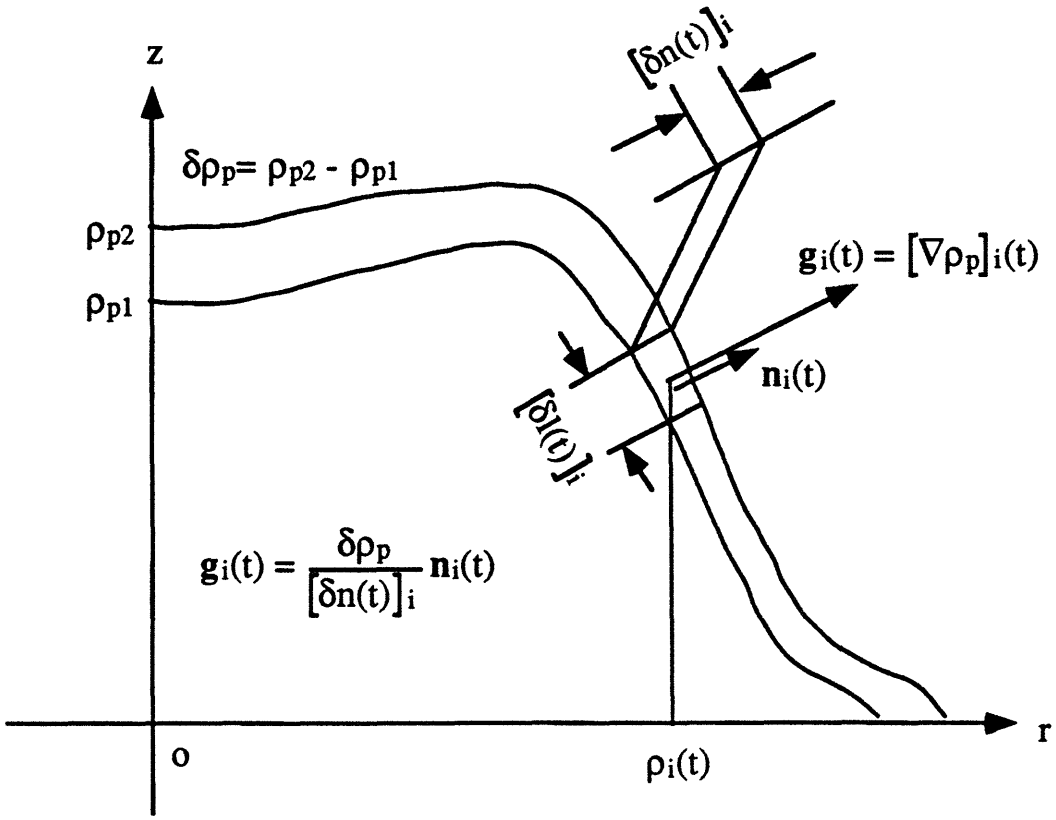

Figure 5.3.2. A schematic diagram showing the notations used for the derivation of transport element method in axisymmetric flow with variable density.

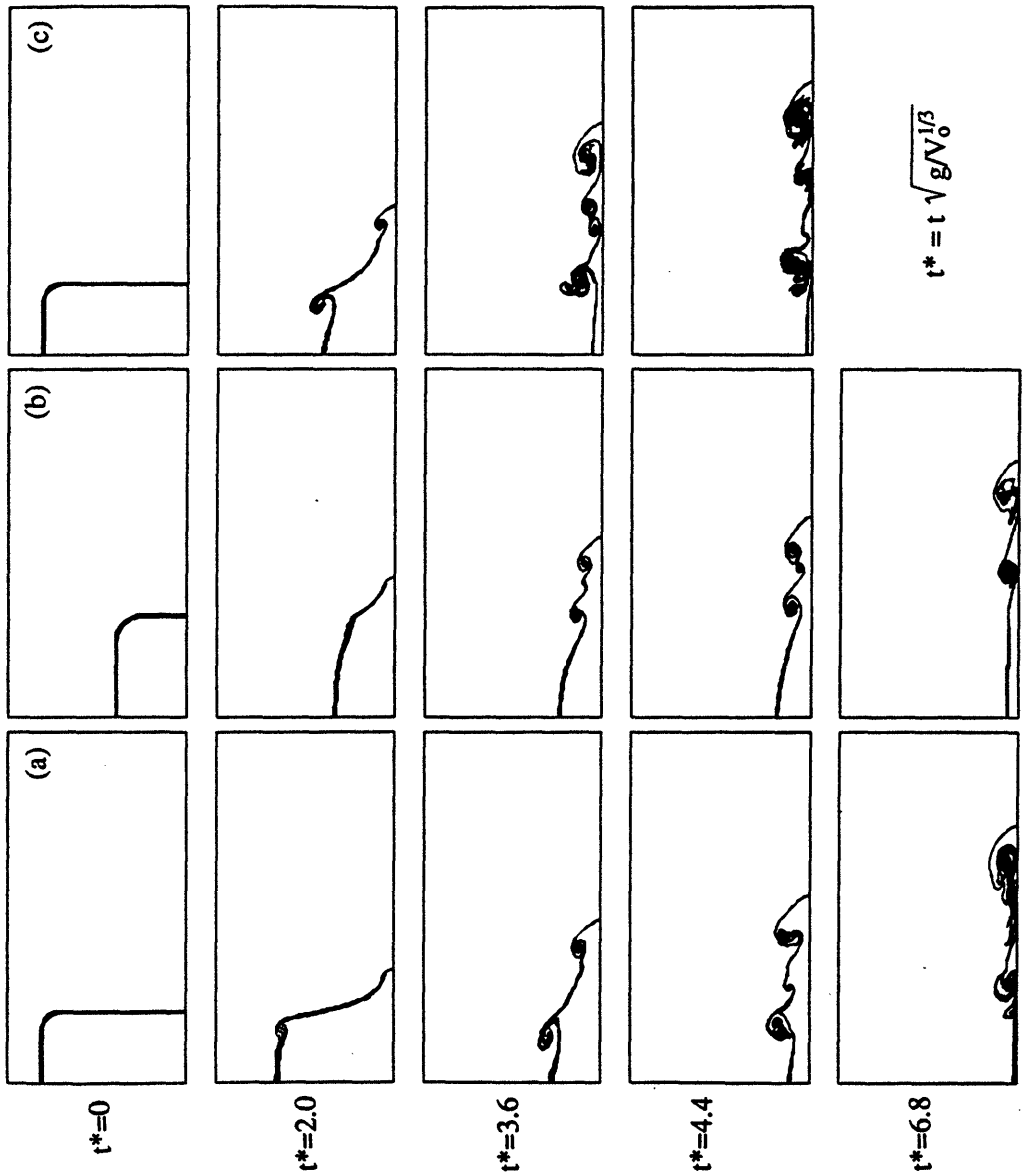

Figure 5.4.1. Results of three numerical simulations on the evolution of dense cloud collapse and spread in terms of cloud shape; (a) Case 1: $D_o/H_o=1$, $\rho_o/\rho_a = 1.5$; (b) Case 3: $D_o/H_o=3$; $\rho_o/\rho_a = 1.5$; and, (c) Case 4: $D_o/H_o=1$, $\rho_o/\rho_a = 4$.

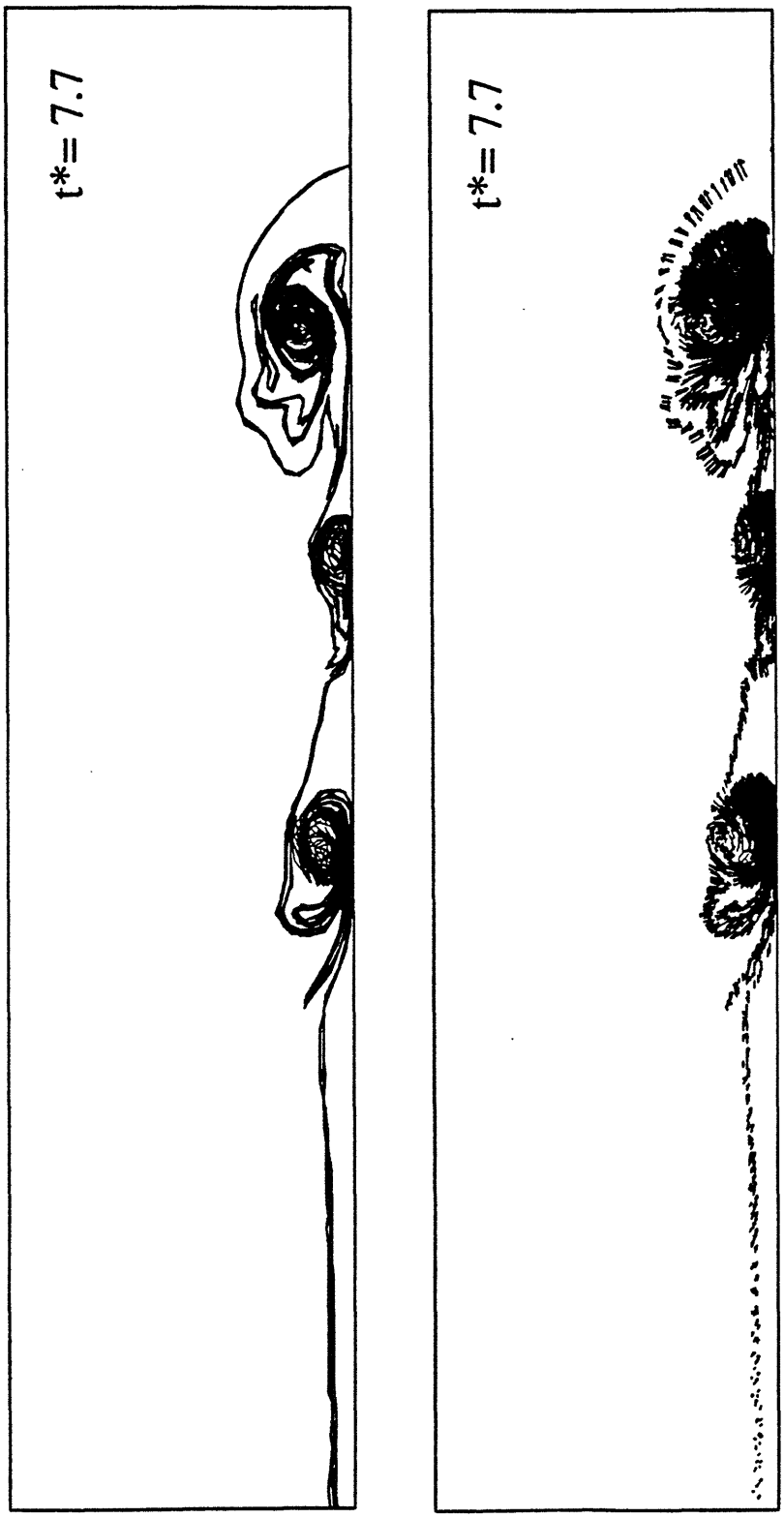

Figure 5.4.2. The cross sections of dense cloud for Case 5: $D_o/H_o=1$, $\rho_o/\rho_a = 3$ at $t^*=7.7$; (a) the cloud shape; (b) the positions and velocities of the computational elements.

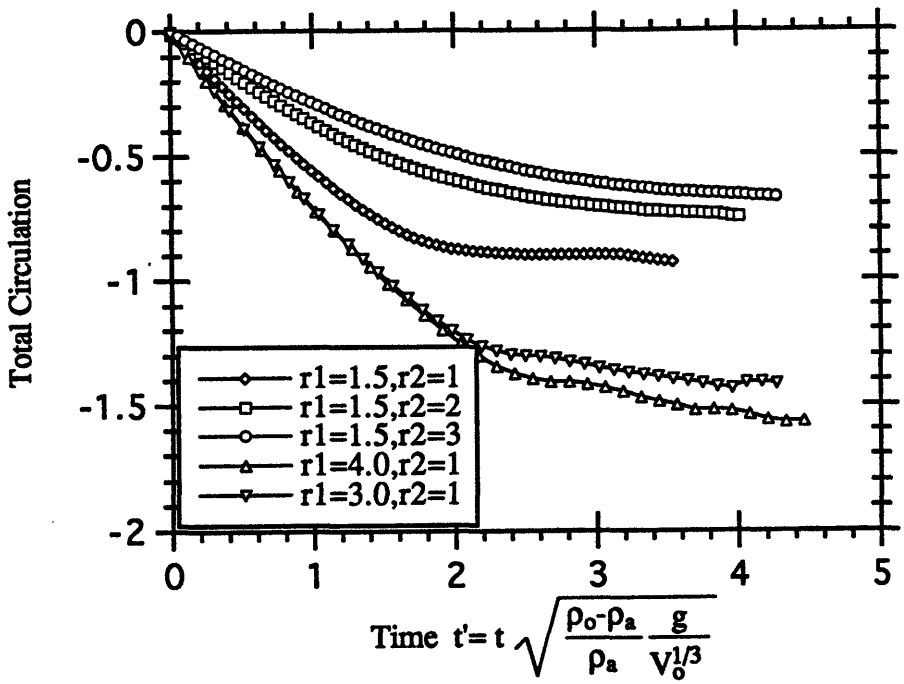

Figure 5.4.3. The evolution of the total circulation integrated over a meridional plane during the dense cloud collapse for the five cases, where $r1=\rho_o/\rho_a$ and $r2=D_o/H_o$.

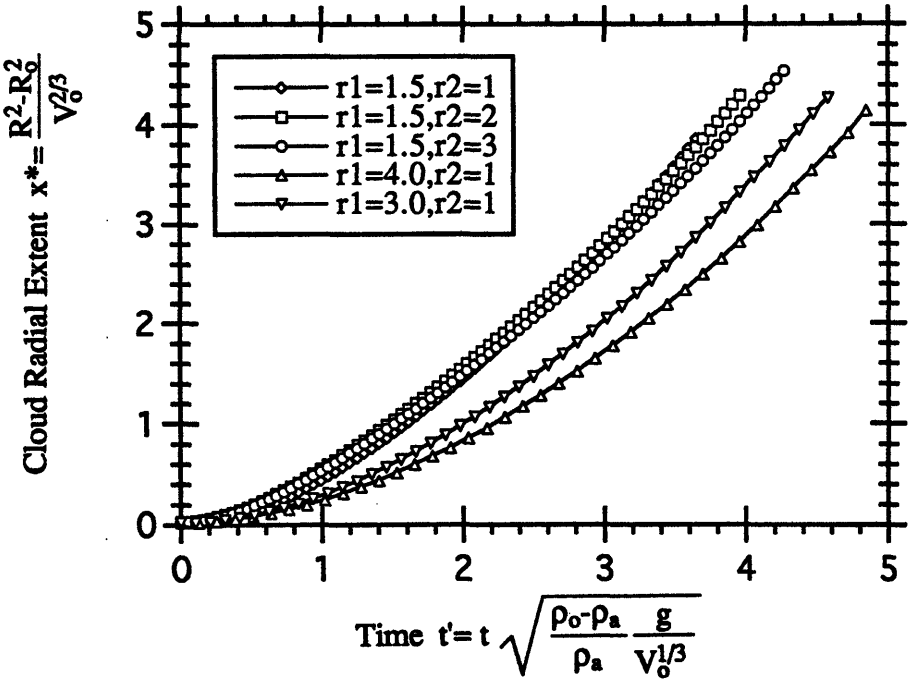

Figure 5.4.4. The increase in the top cloud area after the collapse of the dense cloud versus time, $t' \equiv t\sqrt{\frac{\rho_o-\rho_a}{\rho_a}\frac{g}{V_o^{1/3}}}$, for five cases, where $r1=\rho_o/\rho_a$ and $r2=D_o/H_o$.

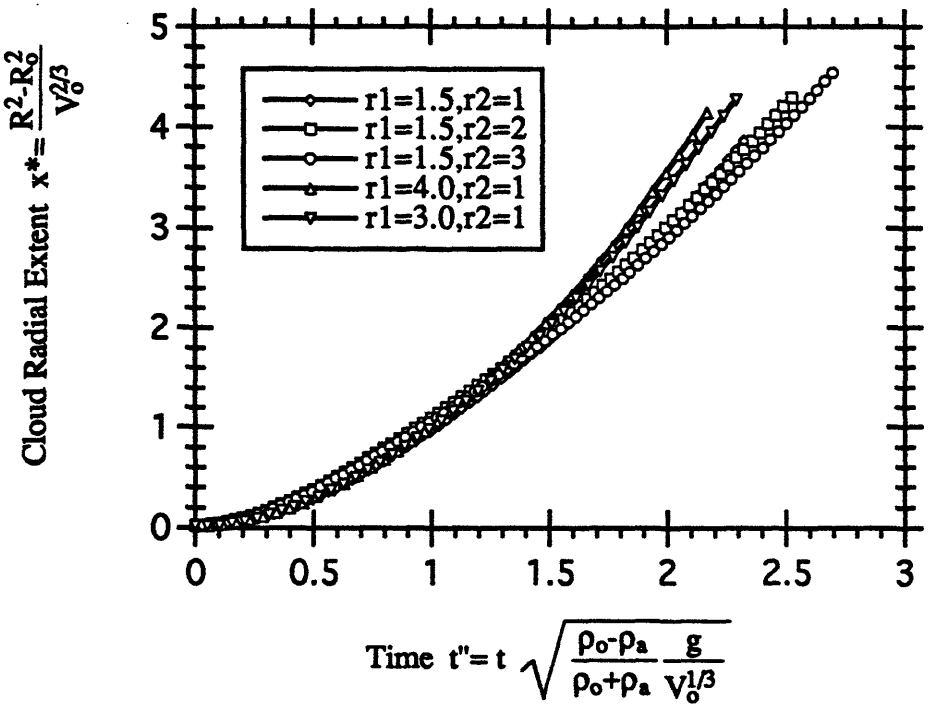

Figure 5.4.5. The increase in the top cloud area after the collapse of the dense cloud versus time, $t'' \equiv t\sqrt{\frac{\rho_o-\rho_a}{\rho_o+\rho_a}\frac{g}{V_o^{1/3}}}$ for five cases, where $r1=\rho_d/\rho_a$ and $r2=D_d/H_o$.

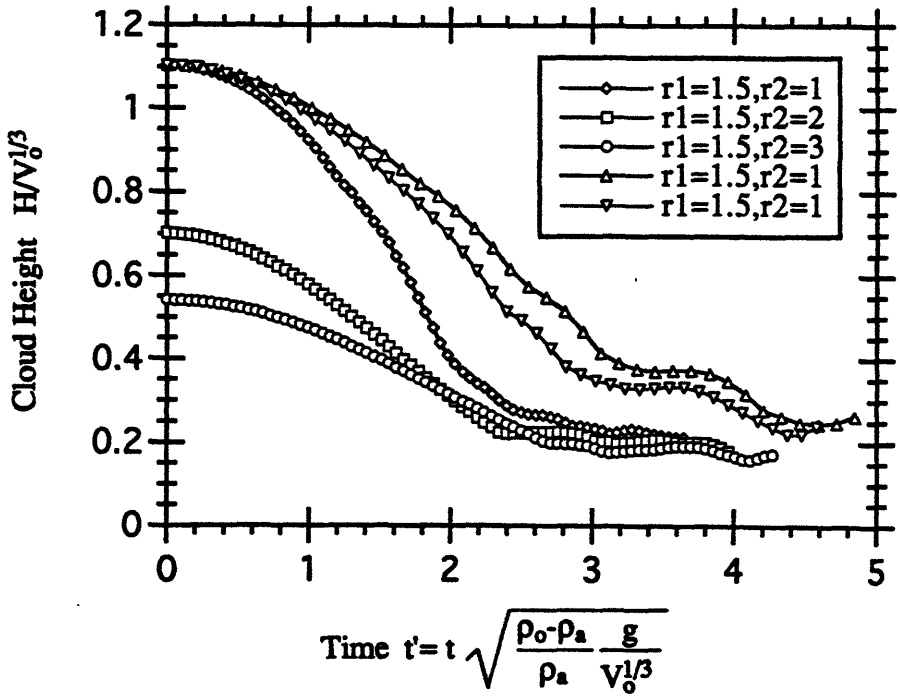

Figure 5.4.6. The maximum could height versus time for five cases, where $r1=\rho_d/\rho_a$ and $r2=D_d/H_o$.

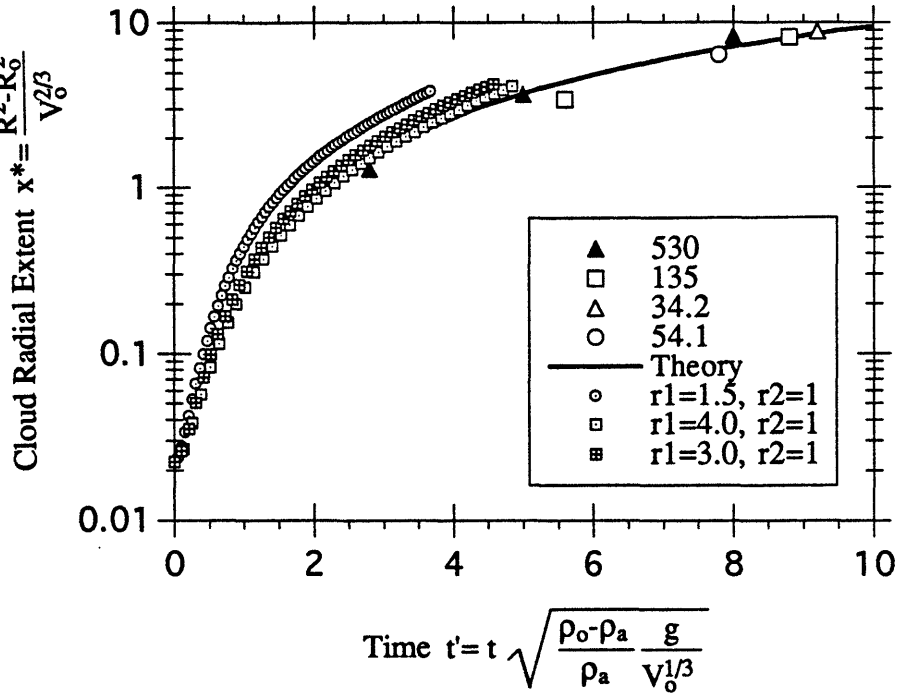

Figure 5.4.7. The increased top cloud area versus time. Comparison among numerical results, theoretical predictions, and laboratory measurements of clouds with, $\rho_o/\rho_a = 4.19$, $D_o/H_o = 1.0$, and volumes as shown in liters, where $r1=\rho_o/\rho_a$ and $r2=D_o/H_o$.

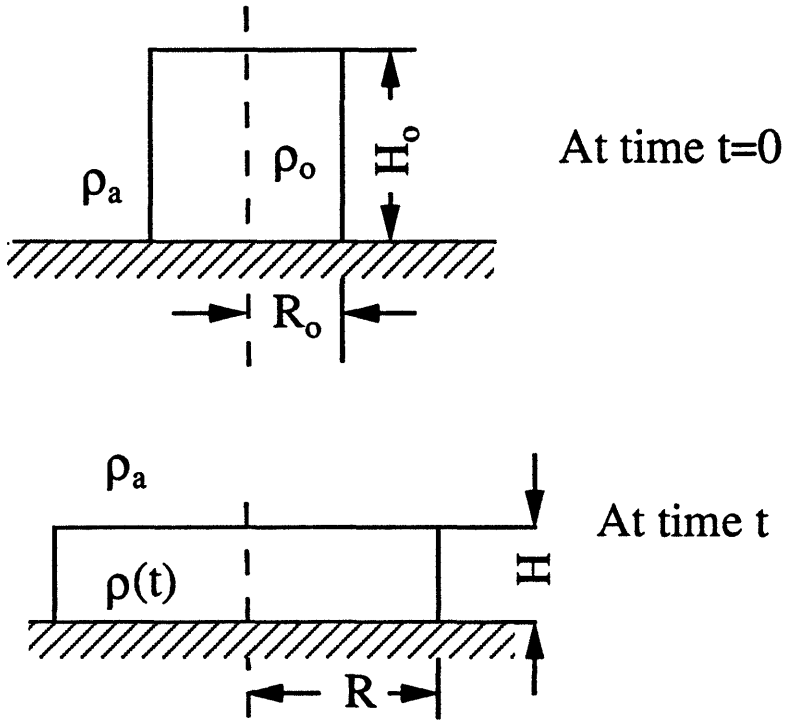

Figure 5.5.1. A schematic diagram showing the analytical model for the dispersion of instantaneously released dense cloud.

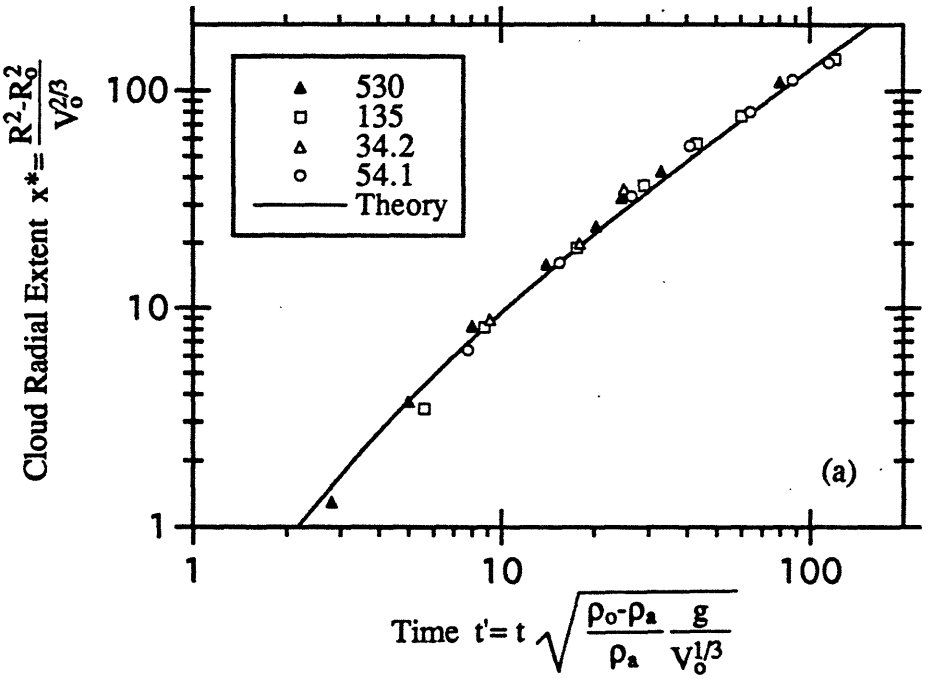
Cloud Radial Extent $x^*=\frac{R^2-R_o^2}{V_o^{2/3}}$
100
10
1
1
10
100
530
135
34.2
54.1
Theory
(a)
Time $t'=t\sqrt{\frac{\rho_o-\rho_a}{\rho_a}\frac{g}{V_o^{1/3}}}$

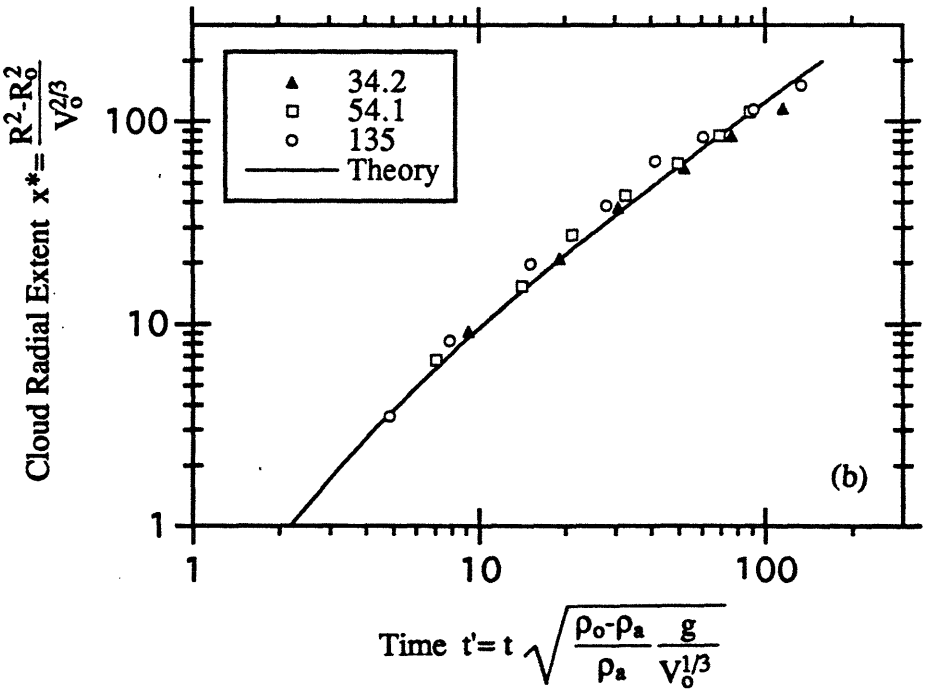
Cloud Radial Extent $x^*=\frac{R^2-R_o^2}{V_o^{2/3}}$
100
10
1
1
10
100
34.2
54.1
135
Theory
(b)
Time $t'=t\sqrt{\frac{\rho_o-\rho_a}{\rho_a}\frac{g}{V_o^{1/3}}}$

Figure 5.5.2.

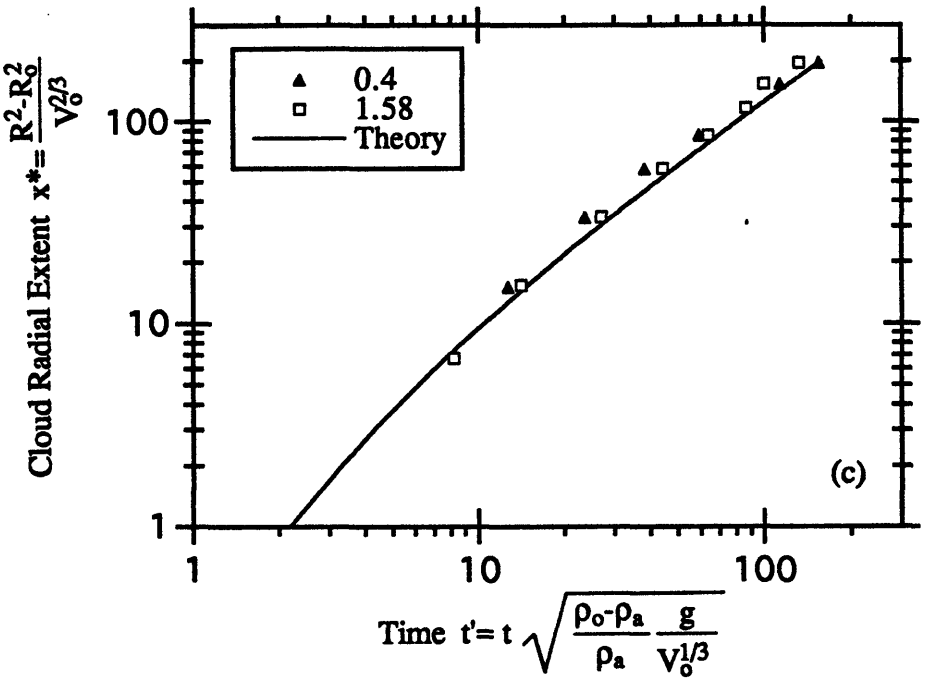

Figure 5.5.2. The increase in the top side of the cloud area versus time. Comparison between analytical model result and the laboratory measurements of: (a) $D_o/H_o = 1.0$, $\rho_o/\rho_a = 4.19$, with different initial cloud volumes (liters); (b) $D_o/H_o = 1.0$, $\rho_o/\rho_a = 2.92$, with different initial cloud volumes (liters); and (c) $\rho_o/\rho_a = 4.19$, $V_o = 54.1$ liters, with different initial aspect ratios (H_o/D_o).

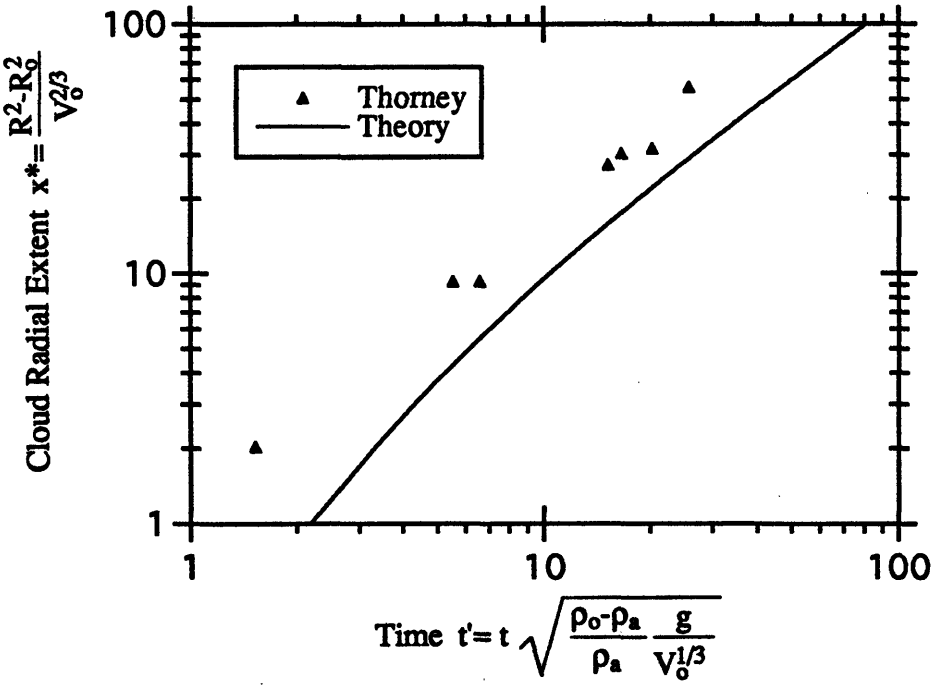

Figure 5.5.3. The increase in the top side of the cloud area versus time. Comparison between Thorney Island experimental measurements and theoretical model predictions.

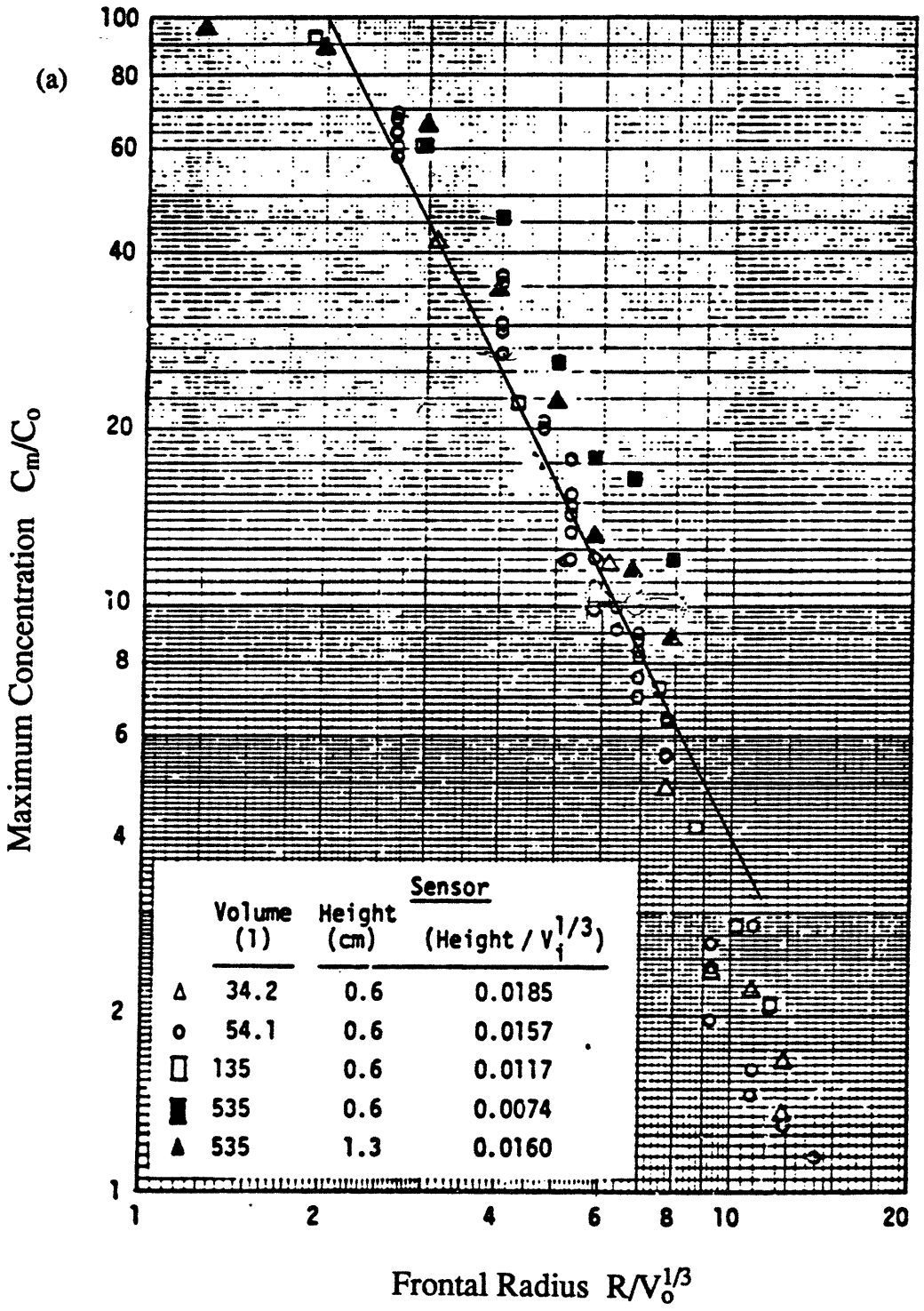
(a)
Maximum Concentration C_m/C_o
Frontal Radius $R/V_o^{1/3}$
100
80
60
40
20
10
8
6
4
2
1
1
2
4
6
8
10
20
Sensor
Volume (l)
Height (cm)
(Height / $V_l^{1/3}$)
Δ 34.2 0.6 0.0185
o 54.1 0.6 0.0157
□ 135 0.6 0.0117
■ 535 0.6 0.0074
▲ 535 1.3 0.0160

Figure 5.5.4.

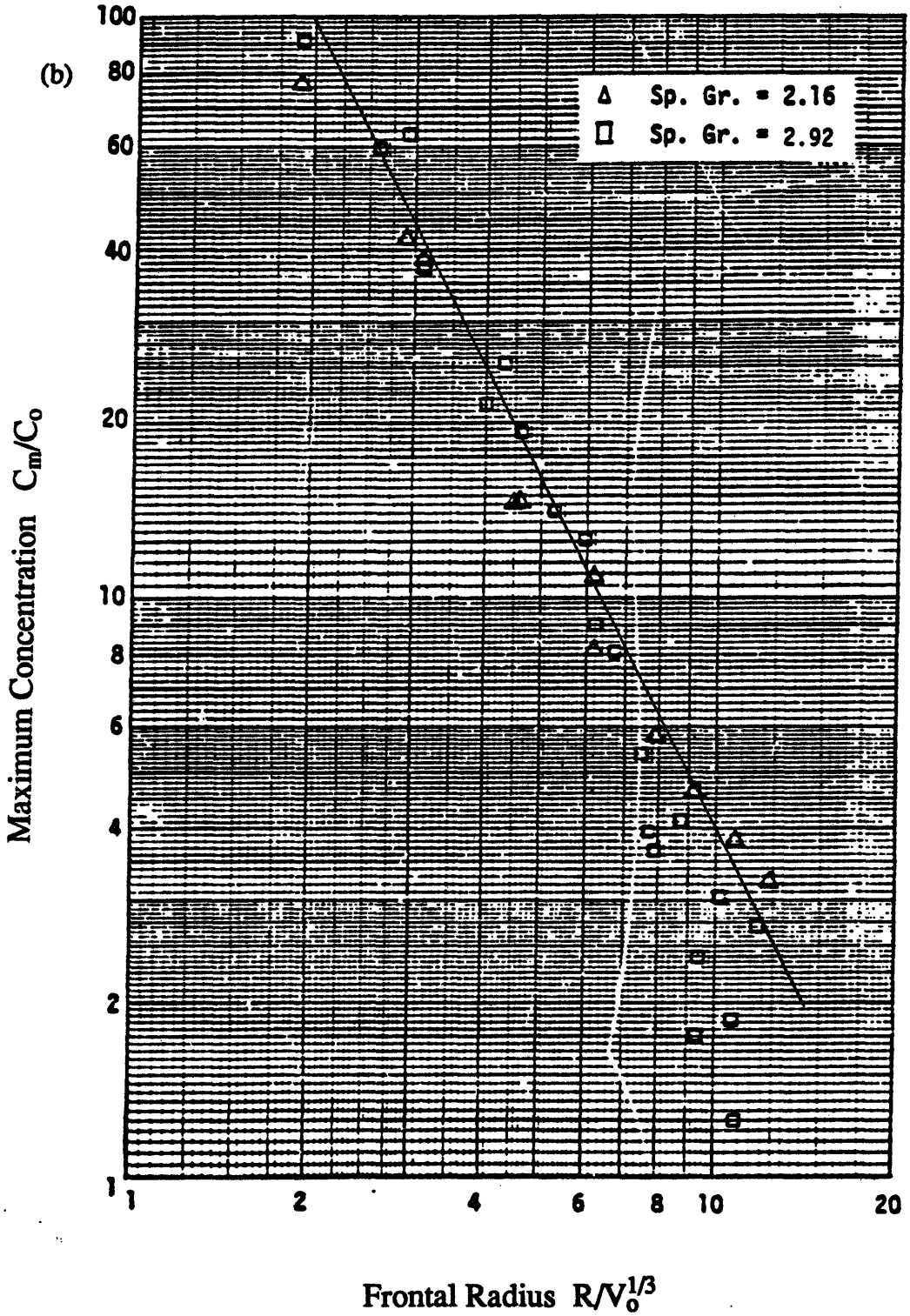
(b)
Δ Sp. Gr. = 2.16
□ Sp. Gr. = 2.92
Maximum Concentration C_m/C_o
Frontal Radius $R/V_o^{1/3}$
100
80
60
40
20
10
8
6
4
2
1
1
2
4
6
8
10
20

Figure 5.5.4.

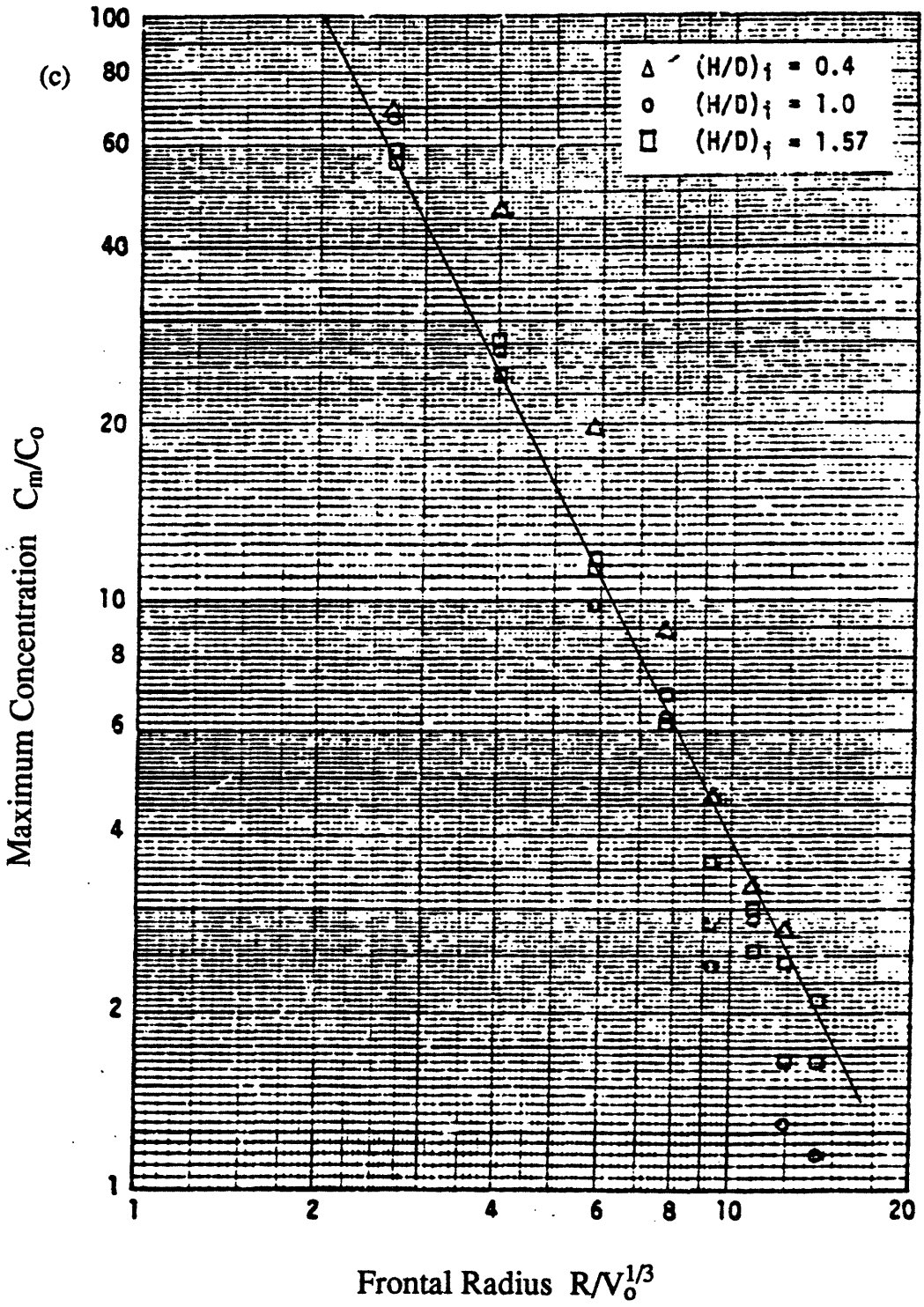

Figure 5.5.4. The maximum concentration of the spreading dense cloud versus the radius of the front. Comparison between the analytical model results (solid lines) and the laboratory measurements of: (a) $D_o/H_o=1.0$, $\rho_o/\rho_a = 4.19$, with different initial cloud volumes (liters); (b) $D_o/H_o=1.0$, with different initial density ratios (ρ_o/ρ_a); and (c) $\rho_o/\rho_a = 4.19$, $V_o=54.1$ liters, with different initial aspect ratios (H_o/D_o).

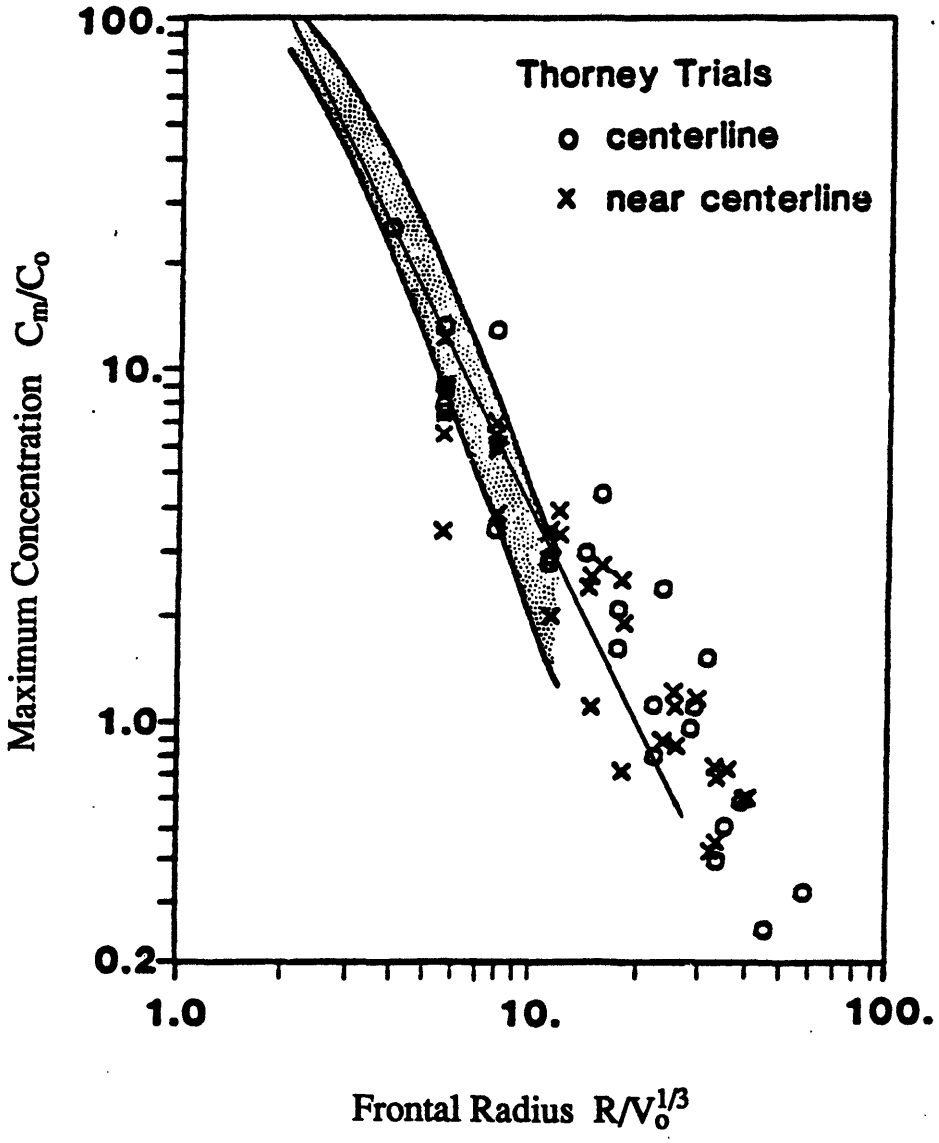

Figure 5.5.5. The maximum dense cloud concentration versus the radius of the cloud front. Comparison between Thorney Island experimental measurements with model predictions (solid line). Shaded area represents the laboratory measurements of Spicer and Havens (1985).

CHAPTER 6

A COLLECTION OF PHOTOGRAPHS AND DIAGRAMS ON PLUME RISE AND DISPERSION

Figure 6.1. Plume generated by large oil tank fire in density-stratified environment, taken from List (1959). The plume trajectory shows that it rises, overshoots and finally stabilizes at an equilibrium height.

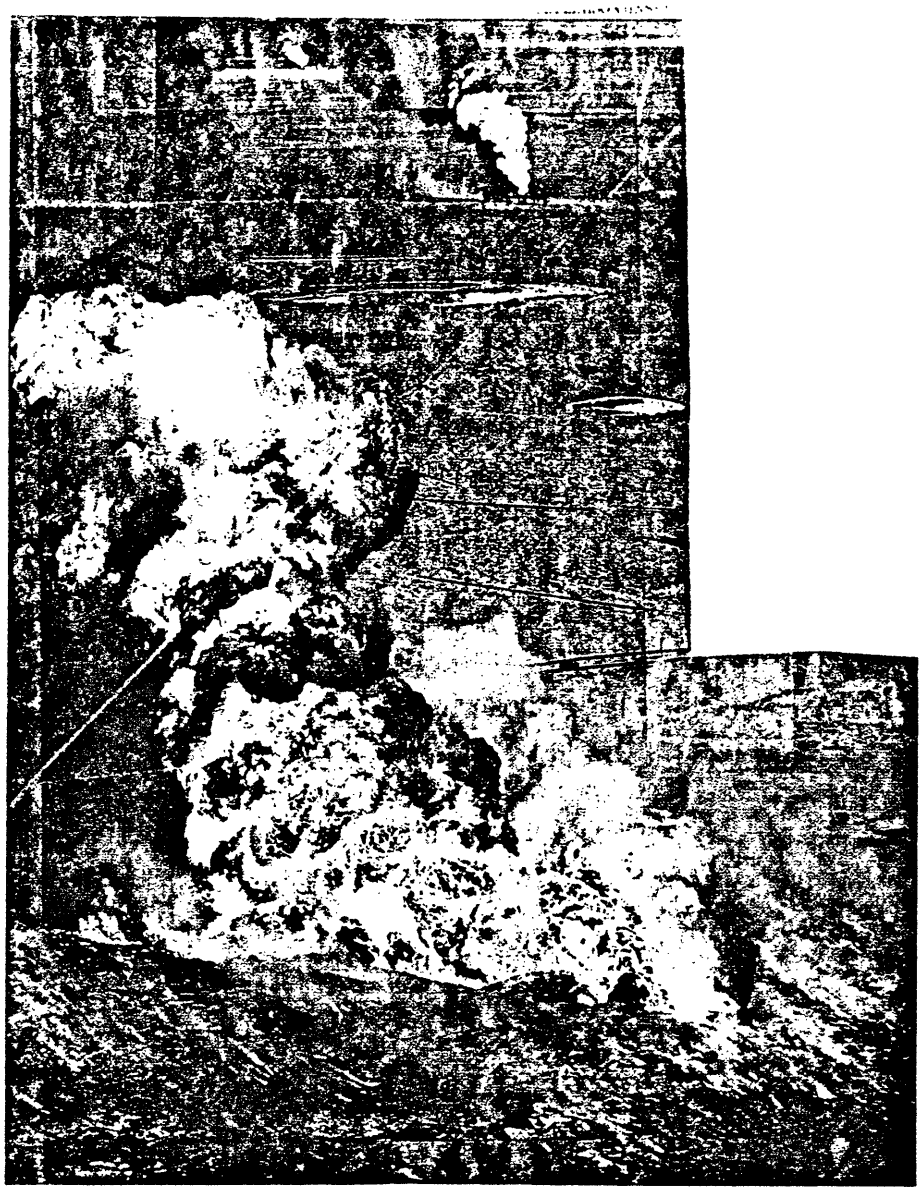

Figure 6.2. A typical large, buoyant plume, generated by burning oil spill at sea surface, taken during the Gulf War, from *TIME* magazine.

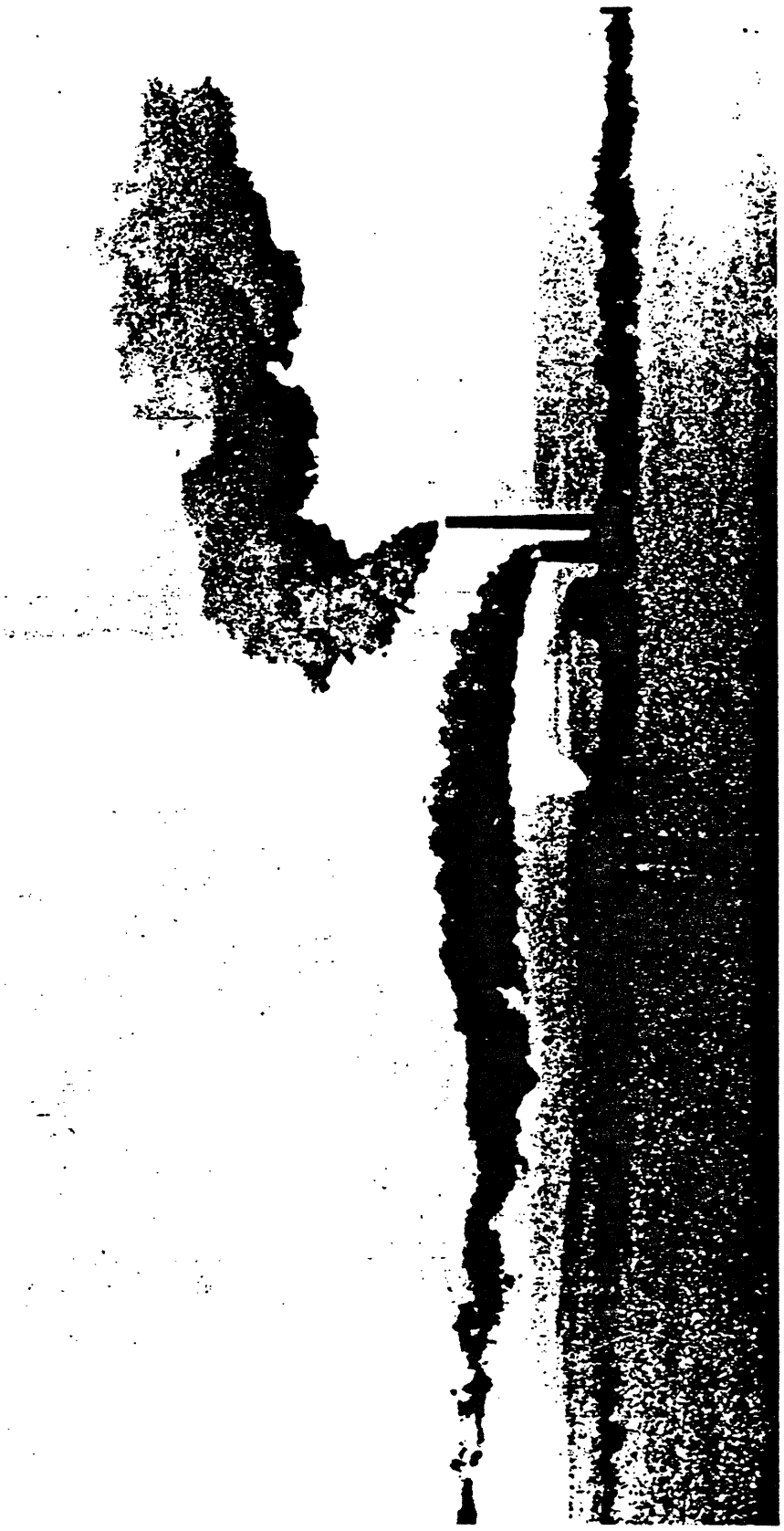

Figure 6.3. The trajectories of plumes in an environment where both density and wind are stratified. The stacks are 75m and 150m high in Salem, Massachusetts. Taken by Ralph Turcotte on a very cold February morning, from *Beverly Times*.

Figure 6.4. A photograph of the underside of fire plume taken 600m downwind location, looking upward and upwind, from Church, Snow and Dessens (1980). This plume clearly shows the bifurcation into a pair of large counterrotating roll vortices that act to move air up and into the plume along its centerline.

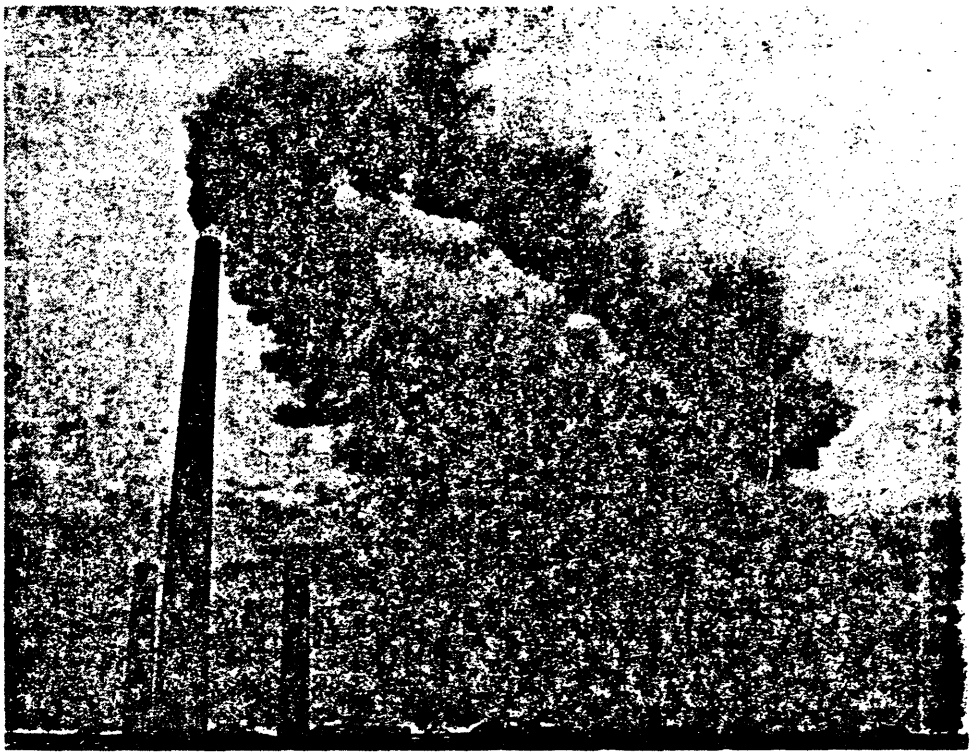

Figure 6.5. Bifurcation of buoyant plume from tall industry stack, from Fanaki (1975).

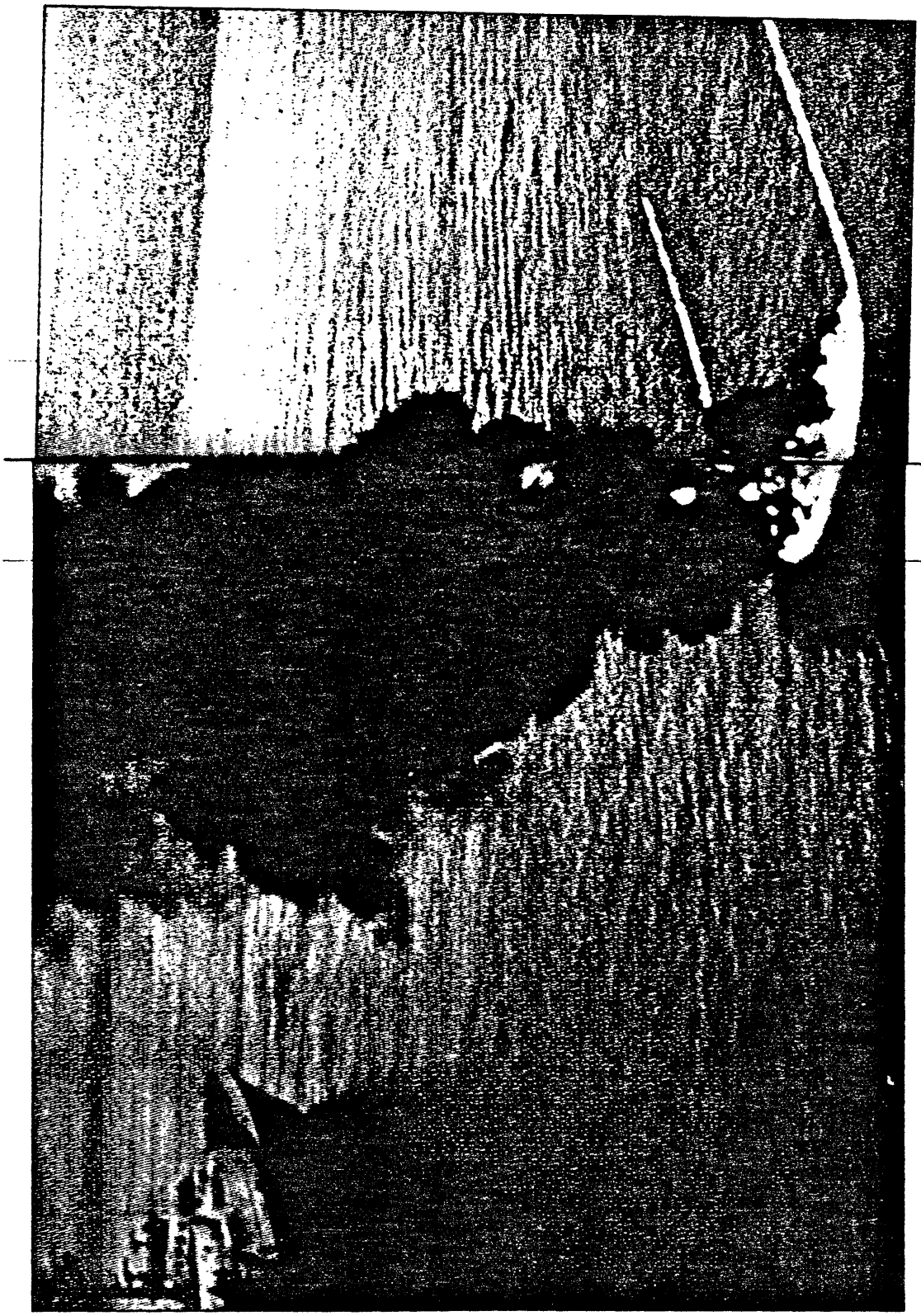

Figure 6.6. Field experiment on the burning of spilled oil at sea surface, from Busch (1993).

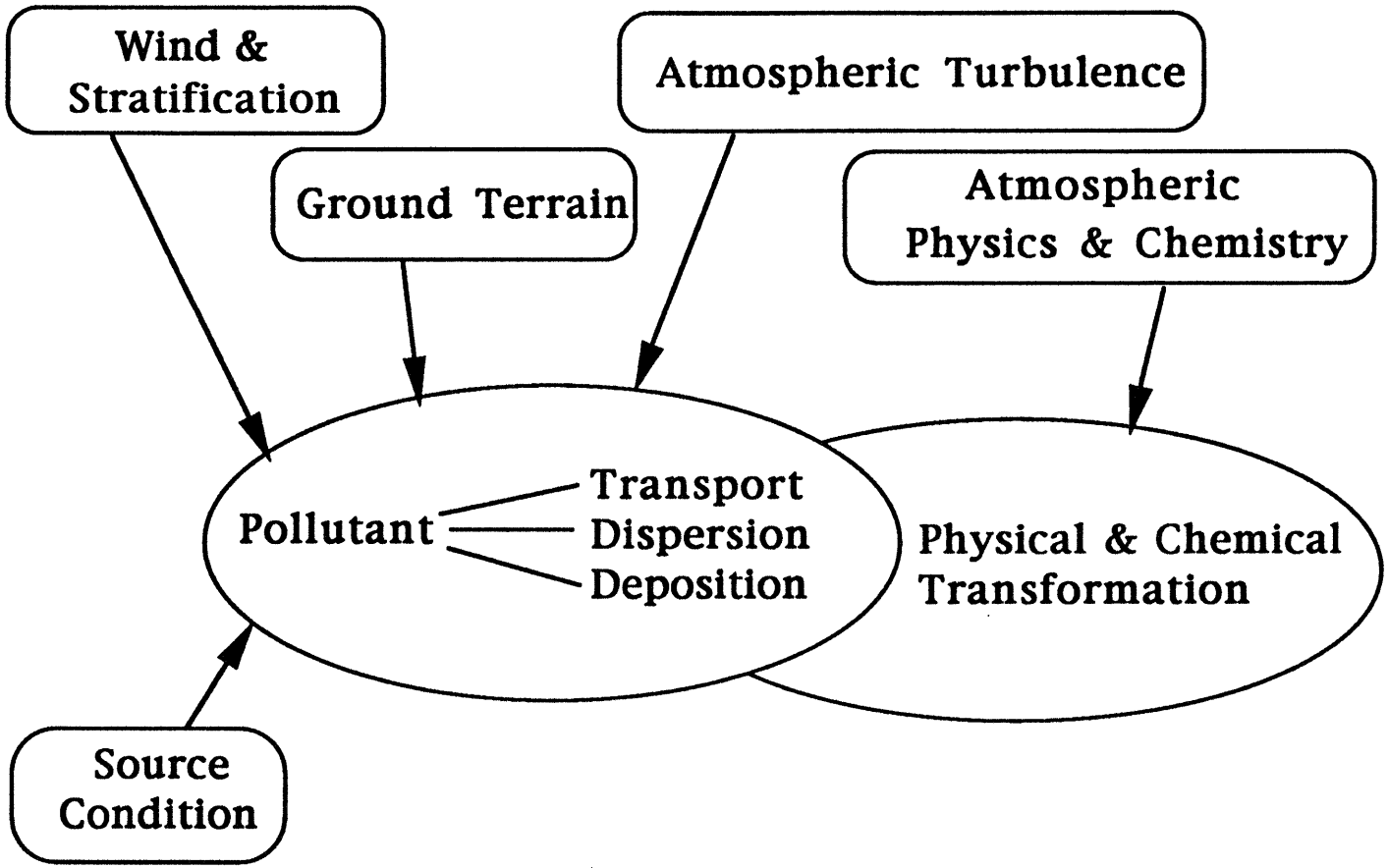

Figure 6.7. A schematic diagram showing the important factors in the plume dispersion modeling.

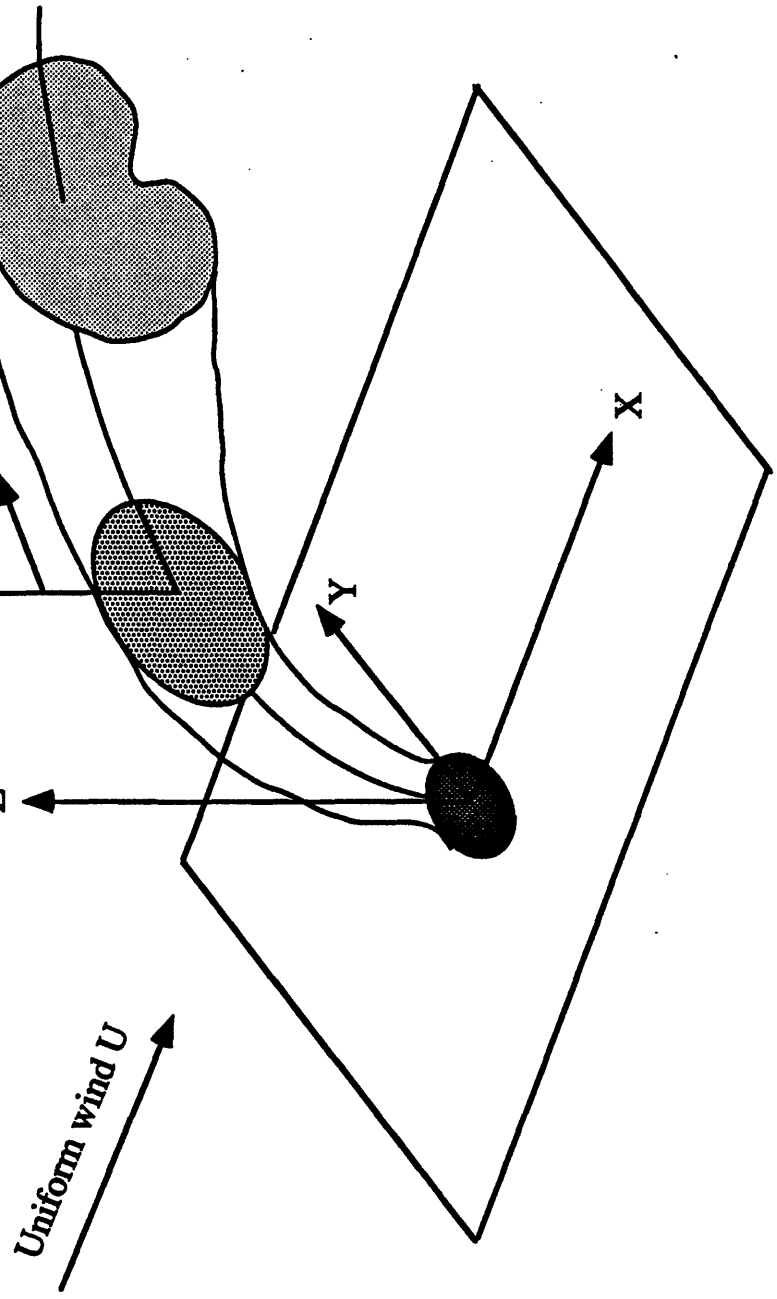

Figure 6.8. A schematic diagram showing the plume rise and dispersion problem and coordinate system. Chapter 1, 2 and 3 model the plume from stage A, where plume translates with ambient wind speed in the x direction, to a distance where the atmospheric turbulence becomes important.

REFERENCES

Busch L. (1993) To burn or not to burn, *Technology review*, edited at the Massachusetts Institute of Technology, January, 18, 1993, 18-19.

Church C. R., Snow J. T. and Dessens J. (1980) Intense atmospheric vortices associated with a 1000 MW fire, *Bull. Am. Meteorol. Soc.*, **61**, 682-694.

Fanaki F. H. (1975) Experimental observations of a bifurcated buoyant plume, *Boundary-Layer meteorology*, **9**, 479-495.

List E. J. (1959) Mechanics of turbulent buoyant jets and plumes, Rodi W. ed., *Turbulent buoyant jets and plumes*, Pergamon, 1-68.